



SAPIENZA  
UNIVERSITÀ DI ROMA

## Advanced modeling of a micro solar CHP system for residential applications

Dipartimento di Ingegneria aeronautica, elettrica ed energetica  
Dottorato di Ricerca in ENERGIA E AMBIENTE – XXXIII Ciclo

Candidate

Roberto Tascioni  
ID number 1210923

Doctoral Advisor  
Prof. Emanuele Habib

Co-Advisors  
Prof. Enrico Bocci  
Prof. Luca Cioccolanti

February 2021

Dissertation defended on 2 February 2021  
in front of a Board of Examiners composed by:  
Prof. (chairman)  
Prof.  
Dr.

---

**Advanced modeling of a micro solar CHP system for residential applications**

Ph.D. thesis. Sapienza – University of Rome

ISBN: 000000000-0

© 2021 Roberto Tascioni. All rights reserved

This thesis has been typeset by L<sup>A</sup>T<sub>E</sub>X and the Sapthesis class.

Version: February 15, 2021

Author's email: [robeto.tascioni@uniroma1.it](mailto:robeto.tascioni@uniroma1.it)

*To*  
*my family* ♡



## Abstract

Nowadays, thanks to the Renewable Energy Resources (RES), the energy supply is shifting towards a hypothetical nearly zero emissions society. Distributed Energy Resources are the most promising way to integrate RES into the thermal and electrical grid, realizing the so-called 4<sup>th</sup> generation District Heating networks. In this dissertation a possible solution to the energy supply issues is shown, it is based on the most abundant resource, namely solar energy. The micro solar plant here analyzed was conceived and tested both in cogeneration and trigeneration, because this is one of the optimal configurations to efficiently convert a thermal power source. The design specifications concerning the system size agrees with other scientific research, thus remarking the feasibility of these choices. In this regard, although medium and large plants are available in this small market segmentation, many efforts have to be spent in order to reduce the investment cost and increase the electric efficiency of this kind of power plants. This dissertation investigates the current potential of such technology at this small scale trying to find rooms for improvement.

Nevertheless, few scientists investigate micro solar CHP plants, even less with latent heat thermal energy storage placed between the solar field and the power block. The basic plant solution consists of: (i) a Linear Fresnel Reflector (LFR of 80 kWth), (ii) a latent heat thermal storage (TES of 4h) and (iii) a micro Organic Rankine Cycle (ORC of 2 kWe). The system was designed for 250-300 °C, namely a reasonable temperature derived from technical and economical constraints.

The contribution in innovation of such micro CHP plant, leads to face up with many open research lines: (i) Phase Change Materials selection considering the toxicity, corrosion, stability after several thermal cycles, phase change temperature close to 250-280 °C, cost, thermal conductivity; (ii) heat pipes designed for withstand at mid-high temperature, ability to transfer heat into the storage medium; (iii) the maximization of the electric output of the micro ORC keeping a feasible cost; (iv) trying to find out novel rules to manage the energy system efficiently, maintaining high levels of reliability. Modeling solar ORC plants encompasses all the heat transfer problems, for example the most complicated ones regard the optical characterization of the LFR (far more complex than parabolic trough), or phase change: in the Heat Pipes, plate heat exchanger (ORC), phase change material etc. A trade-off between CPU burden and quality of the output results was found. For this purpose, ad-hoc subroutines for each subsystem were written in MATLAB and the numerical investigations accomplished to characterize the plant performance with the specific degree of accuracy. Particular attention was paid for modeling the dynamic behavior of most critical subsystems in order to increase the dynamic response fidelity of the system in light of the subsequent testing of the control system.

This dissertation shows the potential production of such kind of plants, for example with a mirror ground area of about 246 m<sup>2</sup>, in the city of Lerida (Spain), the annual electric and thermal energy production is about 6500 kWh and 58,800 kWh respectively. Preliminary numerical investigations showed high thermal losses of the pipelines, thus new mathematical models were developed to increase the precision of such results. Moreover, to reduce the wasted heat of the thermal storage,

due to its low State of Charge level (unexploitable by the ORC) a novel strategy for the thermal management was presented, it was able to increase 5 % the annual energy production. Coupling the simulation system with a building is it possible to assess the influence of the user demand on the system performance. More precisely, an additional low temperature storage was added in bottoming to the ORC and the heat source was used for space heating and space cooling. Moreover, an absorption chiller was added to recover the large wasted heat in summer seasons. The new set-points of the ORC cooling water and the non-contemporaneity between the thermal source and the user demand was taken into account to quantify the coverage level from solar energy, and hence the extra cooling and heating power required from the vapor compression pump and boiler respectively. Basically, the optimal number of apartments was found to cover as much as possible the required thermal and electrical demand with RES. A further investigation dealt with the inner wall temperature prediction of the receiver tube in the solar field, by its knowledge the plant can be operated in safer conditions avoiding thermal stress and getting a more accurate thermal efficiency. Finally, a communication framework for testing the plant control Hardware with the in the Loop approach was developed. An external control board was connected to the simulated plant to optimize preliminary control strategies. This study allowed to significantly reduce the time spent in designing the control architecture.

Concluding, the numerical investigations here accomplished underlined to what extent the thermal losses are critical in such kinds of plants and how they can be accounted for with more accuracy. Despite the high plant complexity and cost, in the trigeneration configuration it can be a valuable alternative to integrate conventional space heating, cooling and domestic hot water systems. The simulated plant can considerably reduce the control system design by means of Hardware in the Loop technique.

## Ringraziamenti

*Prendendo una citazione di Karl Popper: "le scienze esatte nascono per essere smentite", si può intuire come il processo di apprendimento non abbia mai fine. Abilità, preparazione, intuito, permettono di ottenere delle risposte, che fortunatamente (a mio parere) generano altre domande, dandoci la possibilità di affrontare sempre nuove sfide entusiasmanti alla scoperta del misterioso mondo che ci circonda.*

*Detto ciò, ringrazio il mio tutor **prof. Emanuele Habib**, che dal lontano 2010 ad oggi mi ha accompagnato in questo percorso di studi in Sapienza. Grazie ai suoi insegnamenti sono riuscito in qualche modo a migliorare l'approccio scientifico allo studio dei problemi, ad esempio migliorando notevolmente la qualità di alcuni studi che fin da subito sembravano avere poco valore scientifico, ma alla fine, dopo una attenta rielaborazione sono risultati invece molto interessanti. Grazie inoltre per avermi dato una mano sostanziosa a sbrigare le molte attività burocratiche, con le quali sono riuscito ad aggiudicarmi due bandi di avvio alla ricerca, mobilità del dottorato e l'accordo Erasmus+ con l'Università di Lleida.*

*Il **prof. Enrico Bocci** è stato un valido accompagnatore alla scoperta del mondo della ricerca insegnandomi davvero molte cose riguardo molteplici aspetti, a lui un grazie particolare. Difatti, se non avesse avuto fiducia nelle mie capacità non sarei qui a scrivere questo tema di ricerca che mi ha molto appassionato negli ultimi 4 anni.*

*Per quanto concerne invece il progetto Europeo a cui la mia ricerca si appoggia, ringrazio la **prof.ssa Alessia Arteconi** ed in particolare il **prof. Luca Cioccolanti**. Abbiamo scritto davvero molti articoli scientifici insieme, mi hanno trasmesso la metodologia necessaria per donare ai risultati ottenuti il loro reale valore nel relativo contesto di ricerca. Di non secondaria importanza invece è l'aspetto che riguarda il lavoro in team, le scadenze dei Work Packages del progetto EU hanno implicato ritmi serrati di lavoro, i risultati dovevano e devono essere programmati all'interno orizzonte temporale ben definito. Se a questo si aggiunge la collaborazione e l'interfacciamento con gli altri partners internazionali, si evince chiaramente come nel complesso, tutte queste attività mi abbiano arricchito anche dal punto di vista organizzativo e manageriale, rendendo il lavoro ancor più emozionante.*



# Contents

<b>1</b>	<b>Objectives</b>	<b>1</b>
1.1	Main Objective . . . . .	1
1.2	Specific Objectives . . . . .	1
<b>2</b>	<b>Methodology</b>	<b>3</b>
<b>3</b>	<b>Micro solar CHP: introduction and basic technologies</b>	<b>5</b>
3.1	Transition to Renewable Energy Resources . . . . .	5
3.2	Review of concentrating Solar Power technologies . . . . .	13
3.2.1	Linear Fresnel Reflectors . . . . .	15
3.2.2	Parabolic Trough Collectors . . . . .	16
3.2.3	Parabolic dish . . . . .	17
3.2.4	Central tower . . . . .	17
3.3	Review of power conversion technologies . . . . .	19
3.3.1	Organic Rankine Cycle . . . . .	20
3.3.2	Stirling engine . . . . .	24
3.3.3	Kalina Cycle . . . . .	26
3.3.4	Goswami Cycle . . . . .	28
3.3.5	Externally fired micro-turbine . . . . .	31
3.4	Review of thermal energy storage systems . . . . .	34
3.4.1	Sensible heat storage . . . . .	35
3.4.2	Latent heat storage . . . . .	36
3.4.3	Thermochemical storage . . . . .	37
3.4.4	Comparison of thermal energy storage technologies . . . . .	38
<b>4</b>	<b>Motivation for the micro CHP plant</b>	<b>41</b>
4.1	Concept design of the micro CHP . . . . .	43
<b>5</b>	<b>Outline of dissertation</b>	<b>51</b>
<b>6</b>	<b>System modeling</b>	<b>53</b>
6.1	Linear Fresnel Reflector . . . . .	53
6.1.1	Introduction . . . . .	53
6.1.2	Modeling . . . . .	56
6.1.3	Wall-to-fluid heat transfer . . . . .	65
6.2	Latent Heat Thermal Energy Storage . . . . .	78
6.3	Organic Rankine cycle . . . . .	80

6.3.1	Introduction . . . . .	80
6.3.2	Modeling . . . . .	81
6.4	Pipeline . . . . .	86
6.4.1	Introduction . . . . .	86
6.4.2	Modeling . . . . .	88
<b>7</b>	<b>Dynamic simulation test cases</b>	<b>93</b>
7.1	Global system performance . . . . .	93
7.1.1	Global energy evaluations . . . . .	93
7.1.2	Effect of the pipelines modeling . . . . .	105
7.1.3	Effect of the storage partialisation . . . . .	114
7.2	System performance evaluation in building integration . . . . .	127
7.2.1	Introduction . . . . .	127
7.2.2	Methods and modeling . . . . .	132
7.2.3	Building specifications . . . . .	134
7.2.4	Results and discussion . . . . .	137
7.2.5	Conclusions . . . . .	148
7.3	Wall temperature prediction of the LFR receiver tube . . . . .	150
7.3.1	Material and methods . . . . .	150
7.3.2	Results and discussion . . . . .	151
7.3.3	Conclusions . . . . .	154
7.4	Hardware-In-the-Loop aided control design . . . . .	156
7.4.1	Introduction . . . . .	156
7.4.2	Methods and modeling . . . . .	158
7.4.3	The hardware-in-the-loop framework . . . . .	165
7.4.4	Results and discussion . . . . .	167
7.4.5	Conclusions . . . . .	175
<b>8</b>	<b>Conclusions and future works</b>	<b>179</b>
8.1	Conclusions . . . . .	179
8.2	Future works . . . . .	182
<b>A</b>	<b>Simulink models</b>	<b>183</b>
A.1	Solar generator . . . . .	185
A.2	LFR . . . . .	205
A.3	TES . . . . .	221
A.4	ORC . . . . .	225
A.5	Pipeline . . . . .	233
A.6	Tee and diverters . . . . .	239
A.7	controller . . . . .	242
<b>B</b>	<b>Empirical correlations for the LFR wall heat transfer coefficient</b>	<b>245</b>
<b>C</b>	<b>LFR wall temperature and Re number matrix</b>	<b>253</b>

# Chapter 1

## Objectives

### 1.1 Main Objective

To develop a detailed numerical model for a micro solar Combined Heating and Power plant suitable for investigations about performance and control system design.

### 1.2 Specific Objectives

- Select a novel technology for a decentralized energy system as a cogeneration unit, using concentrated solar power for small scale building applications.
- Develop ad hoc sub-routines in *MATLAB* for each subsystem of the plant that accurately reproduces the dynamic effects of the plant.
- Create a basic communication architecture with the *ModBus* protocol under a Hardware in the Loop approach to enable externally control unit to be tested by means of the developed micro solar simulation model.
- Find an optimal control of the valves and pump installed in the plant to facilitate the plant commissioning in a real scenario when the prototype will be operative.
- Evaluate the thermal (heating and cooling) and electrical demand coverage for a multi-family house within a simulated environment coupling and external building model.
- Try to investigate the effects of the chosen control strategy aimed at managing the plant on the thermal stress of the solar receiver tube.
- Try to extrapolate from the simulated wall temperature of the receiver tube a new correlation in order to prevent thermal stress.



## Chapter 2

# Methodology

On the basis of the above defined objectives for this dissertation, the methodology followed for the present work can be divided into different stages. The well known Energy supply issues lead to study of new solutions to reduce the environmental impact, here is presented a novel technology whose challenge is overcoming the common barriers that prevent the implementation of micro Concentrated Solar Power systems at building level. Different solutions for the subsystems are selected even though some parts are not currently marketable products, indeed part of the research of this work intended minimizing this technology gap.

Secondary aspect concerns the development of a preliminary control strategy of the whole system aimed at maximizing the energy production and making its operation more stable and reliable. On this purpose, the technical specifications of the prototype under construction within the European project *Innova MicroSolar* are taken as a sample.

All the assessments to achieve the aforementioned objectives are summarized up next:

- *Literature review:* In this stage, the possible candidates technologies to build a micro Solar *Combined Heating and Power* systems (CHP) are compared and selected. Advantages and disadvantages of the current SoA (State of Art) technologies in energy conversion and storing are analysed, with particular regard to compliant with reliability and building integration requirements. The recent trends on the technology improvements provide the motivations behind the choice of each subsystem.
- *System implementation:* since the novelty introduced by this power system, and the detail level required for these studies, ad hoc subroutines are developed for each subsystem. The dimensional level of discretisation is chosen to highlight the dynamic behavior of the plant and the critical issues that may occur in such kinds of plants.
- *System validation:* despite the lacking experimental data, a careful examination of literature allows to validate the majority part of the mathematical models here accomplished with MATLAB code.
- *System testing:* many test cases are carried out aimed at investigating some performance parameters of the plant connected with a simulated building,

or with the purpose of improving the electric power generated reducing the thermal losses. Moreover, some analyses are conducted to outline the effect of the controller action on the parameters of the plant.

## Chapter 3

# Micro solar CHP: introduction and basic technologies

Before to explain the concept design of the micro CHP, it is important to underline the research motivations behind which this study was undertaken, namely the global warming and the gradual transition towards Renewable Energy Resources. Said that, a brief survey on the current technologies for (i) energy production, (ii) energy storage, (iii) power production from a mid temperature hot source is addressed. A basic characterization and comparison of each technology is carried out, it is aimed at showing the main advantages and disadvantages in perspectives of an implementation in a solar microCHP plant.

### 3.1 Transition to Renewable Energy Resources

Energy has been the main industrialization driver for centuries, playing an important role in the generation of wealth. An example is shown in fig. 3.1 where the gross domestic product is compared with the CO<sub>2</sub> emissions: countries begin in the bottom-left of the chart at low CO<sub>2</sub> and low Gross Domestic Product (GDP), and move upwards and to the right. Historically, where fossil fuels are the dominant form of energy, we therefore see increased CO<sub>2</sub> emissions as an unintended consequence of development and economic prosperity. In fig. 3.1 the CO<sub>2</sub> emissions per capita are measured in tonnes per person per year. GDP per capita is measured instead in international \$ (2011) prices to adjust for price differences between countries and inflation.

On the other hand, the global increase in the world's population leads to higher energy consumption, the demand is expected to grow in the next decades.

At present, the *International Energy Agency* (IEA) [7] asserts that more than 80 % of the total primary energy derives from fossil fuels. The current massive use of fossil fuel promotes global warming. As a result the fossil fuel demand sharply increases as depicted is fig. 3.2 (annual CO<sub>2</sub> emissions from different fuel types, measured in tonnes per year).

Coal is still used intensively in developing countries since its affordability and for supply reasons, China is one of the most consumer, the consequences are clearly visible in fig. 3.3.

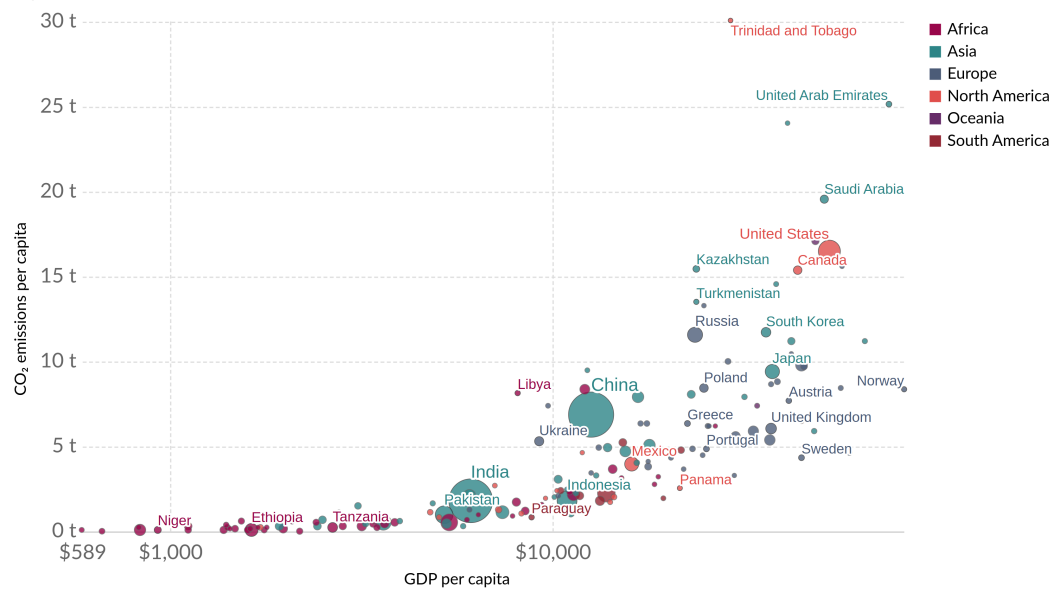


**Figure 3.1.** CO<sub>2</sub> emissions per capita Vs GDP per capita, 2016.  
Source: Global Carbon Project, Maddison (2017).

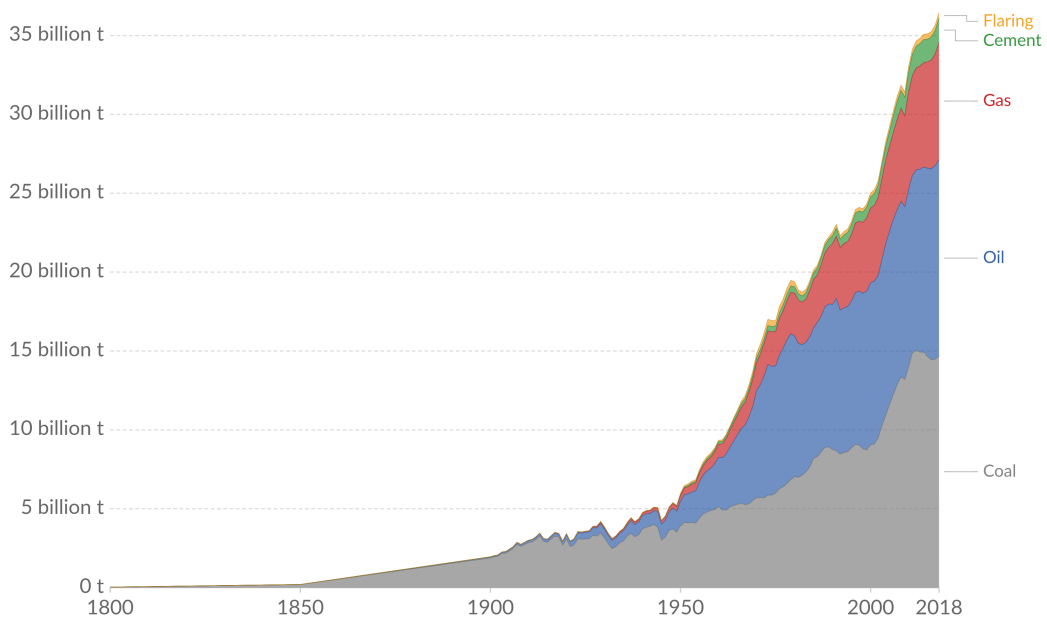


**Figure 3.2.** CO<sub>2</sub> emissions by fuel type, World.  
Source: Global Carbon Project (GCP) DDIAC.

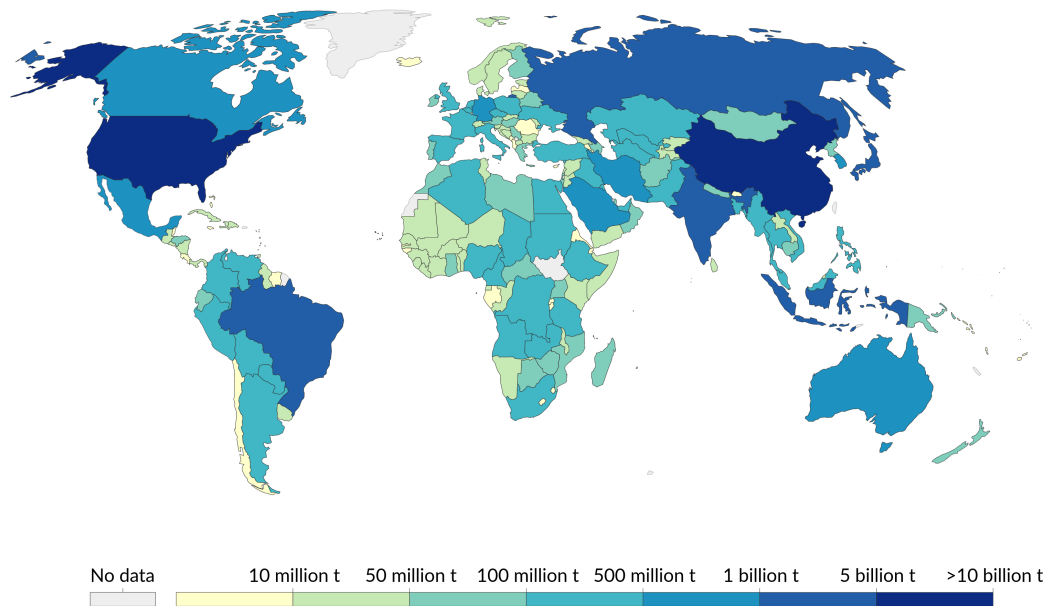


**Figure 3.3.** Total greenhouse gas emissions, 2016.

Source: CAIT Climate Data Explorer via. Climate Watch.

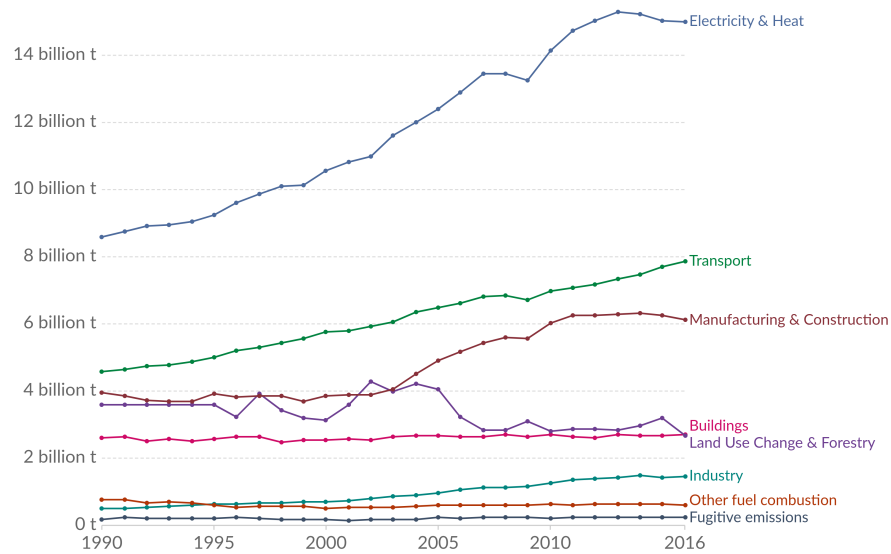
Taking a closer look about the CO<sub>2</sub> emissions share from fossil fuels, categorized by sector in fig. 3.4 (including emissions from land-use change and forestry), it is worth to notice how the energy production has the most relevant impact on the total amount of CO<sub>2</sub> emissions and directly on the global warming effect.

To face with the derived climate changes, the *Intergovernmental Panel on Climate Change* (IPCC) asserts a reduction of at least 50 % in the global CO<sub>2</sub> emissions with respect to 2000 emissions has to be reached within 2050 to limit a long term global temperature rise predicted to be between 2.0 °C and 2.4 °C [64].

In 1987, started the concept of sustainable development with regard to the environment, the economy and society with the publication of the Brundtland Report [82]. The international Kyoto agreements of 1997 introduced an environmentally measured sustainability aspect to energy policy fixing the emission reduction targets [22]. The most recent Paris climate conference (December 2015) bound its adopters to a global agreement to limit global warming to below 2 °C [27].

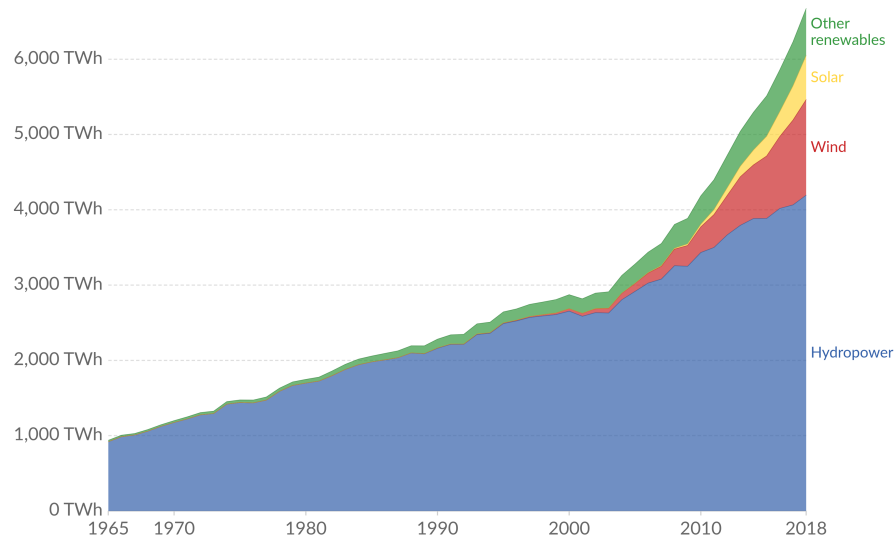
The first impulse to a change towards the *Renewable Energy Resources* (RES) was determined by the fossil fuel crisis of the 1970s, which resulted in rising fuel prices and the realisation of the finiteness of fossil fuels. As a result, new energy technologies based on renewable energy resources, such as sun, wind and electricity-heat cogeneration, started to appear to increase self-sufficiency and security of supply. One of the biggest drawback concerns the rise in technical and economical challenges with respect to conventional power generation.

Figure 3.5 depicts the current energy share of different technologies, even if the hydropower is the largest, wind and solar energy are growing in the last decade with 8.8 % and 18 % respectively. Broadly speaking, RES are steadily becoming a greater part of the global energy mix, their penetration in the energy supply is



**Figure 3.4.** CO<sub>2</sub> emissions by sector, World.

Source: CAIT Climate Data Explorer via. Climate Watch.



**Figure 3.5.** Renewable energy generation, world, 1965 to 2018.

Source: BP Statistical Review of Global Energy, 2019.

increasing year by year as shown in fig. 3.6, they account for 22 % of the global share in electricity production <sup>1</sup>.

So far, many technologies have been studied, each one having its own advantages and disadvantages, but they globally have in common a lower energy density compared with conventional fossil fuels [177] which somehow reflects into higher costs and less competitiveness.

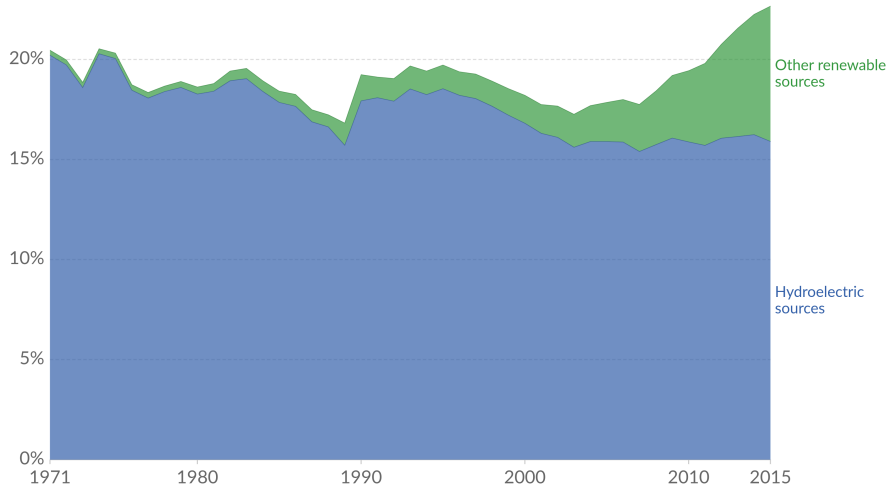


**Figure 3.6.** Share of electricity production from renewable sources, world, 1971 to 2015.  
Source: International Energy Agency (IEA) via World Bank.

Residential consumers in Europe are in line with the global trend in energy consumption, they are responsible for 30-40 % of the total energy consumption by sector [19], however the conventional power system infrastructure requires a redesign in light of the recent developing of these technologies in terms of cost and efficiency, thus being able to install them at residential level. Small-scale technologies located close to or at the premises of end-consumers in the grid (so called *Distributed Energy Resources* (DER)) are one example of developments in the residential sector.

In the last decade the research is addressed in integrating the RES with the grid, because the network is progressively becoming active, is a crucial point realizing an infrastructure that incorporates information communication techniques with physical devices to automatically collect and exchange data. This goal is reached with the smart grid that provides efficient, reliable, and cost-effective electricity power service to users via the integration of modern information and communication technologies in the traditional power grid [25]. Integrating distributed energy resources with energy storage devices using a smart grid can reduce the generation costs, smooth the curve of bulk power generation over time, reduce bulk power generation and distribution losses, and provide sustainable user service reliability [191]. Recent black out in the world have highlighted the weakness of centralized power generation, on the contrary, DER can decrease electrical network losses due to smaller scales and the absence of long-distance transmission networks. Moreover, cogeneration and trigeneration can be often adopted by means of small district heating networks,

<sup>1</sup>Other renewable resources includes solar photovoltaic (PV), wind (offshore and onshore), geothermal and biomass electricity production

while in the centralized power production, the investment cost can be affordable only in some cases where the users are enough close to the power block.

Among all the RES, solar energy is the most abundant one, its exploitation is very attractive, indeed only giving an idea concerning its potential: by a rough estimation 30 minutes of solar radiation impinging onto the earth's surface is equivalent to the world's energy demand for one year.

*Photovoltaics (PV)* and *Concentrating Solar Power (CSP)* are the two technologies in rapidly growing, one worth parameter to estimate this trend is represented by the Cumulative PV and CSP power installed capacity during the years [114, 42], shown in figs. 3.7 and 3.8. One may observe, even though the cumulative installed capacity of PV is currently 2 order of magnitude higher than that of CSP, the growth rates during the last period have been similar for both technologies.

The PV investment costs are always lower than those of CSP. On the other hand, it must be taken into account that the load factor of CSP is higher than that of PV if storage systems are installed, which would decrease differences in LCoE (levelized Cost of Electricity) between PV and CSP becoming it often more financially viable. Alike of PV, CSP systems are more suited in areas where annual global irradiations are above  $1300 \text{ kW-h/m}^2$ . This is due to the fact that concentrating technologies can only take benefit of *Direct Normal Irradiance (DNI)*, but not diffuse irradiance (as instead occurs in PV), which is predominant in cloudy and humid regions, typical of areas close to the equator. In addition, in high latitude regions the sunlight must cross a larger distance of the atmosphere that increases absorption and scattering, and thus increases diffuse irradiance.

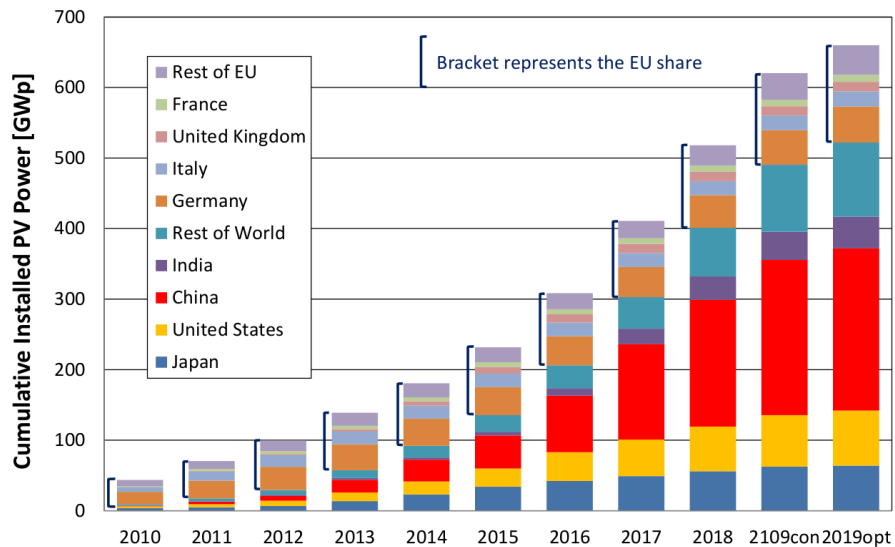


**Figure 3.7.** Cumulative PV system installations from 2010 to 2019 estimates.

Source: IEA 2019.

Resuming the concept of cogeneration and trigeneration, even if PV systems are suitable for DER, they can not provide heating or cooling directly, unless their electric energy is further converted by means of a heat pump or similar. Storing heat or electricity is highly costly for PV, while CSP are designed to do it.

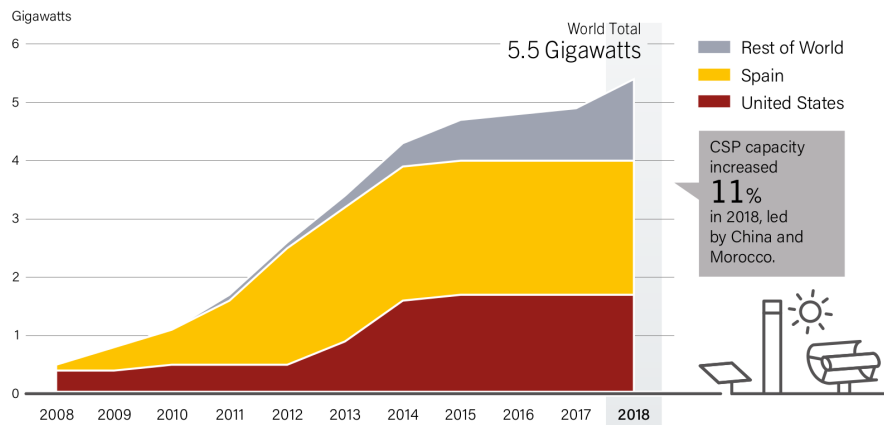


**Figure 3.8.** Concentrating solar thermal power global capacity, by country and region, 2008-2018.

Recently, to reduce the need for electrical storage and take advantage of the increasing efficiency and diminishing costs of PV, the *US Department of Energy's Advanced Research Projects Agency–Energy* (ARPA-E) has created the *Full-Spectrum Optimized Conversion and Utilization of Sunlight* (FOCUS) program to link PV and CSP [4]. Spectral beam splitting in hybrid PV/T systems for power generation are some lines of research, but actually for long the main issue regarding CSP plants concerns the high cost at small scale. To figure out this techno-economic gap, the use of *Combined Heating and Power* plants (CHP) integrated in buildings can reduce from one side the current large CO<sub>2</sub> emissions in electricity and heat (fig. 3.4), and from the other it can increase the RES penetration inside the network not only considered from an electrical point of view, but also in heating and cooling with district heating. At present, this transition is under study with the 4<sup>th</sup> generation *District Heating* networks [124] where all the RES mix interacts with the network for efficient heat supplying. Under these considerations, micro solar CHP technology can sustain the gradual transition towards DER, provided that significant progress in research and development is done, especially for thermal storage, which is still a challenge not only for the electrical one, but also in CSP applications if compactness and reliability are needed.

Phase change materials represent the most promising way to store heat effectively, they can store or release heat using the high latent heat capacity, thus increasing the specific energy per weight, but at the same time they allow to exploit heat at higher temperature, raising the electrical efficiency during the conversion.

In this dissertation the mathematical model of a micro solar CHP with a phase change thermal storage is investigated, in particular a performance assessment is carried out considering the integration at building level. Moreover, other studies are addressed to measure the impact on the performance with varying specifications of the plant, for example partializing the thermal storage. Other not secondary aspects of this research deal with control design and operation modality, in fact excessive thermal stress or not efficient work can arise if the plant is not properly controlled. The outcomes of this research provide useful information to the plant under construction in the European project *Innova Microsolar* [21], at the same

time scientific community can get the limitations and the potentiality of this kind of small scale solar CHP for future applications in *Distributed Energy Resources*.

## 3.2 Review of concentrating Solar Power technologies

Broadly speaking, solar field can be classified in four typologies [113] as depicted in figure 3.9: *Linear Fresnel Reflector* (LFR), *Parabolic Trough Collector* (PTC), *Central Tower* (CT) and *Parabolic Dish Collector* (PDC). Due to the fact that punctual collectors achieve higher concentration ratios than linear collectors, they drive the receiver to higher theoretical temperatures. That is to say, parabolic dishes and central towers attain higher concentrations than parabolic troughs and linear Fresnel Reflectors respectively.

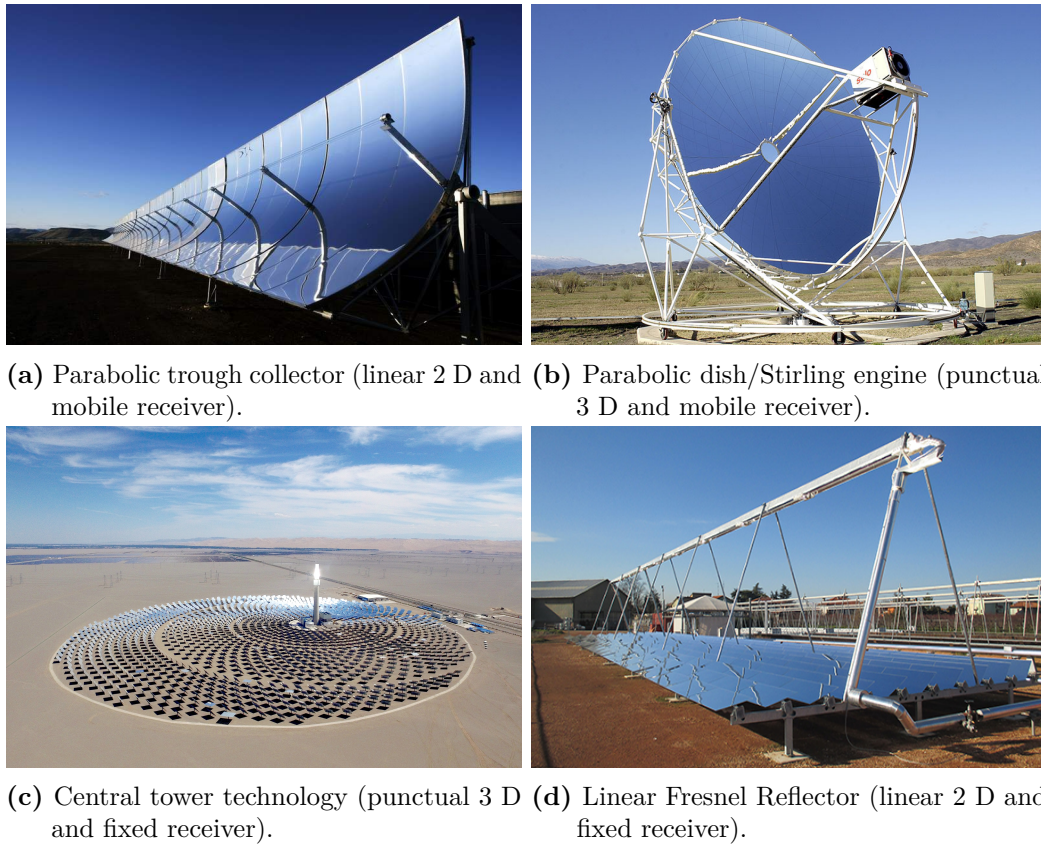


**Figure 3.9.** Classification of solar field technologies.

Another aspect concerns the solar tracking, biaxial tracking systems can achieve higher concentration factors and efficiencies than those monoaxial, these latter are in turn preferable than static solar field (for example flat plate collectors). There are several reasons: firstly, shading and blocking effects are negligible or sometimes absent thanks to the fact that the whole reflecting surface of each collector moves as a rigid body. Secondly, the aperture is perpendicular to the impinging sunlight, which minimizes cosine factor losses. Main characteristics of the solar field technologies here presented are summarized below:

**Table 3.1.** Comparison of the main solar technologies [163].

	Parabolic Trough	Solar Tower	Linear Fresnel	dish Stirling
Typical capacity (MW)	10-300	10-200	10-200	0.025-0.1
Operating temperature (°C)	350-550	250-565	390	550-750
Plant peak efficiency (%)	14-20	23-35	18	30
Annual solar-to-electricity efficiency (net) (%)	11-16	7-20	13	12-25
Annual capacity factor (%)	25-28 (no TES) 29-43 (7 h TES)	55 (10h TES)	22-24	25-28
Collector concentration	70-80 suns	>1,000 suns	>60 suns (depends on secondary reflector)	>1,300 suns
Receiver/absorber	Absorber attached to collector, moves with collector, complex design	External surface or cavity receiver, fixed	Fixed absorber, no evacuation secondary reflector	Absorber attached to collector, moves with collector
Storage system	Indirect two-tank molten salt at 380 °C (dT = 100 K) or Direct two-tank molten salt at 550 °C (dT = 300 K)	Direct two-tank molten salt at 550 °C (dT = 300 K)	Short-term pressurised steam storage (< 10 min)	No storage for Stirling dish, chemical storage under development
Cycle	Superheated Rankine steam cycle	Superheated Rankine steam cycle	Saturated Rankine steam cycle	Stirling
Steam conditions (°C/bar)	380 to 540/100	540/100 to 160	260/50	n.a.
Maximum slope of solar field (%)	<1-2	<2-4	<4	10% or more

### The heat transfer fluid

The task to remove heat from the receiver and transfer it either to the storage system or to the final use (the power block) is accomplished by *Heat Transfer Fluids* (HTFs). They can be liquid, gaseous, depending on the applications, currently the most used are: synthetic oil, molten salt, water, gases.

If operating temperatures below 400 °C are needed, synthetic oils or in general organic fluids, like for example *Therminol VP1* or *DowTherm* are the most commonly choice, their thermal stability is kept in a wide temperature range, moreover, unlike the common oil it has been designed to maintain its thermal properties unchanged, such as viscosity and thermal conduction do not change too much with temperature. Thanks to these properties, the heat transfer coefficient is very good, while the pumping losses are kept low (per unit of energy transferred). It is worth saying that no high pressure tanks are needed, but in some conditions they can be flammable and a careful design during the construction phase must be paid for security reasons.

Molten salts are thermally stable up to 570 °C, thus are suitable for solar fields with high concentration ratio, they theoretically allow to obtain thermal efficiency very close to those in boiler power plants (the maximum temperatures are close to 600 °C). Unfortunately, they freeze and solidify at relatively high temperature, 220 °C for binary salts (mostly used due to their lower cost) and 120 °C for ternary salts. To maintain the power block operative, the lower temperature tank must be maintained at 290 °C, when the solar energy is not enough, fossil fuels are used in order to maintain the tanks above the minimum desired temperature.

Unlike the previous solutions, *Direct Steam Generation* (DSG) has the advantage to drive the steam turbines without additional heat exchangers, reducing the cost and complexity of the plant and increasing the global efficiency. Moreover, it is cheap and not flammable or toxic, however it requires a high pressure piping system and cannot be stored efficiently. The heat transfer coefficient is good during preheating, very high during evaporation and very low when superheating, thereby it implies that the evaporation in horizontal tubes can drive to different flow patterns causing thermal stress in PTCs, especially in the superheating process which occurs at high temperature and the HTF can not be effective in heat extraction. Nonetheless, the very low density of superheated steam leads to higher pumping losses.

Gases eliminate the temperature limits and generally do not have safety and environmental issues. Two main drawbacks hinder its massive use in solar plants: at parity of enthalpy jump, gases need high pumping energy and the heat transfer coefficient is not comparable to liquid fluids. To partially reduce this gap, pressurized gasses are used (20 bar or more) in open gas turbines.

#### 3.2.1 Linear Fresnel Reflectors

The Linear Fresnel Reflector technology as depicts in fig. 3.10 concentrates the solar energy onto a receiver placed above the ground through a series of ground-based mirrors. The mirrors can be moved independently each other by means of a monoaxial tracking system, furthermore they are designed with a specific curvature able to approximate the ideal parabolic shape. Comparing to the PTC, the approximation of the parabola shape leads to a lower ideal optical efficiency, this aspect may be

improved using a secondary reflector. The use of ground-based mirrors allows cost reducing because of a lighter framework, moreover the fixed absorber does not need expensive rotating joints and a lower land occupation than PTCs. On the other hand, the above mentioned advantages have to face with the lower optical efficiency, the main inefficiencies of LFCs are due to shading and blocking, which affect differently mirrors depending on its location above the horizontal plane.

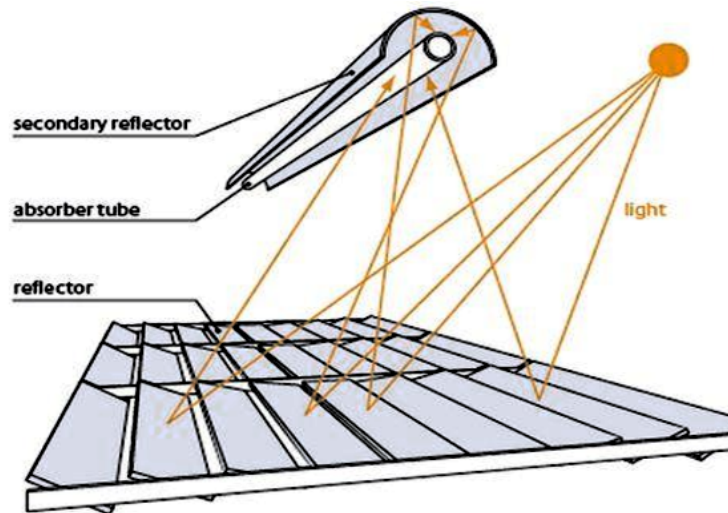
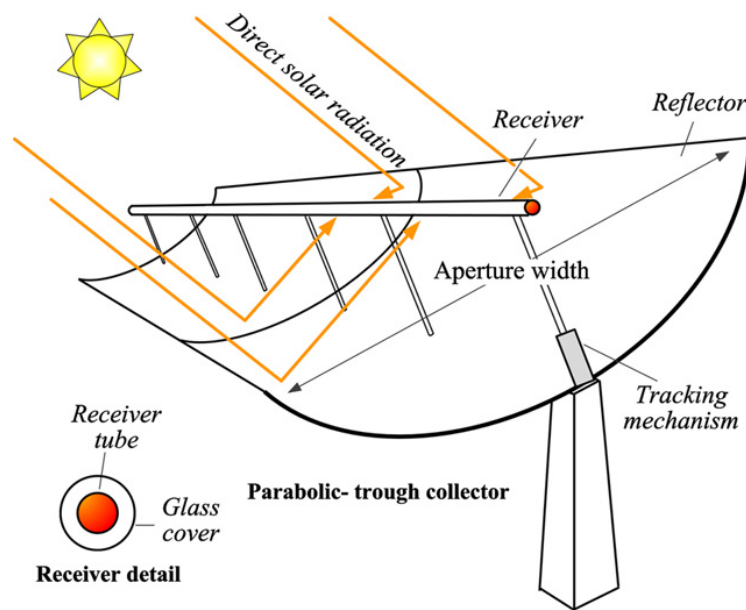


Figure 3.10. Schematic of a Linear Fresnel reflector.

### 3.2.2 Parabolic Trough Collectors

A PTC is a linear-focus solar collector, basically composed of a parabolic-trough concentrator that reflects the impinging sunlight onto a receiver or absorber tube located in the focal line of the parabola, see fig. 3.11.

Obviously they own a monoaxial tracking system and they are placed with a precise distance preventing the mutual shading and blocking effect, but this characteristic results in a bigger encumbrance if compared with LFRs. PTCs are the most popular CSP systems in the current development of solar thermal power, particularly in Spain, in fact they represent the biggest share of the world energy production via CSP. In order to maximize thermal efficiency, all receivers installed consist of an evacuated tube, with an outer glass envelope and an inner steel tube. The vacuum annulus permits not only the elimination of convective losses, but also the use of selective coatings with very high absorptivities in the solar spectrum while very low emissivities in the infrared spectrum. In addition to the use of selective coatings, the glass surface is treated with anti-reflective coating in order to enhance the transmission of the sunlight. It is of particular importance the potential leakage of thermal fluid through the rotating joints, they have to be designed to withstand at high temperature (above 500 °C) maintaining a good flexibility during the time. Due to the thermal expansion of the absorber tube, the adoption of bellows is necessary to avoid the failure of the heat collector element thus representing an important share of the *Heat Collector Element* (HCE) investment cost. Typically, large scale



**Figure 3.11.** Schematic of a parabolic-trough collector.

PTC has a constraint that limits the aperture dimension, i.e. the wind drag effect, as matter of fact the biggest parabolic trough has an aperture in the range 5.5 m - 6 m. The total length of a solar collector assembly reaches the value of about 100 -150 m, whereas the absorber tube length is usually limited to a value of 4 m because of mechanical bending.

### 3.2.3 Parabolic dish

It consists of a parabolic dish that is perpendicular to the sunlight at all times, thus it is equipped with a two-axes tracking system, concentrating solar rays to the optical focus where the receiver is located. The simple schematic of the parabolic dish is depicted in fig. 3.11.

Generally, either a Stirling engine or an open air gas turbine is usually placed at the focal length. Thanks to its geometry, high concentrating factors are achievable by this technology, i.e. up to 4,000 suns, which permits to heat up HTFs up to 1000 °C. As a result, solar dishes can achieve the maximum solar to electricity efficiency, around 30% tab. 3.9; it must be noted that such a range of efficiencies was already obtained during the 1980s. This demonstrates that efficiency is not a key feature of CSP plants. Most parabolic dish modules generate nominal powers from 10 kW to 25 kW, i.e. with diameters up to 10 m, therefore they are not suitable in large centralized fields. As occurs in PTCs, the wind drag effect implies higher structural straightness, and thus higher costs. Another important drawback is the absence of energy storage, as a consequence it makes them compete directly with PV modules.

### 3.2.4 Central tower

As in parabolic dishes, Central tower is equipped with a two axial tracking system, but it is made up of a set of heliostats placed over the ground, which are spaced in

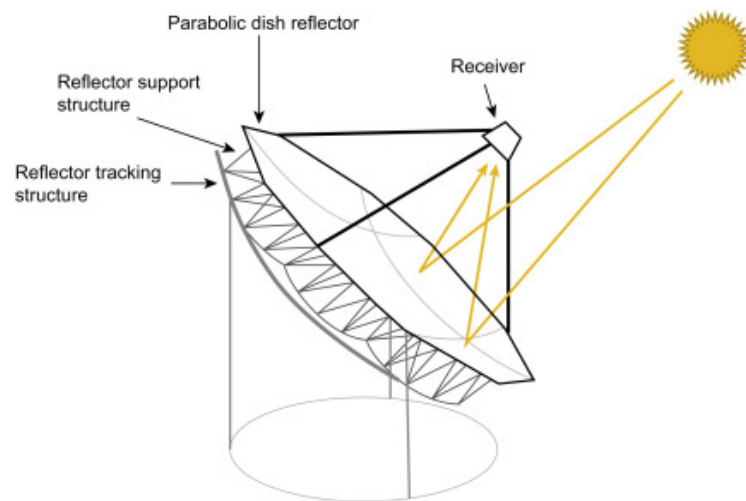


**Figure 3.12.** Schematic of a parabolic dish.

a field to avoid mechanical or optical interference. Moreover, they have a pivot to reflect incident direct-beam sunlight onto an elevated receiver or secondary reflector located in the center of the solar field as shown in fig. 3.13.

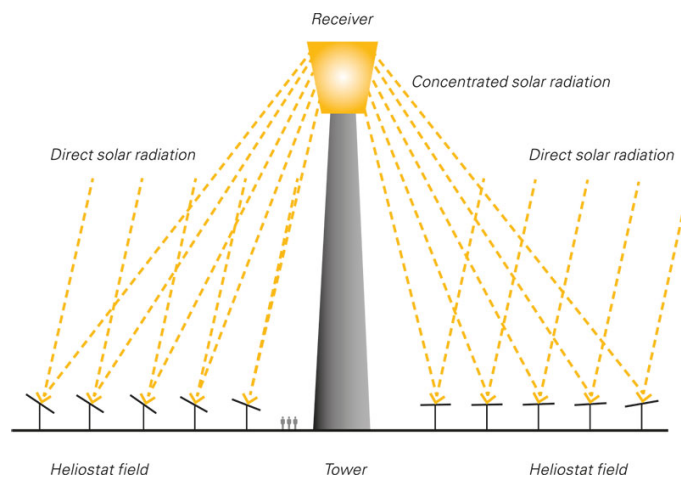


**Figure 3.13.** Schematic of a central tower.

CT has the advantage of locating the receiver in one only "point" of the field, which greatly reduces the thermal losses due to the higher compactness of the power system at elevated temperature. In addition the HTF is pumped only in a narrow region close to the power block reducing the pumping losses. Sometimes, the heliostats instead of surrounding the receiver are placed only on one side. There are several factors that affect the CT optimal size:

- as the size of the solar field rises, the distances from mirrors to receiver increase as well, as a result hitting the target is a problem and ray distortion by atmospheric effects (hot air lenses) hampers the achievement of good focusing onto the receiver;

- at larger distance, mirrors need a more precise construction and a more sophisticated tracking system to hit the target;
- at higher concentration ratios the flux rises, though a reduction in the receiver surface is beneficial regarding the thermal losses, it implies higher costs due to higher thermal constraints;

### 3.3 Review of power conversion technologies

In this section the main power conversion technologies are compared to highlight advantages and disadvantages relating to the micro CHP applications. The power block converts a fraction of the thermal energy in input to electricity, the previous described CSP technologies achieve temperatures between 300 °C and 1000 °C, which are commonly exploited by thermodynamic power cycles in combination with fossil fuels or geothermal. Even though combined power cycles (made up of gas turbines in series with steam Rankine cycle) are used in large power plants providing electric efficiency close to 60 % at the nominal conditions, at small scale other solutions have to be found. Open-cycle or closed-cycle turbines are neither technically nor economically beneficial, it depends from case to case. Before to discuss the main power conversion technology the fig. 3.14 deserves attention. For low power applications the ORC and the Stirling cycles are the most effective in power conversion, but ORCs are more indicated for low temperature waste heat recovery. Kalina cycle and Steam cycle are preferred at high power applications, even if the first one has applicability also at kW scale. Currently, CO<sub>2</sub> cycle and Flash cycle are the most advanced technologies studied, they cover low and high grade waste heat recovery suitable for middle size power plants. The Brayton cycle with an open gas turbine is not shown in the fig. 3.14 [121], but it can be stated that all the power out plane, with more than 500 °C can be entirely covered by regenerative gas turbines.

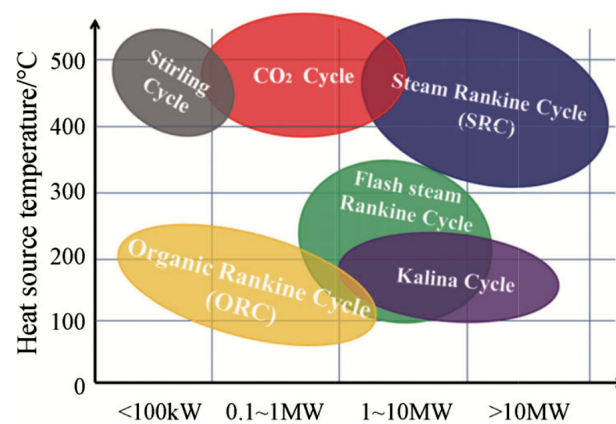


**Figure 3.14.** Main technologies fields in the heat source temperature-power output plane.

*Organic Rankine Cycle* (ORC) can be a valuable substitute of steam cycle at low temperature applications. Indeed, the broad variety of the refrigerants allow

the designer to choose the correct one to maintain the maximum working pressure below 30 bar and the dry saturation curve which does not require additional vapor superheating to prevent droplets in turbine. Maintenance requirements for ORCs are extremely low, unlike steam the working fluid is non-eroding and non-corroding for valve seats tubing and turbine blades allowing for long operational life, as a result the operation can be extended over 80,000 hours. Currently, the ORC technology is the most mature for small scale power plants and they are installed in CSP or recovering waste heat from industrial processes, with an interesting payback period. Stirling engines were used in world war 2, since their low noise, moreover thanks to the external combustion, emissions such as  $\text{NO}_x$ , CO, can be significantly reduced. They have good thermal efficiency and low maintenance. Despite these advantages, many companies involved in the production of such systems no longer exist. Other alternatives more advanced under research and development are the Kalina cycle, the Goswami cycle and the micro (air) gas turbine. Unlike ORCs, Kalina cycle is more indicated for very low temperature heat sources (around 100 °C), because of its binary mixture properties, in fact during the evaporation a glide occurs giving the possibility to extract more heat and reducing the irreversibilities associated with it [132]. Despite this valuable feature the Ammonia solution used into the cycle fixes the maximum operating pressure, thus the benefits mentioned cannot be technically achieved over 250 °C. The Goswami cycle has the same range of applicability of Kalina cycle since it uses the same binary mixture, the difference consists of providing not only power, but also a cooling effect typical of the ammonia absorption chillers. The electrical efficiency is greater than the ORC technology, but is still in the research phase, whereas nowadays there are some examples of commercial power plants running, for instance the power plant of 3.6 MW commissioned in 1999 by Sumitomo Metal Industries. Finally, the micro gas turbine driven with solar dish is another promising technology recently tested by *ENEA* [14] in the European project *Optimised Microturbine Solar Power* system (OMSOP) able to convert 70 kWth of radiant power to 15 kW of electric power. As already said a parabolic dish has a high concentrating ratio, hence the turbine inlet temperature can reach 800/900 °C.

### 3.3.1 Organic Rankine Cycle

The steam Rankine cycle can not work properly below 2 MWe [99], under that size the investment cost sharply rises making it no longer competitive with Organic Rankine cycle. Basically, for low temperature resources below 370 °C, thermal efficiencies also decrease to the point where steam cycles are no longer cost effective or efficient [109, 174]. The basic, ideal Rankine cycle begins with saturated water at state 1 pumped to a high pressure at state 2 and then heated isobarically to superheated steam at state 5. The superheated steam can then be expanded to state 6 through a turbine to generate power and then condensed back to saturated water at state 1. To improve the thermodynamic efficiency an additional heat exchanger is added to recover the waste heat from the turbine, state 6-7 to preheat the fluid before the evaporator state 2-3. in figure 3.15 is depicted the base scheme of an ORC unit and its T-S diagram with colored lines from red (high temperature) to blue (low temperature), while the heat source and cold source lines are placed above and below the cycle respectively based on the efficiency of each heat exchanger.

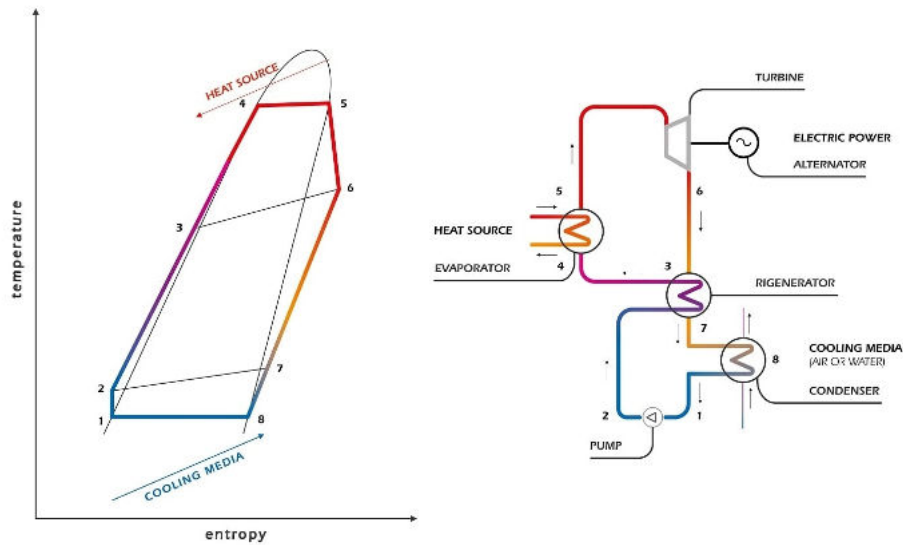


**Figure 3.15.** Schematic of a regenerative ORC and its T-S diagram.

Research is mainly focused on working fluid selection, because the performance and the environmental impact are strictly bonded to it. Currently, the desirable organic fluid should have a positive isentropic saturation vapor curve (dry), preventing the turbine from damaging. A low viscosity and a large saturation curve reduces the flow rate and the friction viscosity, reducing the pump losses significantly. To work at high temperature a good thermal stability is required, but possibly at feasible evaporating pressure (below 30 bar). From the environmental point of view they should have a low *Ozone Depleting Potential* (ODP), low *Global Warming Potential* (GWP) and High safety level (no toxicity or flammability). Even though many fluids are studied for scientific purposes, actually only few of them are used in commercial plants. For low power applications the subcritical cycle is dominant, unfortunately the electric efficiency rarely goes beyond 16 %, while in small scale plants (10 kWe) are usually half. Among all the cycle configurations, ORCs can be classified in three categories: pure fluid subcritical, zeotropic and transcritical, an example of the T-S diagram is shown in fig. 3.16.

One of the major sources of irreversibilities for ORCs stem from the heat addition process. The thermal energy source and working fluid must be separated by some temperature difference in order to heat transfer occur; however, heat transfer across a finite temperature difference inherently causes irreversibilities. Therefore, it is important to maintain good temperature matching between the heat exchanger streams to minimize these types of irreversibilities [178]. Alongside the HTF fluid path, in countercurrent flow direction there is the working fluid which is first heated as a liquid, then it undergoes to liquid-vapor phase change, and if necessary, is further superheated as a vapor thereafter. This process causes a pinch point formation, reducing heat exchanger effectiveness, and destroying potential work or exergy. The exergy destruction caused by temperature mismatching can be qualitatively seen as the area of the plot between the thermal energy reservoir and working fluid stream in fig. 3.17. The worst behavior is given by the single component ORC, while

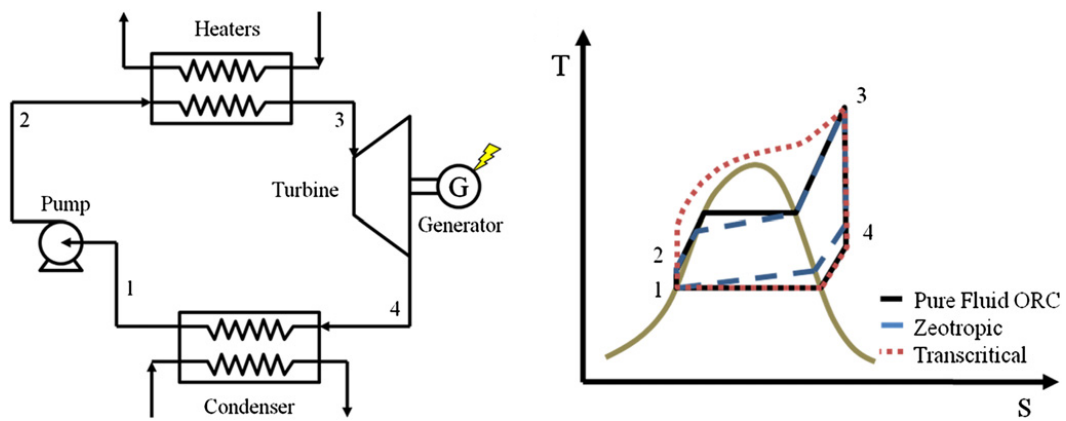


**Figure 3.16.** Plant schematic and T-S diagram for basic pure fluid ORC, zeotropic Rankine cycle, and transcritical Rankine cycle [104].

some roof of improvements are obtained in transcritical regime, where "wet" fluids perform better than "dry" [196], zeotropic fluid instead are the more attractive since their temperature mismatch is considerably decreased, the same principle used in the Kalina cycle and Goswami cycle in the next sections. Another solution to the pinch point problem can be a multi pressure boiling, but it introduces a noticeable complexity to the power plant, this solution is used only in large steam Rankine cycles that are outside the purpose of this dissertation. Finally, flash cycle in fig. 3.17 configuration enables near perfect temperature matching to the fluid stream from the finite thermal energy source.

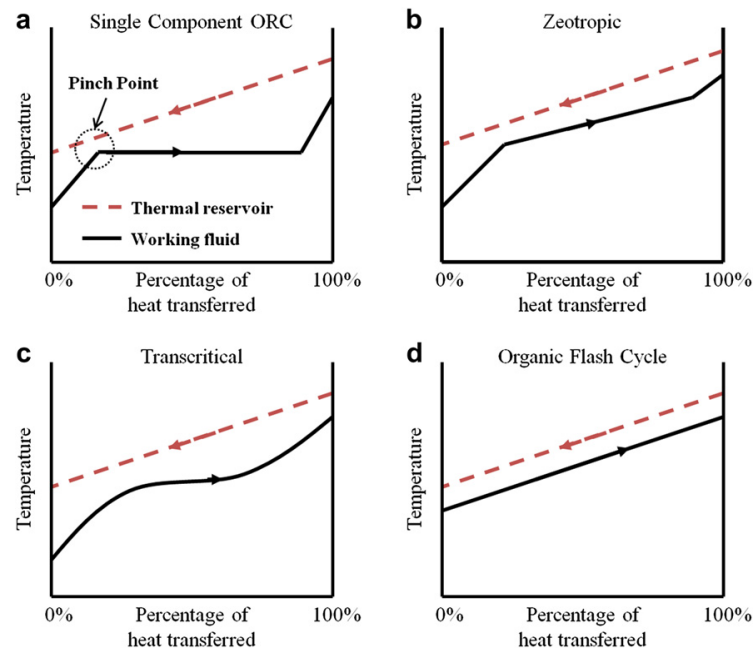


**Figure 3.17.** Variation in stream temperatures during heat addition process for single component (a), zeotropic (b), transcritical (c) and flash cycles (d)

Expanders, in general, can be categorized into two types: the velocity type,

such as axial turbine expanders and the volume type, such as screw, scroll and reciprocal piston expanders. Turbine is more indicated over 100 kWe [99], whereas screw expanders cover the range around 100 kWe, finally scroll is more indicated around 10 kWe or below. Selecting an expander for a specified application is not straightforward, many important parameters have to be taken into account: such as high isentropic efficiency, pressure ratio, power output, lubrication requirements, complexity, rotational speed, dynamic balance, reliability and cost. On the basis of the above mentioned parameters, one can summarize the two types of expanders as shown in the tab. 3.2.

**Table 3.2.** The comparison of various types of expanders suitable for ORC system [57].

Type	Capacity range (kW)	Rotate speed (rpm)	Cost	Advantages	Disadvantages
Radial-inflow turbine	50-500	8000-80,000	High	Light, weight, mature manufacturability and high efficiency	High cost, low efficiency in off-design conditions and cannot bear two-phase
Scroll expander	1-10	<6000	Low	High efficiency, simple manufacture, light weight, low rotate speed and tolerable two-phase	Low Capacity, lubrication and modification requirement
Screw expander	15-200	<6000	Medium	Tolerable two-phase, low rotate speed and high efficiency in off-design conditions	Lubrication requirement, difficult manufacture and seal
Reciprocating piston expander	20-100	-	Medium	High pressure ratio, mature manufacturability, adaptable in variable working condition and tolerable two-phase	Many movement parts, heavy weight, have valves and torque impulse
Rotary vane expander	1-10	<6000	Low	Tolerable two-phase, torque stable, simple structure, low cost and noise	Lubrication requirement and low capacity

For small scale applications, one can evince by the previous statements that due to the cost and efficiency constraints, subcritical cycle is often used at low temperature in combination with scroll expander. Actually, many researchers in literature have tried to find new solutions to push the technology beyond its limits regarding for example the expanders or exchangers, see tab. 3.2. In the first case, for instance Tomasz Z. [115] experimentally studied a new microturbine of 2.5 kWe able to reach 71 % of isentropic efficiency at 22,440 rpm, while conventional turbines efficiency usually work at 40 - 50 % (at parity of power output). Concerning the heat exchangers, if a low temperature source is used (around 100 °C), the solution found by Ruiqi Wang et. al [183] its interesting, because by means of a thermal

driven pump they increased the exchanger efficiency from 45.8 % to 51.3 % when the evaporating temperature increases from 75 °C to 100 °C. On the other hand, this solution is able to reduce the exergy destruction previously described in fig. 3.17, leading it to 62 %, when a conventional ORC attains to 59.9 %. Another interesting feature concerns the lower cost and better compactness than conventional heat exchangers, very useful characteristics for small scale targets applications.

### 3.3.2 Stirling engine

Originally invented in 1816 by Robert Stirling, at that time, these engines competed with steam engines because of their safety, in fact these latter requires strength materials to withstand high pressure, they sometimes exploded injuring nearby workers. Concerning the construction framework, three different typologies can be identified: alpha, beta and gamma as reported in fig. 3.18, in all the cases there are two chambers, one in the hot side and another in the cold side and a regenerator placed between them.

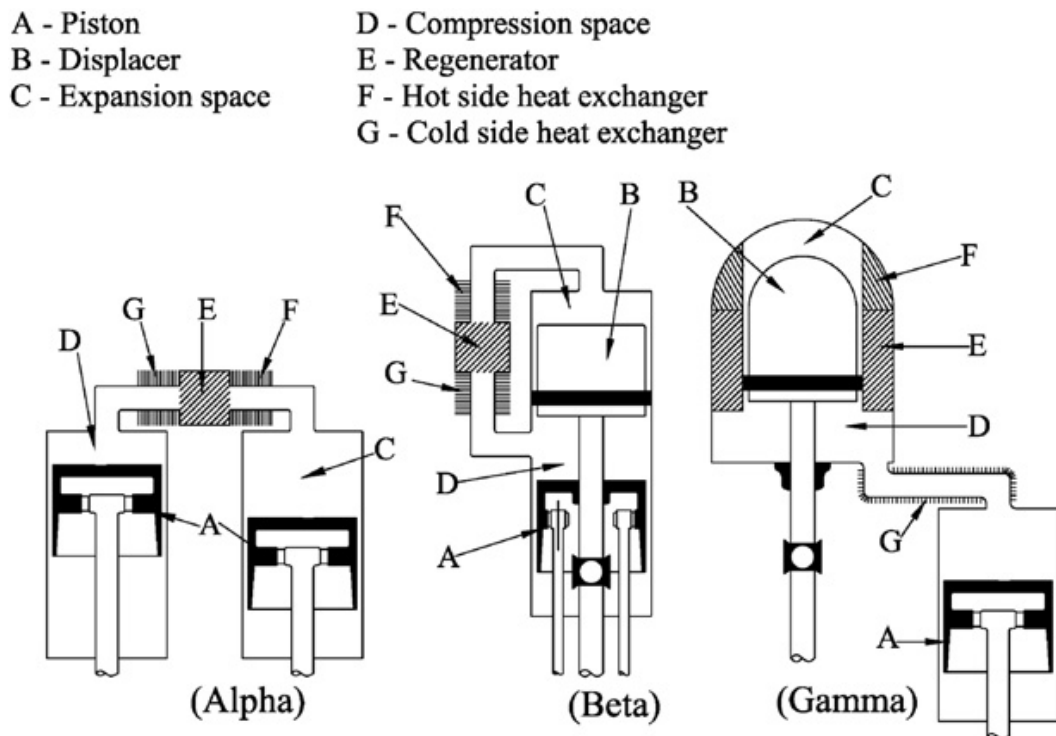


**Figure 3.18.** Three basic mechanical configurations for Stirling engine.

Particular feature of this engine consists of using an external heat combustion chamber, this makes it capable of using a wide variety of heat sources, for example biofuels, without fouling issues in the combustion chamber or contamination of the lubricant. Moreover, it is silent, not much vibration are generated from its motion unlike internal combustion engines where a fast combustion takes place.

From the thermodynamic point of view, it is worth to say that Stirling engine is able to potentially accomplish a cycle with the Carnot's efficiency, in addition it

can generate even more work. More precisely, the idealized Stirling cycle consists of four thermodynamic processes acting on the working fluid in fig. 3.19: (i) an isothermal heat addition (expansion), (ii) isochoric heat removal (constant volume), (iii) isothermal heat removal (compression), (iv) isochoric heat addition (constant volume). Actually, the real cycle is slightly different because of the not perfect regeneration (the regenerator has a limited heat exchanger effectiveness), the real gas effects and the impossibility to involve all the fluid in the thermodynamic cycle (part of it does not participate because of its construction constraints). In light of these considerations the fig. 3.19 shows also the (inner) real cycle based on the crank shaft position of a gamma and beta Stirling engine, obviously the real cycle significantly reduces the conversion efficiency of such technology. Ranieri et. al. [156] carried out a detailed analysis on the thermal efficiency reduction above mentioned. At their given temperature of the hot and cold source, the ideal cycle in alpha type Stirling totals 61.5 % in thermal efficiency (same of Carnot cycle), whereas the sinusoidal cycle achieves 34.4 %, which corresponds to a reduction of 27.1 % from the maximum attainable efficiency. The beta and gamma-type Stirling engines are slightly affected by the thermal efficiency reduction, with a 25.7 %.

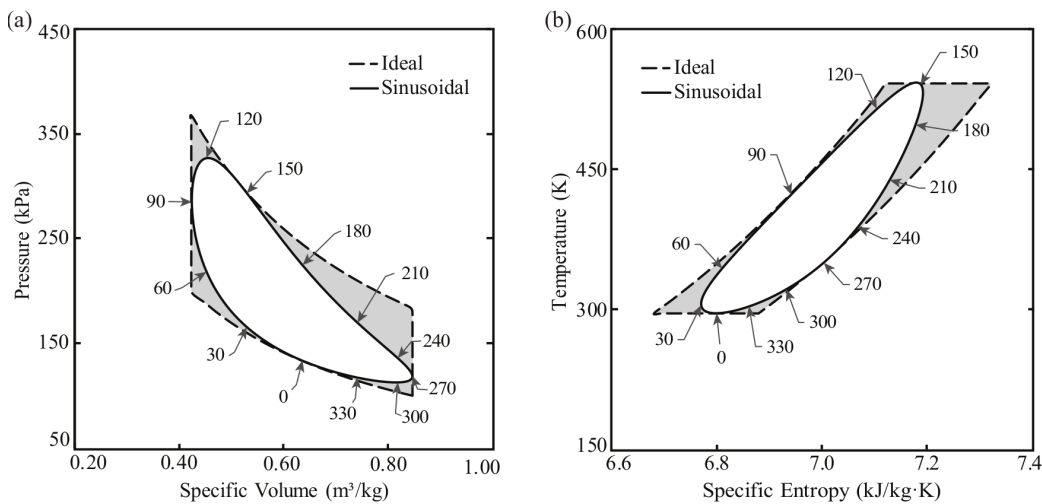


**Figure 3.19.** Sinusoidal and ideal cycle plots in (a) P-v and (b) T-s diagrams for the beta and gamma-type Stirling engines.

Nowadays, biomass-fuelled and dish Stirling engines can be considered the most studied and commercialized versions of this technology, Ferreira [89] compared an alpha-Stirling engine supplied with these two RES with a simulation analysis. The biomass-fuelled Stirling engine provided 87.5 % more power output than the solar energy source. It provides a power output of 4.3 kWe with a total efficiency of 46.67 %, whereas the solar system results in a system with 2.30 kWe of power with an efficiency of 31.33 %. Also, the average receiver temperature from the solar source is about 775 K, whereas, in the boiler bed, the temperature reaches the value of 1288 K. These results show that the energy source plays an important role and results in different engine performances. The lower efficiency reflects also in greater LCoE for the solar-power system: about 0.166 €/kWh, against 0.109 €/kWh of

the biomass-fuelled system. Broadly speaking, because Stirling engines are capable to operate with high temperature heat source between 800 °C and 1250 °C, as a consequence their conversion efficiency is relatively high if compared with the other systems described in the dissertation, this is the reason why solar dish is more indicated among the CSP systems from this point of view. One of the most efficient Stirling engines ever made was the MOD II automotive engine, it reached a peak thermal efficiency of 38.5 %.

Ferreira [89] did also a literature survey regarding the small and micro-scale biomass-fuelled CHP systems suitable for applications in domestic buildings. One can evince that hardly any of the electric power output exceeds 35 kW, commercial Stirling engines size for micro-CHP using biomass ranges around 2-3 kWe.

The characteristics both in thermodynamic and operation are somewhat attractive for a stationary power generation in DES, unfortunately there are many drawbacks that prevent a wide diffusion. For example, the real engine will always have some leakages, however small. If using air as the working gas you must have a small compressor to maintain engine pressurised. To reach high thermal efficiency, hydrogen or helium should be used, both the gasses have a strong tendency to be dispersed, especially the hydrogen which has a remarkable diffusivity coefficient in high pressure steel vessels. Just to give an idea: in the best scenario, steel diffusivity coefficient accounts for about  $10^{-9}$  (m<sup>2</sup>/s) at room temperature [88]. This means that for a steel vessel with 1 square meter surface area, 1 cm thick walls with 200 bar pressure difference, the diffusion rate is:  $J = (1 \cdot 10^{-9} \cdot (200 \cdot 44.5 / 0.01)) = 0.00089$  [mol/s], that is to say 0.15 kg/day. Moreover the diffusivity rises at higher temperature climbing about 2 orders of magnitude to  $10^{-5}$  (m<sup>2</sup>/s) at 1000 K. As hydrogen diffuses through the container material, it occasionally forms bonds with the iron atoms, transforming the iron into a different molecular structure, and in the process it changes the crystal structure (decarburization, intergranular fissuring, or blistering) with additional boundaries or dislocations. Over a long period of time this lowers the maximum elastic stress and thus toughness of the steel, this phenomena is called hydrogen embrittlement. Composite tanks are much lighter than steel or aluminum for the same amount of storage, but they have even worse leakage properties. When using biomass as heating fuel for the heater (such as wood chips or switch grass), one must be careful of ash buildup on the heater tubes. The airborne ash can melt due to the high temperature, and form an insulating layer on the heater tubes, preventing heat from getting through reducing the performance. From the experimental tests carried out by Ferreira [89] is clear that a radiative heat exchange has to take place in order to make the heat transfer rate more effective, this is not simple to accomplish in a real test bench as it is mentioned. Also the automotive applications failed because of the time lag between the power request and that one provided to the user, only in the naval sector there are some existing applications.

### 3.3.3 Kalina Cycle

The Kalina cycle was invented by Russian engineer Alexander Kalina in 1983, it was considered as a worthwhile alternative to the conventional steam Rankine cycle applied in combined power plants as a bottoming cycle. The conventional version of the Kalina cycle uses a 70%/30% ammonia/water mixture as the primary



is liberated (enthalpy of dissolution), thereby it is recovered from the stream 3 by means the low temperature recuperator, while the high temperature exchanger allows the temperature of stream 10 to fall before the mixing in MX.

Regarding the applicability in CSP plants, A. Modi et. al [134] presented a thermoeconomic optimization of a Kalina cycle designed for a net electrical power output of 20 MW with a turbine inlet temperature of 500 °C supplied by a PTC. At the design point, they assumed a turbine isentropic efficiency of 85 %, while the pumps totaled 70 %. In this analysis they compared the Kalina cycle with a steam Rankine cycle at the same size, they modeled the part-load conditions due to the solar source variation throughout the day, and all through the year. Finally they tried to optimize by means of optimization algorithms the thermodynamic cycle to reduce the LCoE. Despite the minimization of the levelized cost of electricity, their simulations resulted in the levelized costs of electricity between 212.2 \$ /MWh and 218.9 \$/MWh. For a plant of the same rated capacity, the state-of-the-art steam Rankine cycle has a levelized cost of electricity of 181.0 \$/MWh. These outcomes stem from two factors (i) worse power cycle efficiency than the corresponding steam Rankine cycle configuration resulting in a larger solar field requirement for the same net electrical power output, and (ii) the higher capital investment cost for the power cycle itself. All in all, the results reflect the same statement previously said, i.e. it is not beneficial to use the Kalina cycle for high temperature concentrating solar power plants.

Y. Wand et. al [184] compared the Kalina cycle and ORC with a given temperature source of 80 °C, 120 °C, 180 °C, considering a multi-stream waste heat composite curve divided into three typologies: straight, convex and concave. In this way is simulated an industry process with multiple waste heat streams and different heat capacity flow rates, for example: if the curve is concave the heat capacity flow rate with lower temperature is greater than that with higher temperature. The shape of the curve, thus the area between the hot and cold composite curves provides an indirect measure of the magnitude of exergy loss during the heat exchange between the waste heat and the working fluid. Thanks to the zeotropic effect they claim that in all the cases of all the three kinds of waste heat, the waste heat recovery efficiency (recovered heat divided by the total waste heat) of the Kalina cycle is higher than that of the ORC. Anyway, they identify two key features with relating to the most suitable application, i.e. the concave/convex degree and the position of the most (salient or concave) point, this means that there is not a technology better than another one, the solution should be tailored on the specific application. Despite its complexity, presently, the Kalina cycle is second only to the ORC in terms of popularity in actual implementation and it is seen as the primary alternative to the ORC.

### 3.3.4 Goswami Cycle

In 1995, a novel thermodynamic cycle was proposed by Goswami, this system is still in the early stage of development. It uses an ammonia–water binary mixture as the working fluid, but unlike Kalina cycle it produces both power and refrigeration simultaneously. This cycle combines a Rankine and an absorption refrigeration cycle, the schematic is shown in fig. 3.21, and as ORC and Kalina it is suitable



Secondly the fluid recovers heat from the returning weak ammonia liquid solution and then it enters the boiler (stream 3).

In the boiler, the basic solution is evaporated through a rectifier to split the vapors in a weak ammonia liquid, with a high concentration of water, and a rich vapor with a very high concentration of ammonia. In the separator, the two phase mixture is separated with an additional cooling stream and the weak liquid (stream 9) enters the recovery heat exchanger. The poor solution (stream 10) is then throttled to the system low pressure side and it is sprayed into the absorber (stream 11) releasing heat.

After that, in the rectifier, a cold stream (spilled for example by the stream 3) cools down the saturated rich ammonia vapor (state 5) to condense out any remaining water. The ammonia stream of state 5 can be superheated (stream 6) before entering into the expander where the fluid reaches the low-pressure side (stream 7). If the expander does not extract all the power from the stream 6, the temperature of the stream 7 can be significantly lower than ambient temperature and it can provide cooling output in the refrigeration heat exchanger (stream 8). Finally, the ammonia vapor rejoins the poor solution in the absorber rejecting heat, as a result the basic solution is regenerated again.

To give an estimation of the Goswami cycle potential, it can be compared with the most utilized cycle described in the previous section, namely ORC and the ideal Carnot in the same conditions at low temperature source. For a given boiler temperature of 400 K at 30 bar, and a condenser/rectifier temperature of 360 K, a superheater temperature of 410 K and fixing a turbine exit pressure of 2 bar, the tab. 3.3 shows the performance comparison. Starting from a heat source of 421.6 kW/kg it is able to produce 76 kWe/kg and a refrigeration output of 25.9 kWth/kg. It is noteworthy that the evaluation of the first law of efficiency is not as straightforward as one can think, due to the fact that there are two different simultaneous outputs, namely power and refrigeration. Vijayaraghavan together with Goswami, D. Y. in their study [179] delineated the first law and second law of efficiency for the combined cycle based on existing definitions in the literature.

**Table 3.3.** Performance comparison of the Goswami cycle.

cycle	first law efficiency
Goswami	20 %
Rankine	16 %
ideal Carnot	31.7 %

in this study [122] is possible to understand how the Goswami cycle responds in off-design conditions. They vary the hot and cold source temperature, or the ammonia flow rate inside the cycle to show its behavior. For example, at a fixed hot source temperature of 360 K, the initial refrigeration temperature of 265 K is allowed to let it down for steps of 10 K until no power is produced by the cycle. Both first and second law efficiencies increase slightly at first, then they drop monotonically, showing that there is an optimum refrigeration temperature, in this case 245 K. The first law efficiency has a maximum of 17.41 % and the second law efficiency has a maximum of 63.7 %, a very good achievement for an ambient temperature of 290 K

(70 °C of difference in temperature). During the process previously described both the ammonia solution in the absorber (mass fraction) and absorber pressure so as the turbine inlet pressure follow the same trend of the first law efficiency having a maximum at its maximum efficiency. A slight difference regards the normalized work and the refrigeration output with the refrigeration temperature. Indeed, as the refrigeration temperature falls from 245 K to 205 K both decrease in the same way, on the other hand, above that temperature the normalized work exhibits a little increment, while the refrigeration output having reached the maximum point at 245 K it decreases again. The reason for this difference is bounded with the second law of efficiency, in fact when the refrigeration temperature is above 245K, the ideal COP augmentation would provide a very large contribution to the second law efficiency together with the increment in the normalized work. Actually, as stated before, the second law efficiency decreases, as a result refrigeration output has to drop when the refrigeration temperature goes above 245 K.

### 3.3.5 Externally fired micro-turbine

The first study of the concept of solarized gas turbines was sponsored by the United States *Department of Energy* [8] in early '80. The first appearance of micro turbines for distributed generation occurred with the US patent 4754607A, filed by Robin Mackay in 1986, till that time they were used by the aeronautical industry as auxiliary power units only. The stationary application in the distributed generation requires more reliability, because of the greater number of operating hours, thus their design must be properly addressed. Nowadays, the most important manufacturer of microturbines is the *Capstone Turbine Corporation* [5], the most common application regards the micro-CHP systems fed by fossil fuels, sometimes also by biomethane after a careful gas treatment to avoid tracks of acids that can damage the turbine at high temperature. To fix this issues, biofuels can be also utilized in externally fired micro-turbine. A way to use RES in combination with micro-turbine replacing biofuels can be the CSP technology, since a temperature above 800 °C is needed (common gas turbine inlet temperature in stationary applications is 1200 - 1400 °C), an high concentration ratio must be achieved using punctual collectors, such as heliostat or parabolic dishes. Central towers with a secondary concentrator do this work, in particular the optical efficiency (ratio of the heat energy delivered to the air passing through and exiting the receiver to the solar energy hitting the aperture) can attain value between 86 % and 89 % [48].

The externally fired micro-turbine derives from a turbo-compressor, the same device installed in turbocharged vehicles, the high temperature stream comes from a combustion chamber, or a secondary receiver in CSP.

Figure 3.22a depicts a micro-turbine sold by Capston. Its operation can be summarized as follows: The exhaust gases from an internal combustion engine enter the turbine housing and using the turbine wheel, momentum is transferred from the gases to the main shaft. The exhaust gas leaves at a lower temperature, while from the other side of the turbo-compressor, incoming air enters the compressor housing. Inside it, the compressor wheel using the momentum got from the turbine increases the air pressure and reduces its volume. As a result, a higher amount of fuel per stroke can be added to the same engine due to the reduced volume the air takes now.

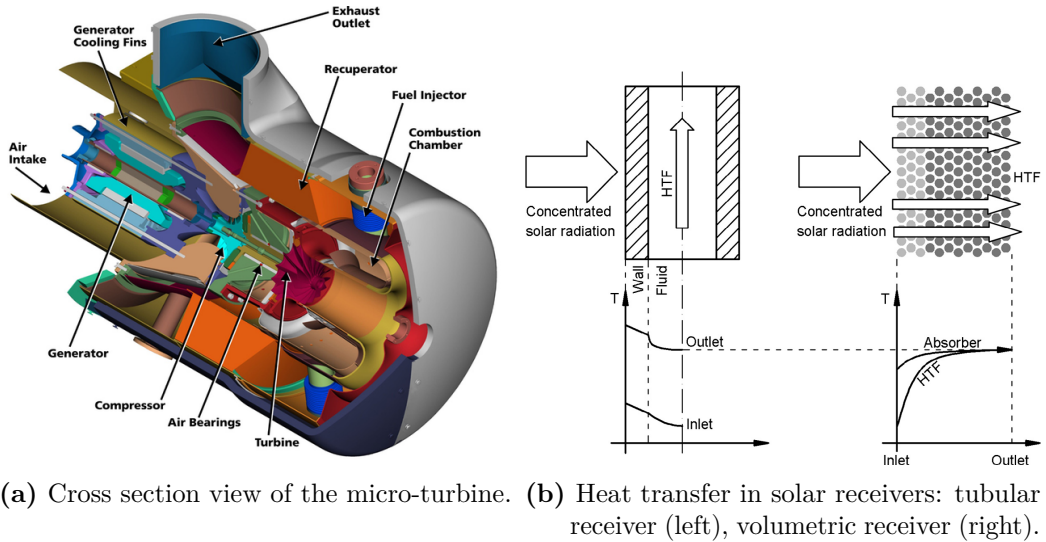


Figure 3.22

As a consequence more mechanical power and higher efficiency is obtained, limited only by the maximum thermal stress allowed by the turbine blades. The process described for the turbo-compressor is modified and coupled with a Brayton cycle. Key feature in CSP driven micro-turbine is the receiver, there are two different types: tubular and volumetric receivers 3.22b [46], the temperature profile in the tubular case has a greater gradient between the receiver and the working fluid. Whereas in the volumetric one, at the receiver outlet, the temperature of the receiver and the working fluid is the same, proving a better heat transfer efficiency.

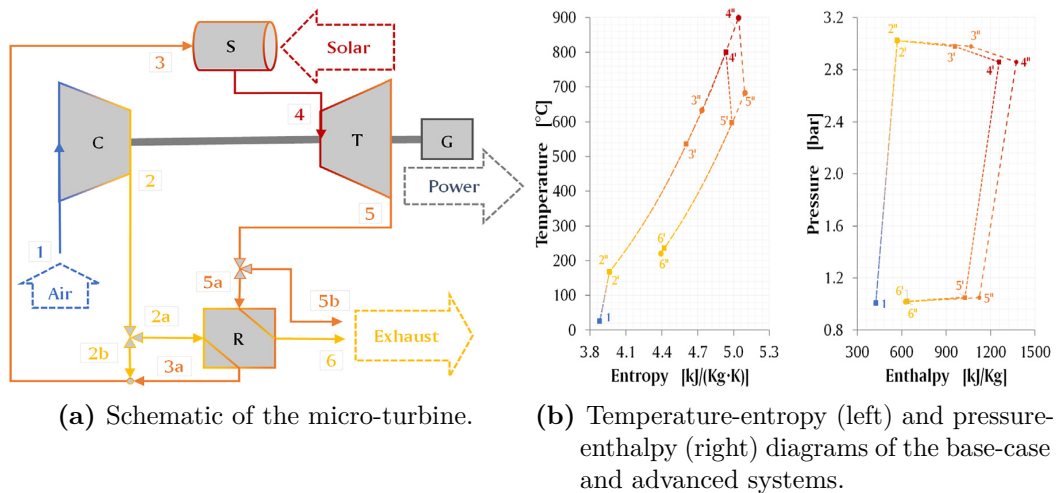


Figure 3.23

An example of a single-shaft recuperative micro-turbine with integrated solar receiver is depicted in fig. 3.23a. First, the air flow pass through the compressor (C) (adiabatic compression); second, the stream 2 is further preheated with the recuperator (R), then it is isobarically heated up to 800 °C in the receiver (S)

Finally, the adiabatic expansion in the turbine (T) provides work and the wasted heat is recovered by the recuperator. When the available solar radiation exceeds a maximum value (upper threshold), a fraction of the total mass flow through the turbine bypasses both sides of the recuperator, thus reducing the inlet temperature to the solar receiver (stream 3) and avoiding overheating of the system. A careful design of the electric generator (G) is needed since the high rotating speed (in the range 100–150 krpm). T-S and P-H diagram in fig. 3.23b show the aforementioned Brayton cycle.

An interesting performance assessment of CSP driven micro-turbine can be found in Gavagnin et. al. [97]. They numerically investigated two different sets of turbine inlet temperatures and recuperator effectiveness: 800 °C-85 % for the base-case and 900 °C-90 % for the advanced system. In their study they carried out a yearly dynamic simulation in three different sites to spot out: (i) the global efficiency (the ratio from the net annual electricity produced to the available solar energy input over the year), (ii) the duped factor (the ratio from the solar energy that is available but not harvested by the system to the available solar energy input), (iii) the capacity factor (the ratio from the annual yield to the electric energy that would be produced if the system worked at the nominal output throughout the year). From their study, they found that the performance of the system can vary significantly on the basis of the reference value of DNI considered in the design process; this parameter depends on the hourly distribution and the performance maps of the system (compressor, turbine, etc.). For example, in the yearly simulations they obtained the highest yield in San Diego where the base-case system achieves 15.87 % annual conversion efficiency and 24.77 % capacity factor, with just 10.69 % of the available solar energy being dumped off the system. Seville shows similar performance but, in contrast, the efficiency in Beijing is just 11.13 % and the capacity factor is 10.51 %. These results remark the importance of a proper selection of DNI at the design point for each location due to the intrinsically off design performance of such technology.

### 3.4 Review of thermal energy storage systems

*Thermal Energy Storage* (TES) represents that kind of technology able to decouple the temporal demand of heat or cold energy between user and generation. A first classification of the various storage technologies is shown in fig. 3.24, sensible and latent heat storage uses physical processes unlike thermochemical.

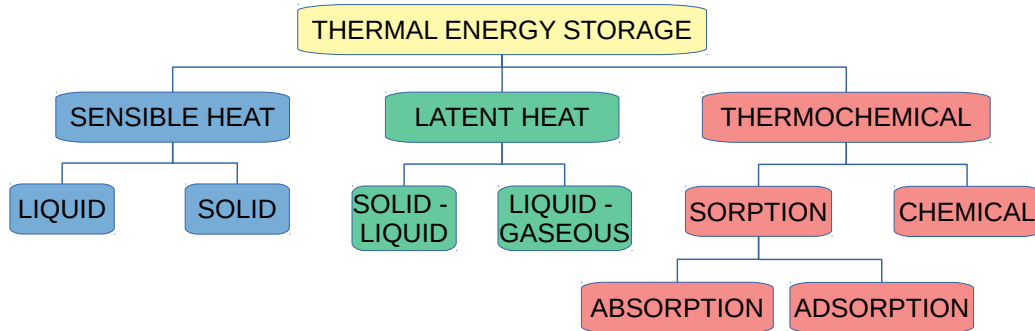


**Figure 3.24.** Classification of thermal storage methods.

Figure 3.25 [100] shows four indicative ranges of storing processes considering a base case of 70 °C in temperature difference for water. *Phase Change Materials* (PCM), reactions based on sorption principle, and chemical reactions are compared based on their energy density. The table 3.4 clearly shows the impact of the energy density on the total volume required for a thermal capacity of 1850 kWh using the technologies above mentioned, but there are several constraints that affect the choice of each one. For example, the temperature ranges of applicability shown in the graph 3.25 derive from a techno-economic evaluation.

**Table 3.4.** Energy density comparison among different storage process.

storage principle	equivalent volume m <sup>3</sup>
chemical reaction	1
Sorption	10
Phase change materials Carnot	20
water	34

The major advantage of CSP plants over solar photovoltaic power plants is that CSP plants may be coupled with conventional power plants to theoretically increase the capacity factor up to 100 %, overcoming the intermittency of solar energy. CSP technologies are mainly implemented with two-tank or single tank systems. The two-tank version stores heat at two temperature levels, high and low. Fluid from the low-temperature tank flows through the solar receiver, there, the solar energy heats it up, then it flows to the high-temperature tank for storage. Finally, the high temperature tank supplies the power block, which in turn gives back the fluid to be sent in the low-temperature tank closing the cycle.

Single tank systems, realize the same process by means of a thermal stratification, thermocline systems are an example par excellence. The solid medium commonly used

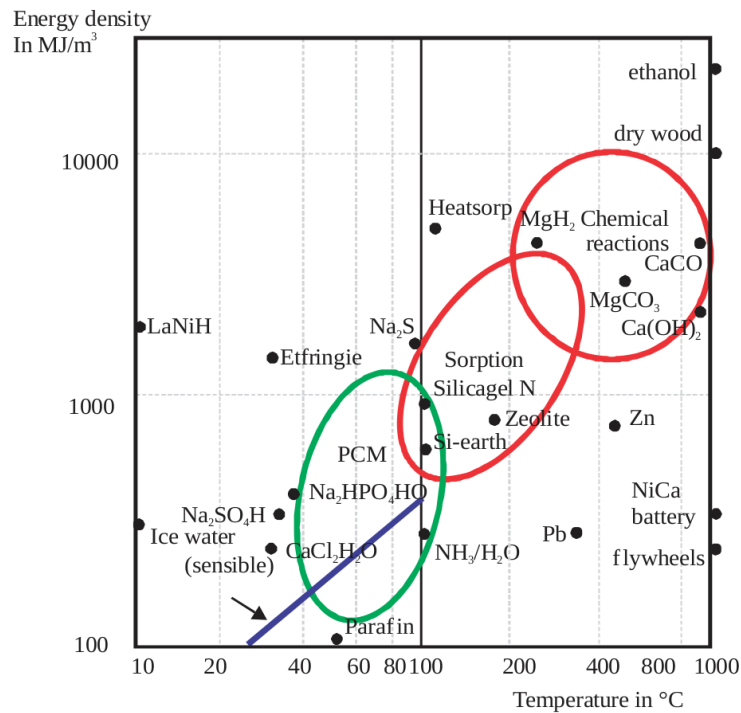


**Figure 3.25.** Classification of thermal storage methods.

is silica sand. The high temperature heat transfer fluid, during the charging process flows into the top of the thermocline and exits to the bottom at low temperature (Downward direction). Reversing, the flow moves the thermocline upward and removes the thermal energy from the storage.

### 3.4.1 Sensible heat storage

By far the most common way to store thermal energy is accomplished with sensible heat. Heat transferred to the storage medium leads to a proportional temperature increase as shown in fig. 3.26, the slope of the line represents the ability of the storage medium to accumulate heat per unit of weight, namely heat capacity at constant pressure.

Sensible heat storage is often obtained from solids like stone or bricks, or from liquids like water, as storage material. Gases have very low density as a consequence the volumetric heat capacity is by far less than the other states, therefore they are not used for sensible storage. Liquids and solids have often opposite physical characteristics, for example liquids own higher heat transfer efficiency than solids, but their vapor pressure and sometimes the corrosive action increase their cost for the materials. Solids are cheap, because they are sometimes traditional construction materials. Hot water heat storages are the example par excellence, used for space heating and domestic hot water. In recent years, seasonal storages are also studied for a long term heat storage under the ground.

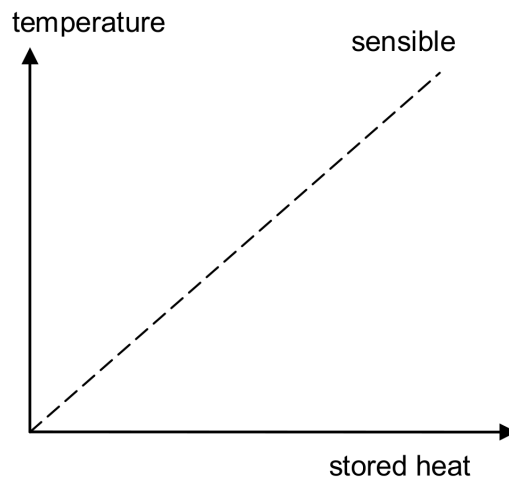


Figure 3.26

### 3.4.2 Latent heat storage

If latent heat storages are used, a phase change takes place in the material and generally this process releases or accumulates large amounts of heat or cold, more than a sensible heat storage per unit of weight. Analogously with sensible storage, the fig. 3.27 depicts the heat exchanged during the temperature increment of the PCM, it is characterized by an isothermal line called melting temperature, also called phase change temperature. The changing in enthalpy between the solid and the liquid phase is called solid-liquid phase change enthalpy, melting enthalpy, or heat of fusion. The dependence of thermal behavior from phase change temperature, can be a feature that allows to tailor the PCM according to the specific application to be realised.

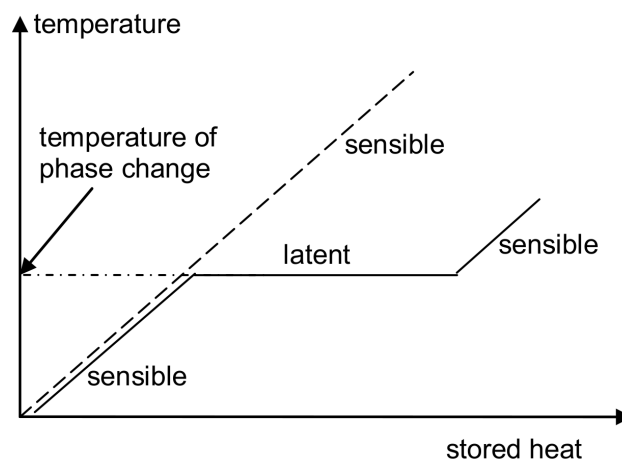


Figure 3.27

### 3.4.3 Thermochemical storage

During a thermochemical reaction, the final enthalpy of the products is different by the initial, this phenomena can be used for heat/cold storage/release. During the charging process heat is supplied to the storage material which causes an endothermic reaction, conversely the exothermic reaction releases heat, an example of an endothermic reaction is depicted in fig. 3.28. The further advantage of this kind of thermal storages regards the ability to store heat for an arbitrary time (almost) without heat losses as long as the products of the endothermic reaction are separated. This feature combined with the outstanding energy density makes *Thermo Chemical Materials* (TCM) very promising for a long term heat storage.

Drawbacks in the use of chemical reaction for energy storage are linked to the fact that they involve chemical bonding, which are strong, and accordingly require a huge amount of energy to be modified, so called activation energy fig. 3.28. Direct consequence is the limited range of applicability, only for high temperature energy storage can overcome this drawback. Some examples of chemical reactions and their corresponding temperature levels are given in table 3.5.

**Table 3.5.** Some chemical reactions for thermal energy storage [164].

	Reaction	temperature (°C)	Energy Density (kJ/kg)
Methane steam reforming	$CH_4 + H_2O = CO + 3H_2$	480-1195	6053
Ammonia dissociation	$2NH_3 = N_2 + 3H_2$	400-500	3940
Thermal dehydrogenation of metal hydrides	$MgH_2 = Mg + H_2$	200-500	3079 (heat) 9000 (H <sub>2</sub> )
Dehydration of metal hydroxides	$Ca(OH)_2 = CaO + H_2O$	402-572	1415
Catalytic dissociation	$SO_3 = SO_2 + 1/2O_2$	520-960	1235

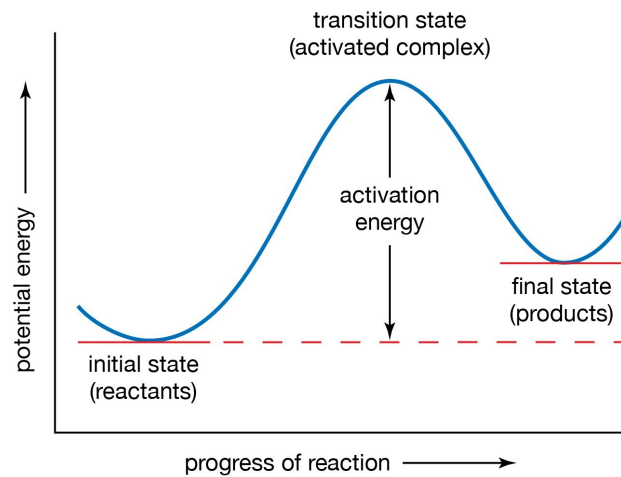


**Figure 3.28**

One line of research is related to the reversible reduction-reoxidation reaction, through this process some redox active oxides can realize enthalpy variations greater than 1200 kJ/kg, remaining stable at high temperatures. Since the product of the cycle will be air at  $T > 1000$  °C, it can be integrated with a CSP plant with an air Brayton system. Despite their high performances shown in fig. 3.25, thermochemical storage systems are not yet commercially viable due to the difficulties in handling

the products of the reaction and controlling the reaction itself.

#### 3.4.4 Comparison of thermal energy storage technologies

The basic technologies for thermal energy storage have been briefly described, the variety of solutions in the literature can not be summarized here, especially regarding the construction methods, but some guidelines for a CSP implementation may be outlined.

In general, it is possible to affirm that sensible storages are commercially available, also in bigger sizes and do not have construction issues. On the other hand, its applicability is limited to short term because of its low energy density.

Latent heat storages present a higher energy density, but they own many drawbacks, for example: application of PCMs is often limited by their degradation (for instance chemical decomposition) over cycling and the low thermal conductivity. The latter issue plays against the higher energy density, because the stored energy may not be released as fast as the user needs.

Thermochemical storages present the highest energy density and have a storage period that is theoretically unlimited, without the need for bulky insulation (less cost). On the contrary, the system layout is complex, this caused a restricted applicability mostly to laboratory scale up to now. To give a more detailed comparison between the available thermal energy storage technologies, from the technical point of view, a list of parameters that are not still described are presented in the tab. 3.6.

**Table 3.6.** Comparison of thermal energy storage technologies.

	<b>Sensible</b>	<b>Latent</b>	<b>Thermochemical</b>
Temperature range (°C)	0÷1200	-100÷1000	150÷1500
Storage density (kWh/t)	10÷50	50÷100	150÷250
Storage density (kWh/m <sup>3</sup> )	50	100	500
Power (kW)	1÷10000	1÷100	10÷1000
Efficiency(%)	50÷90	50÷90	50÷100
Storage period	hours to days	hours to days	hours to months
Lifetime	long	limited due to degradation of materials over cycling	theoretically unlimited
TRL	9	4÷7	4÷6
Environmental impact	negligible	negligible	negligible
Safety issues	no	depends on materials used, but usually limited	limited for sorption TES, higher concern for chemical TES
Corrosion issues	mild	medium to high	low for sorption TES, high for chemical TES
Impact of insulation	high	high	low
Technical complexity of the system	low	medium	high
Flexibility (regulation, partial charge/discharge etc)	high	medium	low



## Chapter 4

# Motivation for the micro CHP plant

Later on, the main technologies for CSP plants, power conversion and thermal storage have been briefly characterized and compared. Large scale CSP plants are commercially available for a long time, roof improvements are still needed to reduce the LCoE gap with the fossil fuel power plants, but maintaining an analogue capacity factor. This issue is more relevant at small scale, due to the plant complexity if compared with other cogeneration units and higher thermal losses (larger shape factor). The final goal is determining the best solution to be installed over a building roof, compactness and structural strength have to be considered as the major design constraints. Moreover, a TRL (Technology Readiness Level) above 5 should be preferred, because another objective is the future construction and testing of a pilot plant.

As a first result, CSP technologies as solar dishes or PTCs must be discarded, as already stated they are subjected to mechanical stress in windy conditions, if damaged some parts may fall down the roof hitting objects or people under the building. Basically, central tower are designed for large power plants, thus they can not be considered as a feasible solution in this study. Compound parabolic collectors and LFRs are the two alternatives, the first one is commercially available and can supply HTF at more than 160 °C, the second solution doubles this limit, if solar salt is used it can also compete with PTCs. Therefore, the LFR technology seems to be in compliant with all the required features. Nonetheless, it should be redesigned to further reduce its encumbrance by means of a lower receiver height, a proper mirrors' curvature and lighter frames. Many studies face up with the optimization procedures to make it more compact, an example is given by Barbon et. al. [59].

Secondly, concerning a power conversion unit, the requirements are: (i) absence of noise (ii) efficient and coherent with the temperature level provided by the previous solution. Since micro gas turbines need a very high temperature HTF level, and the only CSP technology able to reach such temperature is the parabolic dish, consequently they can be excluded at priory. Kalina cycle has a very good potential at low-mid temperature heat sources, but only big power plants are currently running, in this case the cycle complexity makes it difficult to be implemented at small scale. The Goswami cycle is pretty new, is still in development and very few tests were

carried out at lab test scale, thus the TRL constraint can not be fulfilled. Stirling engines and ORCs remain the two candidates at the moment. Despite the low diffusion of Stirling engines they exhibit an interesting potential, but in CSP plants they are driven by solar dishes, because they require an high temperature source in the radiative form to be utilised efficiently. ORC is the most flexible solution, it is silent, reliable, compact and its inlet temperature perfectly overlaps with that provided by LFR technology. The major drawback is the low thermal efficiency, especially at small scale, thus even if it is a marketable product it should be properly designed to improve this aspect, therefore the research activities must be addressed in this sense.

Thirdly, needless to say, thermal storage is needed for minimizing the electricity transfer throughout the grid, increasing the capacity factor and above all to shift the heat availability with the demand in time, especially in winter seasons. As stated before, high temperature processes, as those in thermochemical conversions, have noticeable advantages in terms of compactness, on the other hand they are still closed in the research field and do not allow to build a pilot plant with enough reliability. Moreover, they need many measures to control the process, this fact increases the already high plant complexity, thus this solution has to be rejected. Traditional sensible storage can be a solution, they are already used in the solar panels installed over the rooftops, but the domestic hot water needs are not comparable with the thermal energy required for a micro CHP plant, whose heat generated should also fulfill the space heating needs. The by far higher thermal demand results in infeasible storage volume, moreover the large weight is not bearable for the building. Phase change materials are the best compromise, they have a good specific energy, in addition the latent heat is released at high temperatures enabling better efficiency of the power conversion unit. The drawback is about the peak of power exchanged, PCMs usually have low thermal conductivity, as a consequence the study has to overcome this issue. To increase the heat transfer, graphite foam may be added, it is cheap and thermo-chemically stable over time, heat pipes for example, may reduce the thermal resistance between the HTF and the PCM.

Overall, the challenge of this study leads to a micro solar CHP made up of a LFR coupled with an ORC and uses a latent heat thermal storage thermally enhanced by graphite, equipped with heat pipes. This is one of the possible solutions, for this reason, in the subsequent section is reported the background of this research to actualize the plant within its research context.

Referring back to the DES, it is necessary to estimate an indicative size for this kind of power plant, the major constraint in this case is represented by the rooftop surface width. Supposing to cover a broader user demand, the lower limit beyond which plant construction makes sense is about 2-4 kWe. Therefore, the solar field and the thermal storage must be designed coherently with the solar multiple (installed solar power to the power of the motor block) that realizes the lower LCoE at given latitude. To support the previous statements, Bellos et al. [62] did an optimization of a cogeneration system with LFR and ORC. In their study, different combinations of collecting areas and storage tanks applied in order to determine the best combination in every case. Results showed that the best design according to net present value maximization includes 140 m<sup>2</sup> collecting area, a storage tank of 1.4 m<sup>3</sup> and an ORC operating at 290 °C, which correspond to the design parameters

discussed in the next section.

## 4.1 Concept design of the micro CHP

Needless to say, micro cogeneration and trigeneration have a very interesting potential in households [83] both grid connected and stand alone, several studies have addressed the dynamic performance of such systems in TRNSYS [161, 72]. Even though this dissertation is more focused on CHPs, in the section 7.2 is evident that most of the time more benefits come out from a solar trigeneration than a cogeneration plant, it is obvious, the greatest thermal demand is in winter seasons when solar radiation is weak. To cover a larger part of the electrical demand, the plant has to be sized properly, as a result the amount of unused heat is relevant in summer seasons and it is consequently wasted. Trigeneration plants can fulfill the cooling demand which is predominant in summer where exceeding heat is normally wasted in CHPs. As a consequence, trigeneration can exploit better the solar energy provided curtailing the payback period making the investment more profitable. For example, Angrisani et al. [49] investigated the techno-economic feasibility of a micro-trigeneration system starting from previous experimental tests of the prime mover. The integrated system used to provide air conditioning to a lecture room and domestic hot water to a nearby household has shown interesting performance, synthesized by an 82.1 % overall efficiency in terms of primary energy ratio, and reduced energy consumptions compared to the reference system. They specifically developed a mathematical model of a micro-trigeneration system with the final aim to determine the primary energy saving by means of the *Fuel Energy Saving Ratio* (FESR). They also implemented a sensitivity analysis of primary energy saving, net saving and CHP generation bonus with respect to the electric surplus factor from the CCHP unit. However, attention has not been paid on the influence of design and adjustment parameters on plant performance. Considering the works edited until now on the topic of solar ORC as (CCHP) system, Chang et al. [74] referred to a *Combined Cooling Heating and Power* (CCHP) system consisting of a hybrid *Proton Exchange Membrane* fuel cell and a solar ORC. In particular, they evaluated the effects of solar radiation, current density and operating temperature of the fuel cell and ambient temperature on the performance of the trigeneration system. However, in this study the electric power is provided only by the fuel cell thus mitigating the energy dependence on the solar source because the solar powered ORC expander is coupled with the vapor compressor cycle compressor. Boyaghchi et al. [70], instead, carried out a thermodynamic and thermoeconomic optimization of a solar ORC trigeneration plant for domestic applications by varying some thermodynamic variables. The heat coming from solar collectors is integrated by a natural gas boiler when requested. They focused the attention on the following CCHP key parameters: turbine inlet temperature and pressure, turbine back pressure, evaporator temperature and heater outlet temperature. The considered objective functions were the thermal efficiency, the exergy efficiency and the total product cost rate.

Among the different CSP technologies, LFRs proved to be a very promising solution as solar concentrators for medium and high temperature thermal applications

thanks to their potential to overcome techno-economic constraints associated with conventional reflector based CSP [116]. Compared to PTC indeed, LFRs show an interesting potential in cost reduction terms, thanks to a lighter structure and a fixed receiver, which can be designed for optimum integrated thermal performance [44]. At present, for an installed power lower than few hundreds of kW, the specific cost of a LFR solar field is about 200 €/m<sup>2</sup> of collector area [147], but it can be reduced up to 150 €/m<sup>2</sup> in case of system improvements and large scale production [13].

Although the benefits of their usage in building-façade for power generation have been proven [75], their adoption in buildings has been limited so far. In fact, at residential level evacuated tubes are preferred, because of their ease of installation and absence of tracking mechanisms. However, the use of medium and high temperature solar technologies in buildings can be economical and feasible if the systems are designed reasonably [175], because of the high potential of cogeneration at residential scale [45] where both thermal and electric energy are requested. To efficiently convert solar energy into generated power, ORC systems are considered as one of the most common and competitive technologies [174].

On a large scale, several manufacturing companies for ORC exist and their products are already into the market [153]. However, different factors are boosting the interest for small ORC units, such as the need of power in developing countries, the request of polygeneration systems for grid connected applications in developed countries as well as the deregulation and privatization of the electric generation sector worldwide [174]. There are still several challenges for the exploitation of low grade thermal energy resources by means of ORC systems [200], therefore, academic research is paying a lot of attention to them. For example, Bouvier et al. [69] experimentally investigated the performance of a micro CHP system composed of a solar PTC coupled to a steam Rankine cycle expander for direct steam generation. Recently, Li et al. [119], for example, evaluated the influence of heat source temperature and ORC pump speed on the performance of a small-scale ORC system using *R245fa* as working fluid. Al Jubori et al. [47] instead focused on the influence of several turbine design features on turbine performance in ORC systems with five working fluids. Pei et al. [145] experimentally investigated the performance of a specially designed radial-axial turbine using *R123* as working fluid. The test has shown that a turbine isentropic efficiency of 65 % and an ORC efficiency of 6.8 % can be obtained with a temperature difference of about 70 °C between the hot and the cold sides. The same authors [118] evaluated the energetic and exergetic performance of the updated ORC system and the related thermal efficiency at different heat source temperatures. On the contrary, Quoilin et al. [154] evaluated the thermodynamic performance of low cost solar Organic Rankine Cycles considering different working fluids, expansion machines and system configurations. Although low output electric power and solar-to-electricity efficiency are achieved, the analysis showed the feasibility of adopting such a system for hot water or heating production into a building. Some examples of studies regarding micro solar-ORC systems focused on their performance assessments are discussed as follow.

Taccani et al. [171] tested a small scale micro solar CHP (2 kWe) powered by parabolic trough solar collectors with a collector surface area of 100 m<sup>2</sup>. They indicated that the system can achieve 8 % as gross electricity efficiency. Instead, Xu

et al. [190] evaluated the performance of a LFR-ORC system through a theoretical and simulation study. Results showed that the supercritical ORC system is better than the subcritical one independently from the considered working fluid. Antonelli et al. [50] carried out a dynamic modeling of a low concentration solar plant consisting of static compound parabolic collectors coupled with an ORC unit in *AMESim*. The authors found that the use of a volumetric expansion device with variable rotational speed allows operation without need of any storage system.

However, in order to increase the annual energy production of a small-scale solar ORC, a TES tank is usually employed. TES plays a key role to ensure the normal operation of such systems by reducing the effect of the variable solar radiation as addressed by several studies. Freeman et al. [94], for example, stated that a thermal energy storage is a key feature for their domestic solar-ORC combined heat and power system for year-round operation in the UK, in order to buffer the intermittent input of solar thermal energy to the system. Li et al. [120] analysed the dynamic performance of a solar ORC with TES, finding that a proper TES capacity, which allows to suppress the dynamic impact of solar fluctuations and avoid resonance phenomena in the plant, exists. Even He et al. [120] developed a transient simulation model of a PTC solar field coupled with a single tank TES and an electricity conversion system based on ORC focusing on the effects of several key parameters. In particular, the influence of the volume of the TES on the performance of the system has been considered and its optimal volume with seasonality assessed. Freeman et al. [93] compared sensible and latent TES for a domestic-scale solar combined heat and power system. They found that a 20 % higher total daily electric output per unit storage volume can be achieved with a *Phase Change Material* (PCM) storage compared to a water energy storage. Moreover, the isothermal operation of the PCMs during phase change allows higher energy conversion efficiencies. Manfrida et al. [128], instead, developed a mathematical model of a TES containing PCM and evaluated its application in a solar power ORC over one week period. In particular, results showed that the proposed plant is able to generate power for almost 80 % of the simulated period with a weekly average overall solar-to-electricity efficiency of 3.9 %. At the same time, the analysis revealed that appropriate control logics are required to improve the performance of the system over a more extended period.

An adequate modeling of the different subsystems and the optimal design of the operational strategies of such systems are indeed of paramount importance to achieve higher conversion efficiency and annual performance. Broadly speaking, in the most general case of the solar CHP system, the operation can be set in terms of demand priority. Two possible cases can be taken into account: i) priority to cover heat demand with the solar system; ii) priority to cover electricity demand [96]. Just to give some examples about the incidence of the system control strategy on the global outputs, here are reported some research of interest: in waste heat recovery ORC cycle, second law efficiency can be improved by about 10 % by implementing a proper control strategy which takes into account the heat source variability [152]. In particular, Hernandez et al. [103] designed and experimentally validated an adaptive model predictive control law to optimally recover waste heat with an ORC unit. The analysis proved that the proposed control outperforms the gain-scheduled PID strategy and allows regulating accurately the superheating at the evaporator outlet. When a TES unit is also included in the plant, optimal

design of subsystems and their interactions are fundamental. Petrollese and Cocco [147] evaluated the optimal design parameters of a hybrid LFR coupled with a TES system, an ORC plant and a PV array to follow a constant output power level for different daily time periods. Patil et al. [144], instead, carried out a techno-economic comparison of the performance of a small scale concentrated solar ORC with the performance of a photovoltaic (PV) plant, taking into account their coupling with energy storage systems. In particular, the analysis showed that both systems achieve the minimum LCoE when no storage is included and the solar ORC with storage is more competitive than PV when reliability of power supply is the most important factor to guarantee.

Coming back to the previous speech, the microCHP have to fulfill the residential sector demand, on this regard Barbieri et al. [58] analysed the feasibility of micro-CHP systems to meet the household energy demands of single family users, while Bianchi et al. [66] evaluated the profitability of different micro CHP systems consisting of prime mover, auxiliary boiler, TES and electric energy storage system for residential applications. The optimum number of electric energy storage modules, their specific costs and the maximum number of shut down for each prime mover technology (including micro ORC) have been evaluated according to the Italian scenario. Calise et al. [9] investigated the energy and economic performance of a 6 kWe ORC unit coupled with 73.5 m<sup>2</sup> of innovative flat-plate evacuated solar collectors in different climatic conditions. They showed that while the efficiency of the ORC does not vary significantly during the year, the efficiency of solar collectors is high in summer, but very low in winter. The economic feasibility of such a system is possible in presence of feed-in tariff incentive schemes. Please refer to the section 7.2 where other examples of micro solar CHPs buildings integration are described more in detail.

The study presented here makes use of the collaboration with other universities and industries within the European Union project called *Innova MicroSolar*, indeed the micro solar CHP concept overlaps the solutions found in the previous chapters about the DES implementation at building level. Just to give some details about the European project: *Innova MicroSolar*, acronym of "*Innovative Micro Solar Heat and Power System for Domestic and Small Business Residential Buildings*" is a research and innovation project funded under the *HORIZON 2020 Framework Programme*, Grant Agreement number 723596, and spans for 48 months. It has been conceived from the specific call named "*EE-04-2016-2017 - New heating and cooling solutions using low grade sources of thermal energy*", and it is expected to demonstrate the impacts listed below:

- technologies have to use low valued (low-grade) energy sources (residual and renewable sources of thermal energy) in low-exergy heating and cooling systems;
- technologies have to take advantage of very low and low (moderate) temperature resources, e.g. by upgrading them, in order to generate useful heating and cooling and if relevant electricity. (e.g. heat pumps able to harvest low-grade heat, heat driven chillers and heat driven combined heat and power cycles). Necessary attention should be paid to improving system reliability and automated operation;

- Technology Readiness Level (TRL) 4-6;
- Increased share of residual and renewable sources of thermal energy in the supply heating and cooling demand;
- Gains in the overall efficiencies of heating and cooling systems using very low and low (moderate) temperature sources of thermal energy;

Referring back to the concept design, this project is aimed at accomplishing a small pilot plant consisting of a cost-effective 2 kW<sub>el</sub>/18 kW<sub>th</sub> solar heat and power system, it should provide on-site electricity and heat generation in individual dwellings and small business residential buildings. To do that, solar thermal energy at modest temperatures of 250-280 °C is used. The whole system was expected to be integrated with domestic boiler hot water and space heating system. During a period covering winter and summer seasons it is expected to carry out a field test campaign on the demonstration site, the final demonstration tests should lead the research to a TRL 6 as the objective of this dissertation. The research challenges are the following:

- a novel compact and light Fresnel mirror solar concentrating collector;
- micro and high efficient ORC able to achieve more than 250 °C as inlet temperature;
- an advanced latent heat thermal storage equipped with reversible heat pipes for rapid charging and discharging;

The whole system concept briefly described before is depicted in fig. 4.1 the technological targets to reach with the demonstration plant are summarized in table 4.1.

**Table 4.1.** Targeted technical specification for Innova MicroSolar systems.

Technical specifications:	Targets
Electrical power produced	2 kW <sub>el</sub>
Heating capacity	18-20 kW <sub>th</sub>
Electrical efficiency	10-12 %
Thermal efficiency	80 %
Overall efficiency	90 -92 %
Capital cost	3,000 - 4,000 €/kW <sub>el</sub>
Operational life	24,000 h
Service intervals	2,200 h/year
Specific Power	0.05 kW <sub>el</sub> /kg
Specific Power	21 kW <sub>el</sub> /m <sup>3</sup>
Noise level	<48 dBA @ 1 m
Tempeprature source	Solar @ 250-280 °C

As any other European Project, it involves more than 3 Countries, the participants are expertise over several decades across various disciplines and sometimes proprietary of IP, the following table gives a brief summary.

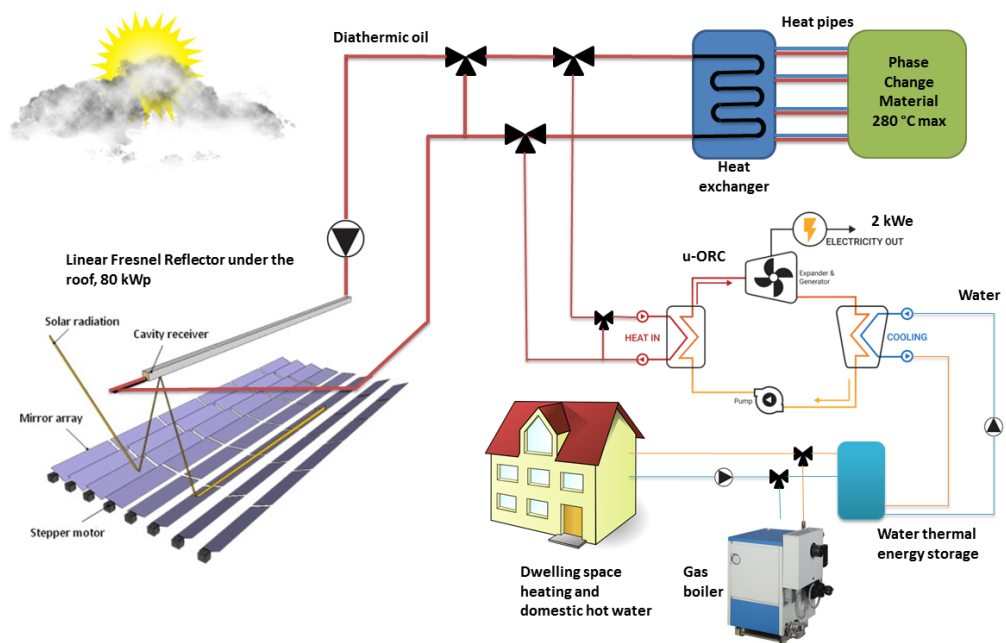


**Figure 4.1.** The functional blocks of the innovative Innova MicroSolar system.

Table 4.2

Partner	Country	Role in the project
Enogia [17]	(France)	development of small and micro scale ORC plants
Elianto SRL [13]	(Italy)	development and manufacturing of highly efficient solar concentrating collectors;
Thermacore Europe [1]	(UK)	development of advanced heat pipe technologies;
Strategie [30]	(Italy)	development of engineering smart control units for integration of solar thermal and boiler systems;
Sinagro Enginyeria	(Spain)	integration of renewable CHP technologies in buildings;
User Feedback Program	(Spain)	socio-economic impact and commercialisation of new renewable energy products;
University of Lleida [36]	(Spain)	R & D of high performance Thermal Energy Storage systems on the basis of Phase Change Materials;
Università eCampus	(Italy)	R & D of CSP systems based on linear Fresnel mirrors;
Northumbria University [26]	(UK)	R & D and optimisation and the development of new PCM and CHP systems and in complex multi-physics modelling;

Thanks to the development of the Innova MicroSolar project, the research here presented can get valuable experimental results for providing a further validation of the mathematical models, especially about the TES, because of its intrinsically complexity (anisotropy, heterogeneity and heat pipes thermodynamic behavior). On the other hand, a reciprocal advantage exists from this collaboration, because the EU project can in turn take advantage of the worth preliminary studies here undertaken. In fact, because of the novelties introduced by this kind of micro CHP plant, the dynamic response of each subsystem can be underestimated or overestimated, unless preliminary outcomes/guidelines are provided to coherently operate the plant, both from the optimisation and safety/reliability point of view, this is also the indirect support of this research.

## Chapter 5

# Outline of dissertation

From the aforementioned motivations for this research, the outline of this dissertation is now briefly described.

Basically, the dissertation faces up with both high level system modeling and detailed investigations of some parts of the subsystems forming part of the microCHP plant. So, in chapter 6 is only shown the modeling framework then used in the next chapters as a starting point for further analyses. More precisely, this chapter contains some independent sections where the mathematical models of the solar field, thermal storage and Organic Rankine Cycle are briefly introduced with a literature review and then explained step by step. In the Appendix A are attached all the codes relative to the Simulink blocks created with the equations described in this chapter.

After being outlined the mathematical approach, chapter 7 reports some dynamic test cases aimed at investigating manifold aspects:

- i section 7.1 deals with the complete energy assessment in terms of input and output energy of each subsystem: the annual thermal and electrical energy production is discussed and tabulated. Moreover the daily trends of the power transferred in different portions of the plant are also shown, in this way are also shown the effects of the control system on the microCHP plant operation. In addition, sections 7.1.2 and 7.1.3 investigates the effect of the modeling detail of the pipeline network on the energy outcomes, and the possible improvements obtained from a thermal energy storage partialization in winter seasons respectively. Since the pipeline network accounts for noticeable thermal losses, it is important to accurately take them into account. Whereby, the first study highlights to what extent it is convenient to increase the spatial discretisation of the tubes to get more accurate results without raise in CPU power. On the other hand, as far as the second study is concerned, the purpose is more or less the same, i.e. to reduce the thermal losses of the storage disconnecting part of it when the solar irradiation is weak.
- ii The microCHP has been conceived for space heating and domestic hot water demand in dwellings, thereby in section 7.2 the interaction between the CHP and a multi apartment block is simulated. In particular, the optimal number of apartments considering a weekly thermal demand is found, after that the

energy coverage throughout a yearly simulation is accounted for. The potential coverage of the thermal demand is further improved by adding an absorption chiller in bottoming to the ORC. In this way it is also able to fulfill the space cooling demand, realizing a trigeneration plant. Finally, some optimisations about the thermal storage size are addressed to maximize the trigeneration outputs.

- iii Regarding a lower level of numerical investigation, section 7.3 addresses the thermal stress aspect in receiver tubes of concentrating solar plants. Here is explained a novel approach to calculate the internal wall temperature under several working conditions occurring in the normal solar field operation. On the basis of these results tabulated in appendix C, a new correlation is found to predict the thermal overheating only from the knowledge of the environmental parameters (already measured by existing sensors). Fundamental part of this study consists of literature review on the heat transfer correlations for constant heat flux, velocity and thermally developed flows in horizontal tubes. Many studies are available in literature, but they hardly any cover some fluid regimes that sometimes occur in the receiver tube, appendix B contains all the investigated correlation currently available in the scientific community.
- iv Finally, the control design with the *Hardware In the Loop* (HiL) approach of the whole plant is reported in section 7.4. By means of a *ModBus* connection. An external *Proportional-Integral* (PI) controller is allowed to regulate the four diverters installed into the simulated plant with the purpose of following a desired flow rate pattern. Three different PI constants are tested (included the optimum one). Furthermore, another test is carried out setting the desired inlet temperature of the Organic Rankine Cycle adjusting the pump flow rate of the plant or the inlet valve of the ORC itself, then the two approaches for problem of regulation are discussed and compared.

## Chapter 6

# System modeling

### 6.1 Linear Fresnel Reflector

#### 6.1.1 Introduction

In Concentrated Solar Power plants, solar energy is mainly collected by means of primary collectors which redirect the sun rays into receiver tubes achieving temperatures even higher than 400 °C [3]. At present, several types of collectors exist, such as Parabolic Trough Collectors, *Compound Parabolic Collectors* (CPC), Dish Collectors and Linear Fresnel Reflectors described in the previous paragraph 3.2. Compared to PTC, LFR represents a good compromise between low encumbrance and weight, but maintaining high concentration ratio allowing the use in small and medium size solar CHP plants. Currently, several researchers are focusing their studies on them: for example, Abbas et al. [44] have optimized the LFR design for the whole day, even with a noticeable fluctuation of the impinging radiation intensity. Even though some commercial plants with LFRs are currently running, research in LFR efficiency improvements is still ongoing owing to the attractive potential of such technology, for example regarding the secondary reflector geometry [73] or finding new solutions for the primary mirrors [61], since the optic is less effective than in PTCs.

The procedure to calculate the exact energy recovered by a thermal solar plant consists of two stages, firstly optical efficiency must be evaluated from the solar source to the receiver surface, secondly the thermal efficiency of the receiver tube must be assessed solving the thermal problem of heat exchange between the HTF and the environment. Since LFR has a complex geometry, it is really tough calculating the actual intensity and the distribution of the concentrated rays on the glass envelope of the receiver tube, PTCs for example have a unique mirrors' curvature, conversely LFR have multiple linear mirrors, because they are placed at different focal length from the receiver they require a own tailored shape. Ray tracing technique performs this task, in particular this process consists of simulating a large variety of solar rays path each one with a specified intensity and direction, ray tracing is capable of simulating a variety of optical effects, such as reflection and refraction, scattering, and dispersion phenomena The result in case of optical efficiency assessment is expressed in term of DNI concentration on the absorption layer of the receiver. Unlike PTC, LFR needs a careful evaluation of the path rays also between the

glass envelope and the receiver tube, as matter of fact the ray's disuniformity is accentuated and the higher impinging angle produces multiple reflections reducing the optical performance.

From the thermal efficiency point of view, when the geometry of the reflector is defined, an accurate heat transfer model of the evacuated tubes is required to properly assess the overall performance of the solar plant. With this aim, the Forristall model [91] is considered a reference in the field. Its results have been satisfactorily validated with experimental data. The Forristall model belongs to the class of uniform models, for which uniform temperature and heat flux around the receiver are assumed, thus approximating the real problem. On the contrary, non-uniform thermal models evaluate the energy balance between the incoming solar radiation and the receiver tube taking into account separately the active and non-active areas of the tube. As a consequence, these kinds of models allow analyzing the local non-uniform solar radiation and the related heat transfer performance characteristics of the receiver tube. In particular, the comparison between the uniform and non-uniform model has been addressed in a recent paper by Cheng [76] with reference to a PTC solar field. If 1 D models are considered, uniform flux distribution can be assumed since no relevant discrepancies are obtained compared to non-uniform models. Nevertheless, several studies demonstrated that some assumptions can affect the final result of the simulations. For example, Padilla et al. [142] showed a deviation from the Forristall's results because they also took care of the view factors for both the thermal interactions between the neighboring surfaces (absorber–envelope, and envelope–envelope) and the thermal radiation losses. In this way their model can consider also the higher radiation losses that otherwise may be underestimated especially at high absorber temperatures. Furthermore, Yilmaz and Soylemez [197] increased the accuracy of the model with respect to the radiation losses from the glass envelope and the conduction losses through the support brackets.

Apart from the potential rooms of improvement in model accuracy in terms of physical phenomena assumptions and correlations, all in all, from the previously mentioned research, the 1 D models seem somewhat in agreement with the experimental data. Furthermore, the better results got with more accurate spatial resolution models can be vain if even small uncertainties are present in evaluating the optical coefficients (mirrors reflectance, dirtiness, geometry errors etc.).

Therefore, 1 D models can be satisfactory adopted in dynamic simulations where low computational efforts are needed to assess the yearly performance of a whole plant. Regarding this aspect, Xu et al. [192] performed transient analysis by means of a uniform model, revealing that the response delay of the receiver tube varies with varying the nature of the heat transfer fluid. Moreover, the response delay of the outlet temperature of the fluid can be correlated with the Direct Normal Irradiance and the changes in the fluid flow rate according to the following exponential function  $y = Ae^{(-x/t)+B}$ . Indeed, the proper estimation of the temperature distribution of the HTF along the receiver tube allows to adopt the optimum operation strategies of the solar field by adjusting accordingly the HTF flow rate [193]. In addition, at part-load conditions the HTF flow rate may be reduced to increase the difference in temperature at the LFR headers or trivially for pump energy savings. As a consequence, the thermal model of the wall adopted by Forristall should be revised since the correlation utilized for the HTF in contact with the internal wall of the

receiver tube is not in the proper validity range. Both in PTC and LFR, non-uniform heat flux distribution around the absorber tube circumference plays an important role regarding the heat exchange between the wall and the HTF inside. Indeed fluid that is heated at the lower edge is pushed upward and replaced by colder fluid drawn down by gravity, this phenomenon is called *buoyancy driven flow*. Even though some authors investigated this effect [101], they only considered turbulent flow regime where buoyancy induced flow is negligible. The strong secondary flow circulation has a major influence in the laminar regime. Other authors [198], investigated the laminar flow in case of non-uniform heat flux distribution, they revealed a much higher Nusselt number than that obtainable neglecting the buoyancy-induced secondary flow. Izuchukwu F. Okafor [138] carried out a 3 D steady-state numerical simulation based on ANSYS Fluent, they assessed the influence of circumferential non-uniform solar heat flux distributions on the internal and overall heat transfer coefficients. They changed the distribution value of 160°, 180°, 200°, 240°, and the 360°, with the Reynolds number range from 4,000 to 210,000 based on the inlet temperature. It is worth to notice that the average internal heat transfer coefficient is not affected by the exterior heat flux distribution; on the contrary the average overall heat transfer coefficient for the circumferential uniform heat flux was greater than that of the non-uniform. The forced convection and the turbulent flow again confirms the assumptions used in the Forristall model, but do not show its behavior in the laminar regime, in particular when free convection effects are dominant. Another important finding regards the temperature distribution in the circumferential direction, the inner-wall-to-fluid bulk temperature difference decreases as the Reynolds number rises and it reaches its maximum to the corresponding most heated lower central portion of the tube, where the solar rays are more concentrated. In the peak portion of the bottom profile it is possible to overcome 20 °C in temperature difference still remaining in the turbulent region ( $Re = 4043$ ), this means that even larger values are expected in the laminar flow under non-uniform heat flux distribution. Nonetheless, the same authors of the previous study: Izuchukwu F. Okafor [139] carried out a numerical study on a PTC with the inlet Reynolds numbers ranging from 130 to 2200, thus only in laminar flow regime. The research clearly shows as the buoyancy effects can enhance the PTC efficiency, when heat flux intensity and incident heat flux angle span of the impinging heat flux increase, the internal heat coefficients rise approx. by a factor of 2.1-2.5, confirming the previous hypothesis in which buoyancy-driven secondary flow has a remarkable effect on the overall heat transfer. These outcomes should be considered for a dynamic simulation where the operating conditions greatly vary. Unlike of the previous authors, Zhen Huang et. al [106] focused their work on the fully developed mixed turbulent flow (the mixed regime occurs when the flow rate decrease to cover the range of the Reynolds number in the real cases), but they better evaluate the non-uniform heat flux taking into account the effect of solar elevation angle within a large operating range, in particular using a Reynolds number of  $2 \cdot 10^4 - 10^5$ , Prandtl number of 1.5 and Grashof number of  $0 - 10^{12}$ . In the research, Zhen Huang et. al used two-equation turbulence model (SST)  $k - \omega$  aimed at find out new criteria under which the effects of buoyancy should be considered. They claim that the Richardson number is not enough to describe the regions of free and forced convection, but it should be modified according with the changing of the sun elevation angle in PTC.

Ultimately, in this Section a 1 D dynamic model, mainly defined on the basis of the well-known Forristall model, is presented. The main objective is readapting the input parameters in the Forristall code developed for PTCs with the specifications of the new receiver tube HCEOI-12 [3], moreover unsteady effects are added to be suitable for dynamic simulations. For the validation, the model is compared to the Forristall one, in steady state conditions. Finally, to maintain a low spatial discretisation, thus a superior computational efficiency, a in deep analysis on the internal wall thermal resistance is addressed to take into account the influence of the part-load operating conditions.

### 6.1.2 Modeling

The dynamic operation of the receiver tube is evaluated considering the energy equation throughout the receiver tube. Neglecting the contribution of conduction heat transfer along the axis of the receiver, as well as that of kinetic energy and pressure drop, it is possible to re-write the governing energy equation of the HTF along the tube length direction as follows:

$$\frac{\partial(\rho c_p T A)}{\partial t} + \frac{\partial(\rho u c_p T A)}{\partial x} = -\dot{Q}_{loss} \quad (6.1)$$

where  $\dot{Q}_{loss}$  is the thermal power dissipated in the external ambient. Density  $\rho$  and heat capacity  $c_p$  are both time dependent, since their value is a function of the HTF temperature. The equation is solved according to the *Finite Difference Method* (FDM), with first order *Upwind* scheme. This solving scheme entails simple applicability and good accuracy especially for fast temperature ramps in transient operations. The upwind scheme shows non-physical ripples when higher order than the first is used. A possible solution to overcome this limitation consists of adding a *Total Variation Diminishing* (TVD) [108], but this implementation lies outside of the scope of this study. With reference to the first order upwind scheme, equation 6.1 becomes:

$$\frac{T_i^{k+1} - T_i^k}{\Delta t} + u_i \frac{T_i^k - T_{i-1}^k}{\Delta x} = -\frac{T_i^k - T_{iw}}{R_{conv,i,int}^k \rho^k c_{p_i}^k A} \quad (6.2)$$

where  $k = 1, 2, \dots, N$  denotes the number of time step,  $i = 1, 2, \dots, M$  denotes the number of longitudinal segments. The thermophysical properties of the HTF are evaluated according to the temperature in the previous time step. The spatial discretization of the above equation is depicted in fig. 6.1.

Uniform distribution of solar radiation and of all modes of heat transfer is considered: (i) convection into the receiver tube, in the vacuumed annulus between the receiver and the glass cover, and from the glass cover to ambient air; (ii) conduction through the metal receiver pipe and the glass envelope walls; and (iii) radiation from the metal receiver tube and the glass envelope surfaces to the glass envelope and the sky respectively.

The energy balance not only must be conserved along the axial direction, but also in the radial one. Therefore from fig. 6.3 and fig. 6.2 a system of equation for the energy balance can be written:

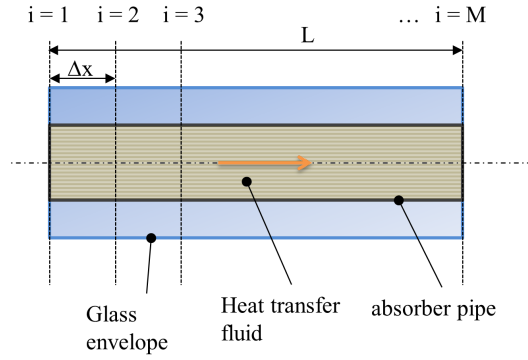


Figure 6.1. 1 D longitudinal discretisation

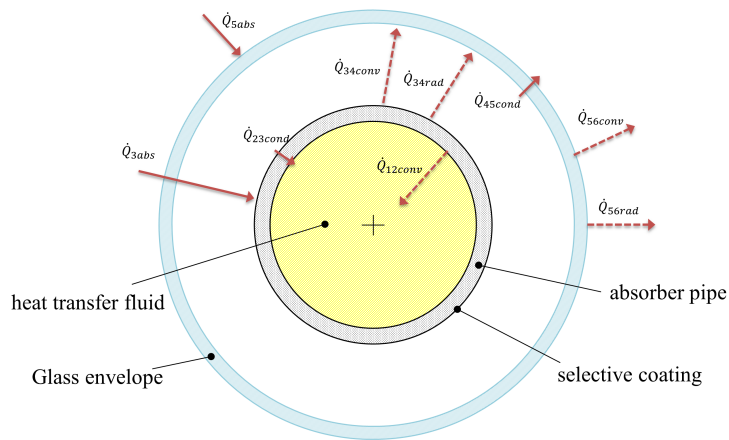


Figure 6.2. Section of the receiver tube.

$$\dot{Q}_{12,conv} = \dot{Q}_{23,cond} \quad (6.3)$$

$$\dot{Q}_{3,abs} = \dot{Q}_{34,rad} + \dot{Q}_{34,conv} + \dot{Q}_{23,cond} \quad (6.4)$$

$$\dot{Q}_{34,conv} + \dot{Q}_{34,rad} = \dot{Q}_{45,cond} \quad (6.5)$$

$$\dot{Q}_{45,cond} + \dot{Q}_{5,abs} = \dot{Q}_{56,conv} + \dot{Q}_{57,rad} \quad (6.6)$$

$$\dot{Q}_{loss} = \dot{Q}_{56,conv} + \dot{Q}_{57,rad} \quad (6.7)$$

It is worth to notice that the absorbed solar radiation by the selective coating and the glass envelope is accounted through the terms  $\dot{Q}_{3,abs}$  and  $\dot{Q}_{5,abs}$  respectively. On the contrary, the thermal losses from the *Heat Collector Element* (HCE) support brackets have been neglected (the deviation is below 10 % of the total thermal losses).

The internal convective term  $\dot{Q}_{12,conv}$  can be calculated as:

$$\dot{Q}_{12,conv} = h_{oil} \pi D_2 (T_{w2} - T_{oil}) \quad (6.8)$$

and the convection heat transfer coefficient at the inside pipe diameter,  $h_{oil}$  is given

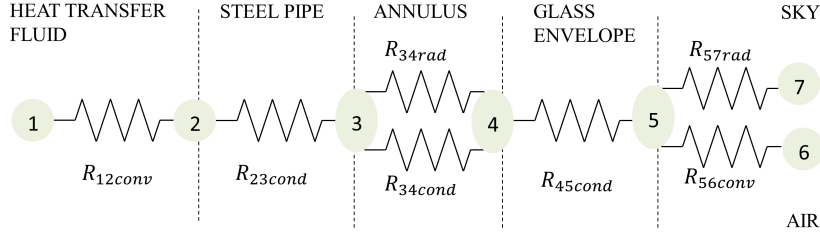


**Figure 6.3.** Equivalent thermal network.

by:

$$h_{oil} = Nu_{D2} \frac{k_{oil}}{D2}$$

where  $Nu_{D2}$  is the Nusselt number evaluated at the Diameter  $D_2$ . In Eq. 6.8, both  $T_{oil}$  and  $T_{w2}$  change only along the fluid direction while are considered constant in the radial one. It goes without saying that all temperatures and properties in the energy model depend only by the longitudinal direction. The flow in the receiver tube is supposed to be within the turbulent flow region and thermo-hydrodynamically fully developed, which is fully correct since it always recirculates inside a closed loop. Gnielinski correlation is broadly used for the Nusselt number estimation in convective heat transfer from the horizontal receiver pipe in forced convection, while in laminar region a constant value is assumed as follow:

$$\bar{Nu}_{D2} = \begin{cases} \frac{(f/2)(Re_{D2}-1000)Pr_b}{1+12.7(f/2)^{0.5}(Pr_b^{2/3}-1)} \left(\frac{Pr_b}{Pr_{D2}}\right)^{0.11} & \text{if } Re_{D2} \geq 2300 \\ 4.36 & \text{if } Re_{D2} < 2300 \end{cases} \quad (6.9)$$

where:

$$f = 1.58 \log_{10}(Re_{D2} - 3.28)^{-2} \quad (6.10)$$

$Pr_b$  is the Prandtl number at the HTF bulk temperature  $T_1$ , similarly  $Pr_{D2}$  corresponds to the internal tube wall. Except for  $Pr_b$ , all fluid properties are evaluated at the mean HTF temperature,  $T_1$ . The correlation assumes uniform heat flux and temperature.

Conduction heat transfer through the receiver pipe wall is determined by the Fourier's law of conduction through a cylinder [111] given as:

$$\dot{Q}_{23,cond} = \frac{2\pi k_{steel}(T_{D2} - T_{D3})}{\ln(D_3/D_2)} \quad (6.11)$$

in this case, the receiver tube thermal conductivity is evaluated at its average temperature between the inside and outside receiver pipe surfaces  $T_{23,mean}$ , i.e.  $\frac{(T_{D2}+T_{D3})}{2}$  (W/m °C). Since stainless steel is used, the thermal conductivity can be obtained [112]

$$k_{steel} = (0.013)T_{23,mean} + 15.2$$

Heat transfer from the receiver pipe to the glass envelope occurs through conduction and radiation. In fact at low pressures ( $<0.013$  Pa), heat transfer is driven by molecular conduction, above that pressure free convection is predominant. Vacuum

in annulus significantly reduces the heat transfer [157] whose value can be calculated by:

$$\dot{Q}_{34,conv} = \frac{(T_3 - T_4)}{R_{34,conv}} \quad (6.12)$$

where:

$$R_{34,conv} = \frac{1}{\pi D_3 \gamma_{34conv}} \quad (6.13)$$

$$\gamma_{34conv} = \frac{k_{34}}{\frac{D_3}{2} \log\left(\frac{D_4}{D_3}\right) + \frac{b \cdot \Lambda}{100} \cdot \left(\frac{D_3}{D_4} + 1\right)} \quad (6.14)$$

$$\Lambda = \frac{C_1 \times 10^{-20} T_{34}}{Pa \xi^2} \quad (6.15)$$

$$b = \frac{9\Gamma - 5}{2\Gamma + 2} \quad (6.16)$$

$$(6.17)$$

The constants are defined as:  $C_1 = 2.331 \times 10^{-20} \frac{mmHg \cdot cm^3}{K}$ ;  $\xi$  is the collision distance shown in Table 6.1 [91],  $\Gamma$  is the ratio  $c_{p,34}/c_{v,34}$  and Pa is the annulus pressure in torr; while  $k_{34}$  is the thermal conductivity of the annulus gas at standard temperature and pressure (W/m-K). This model describes the continuous substance between surfaces 3 and 4 using thermal properties that are evaluated at the average of  $T_3$  and  $T_4$  ( $T_{34}$ ).

**Table 6.1.** Gas constants.

Gas type	$\xi$ (cm)	$\Gamma$
Air	$3.53 \times 10^{-8}$	$-1.5 \times 10^{-7} \cdot T_{34}^2 + 4.5 \times 10^{-5} \cdot T_{34} + 1.402$
Argon	$3.80 \times 10^{-8}$	1.6667
Hydrogen	$2.40 \times 10^{-8}$	$1.293 \times 10^{-7} \cdot T_{34}^2 - 1.455 \times 10^{-4} \cdot T_{34} + 1.437$

Regarding the equation for radiation heat transfer, radiation loss from the absorber tube to the surroundings is the most significant contributor to heat loss for intact collectors. Several assumptions are made as follows:

- conduction heat transfer through the glass envelope
- non-participating gas in the annulus,
- the surfaces are gray
- diffuse reflections and irradiation
- long concentric isothermal cylinders, and the glass envelope is opaque to infrared radiation.

Despite the glass envelope wall and the selective coating are not gray, as well as the glass envelope wall is not completely opaque for the whole spectrum the errors in modeling are negligible. The radiative exchange  $\dot{Q}_{34,rad}$  between the absorber surface at  $D_3$  and the inner envelope surface at  $D_4$  is:

$$\dot{Q}_{34,rad} = \pi D_3 \gamma_{34,rad} (T_3 - T_4) \quad (6.18)$$

$$\gamma_{34,rad} = \sigma (T_3^2 + T_4^2) \frac{T_3 + T_4}{\frac{1}{\epsilon_3} + \frac{D_3}{D_4} (\frac{1}{\epsilon_4} - 1)} \quad (6.19)$$

$$(6.20)$$

Conduction across the intact glass envelope  $\dot{Q}_{45,cond}$  is modeled using the formula for radial resistance in a cylinder as already done in eq. 6.11, assuming the thermal conductance  $k_{45} = 1.04$  (W/m-K).

$$R_{45,cond} = \frac{\log(\frac{D_5}{D_4})}{2\pi k_{45}}$$

External convection is the largest source of heat loss especially in case of wind, the correlations here presented consider a horizontal cylinder with a perpendicular wind direction, in this way results are more conservative.

$$\dot{Q}_{56,conv} = \frac{(T_5 - T_6)}{R_{56,conv}} \quad (6.21)$$

$$R_{56,conv} = \frac{1}{\gamma_{56,conv} \pi D_5} \quad (6.22)$$

$$\gamma_{56,conv} = \frac{k_{56}}{D_5} Nu_{D5} \quad (6.23)$$

$$(6.24)$$

The Nusselt Number based on the glass envelope outer diameter  $D_5$  as well as  $k_{56}$  are calculated at the average temperature  $(T_5 + T_6)/2$ . The Nusselt number is calculated based on natural (no wind) or forced (with wind) conditions. Concerning the natural convection, the correlation developed by Churchill and Chu is used to estimate the Nusselt number [194].

$$\bar{Nu}_{D5} = \left\{ 0.60 + \frac{0.387 Ra_{D5}^{1/6}}{[1 + (0.559/Pr_{56})^{9/16}]^{8/27}} \right\}^2 \quad (6.25)$$

$$Ra_{D5} = \frac{g\beta(T_5 - T_6)D_5^3}{\alpha_{56}\nu_{56}} \quad (6.26)$$

$$\beta = 1/T_{56} \quad (6.27)$$

$$Pr_{56} = \nu_{56}/\alpha_{56} \quad (6.28)$$

$$(6.29)$$

where:  $Ra_{D5}$  = Rayleigh number for air based on the glass envelope outer diameter,  $D_5$ ;  $g$  is the gravitational constant  $9.81$  (m/s<sup>2</sup>);  $\alpha_{56}$  is the air thermal diffusivity (m/s);  $\beta$  is the volumetric thermal expansion coefficient for air (1/K);  $\nu_{56}$  kinematic viscosity for air (m<sup>2</sup>/s);  $Pr_{56}$  Prandtl number for air; all the fluid properties whose subscripts appears as "56" are evaluated at the film temperature  $(T_5 + T_6)/2$  (K). This correlation is valid for  $10^5 < Ra < 10^{12}$ .

In case of wind, the forced convection increases the heat losses, Zhukauskas' correlation for external forced convection flow normal to an isothermal cylinder [111] is used:

$$\bar{N}u_{D5} = CRe_{D5}^m Pr_6^n \left( \frac{Pr_6}{Pr_5} \right)^{1/4} \quad (6.30)$$

$$n = \begin{cases} 0.37 & \text{if } Pr \leq 10 \\ 0.36 & \text{if } Pr > 10 \end{cases} \quad (6.31)$$

where the coefficients "C" and "m" are listed in Table 6.2.

**Table 6.2.** Zhukauskas' correlation coefficients.

Re <sub>D</sub>	C	m
1 ÷ 40	0.75	0.4
40 ÷ 10 <sup>3</sup>	0.51	0.5
10 <sup>3</sup> ÷ 2 · 10 <sup>5</sup>	0.26	0.6
2 · 10 <sup>5</sup> ÷ 10 <sup>6</sup>	0.076	0.7

This correlation is valid for  $0.7 < Pr_6 < 500$ , and  $1 < Re_{D5} < 10^6$ . All fluid properties are evaluated at the atmospheric temperature,  $T_6$ , except  $Pr_5$ , which is evaluated at the glass envelope outer surface temperature.

Radiation heat transfer between the glass envelope and sky is modeled with the same method of eq. 6.18:

$$\dot{Q}_{57,rad} = \sigma D_5 \pi \epsilon_5 (T_5^4 - T_7^4) \quad (6.32)$$

$$T_7 = 0.0552 \cdot T_6^{3/2} + 273 \quad (6.33)$$

Since the solar rays are affected by some attenuation or deviation along their path from the mirrors to the absorber tube the total power available is significantly reduced. To take into account all these undesired effects, some parameters are introduced to estimate effective optical efficiencies; in the *National Renewable Energy Laboratory* (NREL) report are described [148]. The Table 6.3 summarizes the terms, but it should be noted that they do not consider incident angle losses, end losses, reflection and refraction losses, selective coating incident angle effects, so on so forth, because these additional parameters are got by means of a ray tracing method.

The average heat gain per unit length of the receiver is calculated as:

$$\bar{Q} = 1/L \int_{T(x=0)}^{T(x=L)} \rho u A_{cross} c_p dT \quad (6.34)$$

The thermal efficiency of the receiver can be expressed as in 6.35:

$$\eta_{th} = \frac{\bar{Q}_{gain}}{\dot{Q}_{sl}} \quad (6.35)$$

where:

$$\dot{Q}_{sl} = W_{mirr} DNI$$

**Table 6.3.** Optical Efficiency Terms.

$\epsilon_4$	Inner surface glass envelope emissivity
$\epsilon_5$	Outer surface glass envelope emissivity
$\epsilon_{mr}$	Solar Weighted Mirror Reflectivity
$\epsilon_{sh}$	Shadowing
$\epsilon_{tr}$	Tracking error
$\epsilon_{ge}$	Geometry error
$\rho_{cl}$	Clean mirror reflectance
$\epsilon_{dm}$	Dirt on mirror
$\epsilon_{dr}$	Dirt on the receiver glass envelope
$\epsilon_{un}$	Unaccounted

considering the mirror aperture  $W_{\text{mirr}}$  (m). The thermal losses are evaluated according to 6.7.

In this paper the above mentioned model has been developed in *MATLAB* [23] and its validation has been performed on the basis of the results available in [91]. In particular, the KJC Test-loop has been considered as a reference. Furthermore, the considered solar radiation is high and this entails a significant change in the thermo-physical properties of the HTF along the axial direction, thus better highlighting the deviations between the *Engineering Equation Solver* (EES) [10] and the *MATLAB* code results.

The input parameters of the model are listed below:

The HTF used is the Therminol-VP1 [34]. The coating layer has a significant impact on the collector performance; in this case the low emissivity of the “Solel UVAC Cermet avg” absorber coating has been taken into account through a polynomial equation as follow:

$$\epsilon_3 = 1.907 \cdot 10^{-7} T_3^2 + (1.208 \cdot 10^{-4}) T_3 + 6.282 \cdot 10^{-2}$$

The *KJC Test-loop* is 779.52 m long and it was discretized in 10 equal segments as reported in [91] and the coating emittance was set as “user defined” based on the following values: 0.04 at 100 °C and 0.1 at 400 °C. The oil inlet temperature was assumed equal to 225 °C, in the middle of the operative temperature range of the KJC Test-loop, further details can be found in Tab. 6.4.

The validation of the *MATLAB* model with the same in EES (Forristall model) in steady state conditions<sup>1</sup> is done, and the main results reported in Table 6.5. The Validation of the main performance parameters clearly shows a slightly higher thermal efficiency in the present model, probably due to the fact that the losses through the HCE brackets are neglected. The other parameters agree, thus confirming the good implementation of the Forristall model in the *MATLAB* environment and the fairly negligible weight of the bracelet losses on the total thermal dispersion.

The performance of the HCEOI-12 receiver [3] has been analysed. The receiver performances in terms of thermal efficiency and heat losses have been evaluated in steady state at different operating conditions. Firstly, the HCEOI-12 receiver is

<sup>1</sup>As stated before, the only difference between the EES and the *MATLAB* model relies on the dynamic term in the energy balance equation, as well as on the bracelets losses.

**Table 6.4.** LS-2/PTC input parameters list KJC Test-loop.

Ambient conditions		
DNI Solar Irradiation	950	W/m <sup>2</sup>
Wind speed	0	m/s
Ambient Temperature	22	°C
Solar Incident Angle Modifier	0	Degrees
HCE and Collector Properties		
Collector Type	LS-2	-
Absorber Material	321H	-
Absorber Selective Coating	vSolel UVAC Cermet	-
Gas in Annulus	Air	-
Annulus Absolute Pressure	10 <sup>-4</sup>	Torr
Absorber Inner Diameter	0.066	m
Absorber Outer Diameter	0.070	m
Glass Envelope Inner Diameter	0.109	m
Glass Envelope Outer Diameter	0.115	m
Projected Aperture Width	4.8235	m
Glass envelope emissivity	0.86	-
Solar absorption in the glass envelope	0.02	-
Solar absorption on the absorber layer	0.98	-
transmittance of the glass envelope	0.97	-
Optical Properties		
Clean mirror reflectance	0.900	-
Shadowing	0.974	-
Tracking error	0.994	-
Geometry error	0.980	-
Dirt on receiver glass envelope	0.981	-
Dirt on Mirror	0.963	-
General Error	0.960	-

**Table 6.5.** KJC test loop, model validation.

Parameter	EES	MATLAB	Deviation (%)
$\dot{Q}_{gain}$ (W/m)	3248	3345	2.98
$\dot{Q}_{loss}$ (W/m)	149.4	145.8	- 2.40
$\eta_{th}$ (%)	70.87	73.00	3.00
$T_{LFR,out}$ (°C)	368.00	367.65	-0.09
$u_{out}$ (m/s)	3.114	3.119	0.16

compared with the LS-2 considering the same input parameters of the validation test and Therminol 62 [33] as HTF. Then, the optical properties and the total length of the solar field are modified according to those of the Linear Fresnel Reflectors solar field object of this study. With reference to the considered HCE, it was designed for diathermic oil with a working temperature up to 400 °C. More precisely, the manufacturer claims a thermal emissivity of 8.5 % at 400 °C and a solar absorption  $\geq 96$  % (ASTM [0.25...2.5 $\mu$ m]) For sake of conciseness, only the HCEOI-12 specifications that differ from the LS-2 collector have been reported in Table 6.6:

**Table 6.6.** HCEOI-12/LFR input parameter list.

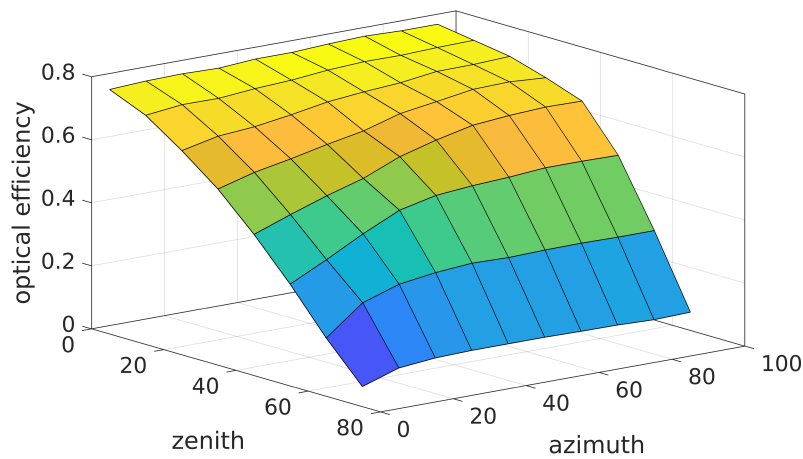
HCE and Collector Properties		
Collector Type	HCEOI-12	-
Absorber Selective Coating	N.A.	-
Glass Envelope Inner Diameter	0.119	m
Glass Envelope Outer Diameter	0.125	m
Projected Aperture Width	4.05	m
solar absorption on the absorber layer	0.96	-
transmittance of the glass envelope	0.969	-
Thermal losses at 400 °C	265	W/m
Ratio of AR coated area to total glass tube area	0.961	-
Total collector length	39.02	m

Table 6.7 reports the main results of the performed comparison with an inlet temperature of 125 °C and same conditions of the KJC test loop. In this case the coating emissivity of the LS-2 HCE has been evaluated as in eq. 6.34, the solar absorption on the absorber layer assumed equal to 0.955 and the transmittance of the glass envelope to 0.965. In these operating conditions, the HCEOI-12 performs better than the LS-2 as reported in Table 6.7. It is also evident the sharp decrease of the thermal losses of the LS-2 compared to the user-defined version previously considered, mainly due to the different absorber coating and glass transmittance (the geometry differs only for the glass diameter). On the contrary, other tests accomplished on the same HCE show the low impact of the replaced HTF (from *Therminol-VP1* to *Therminol 62*) on the performance of the considered receiver tube.

**Table 6.7.** Comparison between LS-2 and HCEOI-12.

Parameter	EES	MATLAB	Deviation (%)
$\dot{Q}_{gain}$ (W/m)	3318.9	3447.8	3.388
$\dot{Q}_{loss}$ (W/m)	68.95	40.64	-41.63
$\eta_{th}$ (%)	72.43	75.24	3.88
$T_{LFR,out}$ (°C)	270.31	275.28	1.84
$u_{out}$ (m/s)	2.986	3.004	0.59

Later on, the above outcomes are obtained fixing the IAM value to 0.8, thereby the solar irradiance is normal to the collector aperture, but as previously mentioned, this value is strongly affected by the current solar position with respect to the solar field during the day. In this regard, thanks to *SolTrace* [29] (software tool developed at the National Renewable Energy Laboratory) it is possible to model and characterize the complex optical systems owned by the LFR. This software uses a *Monte-Carlo* ray-tracing methodology and analogously to the Forristall Model is considered the milestone for all the research activities involved in this topic, it is often used in comparison with other tools for their validation. The optical performances comprehensive of cosine effect and end losses allow to evaluate the missing part for the thermal solution of the receiver tube. In particular, dividing the incident angle  $\theta$  with respect to the longitudinal  $\theta_{\parallel}$  and transversal position  $\theta_{\perp}$  of the LFR, is possible to obtain the IAM for the LFR geometries in the Innova MicroSolar. The 2 D surface of the optical efficiency shown in the fig. 6.4



**Figure 6.4.** Optical efficiency of the HCEOI-12, cosine losses and end losses included.

### 6.1.3 Wall-to-fluid heat transfer

So far, even though the Forristall model well reproduces the global thermal efficiency with a reasonable accuracy, in some operating conditions the included assumptions may fail. More precisely, in the thermal network shown in figure 6.3 the thermal resistance between the steel tube and the HTF ( $R_{12,conv}$ ) might vary considerably based on the current fluid flow regime and the impinging DNI. In the Forristall study, a single correlation for all flow regimes in forced convection is considered, whereas in the laminar case, it shifts directly to the theoretical Nusselt number for fully developed constant heat flux tube as expressed in the eq. 6.9. This assumption does not affect the solution within the validation tests reported in the document, because they have been performed in the nominal conditions at high flow rates and DNI, but it might not be negligible in other cases. Resuming the study of Izuchukwu F. Okafor [139], the global heat transfer undergoes a significant change at low flow rates and non-uniform circumferential heat flux distribution, thanks to the combination of

gravity and the heat placed in the lower side of the receiver tube, buoyancy driven secondary flows occur enhancing the heat transfer from 120 % to 150 % based on the flux intensity, tube diameter and Reynolds number. As known, analogously to the Reynolds number in forced convection, natural convection is governed by the Grashof number, which approximates the ratio of the buoyancy to viscous force acting on a fluid. The definition of the Grashof number is the following:

$$Gr = \frac{g\beta(T_w - T_\infty)D^3}{\nu^2} \quad (6.36)$$

As one can see, it depends on the cube of the tube diameter, while the Reynolds number depends only by  $D$ , this means that at larger diameters the buoyancy effects become predominant especially at low fluid velocity. Broadly speaking, it is necessary to distinguish forced and natural convection based on a criteria. From literature, the Richardson number it is often assumed to delimit the two working areas, when this dimensionless number is equal to 1, a mixed convection occurs, thus it may be assumed one order-of-magnitude to realize pure natural convection from forced:

$$Gr/Re^2 > 10 \quad \text{natural convection} \quad (6.37)$$

$$Gr/Re^2 \approx 1 \quad \text{mixed convection} \quad (6.38)$$

$$Gr/Re^2 < 0.1 \quad \text{forced convection} \quad (6.39)$$

Another important parameter for the natural convection is the Rayleigh number defined as:

$$Ra = GrPr \quad (6.40)$$

The Rayleigh number denotes whether laminar or turbulent flow occurs, an example is depicted in figure 6.5:

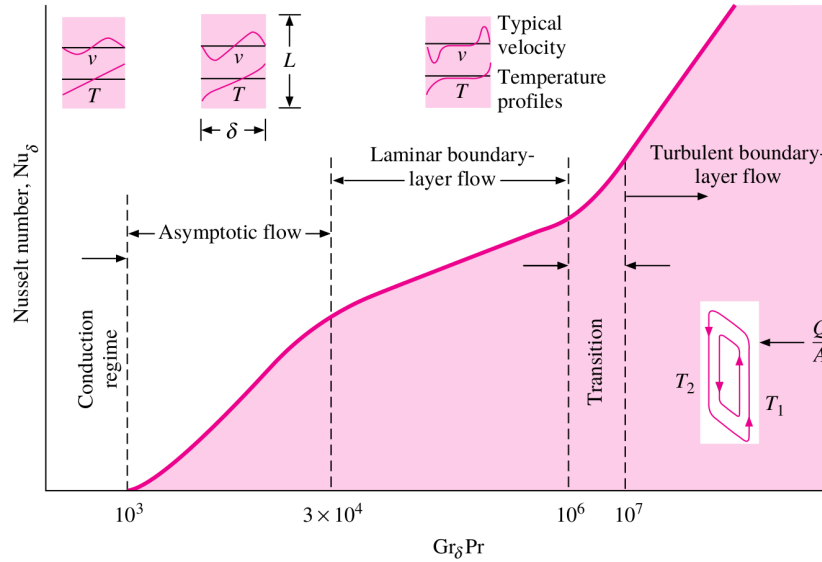


**Figure 6.5.** Schematic diagram and flow regimes for the vertical convection layer.

At very low Grashof numbers, there are very minute natural-convection currents and the heat transfer occurs mainly by conduction across the fluid layer. As the

Grashof number is increased, the fluid progressively is shifted towards the laminar, transitional and finally turbulent region.

As previously stated, the matter consists of evaluating the correct heat transfer in all flow regimes inside an horizontal tube, unfortunately few experimental studies focus on heat exchange inside a cylinder in mixed and laminar flow at constant heat flux superimposition. In addition, the HTF used is the therminol 62 whose Prandtl number is very high if compared with the studies found in laminar/transitional regime, because of the different thermal properties of the fluids in their experiments. Moreover, experimental studies do not go above 20 mm in diameter, and even changing the fluid and working conditions the Grashof number is still low. The receiver tube HCEOI-12 has an internal diameter of 65 mm, which enables the buoyancy driven flow, thus making this survey even more tough.

Many real situations involve convection heat transfer that is neither “forced” nor “free” in nature, a global summary of the cases are depicted in fig. 6.6, where the acronym UWT stands for *Uniform Wall Temperature*, while UHF indicates data for *Uniform Heat Flux*.

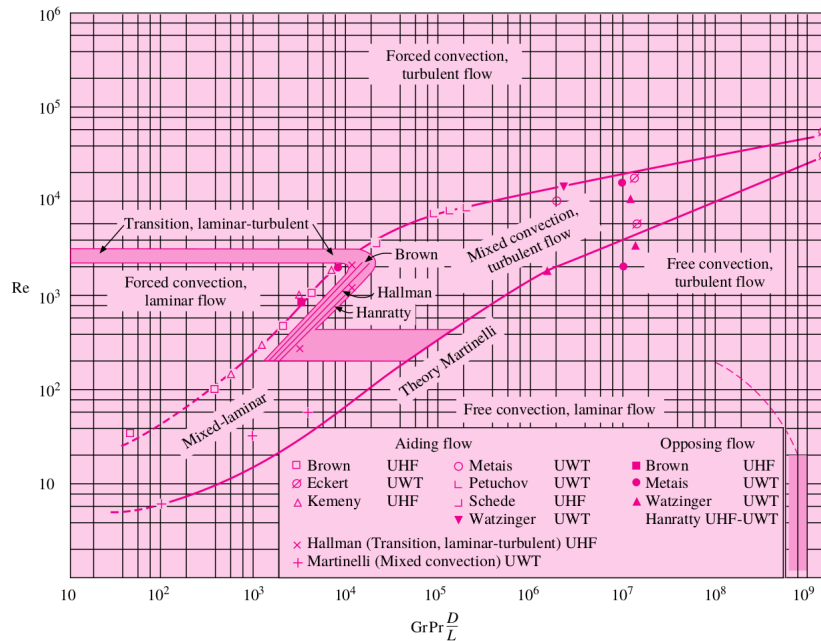


**Figure 6.6.** Regimes of free, forced, and mixed convection for flow through vertical tubes.

It can be stated that a large Reynolds number implies equally large forced-flow velocity, thus less influence of free-convection currents. On the other hand the augmentation in Rayleigh number leads free-convection effects to prevail. The existing UHF flow regime maps as previously shown are accurate for low Prandtl values, but they fail at high Prandtl numbers where the receiver HCEOI-12 works most of the time. Evert [87] tried to reformulate the basis on which the flow regime map is accomplished. In this study, experiments are done at low diameters and low Prandtl numbers, then they are compared with many other authors at larger diameter to cover the flow regime map as much as possible. The final results are

depicted in fig. 6.7, where  $Re_{qt}$  stands for quasi-turbulent Reynolds number, whereas  $Re_{cr}$  is the critical zone, finally the natural convection occurs above a Rayleigh number above approx. 4970.

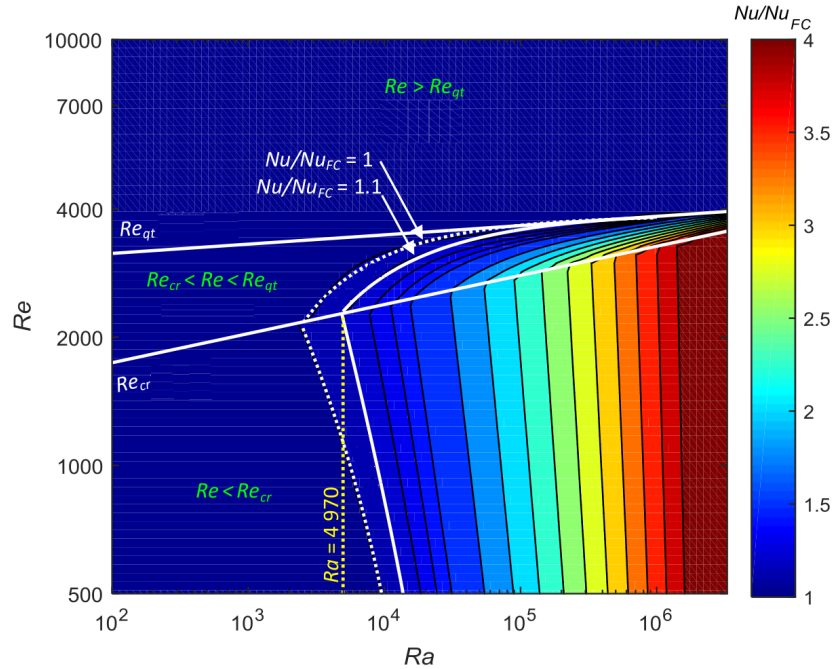


**Figure 6.7.** Flow regime map for fully developed flow for smooth horizontal tubes at a constant heat flux.

Only when the natural convection occurs (At very low Rayleigh and Reynolds number) the Nusselt number is greater than the theoretical value at constant heat flux equal to 4.36 here indicated as  $Nu_{fc}$  (value used by Forristall for the laminar region), it would expect an opposite trend would happen at high Rayleigh and Reynolds couple, this is not true, the natural convection effect arises only at low Reynolds number increasing the Nusselt number by a factor of 4 ( $Nu/Nu_{fc}$ ).

Later on, the main parameters that affect the heat exchange in the absorber tube have been described, hereinafter an in depth analysis is presented aimed at modeling the wall-tube thermal resistance in all the expected fluid regime of the HCEOI-12, but still considering both a uniform heat flux distribution and neglecting the thermal conduction around the circumferential direction. As a result, the mathematical model is not heavily affected by the computational burden subsequent to the addition of a better description of the heat transfer problem. On the other hand, it improves the existing Forristall model especially when the LFR works far from its design point due to the pump operating strategy or at low DNI. Moreover, this further refinement allows the control system to predict the wall overheating owing to the poor thermal characteristics of the diathermic oil, thus saving the collector to critical working conditions.

Several authors studied the heat transfer in cylindrical tubes, the derived Nusselt number correlations are listed in Appendix B. Among them, only a small portion can be applied for dealing with HCEOI-12 and therminol 62, because of the different

ranges of the dimensionless parameters used, furthermore the vast majority refer to the heat transfer evaluated outside the tube surface.

On the basis of the past description, to cover entirely the flow regime map, the following regions have to be investigated:

- forced convection
- mixed convection
- natural convection

each of which can be further divided into other three conditions:

- laminar
- transitional
- turbulent

The selected correlations whose validity better fit the boundary conditions of the HCEOI-12 and therminol 62, are summarized in table: 6.8 for the mixed flow. The unique correlation for the natural convection depends only by the Rayleigh number as shown in table: 6.9, and it has the same framework of Hwang correlation [110], but with a wider validity range. In literature there is a broad variety of correlations for cylindrical tubes in forced convection, here in table 6.10 are shown the most recent. Though Ghajar e Tam [172] in table 6.8 are applicable also in forced convection, to avoid repetitions they have not been included in it. To give a better overview about the MATLAB code implementation for properly selecting the right correlation in the corresponding region, a process flow diagram is drawn and depicted in fig. 6.8.

Once the correlations are found, a preliminary simulation of the whole plant (one year with 1 min of time step described in the next chapters) is needed to identify the variation range of all the dimensionless numbers involved, i.e. Gr, Re, Pr, but this time with the original Forristall model. After that, a matrix of value Re, Ra can be created to test each correlation within its own validity range, assessing if they cover the whole map or if other correlations are needed to avoid some uncovered regions. The results of these investigations are shown in the following figures (6.9) using the colormap of MATLAB and logarithmic scales for the axis.

First of all, in fig. 6.9a is pointed out the Richardson number value into the map, it gives the possibility to distinguish the natural/mixed/forced regions as said before, and thus the corresponding zone where is supposed to apply every single empirical model.

As expected, Ludovisi (2013) [123] 6.9b predicts the Nusselt number in the whole region with natural convection, both in turbulent and laminar flow. The Nusselt number gradually increases as the Rayleigh number rises.

Analogously to Ludovisi, Hwang in fig. 6.9c can predict the mixed convection region in the laminar regime at low Rayleigh numbers where Ludovisi cannot work (it is applicable in the natural convection only). Its trend is the same of Ludovisi, but it provides a slightly different Nusselt number at parity of Rayleigh.

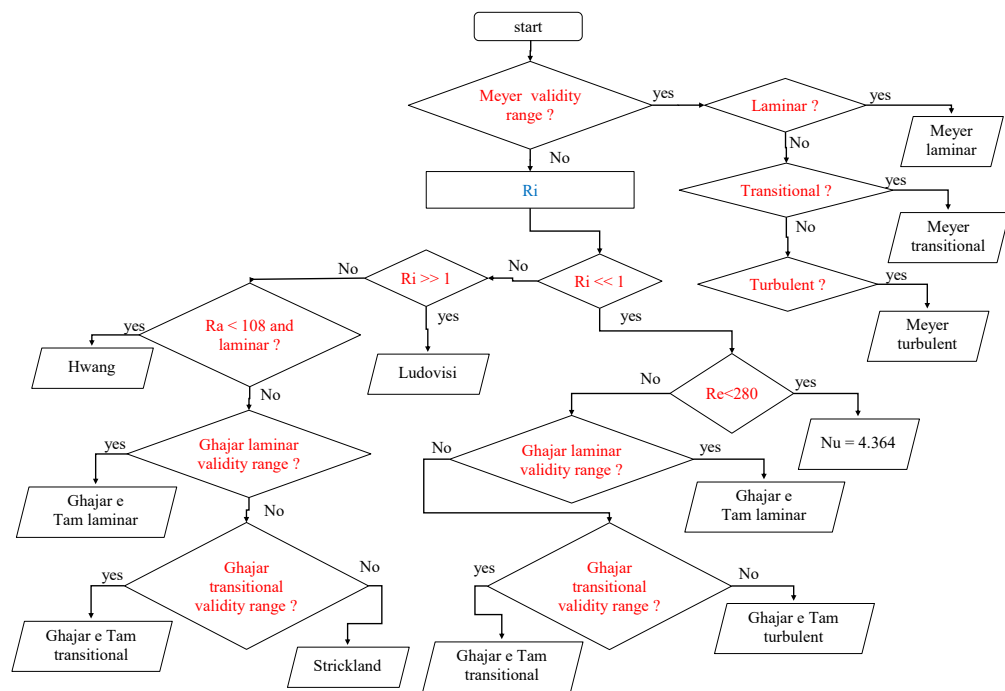


Figure 6.8. Nusselt number evaluation: process flow diagram.

**Table 6.8.** Nusselt number for **mixed convection** for cylindrical horizontal tube.

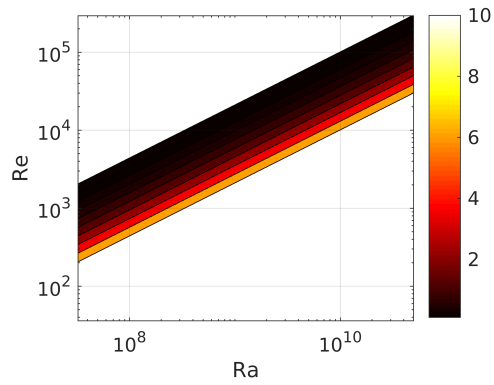
Author name	correlation	B.C.	Validity interval
Ghajar and Tam	$\bar{N}u_l = 1.24 \left[ \left( \frac{RePrD}{L} \right) + \dots \right. \\ \left. 0.025(GrPr)^{0.75} \right]^{1/3} \left( \frac{u_b}{u_w} \right)^{0.14}$	UHF laminar	$3 \leq x/d \leq 192$ $280 \leq Re \leq 3800$ $40 \leq Pr \leq 160$ $1 \cdot 10^3 \leq Gr \leq 2.8 \times 10^4$ $1.2 \leq \mu_b/\mu_w \leq 3.8$
Ghajar and Tam	$\bar{N}u_{tr} = Nu_l + \left\{ e^{\frac{a-Re}{b}} + Nu_t^c \right\}^c$	UHF transitional	$1.6 \cdot 10^3 \leq Re \leq 10.7 \cdot 10^3$ $5 \leq Pr \leq 55$ $4 \cdot 10^3 \leq Gr \leq 2.5 \times 10^5$ $1.2 \leq \mu_b/\mu_w \leq 2.6$
Ghajar and Tam	$\bar{N}u_t = 0.023Re^{0.8}Pr^{0.385} \dots \\ (L/D)^{-0.0054} \left( \frac{\mu_b}{\mu_w} \right)^{0.14}$	UHF turbulent	$7 \cdot 10^3 \leq Re \leq 49 \cdot 10^3$ $4 \leq Pr \leq 34$ $1.1 \leq \mu_b/\mu_w \leq 1.7$
Strickland	$\bar{N}u_t = 6.3 + \left[ \frac{0.079f^{0.5}RePr}{(1+Pr^{0.8})^{5/6}} \right] \\ f^{0.5} = \left[ \frac{1}{2.21 \ln \frac{Re}{7}} \right]$	UHF transitional and turbulent	$3 < Pr < 157.8$ $281 < Re < 5 \cdot 10^4$
Hwang	$\bar{N}u_l = 0.626Ra^{0.269}$	UWT laminar	$10^3 < Ra < 5 \cdot 10^8$

**Table 6.9.** Nusselt number for **natural convection** for cylindrical horizontal tube.

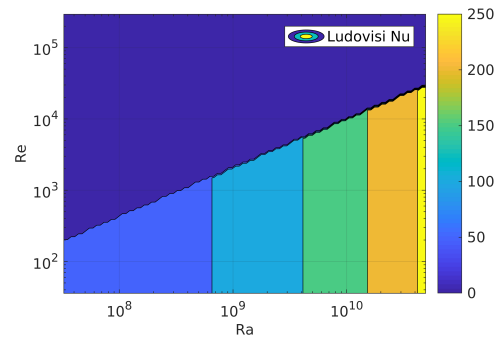
Author name	correlation	B.C.	Validity interval
Ludovisi 2013	$\bar{N}u = 1.15Ra^{0.22}$	UWT	$3 \cdot 10^4 \leq Ra \leq 10^{11}$ $1 \leq Pr \leq 20$

**Table 6.10.** Nusselt number for **forced convection** for cylindrical horizontal tube.

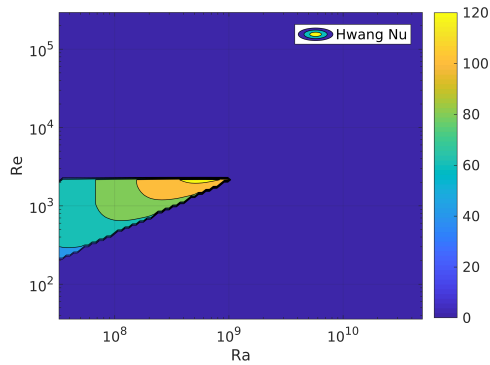
Author name	correlation	B.C.	Validity interval
Meyer	$\bar{N}u_l = 4.36 + \bar{N}u_1 + \bar{N}u_2$		
	$\bar{N}u_1 = \frac{1}{L}(-0.84Pr^{-0.2}L_{tMCD} + \dots$		$3 < Pr_b < 7.4$
	$0.72ReD^{0.54}Pr^{0.34}L_{tMCD}^{0.46})$		$30 < Gr < 2.49 \cdot 10^5$
	$\bar{N}u_2 = \frac{1}{L}(0.207Gr^{0.305} - \dots$	UWT laminar	$467 < Re < 3217$ $2.6 < Gz < 5589$
	$1.19)Pr^{0.42}(ReD)^{-0.08} \cdot \dots$		
	$(L - L_{tMCD})$		
	$L_{tMCD} = \frac{2.4RePr^{0.6}D}{Gr^{0.57}}$		
Meyer	$\bar{N}u_{tr} = (0.00108Re - 2.49) \cdot \dots$		$5.4 < Pr_b < 6.8$
	$Gr^{-0.04}Pr^2$	UWT transitional	$2.8 \cdot 10^4 < Gr < 3.2 \cdot 10^4$ $2520 < Re < 3361$
Meyer	$\bar{N}u_{tr} = [0.417(Re - 1000)^{0.499} - \dots$		$5.5 < Pr_b < 6.9$
	$8.2]Pr^{0.42}$	UWT turbulent	$8.9 \cdot 10^2 < Gr < 1.4 \cdot 10^4$ $2804 < Re < 9787$
Gnielinski (1976)	$\bar{N}u_t = \frac{\frac{f}{2}(Re - 1000)Pr_b}{1 + 12.7(\frac{f}{2})^{1/2}(Pr_b^{2/3} - 1)} \cdot \dots$		$3 \cdot 10^3 < Re < 5 \cdot 10^6$
	$\left(\frac{Pr_b}{Pr_w}\right)^{0.11}$	UHF developed velocity	$0.5 < Pr < 2000$
	$f = (1.58\log(Re) - 3.28)^{-2}$		



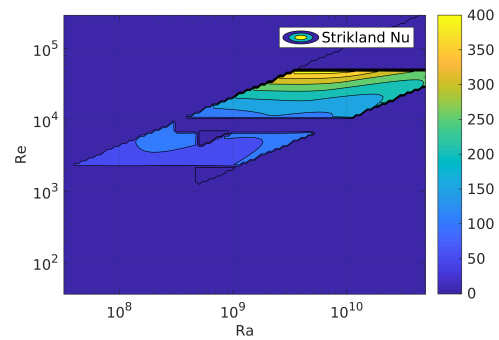
(a) Richardson Number.



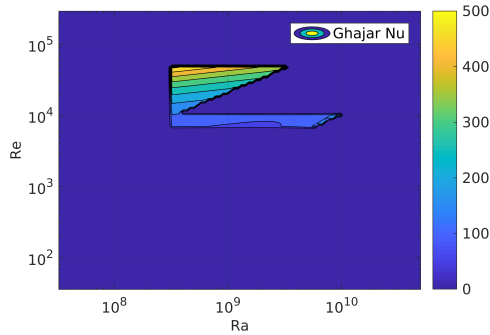
(b) Nusselt number predicted by Ludovisi correlation.



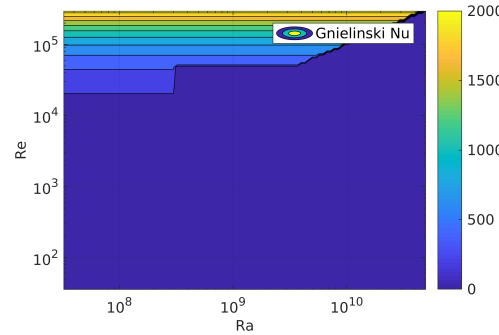
(c) Nusselt number predicted by Hwang correlation.



(d) Nusselt number predicted by Strickland correlation.



(e) Nusselt number predicted by Ghajar correlation.



(f) Nusselt number predicted by Gnielinski correlation.

Figure 6.9

Interesting results are obtained with the Strickland correlation [169] in fig. 6.9d for mixed flow, it provides greater Nusselt number at higher Re and Ra value where there is the combined action of forced-flow velocity and the buoyancy driven flow respectively.

As already stated, in forced convection the buoyancy effects are negligible, thus the Ghajar correlation should not depend on Ra, but mainly by Re. Indeed in fig. 6.9e its value is strongly affected by the Reynolds number and barely from Ra, only due to the variation in Prandtl number since its definition ( $Ra = GrPr$ ). Unfortunately, this correlation shows a limited applicability into the map, mainly due to the narrow validity range regarding the viscosity ratio of the fluid at the bulk and the internal wall respectively. Nonetheless, whether the operating conditions allow a greater difference in temperature between the bulk and wall, for example when the DNI is high and the diathermic oil is still cold, Ghajar can perform a more accurate prediction of the Nusselt number than any other correlation shown here for forced flow convection. For this reason it is preferred in the code (higher priority) implementation with respect to the Gnielinski even if it has a broader validity range. Gnielinski correlation obviously covers the upper region of the map where Ghajar can not operate on as shown in fig. 6.9f. Meyer [87] is not applicable since it was developed for low Prandtl numbers and far too small Ra than that required in this study.

At this point, despite all the correlations reported in the previous tables providing the Nusselt number over the map, a further refining is needed to avoid the different predictions at the boundaries of each one. To perform this step the Richardson number is used to linearly interpolate different correlations applied in the three regions forced/mixed/natural convection. More precisely, each correlation is weighted based on the Richardson value at the region interface, as result, a smoother and more physical solution is obtained. A secondary advantage by the introduction of this further procedure concerns the numerical solution, because of the evident non-linearity owned by the thermal network system in eq. 6.3 a numerical solver is needed, but it should assure the function continuity in the whole domain from the linear interpolation fosters a quicker convergence [107] as shown in the 2 D log graph fig. 6.10 where the Nusselt number is found using the correlations described above.

The overall Nusselt number can be now calculated anywhere, taking into account the empirical correlations for horizontal tubes for a HTF bulk temperature of 200 °C and a wall temperature of 250 °C (supposed to be heated), the results are shown in the fig. 6.11 and fig. 6.10. The scatter points are taken with a constant time interval, this means that the LFR works a longer time span in the region of the map where their density increase. Despite the high concentration of the working points in the top of the map, mainly predicted by the Gnielinski correlation, in the natural convection, both turbulent and laminar the LFR works with a Nusselt number significantly higher than the asymptotic value of 4.36 at constant heat flux used in the Forristall model.

Doing a match between the fluid working points of the yearly simulation without the wall refinement and the Nusselt number found in the map fig. 6.11, it is evident that the LFR operates in all the regions analysed during a dynamic simulation, these outcomes enforce the importance of this additional investigation, but at the moment

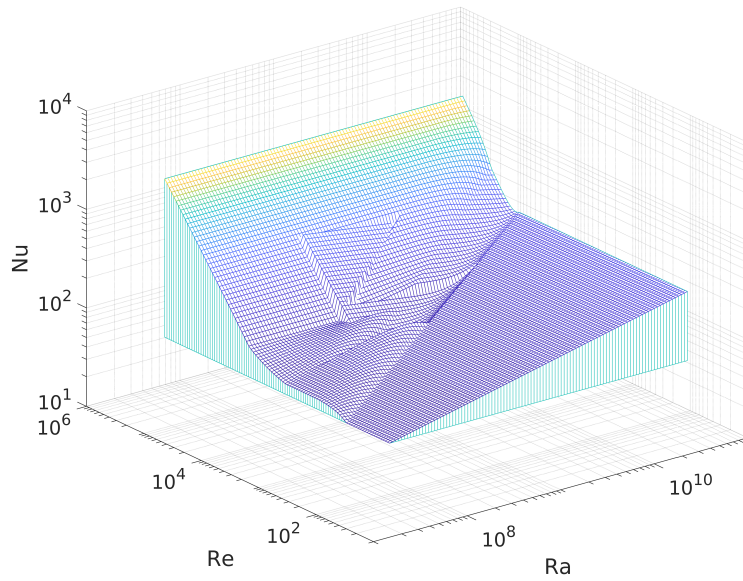


**Figure 6.10.** Predicted Nusselt number in logarithmic plot.

only qualitatively.

So far, PTCs have been considered in the simulations, nonetheless, the LFRs optical properties are significantly different. For example, at noon the *Incident Angle Modifier* (IAM) is not equal to 1 as occurs in the PTC test of table 6.4. but, in this case the nominal value of 0.8 for the IAM has been assumed.

Later on, the performances of the LFR solar field have been simulated in steady state conditions, but as stated at the beginning of this section, the MATLAB code takes into account also the dynamic effects. The thermal capacity of the solar field affects in cascade the thermal response of the bottoming subsystems, thereby particular care has to be taken to model it. Hence, a parametric analysis of the dynamic behavior is carried out considering the following technical specifications<sup>2</sup> of the solar field: (i) an effective area of the primary reflectors of 158 m<sup>2</sup>, (ii) a total active length of 39.02 m, (iii) a Projected Aperture Width of 4.05 m, (iv) the HCEOI-12 receiver tube; and (v) Therminol 62 as HTF. The optical properties have been kept constant and consequently the heat gain increases with solar radiation as shown in 6.12a.

From the analysis of this figure, also the nominal power of the solar field can be obtained. Indeed:

$$\bar{Q}_{design} = \bar{Q}_{gain}L \quad (6.41)$$

With reference to the solar field of the Innova plant, the manufacturer [3] declares 80 kWth of total peak power at 900 W/m. Considering the nominal working temperature of 250 °C the resulting heat gain is 2167 W/m, according to eq. 6.41 a nominal peak power of 84.6 kWth is obtained by the model. This discrepancy depends largely on the fixed optical properties considered for such evaluation.

<sup>2</sup>The same of the Innova MicroSolar plant

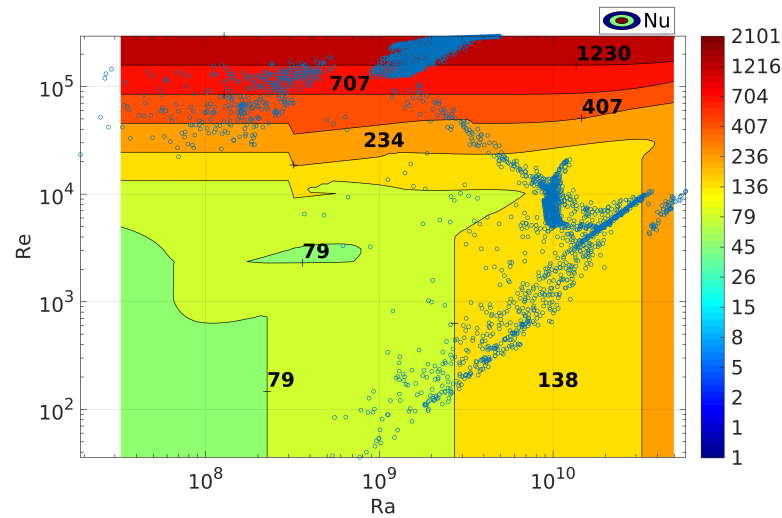


**Figure 6.11.** Predicted Nusselt number in contour plot and scattered working points of the LFR during the yearly simulation.

In the subsequent graphs, the maximum temperature of the HTF above ambient has been set at 250 °C, since the solar field has not been designed for working conditions above 280 °C. As depicted in figure 6.12b, for a given DNI the thermal efficiency is lower at higher temperatures of HTF. This is due to the increase of the heat losses, as expected.

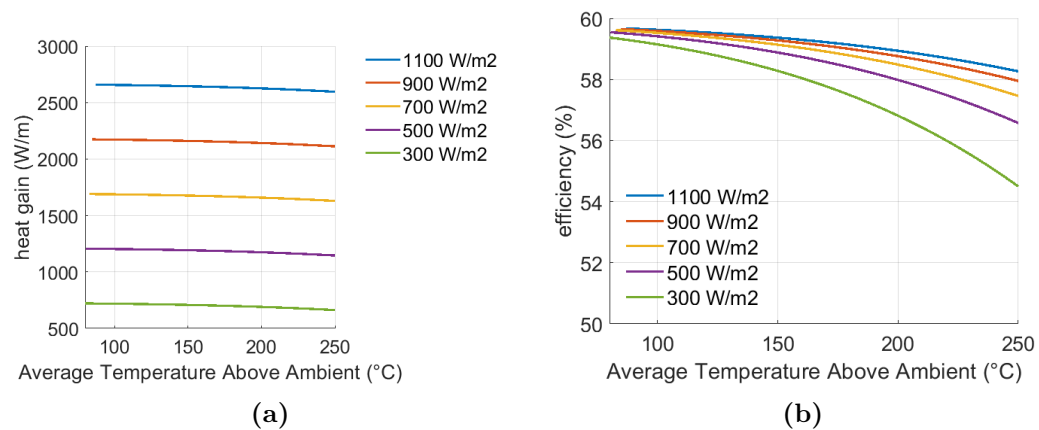


**Figure 6.12.** thermal performance of the HCEOI-12

As regards the losses, they are mainly affected by the HTF temperature, and not significantly by the increasing of DNI as shown in figure 6.13a. Considering the Therminol VP1 at the highest operating temperature of 400 °C, the overall thermal losses of the HCEOI-12 receiver reach 201 W/m (without DNI). With reference to these losses, the manufacturer of the receiver tube Archimede Solar Energy, declares 265 W/m (in the same conditions). Even though these losses are underestimated due to the neglected support brackets, they are really close to the measures reported in

[102]. all in all, the developed model is able to predict the thermal performance of the receiver tube with a fair accuracy suitable for CHP system dynamic simulations.

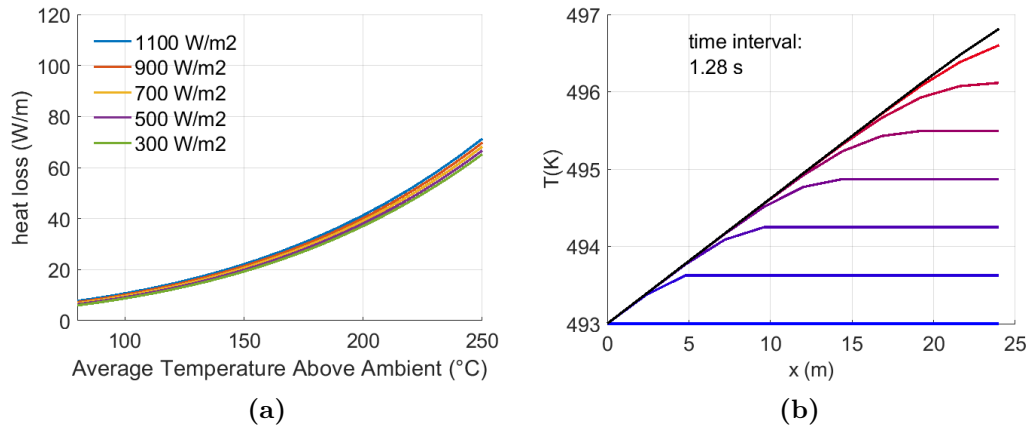


**Figure 6.13.** thermal performance of the HCEOI-12.

Finally, the temperature field along the axis of the pipe is presented at different time steps fig. 6.13b. The DNI is 900 W/m, the oil flow rate is 3 m/s, and the initial HTF temperature is 220 °C, which corresponds to the inlet temperature to the solar field at design conditions. The dynamic simulation has been accomplished with  $\Delta x = 2.4$  m and  $\Delta t = 0.64$  s to satisfy the Courant stability condition. As expected, the receiver tube takes less than 10 seconds to reach the new regime, which approximately corresponds to the traveling time of the HTF from the inlet to the outlet, with a temperature gain just lower than 4 °C.

## 6.2 Latent Heat Thermal Energy Storage

The thermal storage has to be designed to guarantee 4 hours of ORC unit operation with a nominal input power of 25 kW, thus a total of 100 kWh. Since the melting temperature should fall as close as possible to the design temperature of 250 °C, an eutectic mixture of nitrate solar salt  $\text{KNO}_3/\text{NaNO}_3$  (40/60 by wt.) is chosen [127] (melting temperature is in the range 216 ÷ 223 °C [166]). To store 100 kWh, 3.8 tons of solar salts are needed. To enhance the heat transfer between the PCM and the heat transfer fluid, reversible heat pipes are considered. The mathematical model follows the guidelines described in *IEA Task 32 report* on advanced storage concepts [168], where a detailed description of the Type 185 [35] is provided. The model is based on the following main assumptions: (i) material isotropic and isothermal in each internal time-step; (ii) no hysteresis and subcooling effects; and (iii) charging and discharging not simultaneous. The presence of heat pipes is modeled by both limiting the maximum power exchanged to 40 kW and fixing a minimum temperature difference between the oil and the PCM equal to 5 °C (asymptotic condition).

Hence, the temperature variation of the PCM due to the heat exchanged can be obtained by:

$$\Delta T_{PCM(t+1)} = \Delta T_{PCM(t)}^{-[\Delta t_{int-timestep} \cdot f]} \quad (6.42)$$

where:

$$f = \frac{\dot{m}_{oil} c_{p,oil} \left[ 1 - e^{-\left(\frac{h}{\dot{m}_{oil} c_{p,oil}}\right)} \right]}{V_{PCM} \rho_{PCM} c_{p,PCM}} \quad (6.43)$$

$$h_{pipe-PCM} = 20 \frac{\lambda_{PCM} Nu_{pipe-PCM}}{L_{PCM}} \quad (6.44)$$

$$Nu_{pipe-PCM} = 0.046 Ra_{PCM}^{1/3} \quad (6.45)$$

The Nusselt number inside the PCM in contact with the Heat Pipes is obtained from a correlation of convective heat transfer based on the Rayleigh number, this particular correlation is valid in the range  $10^6 < Ra < 10^9$ . The term " $h_{pipe-PCM}$ " is calibrated based on the preliminary experimental tests, indeed the heat pipes can release or acquire heat within a certain range. In particular, the maximum allowable difference in temperature is 30 °C that corresponds to the maximum power exchanged above which can be damaged (dryout). In light of these statements the convective heat transfer  $h_{pipe-PCM}$  is multiplied for this coefficient in order to get 30 °C between the inlet oil temperature and the PCM average temperature at 40 kWh. On the contrary, the heat pipes are not able to transfer heat if the difference in temperature between the evaporator and condenser is below 5 °C, for this reason in the MATLAB code an asymptotic value of 5 °C is considered.

Then, from the temperature variation of the PCM, it is possible to calculate the heat exchanged as:

$$Q_{LHTES(t+1)} = \int_t^{t+1} P_{LHTES(t)} \cdot dt \quad (6.46)$$

Where  $P_{TES(t)}$  stands for the thermal energy exchanged by the PCM during a time step. All the PCM properties are evaluated with an internal time step to increase

the model accuracy at varying the global time step. During the LHTES (Latent Heat Thermal Energy Storage) operation, the power released or acquired is affected by the heat exchange characteristics among diathermic oil, heat pipes and PCM material. This aspect is crucial on the performance of the whole plant, e.g. a slow or ineffective heat extraction from the thermal storage could cause the LFR defocusing or low inlet temperature into the ORC inlet. For a better understanding of the power amount available at different oil temperatures, figure 6.14 show the charging and discharging phases of the LHTES respectively:

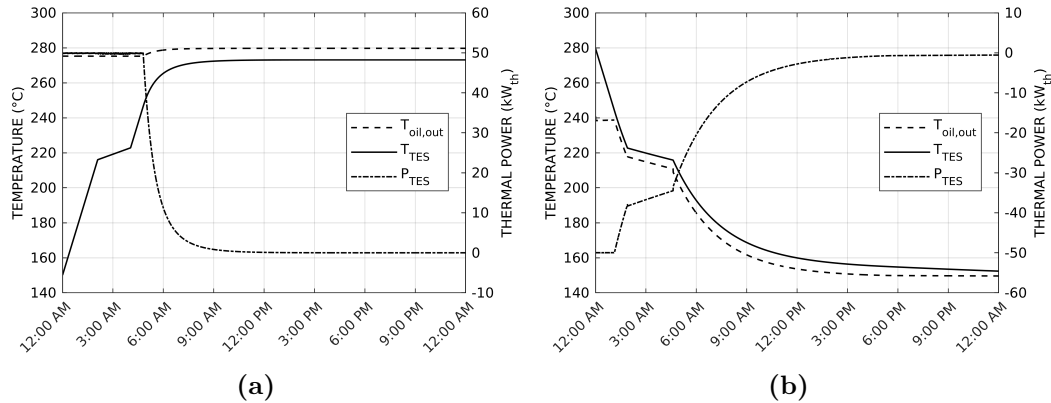


**Figure 6.14.** Charging (a) and discharging (b) process of the LHTES.

From the figures above is evident the power gain available within the melting region and this is the reason why the ORC is set to operate between 215 °C and 217 °C ( $T_{ORC,off}$ ,  $T_{ORC,on}$  respectively). The represented charging phase refers to 3 kg/s of inlet oil flow rate at 280 °C. Similarly, during the discharging phase, PCM is initially at the maximum temperature of 280 °C and heat is removed by oil from the ORC at design conditions (oil temperature 150 °C and oil flow rate 0.22 kg/s). Since that the LHTES in the figures operates beyond the allowed limit (supply temperature much different from the PCM), the thermal power exceed the value of 40 kW<sub>th</sub>. Actually, this step response rarely occurs during the simulations, thus it can be neglected.

## 6.3 Organic Rankine cycle

### 6.3.1 Introduction

ORCs modeling approach can be divided in two branches: stationary and dynamic. If the heat source does not vary significantly during time, and no particular needs for controlling the output power are requested, the stationary model is the most indicated, it is simpler to implement and somewhat numerically robust. Conversely, a dynamic approach is more precise when the heat/cold source fluctuations are relevant, or the thermal/electrical load have to be adjusted in a short time, automotive applications are an example para excellence.

Another important aspect concerns the ability to coherently reproduce the off-design conditions. In this regard, considering either a volumetric expander or a volumetric pump, in both the cases the refrigerant flow rate can be assumed proportional to the respective rotational speed, thus simulating a different working point is not challenging. Conversely, condenser and evaporator behavior is strongly correlated with the temperatures and the mass flow rates in both the exchanger's sides; the two phase zone width and thus the heat transfer rate widely vary. As a result all the operating points of the thermodynamic cycle considerably change. In this case the components often work in off-design conditions during the transitory, consequently the performances are affected. A more accurate modeling of pump and expander in off-design conditions can be accomplished using a polynomial regression for the isentropic efficiency evaluated within their operative ranges.

The choice of a dynamic or a static approach sometimes can also depend by the construction method, for instance, shell and tubes heat exchangers have a greater thermal inertia than plates exchangers. If the mechanical inertia of all the rotating parts may be neglected, the same can not be said for heat exchangers in some circumstances, for example when the flow/temperature variation of the heat/cold source is faster than their dynamics.

In light of the previous observations, here as follow the principal approaches in modeling the ORC components are reported. As far as heat exchangers modeling, two approaches can be distinguished in literature: (i) *Moving-Boundary* (MB or lumped parameters), (ii) *Finite Volume/Difference Methods* (FVM/FDM), carried out both in steady-state and dynamic conditions [143]. The MB approach considers the same thermodynamic conditions (for example heat transfer rate) in the three zones economizer, evaporator and superheating, whereas the FVM divides the channels in several cells regardless whether it is located in the superheating region rather than in the evaporator. MB models can be considered a non-linear implicit problem, in fact the width of each zone is at priory unknown, this fact may lead to convergence issues if no proper guess variables are provided. One example of the MB modeling in steady state conditions is given by Ian et al. [60] who improved the algorithm giving it more robustness to the convergence issue mentioned before, considering both internal and external pinching points. The correlation of heat transfer for each of the three zones depends mainly on the geometry (shell and tubes or plates, in turn from their internal shape) and the fluid type and its regime. A plenty of efforts have been addressed by researchers to find out general correlations applicable to the broader variety of possible cases, some of them are cited in [121].

The dynamic behavior of heat exchangers includes further freedom degrees, thus complexity to the problem. Basically the convective heat transfer coefficients are affected by the fluid density, heat capacity, thermal conductivity, and in the two phase zone by the surface tension, void fraction (the fraction of vapor area on the local fluid interface), and relative velocity between vapor and liquid phase. To adequately capture the transient effects mass and energy balance equations are often not enough, especially when the internal pressure loss are not negligible, the momentum equation must be taken into account to determine the internal mass flow interactions [151, 150].

Lastly, just for mentioning, in the early two years a new topic is coming up in the scientific community: the charge-sensitive models for ORC systems modeling. As mentioned by Liu [121] the e degree of superheat of the outlet refrigerant from the evaporator as well as the degree of subcooling at the condenser outlet are affected by the initial charging level in the liquid receiver. This further feature can improve the current methodology in ORCs system modeling.

### 6.3.2 Modeling

The conversion of the thermal energy in electrical energy is demanded by a small ORC unit of 2 KWe/18 kWth, it should be integrated in a building, thus it has to be very compact.

Another important aspects concern the environmental compliance, organic fluid used should be designed as replacements for *Ozone Depleting Substances* (ODSs) and compounds with high *Global Warming Potentials* (GWPs) such as sulfur hexafluoride (SF6) and hydrofluorocarbons (HFCs), such as HFC-134a and HFC 245fa, it should not be flammable or even toxic, but all these constraints reduce the number of possible candidates to be used in this small ORC. In fact, large part of high performance fluids are fairly flammable, because in the power plant is supposed to use a medium-low temperature heat source (250-280 °C), the electrical performance is inevitably affected.

Subcritical cycles are preferred because of their low operating pressure at the evaporator section<sup>3</sup>, since the big part of the ORC cost is attributable to it, obviously higher temperature means high material quality and particular construction techniques. On the other hand, to recover the efficiency gap given by these design strategies a regenerative cycle has to be preferred, the additional exchanger is cheaper than the evaporator and allows to be in agreement with the targets declared in the proposal in tab. 4.1.

On this purpose, Enogia [17] designed a micro ORC, it has *Plate Heat Exchangers* (PHEs) and a micro turbine with magnetic levitation bearing able to reach 60,000 rpm. The technical specifications of this small ORC unit can be useful for this study to address the next numerical investigations. The Enogia's company decided to use the *Novec649* engineered fluid because it has very low GWP and a quite high thermal conductivity and above all no flammability. These outstanding physical properties allow it to be used also in cooling techniques for green data centers server [20] called *immersion cooling* enhanced by pool boiling (thanks to the low boiling

---

<sup>3</sup>It is worth to say that some supercritical/transcritical cycles can work also at low pressures as well.

point at ambient temperature). The main physical properties of the Novec649 are reported in tab. 6.11, as one can see it has no enough critical temperature if compared with the heat source of 250 °C, as a consequence the fluid evaporation occurs at low temperature (subcritical cycle) thus reducing the Carnot efficiency of the cycle.

**Table 6.11.** Physical properties of Novec649.

Properties	3M <sup>TM</sup> Novec <sup>TM</sup> 649 Fluid
Ozone Depletion Potential (ODP)	0.0
Global Warming Potential (W/m)	1
Atmospheric Lifetime (years)	0.014
Boiling Point (°C)	49
Critical Temperature (°C)	169
Critical Pressure (MPa)	1.88
Heat of Vaporization <sup>4</sup> (kJ/kg)	88
Specific Heat <sup>5</sup> (J/kg-K)	1103
Thermal Conductivity <sup>6</sup> (W/m-K)	0.059

After a brief overview about the choices that impact on ORC designing, the mathematical modeling and the outcomes derived by the cycle solution are now described in detail.

Considering the whole micro CHP system, the ORC unit has a very low dynamic for two aspects: (i) the thermal capacity of the PHEs is negligible if compared with the pipeline and the storage, (ii) the high heat transfer on the PHEs enables a quick response due to the temperature and flow rate variation (time constant about 1-2 min), (iii) their compactness reduce the temperature delay due to crossing. All in all, the dynamic effect of the ORC can be neglected, hence it can be modeled with a simple *thermodynamic cycle* in a *quasi-steady-state* conditions, that is to say during the dynamic simulation the output is not affected by the previous time step ("quasi" expression).

The following assumptions have been considered for the ORC unit:

- no pressure drops across the components;
- no thermal capacity of the components;
- minimum driving temperature difference between the evaporator and the condenser and pressure ratio at the expander equal to 50 °C and 2.5;
- constant isentropic efficiency of the pump (70%);
- constant electric efficiency of the pump motor and electric generator (90%);
- constant mechanical efficiency of the pump motor and electric generator 95%;

<sup>4</sup>at the boiling point of 49 °C

<sup>5</sup>in liquid phase

<sup>6</sup>in liquid phase

- expander isentropic efficiency varying in the range 46-60%<sup>7</sup>;
- constant effectiveness of the PHEs;
- steady state conditions;
- no subcooling;
- constant superheating.

The temperature difference between the inlet oil and the organic fluid evaporating temperature is assumed constant and equal to 34 °C obtained by the manufacturer datasheet [31] at the design point, since the cycle is subcritical, the evaporating temperature is set 10 °C lower than the critical temperature, while it is allowed to fall if the heat source temperature decreases, this method is called *sliding pressure* part-load control [56]. At the evaporator outlet a minimum superheating of 5 °C is considered, while at the condenser outlet the working fluid is at saturated conditions (no subcooling).

The refrigerant flow rate varies according to an iterative procedure developed in MATLAB using the open source library Coolprop [37], 5 °C overheating are fixed in the evaporator and a 159 °C maximum evaporation temperature is chosen. The implemented code framework is depicted in the flow chart of fig. 6.15, the points whose chart refers to should be compared with those in the T-S diagram of fig. 6.16.

The fig. 6.16 clearly shows the dry properties of the refrigerant, but at expense of high irreversibilities at low vapor quality (points 1,2,6,7). To better understand how the code works with the sliding pressure method two different operating conditions are chosen: at low and high input temperature of 150 °C and 250 °C respectively (the last one is shown with dotted lines), but fixing the oil and water flow rate at the nominal point (0.22 kg/s and 0.5 kg/s respectively), so as the water inlet temperature at the condenser of 30 °C.

As the oil inlet temperature increases, the point 2 rises, 34 °C between the inlet oil and the refrigerant evaporating temperature are fixed; as soon as the point 2 reaches its maximum (10 °C below the critical temperature of the Novec649), the thermodynamic point no longer change. Even though the regenerator provides better results in effectiveness, the limited critical point of the Novec649 associated with a subcritical cycle do not allow to exploit the high temperature from the heat source. As already stated, the equations used are steady, thus no turbine and pump inertia is present, either thermal capacity of the refrigerant or metal case in direct contact with the HTF.

As one can evince from the introduction at this section, PHE modeling is somewhat complex also in steady state conditions, moreover, it is often difficult to find out a correlation for each fluid region with regard to the internal geometries (chevron angle, corrugation pitch and depth), moreover this data is often protected by PI rights.

In this study MB and FVM are discarded because the control system runs the ORC most of the time in the design conditions, indeed the thermal storage provides a great help in this sense. The *Number of Transfer Units* (NTU) method for PHE

<sup>7</sup>the experimental curve comes from Enogia's company

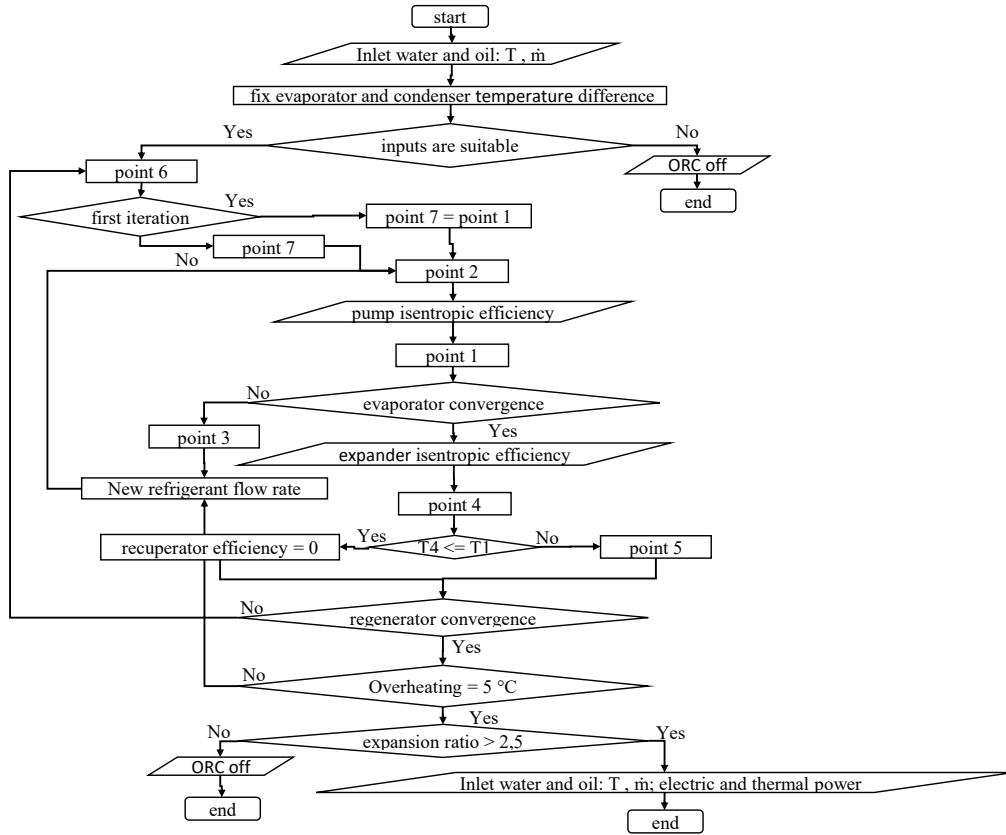


Figure 6.15. ORC solver flow chart.

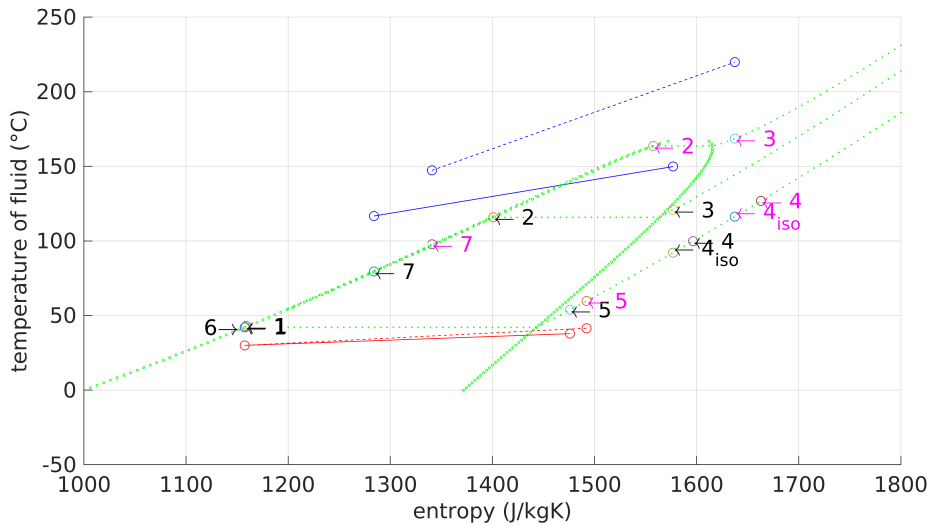


Figure 6.16. ORC T-S diagram with Novec649 at  $T_{ORC,in} = 150-280 \text{ }^\circ\text{C}$ .

modeling is used with a future vision of improvements, due to its robustness and simple applicability, and not less important computational efficiency required for such long dynamic simulations. The implemented equation to calculate the effectiveness for counter flow PHEs is:

$$\epsilon = \frac{1 - e^{-NTU(1-c_r)}}{1 - c_r e^{-NTU(1-c_r)}} \quad (6.47)$$

Where  $c_r$  is the heat capacity ratio (minimum heat capacity over maximum heat capacity of the used fluids). When phase change condensation or evaporation is occurring in the heat exchanger the heat exchanger behavior is independent of the flow arrangement, therefore the equation for the effectiveness should be changed. It is worth saying that the NTU term in the previous equation is calculated from the datasheet provided by Swept manufacturer [31] at the design point, thus regardless the multiphase regions, but it has been conceived as a lumped model<sup>8</sup>. As a matter of fact, if a single formula is considered, when for example the water mass flow rate suddenly decreases from the nominal conditions, the outlet temperature of the condenser can rise over a physical value giving a negative pinch point (unless a proper correlation for off-design conditions is used). Because no particular needs for the condenser flow partialisation, the water mass flow rate is always kept at nominal flow rate, while the evaporator has no issues since it has a fixed temperature difference between the inlet oil and the evaporation temperature (refrigerant side). The heat capacity does not change significantly, thus the effects on the numerical solution are negligible.

Based on the constant electrical efficiencies  $\eta_{el,pump}$   $\eta_{el,gen}$  of the pump and generator, as well as their mechanical efficiencies  $\eta_{m,pump}$   $\eta_{m,gen}$ , the electric power output from the ORC is:

$$P_{el,ORC} = \dot{m}_f [\eta_{m,gen} \eta_{el,gen} \Delta h_e - \Delta h_p / (\eta_{m,pump} \eta_{el,pump})] \quad (6.48)$$

The thermal power output from the ORC unit is evaluated as:

$$P_{th,ORC} = \dot{m}_c c_{p,c} (T_{out,cond} - T_{in,cond}) \quad (6.49)$$

where  $\dot{m}_c$  is the cooling water flow rate,  $c_{p,c}$  the specific heat of the cooling water and  $T_{out,cond}$  and  $T_{in,cond}$  the outlet and inlet temperatures of the cooling water at the condenser. The ORC thermal and electric efficiencies are defined respectively as:

$$\eta_{th,ORC} = \frac{P_{th,ORC}}{P_{in,ORC}} \quad (6.50)$$

$$\eta_{el,ORC} = \frac{P_{el,ORC}}{P_{in,ORC}} \quad (6.51)$$

the inlet thermal power  $P_{in,ORC}$  is 25 kW and the  $\eta_{th,ORC}$  is fixed at 0.8. The ORC model discussed above is validated using R134fa as working fluid and a not regenerative cycle [81], on the basis of the experimental results presented by Bianchi et al. [68, 65] who got three different sets of experimental data of the *Newcomen*

<sup>8</sup>The NTU method can be applied in a discretized PHE, thus considering a own NTU for each segment.

ORC unit. Consequently, a different efficiency curve of the expander is chosen since it is a piston.

The table 6.12 shows that the model proved (whose heading of column indicated as “mod.”) to be in good agreement with the experimental results (whose heading of column indicated as “exp.”) with a deviation in the range  $\pm 5\%$ .

**Table 6.12.** Model validation: comparison between experimental and model data.

Parameter	exp. 1	mod. 1	Dev. (%)	exp. 2	mod. 2	Dev. (%)	exp. 3	mod. 3	Dev. (%)
$T_3$ (°C)	64.6	63.9	1.1	73.8	73.8	0.0	86	88.8	-3.3
$T_4$ (°C)	41.7	40.11	3.8	51.2	51.38	-0.4	63.8	67.2	-5.3
$T_7$ (°C)	34.5	32.5	5.8	40.35	38.2	5.3	47.9	47	1.9
$T_6$ (°C)	23	22.65	1.5	22.9	22.65	1.1	23.1	22	4.8
$\dot{m}_f$ (kg/s)	0.1	0.1	0.0	0.1	0.1	0.0	0.09	0.09	0.0
$\eta_{e,ORC}$	3.67	3.79	-3.3	3.98	4.06	-2.0	4.2	4.28	-1.9
$P_2$ (bar)	14.3	14.5	-1.4	14.3	14.5	-1.4	14.3	14.4	-0.7
$P_6$ (bar)	6	6.07	-1.2	6	6.08	-1.3	6	6.08	-1.3

On the basis of the validated code, some simulations of the thermodynamic cycle are carried out to assess the theoretical electric efficiency at varying the inlet temperatures both in hot and cold side. The parametric analysis in fig. 6.17, shows the strong variation of the electrical efficiency due to the condenser temperature, it can double from 70 °C to 20 °C. The wavy effect on the curves is attributable to the sliding pressure control in combination with the TS curve of the refrigerant. Another interesting feature of this analysis regards the nominal conditions, in all the cases the design temperature is reached at 210 °C, which corresponds to the evaporation temperature of 159 °C. In fact, as stated before, above this point the evaporator pressure and temperature is fixed and the thermodynamic efficiency can not rise. On the other hand, greater power can be extracted from the heat source using more refrigerant flow rate at expense of the efficiency (higher irreversibilities). For these reasons, in cogeneration applications, unless a radiant floor is adopted by the final user, the electric efficiency target of 10 % can not be reached with this fluid using the common radiators supplied at 60 °C.

## 6.4 Pipeline

### 6.4.1 Introduction

In previous works [180, 79], the performance of a micro solar ORC plant have been investigated. Among the obtained results, they found a significant amount of thermal loss in the pipelines connecting the different subsystems. More precisely, the thermal inertia of the pipelines, the multiple-supply temperature levels of the transfer medium and the variability of the local renewable energy source entailed significant fluctuations of the plant operation also, according to [187]. Indeed, any shutdown and restart of the system as well as variations in the oil flow rate affect the

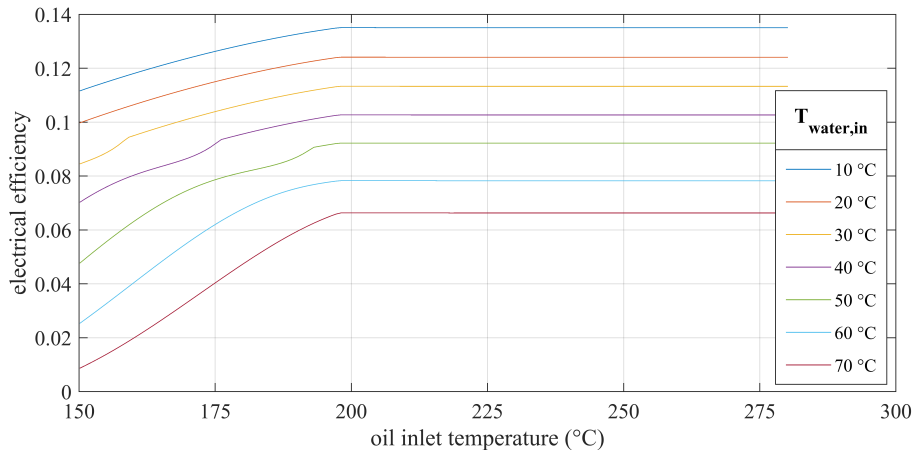


**Figure 6.17.** electrical efficiency Vs  $T_{\text{ORC,in}}$  Vs  $T_{\text{water,in}}$ .

solar field ability to generate thermal power or that of the TES to rise in temperature because of the thermal gradient along the pipe itself.

So far, many researchers have addressed such issues by modeling the thermal dynamic behavior of the pipeline networks. For instance, Van der Heijde et al. [176] presented the mathematical derivation and software implementation in *Modelica* of a thermohydraulic plug-flow model of thermal networks. They highlighted that the advantages of the plug-flow model in comparison with the use of multiple control volumes are the grid size and the time-step independence with flow velocity and the absence of numerical diffusion. Another example of improvement concerning the plug-flow model is reported by Denari et al. [86]. In particular, their approach provided the same accuracy of the finest-discretization finite volume method, while being 103 times faster and without introducing the smoothing effect of sharp temperature variations. Instead, Del Hoyo Arce et al. [84] developed a distribution pipe model, simpler and less computationally costly than detailed models, obtaining errors lower than 5 % and 0.02 % in the mass flow rate and temperature, respectively. However, the transient analysis showed differences in the pure delay of temperatures within the network. On the contrary, Chertkov and Novitsky [77] have considered the dynamic/transient advection diffusion-losses equations by keeping the velocity flow steady and adjusting the temperature at the heat-producing source, thus bypassing the computationally expensive *partial differential equations* (PDEs) solution. An alternative to the FVM is the finite difference method. In [182], the authors have applied the third-order Euler discretization method with *Total Variation Diminishing* (TVD) to assess the thermal behavior of the pipe in a DH network. In particular, they proved an effective elimination of the numerical dissipation and dispersion even in rather coarse grids. Indeed, the TVD is able to prevent oscillations of the solution near the sharp front of temperature variation where other numerical schemes, such as *Lax-Friedrich*, *Lax-Wendroff* and *Crank-Nicolson*, fail [108]. One of the most used numerical schemes for solving the advection-diffusion equation is the upwind scheme, thanks to its simple applicability and good accuracy also during fast rising or falling edge in temperature. Wanga et al. [185] have compared the implicit upwind scheme

with the characteristic line method, finding that the first one is unconditionally stable and more informative in simulating the temperature distribution along a pipeline. Anyhow, the major problem of this solving method consists of an additional numerical diffusion due to the *Courant number* and the grid refinement. Hence, while extensive research activity has been carried out with respect to pipelines in DH networks, this aspect has not adequately been investigated in the case of small-scale CHP plants. Among the different renewable energy resources to be used in CHP systems, solar energy is considered the one with the greatest potential, thanks to its worldwide diffusion. In addition, the use of solar-concentrated technologies allows achieving medium and high temperatures which are preferable for cogeneration applications in buildings and can compete with evacuated tubes if the involved systems are properly designed. For this reason, in recent years many researchers have paid attention on the coupling of concentrated solar power technologies with organic Rankine cycle units.

### 6.4.2 Modeling

In general, a numerical model needs to be a good compromise between accuracy and computational effort. Indeed, in dynamic simulations of complex energy systems the computational time is usually a tight constraint and as a consequence, simplified models have to be adopted. In this paragraph different models used to predict the thermal transient behavior of the fluid inside a pipe are discussed in detail. In particular, the following models are considered: (i) a two-dimensional model, (ii) a one-dimensional radial model, (iii) a one-dimensional longitudinal model and (iv) a lumped model. Hence, the accuracy of the different models are tested for a linear increase of the inlet temperature having a different angular ratio and for different fluid velocities. Then, these results are related with the fluid regime obtained by the dynamic simulation of an innovative micro solar CHP system (in terms of temperature derivative and flow rate) and compared with each other.

As regarding the resolution schemes, a first-order-explicit upwind scheme is adopted for the fluid, whilst a first-order in time and a second-order-in-space Euler method is used for the insulating walls. Such choice is due to their simple applicability and good effectiveness for the expected application.

#### Two-Dimensional Tube Model

In general, predicting the thermal transient behavior of the oil inside a pipeline requires the resolution of the transport equation of energy throughout the pipe. Considering one-dimensional flow, both the internal energy and the heat losses depend on the axial position in the pipe and on the time  $t$ , as reported in eq. 6.52:

$$\frac{\partial(\rho c_p T A)}{\partial t} + \frac{\partial(\rho u (c_p T + p/\rho) A)}{\partial x} = u A \frac{\partial p}{\partial x} + \dots \quad (6.52)$$

$$\frac{\rho u^2 |u|}{2} f r_D S + \frac{\partial}{\partial x} \left( k_{HTFA} \frac{\partial T}{\partial x} \right) - \dot{Q}_{loss}$$

where the source term  $\dot{Q}_{loss}$  included in the advection 6.52 can be positive in the case of heat losses from the internal fluid to the ambient and vice versa. Considering

that the pipelines under investigation are referred to a microscale CHP plant, a detailed solution of the equation as for DH networks is not necessary whilst the robustness and the velocity of the solving code are preferred. Hence, all the terms of the second member of eq. 6.52 can be deleted and the source term excluded, with good approximation. Indeed, Van der Heijde et al. [176] have shown that the diffusivity term can be neglected, while the pressure difference and the wall friction are not relevant in comparison with the total energy in common operating conditions. In light of these considerations, the resulting advection equation can be rewritten as in Equation 6.1

According to *Fourier's* law, in an isotropic medium the one-dimensional heat transfer equation can be written in cylindrical coordinates as follows:

$$\frac{1}{\alpha} \frac{\partial T}{\partial t} = \frac{1}{r} \frac{\partial T}{\partial r} + \frac{\partial^2 T}{\partial r^2} \quad (6.53)$$

In the case under investigation, the metal tube is neglected from the thermal point of view, because of its high thermal conductivity and low heat capacity compared with the fluid. Hence, in order to ensure the correct heat transfer across the interface between the heat transfer fluid (HTF)-insulation and insulation-ambient, a *Von Neumann boundary condition* needs to be included. Therefore, the equations are discretized using the finite difference method by dividing the pipeline into O circumferential sections along the radial direction and M segments in the axial direction. The time and the spatial derivatives of the oil temperature, instead, are replaced by finite difference quotients. Hence, applying the one-order-explicit upwind scheme to solve the advection eq. 6.54, it can be written:

$$\frac{T_{i,j}^{k+1} - T_{i,j}^k}{\Delta t} + u_i \frac{T_{i,j}^k - T_{i-1,j}^k}{\Delta x} = - \frac{T_{i,j}^k - T_{iw}^k}{R_{i(conv,int)} \rho^k c_{p_i}^k A} \quad (6.54)$$

where  $k = 1, 2, \dots, N$  denotes the number of time steps,  $i = 1, 2, \dots, M$  denotes the number of longitudinal segments, while  $j = 1$  since it is referred to the fluid and it is the first nodal point along the radial direction. As regards the thermophysical properties of the fluid, they are evaluated as a function of its temperature in the previous time step. On the other hand, the one-order-explicit Euler scheme is used for the time derivative whilst the second-order scheme is adopted for the spatial derivative of eq. 6.55. Therefore:

$$\frac{1}{\alpha^k} \frac{T_{i,j}^{k+1} - T_{i,j}^k}{\Delta t} = \frac{1}{r_i} \frac{T_{i,j+1}^k - T_{i,j-1}^k}{2\Delta r} + \frac{T_{i,j+1}^k - 2T_{i,j}^k + T_{i,j-1}^k}{\Delta r^2} \quad (6.55)$$

where the subscripts and superscripts have the same meaning previously mentioned whilst  $j = 1, 2, \dots, O$  represents the circumferential discretization of the pipeline. In addition, in this case the thermal diffusivity depends on the thermophysical properties of the fluid at the previous time step:

$$\alpha^k = k_{i,ins}^k / (\rho_{ins}^k c_{p,ins}^k).$$

With respect to the internal interface between the heat transfer fluid and the insulation, the boundary condition can be written as:

$$\frac{T_{i,j=1}^k - T_{i,j=2}^k}{R_{i(conv,int)}^k} = \frac{T_{i,j=2}^k - T_{i,j=3}^k}{R_{i(cond)}^k} \quad (6.56)$$

The same procedure is performed for the external interface where the radiative heat transfer can be neglected:

$$\frac{T_{i,j=o-1}^k - T_{i,j=o}^k}{R_{i(cond)}^k} = \frac{T_{i,j=o}^k - T_{amb}^k}{R_{i(conv,ext)}^k} \quad (6.57)$$

and the external convective resistance evaluated in the case of wind and no-wind conditions. In particular:

$$R_{conv,ext} = \frac{1}{h_2 \pi D_2} \quad (6.58)$$

and in the case of no wind, the Churchill and Chu's correlation can be used to estimate the Nusselt number according as already done in eq. 6.25:

$$\bar{Nu}_2 = \left\{ 0.60 + \frac{0.387 Ra_2^{1/6}}{[1 + (0.559/Pr_{2-amb})^{9/16}]^{8/27}} \right\}^2 \quad (6.59)$$

$$Ra_2 = \frac{g\beta(T_{i,j=o}^k - T_{amb}^k)D_2^3}{\alpha_{2-amb}\nu_{2-amb}} \quad (6.60)$$

$$\beta = 1/\bar{T}_{2-amb} \quad (6.61)$$

$$Pr_2 = \nu_{2-amb}/\alpha_{2-amb} \quad (6.62)$$

$$(6.63)$$

with  $10^5 < Ra < 10^{12}$ . In case of wind, instead, the Nusselt number is estimated according to the Zhukauskas' correlation (as in eq. 6.30, valid for  $0.7 < Pr_{ext} < 500$  and  $1 < Re_2 < 10^6$ ). More precisely:

$$\bar{Nu}_2 = C Re_2^m Pr_{amb}^n \left( \frac{Pr_{amb}}{Pr_2} \right)^{1/4} \quad (6.64)$$

$$n = \begin{cases} 0.37 \text{ if } Pr \leq 10 \\ 0.36 \text{ if } Pr > 10 \end{cases} \quad (6.65)$$

where the coefficients "n" and "m" are listed in Table 6.2. As regards the internal convective resistance:

$$R_{conv,int} = \frac{1}{h_1 \pi D_1}$$

where the convective heat transfer coefficient can be written as:

$$h_1 = \frac{k_{HTF}}{D_1} Nu_1$$

In case the HTF regime has a  $Re > 2300$ , the Nusselt number can be expressed according to the Gnielinski's correlation reported in table 6.10, on the contrary, when the HTF flow is laminar this value is fixed to 4.36.

Despite the external convective heat transfer coefficient is not negligible, the predominant term of the total thermal resistance is the insulating material, which can be calculated as follows:

$$R_{i(cond)} = \frac{\ln\left(\frac{r_{i+1}}{r_i}\right)}{2\pi k_{ins} T_{r_i}}$$

Considering mineral wool as insulating material, its thermal conductivity  $k_{ns}(T)$  strongly depends on its temperature, as reported in table 6.13:

**Table 6.13.** Thermal properties of PROPOX PS964 mineral wool (EN ISO 8497)

Temperature (°C)	Thermal Conductivity (W/m · K)
50	0.042
100	0.049
150	0.059
200	0.071
250	0.086
300	0.105

### One-Dimensional Longitudinal Model

In the case of the 1 D longitudinal model, eq. 6.54 previously reported also includes the total thermal resistance towards the ambient while the thermal capacity of the insulation can be neglected. Therefore, the energy balance can be written as:

$$\frac{T_{i,j}^{k+1} - T_{i,j}^k}{\Delta t} + u_i \frac{T_{i,j}^k - T_{i-1,j}^k}{\Delta x} = - \frac{T_{i,j}^k - T_{amb}^k}{R_{i(conv,ext)} + R_{i(cond,int)} \rho^k c_{p_i}^k A} \quad (6.66)$$

where  $k = 1, 2, \dots, N$  is the number of time steps,  $i = 1, 2, \dots, M$  the number of longitudinal segments while  $j = 1 \forall k$ . For the purpose of this analysis, the internal convective resistance is neglected while the conductive resistance evaluated at the mean temperature between the HTF and the ambient.

### One-Dimensional Radial Model

In the 1D radial model, instead, a linear temperature distribution along the tube length is assumed. So, the energy-balance equation in a single pipeline segment can be written as follows:

$$\dot{Q}_{in} - \dot{Q}_{out} - \dot{Q}_{loss} = \rho A L c_{p_i}^k \frac{\partial \bar{T}^k}{\partial t} \quad (6.67)$$

where the first two terms depend on the mean temperature of the pipeline segment. Hence:

$$\dot{Q}_{in} - \dot{Q}_{out} = 2\dot{m} c_p (T_{in}^k - \bar{T}^k) \quad (6.68)$$

By combining of equations 6.67, 6.68 and using eq. 6.55 for the internal domain of the insulating material, the governing equation of the 1 D radial model is:

$$2\dot{m}c_p(T_{in}^k - \bar{T}^k) - \left( \frac{\bar{T}^k}{R_{conv,int}} \cdot \frac{R_{cond}\bar{T}^k R_{conv,int} T_{j=2}^k}{R_{conv,int} + R_{cond}} \right) = \rho ALc_p^k \frac{\partial \bar{T}^k}{\partial t} \quad (6.69)$$

### Lumped Model

In the lumped model, or 0 D model, a linear temperature distribution of the HTF is assumed as in the case of the radial model since there is no discretization along the radial direction and all the thermal resistances are included into a single equation:

$$2\dot{m}c_p(T_{in}^k - \bar{T}^k) - \left( 2\pi L \frac{\bar{T}^k - T_{amb}}{\frac{1}{k_{ins}} \ln \frac{r_2}{r_1} + \frac{1}{h_2 r_2}} \right) = \rho ALc_p^k \frac{\partial \bar{T}^k}{\partial t} \quad (6.70)$$

In the above equation the inlet temperature  $T_{in}$  is given at time  $t = 0$ :

$$T_{in}^k = T_{in}^{k=1} + rr \cdot t \quad (6.71)$$

where "rr" is the angular coefficient of the temperature increase/decrease. Both in the 1 D longitudinal model and in the 0 D model the heat capacity of the insulating material is neglected. Moreover, in the case of the 0 D model, eq. 6.70 is solved analytically obtaining the mean temperature of the HTF in the single cell. Then, based on the linear temperature distribution assumed, the outlet temperature is calculated. Hence, since the term of the equation used for the transport properties is neglected, a delayed output is introduced. This delay is calculated as:

$$\Delta t_{del} = L/u$$

## Chapter 7

# Dynamic simulation test cases

In this chapter, the mathematical models previously defined are used to undertake some numerical investigations in dynamic conditions. Additional controllers/models have been developed or got by existing software libraries to address the specific task of the analysis, they are described in each section independently.

### 7.1 Global system performance

In this section a preliminary estimation of the overall system performance is presented with the purpose of providing useful information for its forthcoming real operation. In particular, according to the varying ambient conditions, the influence of different operation modes of the prototype plant are evaluated. The dynamic simulation analysis has shown an interesting performance of the system in terms of annual operating hours, power production and conversion efficiencies. More precisely, the organic Rankine cycle unit is able to operate for more than 3374 h/year, achieving the design performance when solar power is sufficiently high, producing about 6500 kWh/year. For the considered operating set-point temperatures of the thermal energy storage, the plant achieves high conversion efficiency also when the organic Rankine cycle unit is supplied by discharging the energy stored in the storage tank, for about 1135 h/year. Hence, the work has provided some useful insights into the best working conditions of such micro combined heat and power system to be integrated in residential buildings. Moreover, the analysis could serve as a general guide for the design and optimization of the mutual interactions of the different subsystems in small-scale concentrated solar organic Rankine cycle plants.

#### 7.1.1 Global energy evaluations

##### Materials and Methods

Starting from the research background in chapter 4 that outlines the main motivations behind the concept design, the dynamic simulation model of the prototype plant is here tested.

Due to the complexity in the power plant modeling (several subsystems involved, many parameters to diagnose in the simulation), the use of an object oriented software allows a better managing of the variables during the run, simplifying the

bug recognition and providing a more clear global view. Under these considerations the *Simulink* platform [23] is used, and the advantages are twofolds: Simulink is an object oriented software; moreover, it has the benefit of a command line software in terms of flexibility in coding, thus it allows to write also ad-hoc subroutines by means of MATLAB function blocks. This latter feature gives to users the possibility to be unconstrained from the adoption of standard libraries, a considerable advantage when new or tailored models have to be created.

On the basis of the section 6 the following main components have been considered: (i) a LFR solar field; (ii) a micro ORC plant; (iii) a PCM thermal energy storage tank equipped with reversible heat pipes; (iv) pipes connecting the main components. In this test case, the plant is set to produce electricity at its maximum and the thermal load is considered as a by-product which can be entirely collected and used by final users. Therefore a detailed heating demand has not been assumed and the domestic hot water boilers have not been included in the model at this stage. fig. 7.1 reports a scheme of the system under consideration, in particular, the pipeline network exactly reflects the future construction geometry of the micro CHP. In this way the future experimental data (especially the plant performance) derived from a real test are expected to be closer with the simulated.

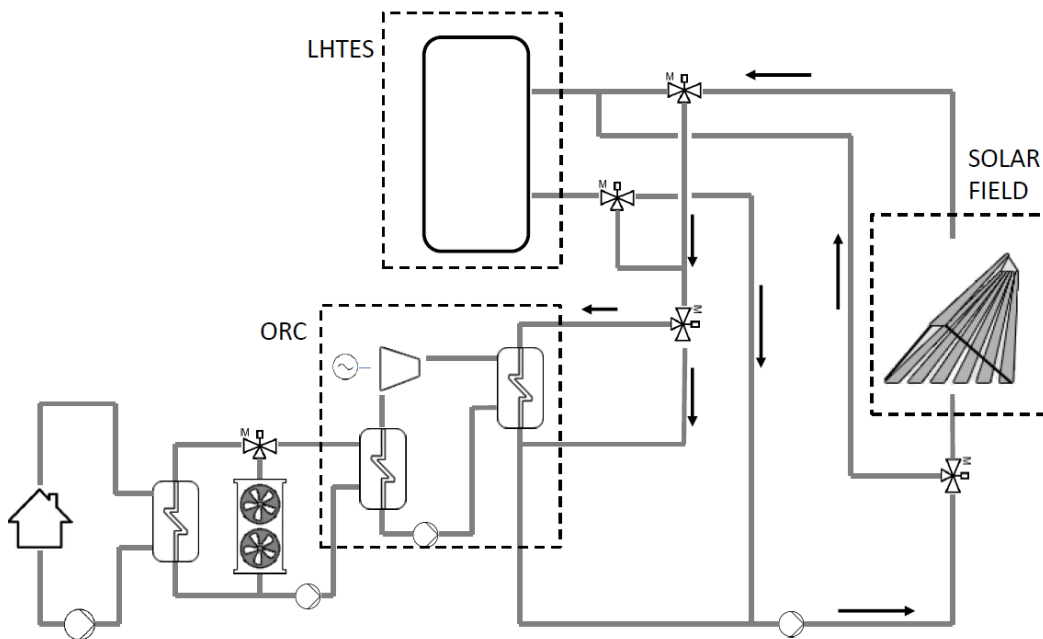


**Figure 7.1.** Micro solar CHP scheme.

The innovative micro-CHP plant here tested under a yearly dynamic simulation owns the technical specifications previously reported in the chapter 4.1, for sake of conciseness, the reader is invited to refer to the mentioned chapter.

From the scheme in fig. 7.1, it is worth noticing that four diverts are installed in such way that the plant can work in different operation modes (OM). Based on the system state and the solar irradiation available, the implemented controller inside the model selects the proper OM for maximizing the electricity production,

consequently the subsystems involved in the specific OM are connected together as reported in table 7.1.

**Table 7.1.** List of the possible connections among the subsystems and the respective pump flow rate settings.

	OM Connected subsystems	pump mass flow rate
-1	LFR (defocused) + ORC	$\dot{m}_{pump} = \dot{m}_{ORC,max}$
0	LFR recirculation	$\dot{m}_{pump} = \dot{m}_{LFR,max}/3$
1	LFR + ORC	$\dot{m}_{pump} = \frac{P_{LFR} - P_{LFR,min}}{P_{LFR,max} - P_{LFR,min}} (\dot{m}_{ORC,max} - \dot{m}_{ORC,min}) + \dot{m}_{ORC,min}$
2	Plant off	$\dot{m}_{pump} = 0$
3	LFR + LHTES	$\dot{m}_{pump} = \dot{m}_{LFR,max}$
4	LFR + LHTES + ORC	$\dot{m}_{pump} = \frac{P_{LFR} - P_{LFR,min}}{3P_{LFR,max} - P_{LFR,min}} (\dot{m}_{LFR,max} - \dot{m}_{ORC,min}) + \dot{m}_{ORC,min}$
5	TES + ORC	$\dot{m}_{pump} = \dot{m}_{LFR,max}$
6	LFR + LHTES + ORC	$\dot{m}_{pump} = \dot{m}_{LFR,max}$

To facilitate the overall heat transfer across the subsystems the HTF is allowed to vary within a certain range when possible. With reference to tab. 7.1,  $\dot{m}_{ORC,min}$  and  $\dot{m}_{ORC,max}$  are the minimum and maximum oil mass flow rates compatible with the ORC evaporator (equal to about 0.11 and 0.22 kg/s respectively),  $\dot{m}_{LFR,max}$  the maximum oil mass flow rate in the solar field which corresponds to about 3 kg/s,  $P_{LFR}$  the collected thermal power by the LFR solar field,  $P_{LFR,min}$  and  $P_{LFR,max}$  the minimum and maximum collected thermal power by the LFR needed to run the ORC unit (equal to 15 kWth and 28 kWth respectively). Thereby, the mass flow rate of the oil in OM1 varies proportionally with the Direct Normal Irradiance up to 0.22 kg/s, while since the higher available power in OM4, the HTF varies in the range 0.22-3 kg/s, consequently the extra mass flow rate is recirculated through the LHTES.

The simulation is solved with a discrete fixed step solver, 1 minute time step is set to properly capture all the dynamics of the different subsystems. Weather data are taken from *Energy+* database for the location of Lerida (Spain), 50 km from Almatret where the prototype plant is located. The plant is oriented along the North-South direction to maximize the thermal energy over the year. The hourly weather data are pre-processed using spline interpolation in order to be suitable for the simulation study with the time step mentioned above. Moreover, all the dynamic models have their own internal time step lower than or equal to the simulation time step in order to assure the convergence of the simulation. In particular, both the pipelines and the LFR solar field models have been developed considering the finite difference method and their internal time step satisfies the Courant condition (explicit solver). The performance of the ORC system is significantly affected by the condensing temperature which has been fixed to 60 °C. At this temperature level,

indeed, the system can supply also the high temperature radiators often installed in existing buildings for space heating during the winter season.

As the system consists of 3 main subsystems (see fig. 7.1), 8 different OM are identified as follow:

- *OM-1*: this OM is activated if the LHTES reaches the maximum allowed temperature of 280 °C and the LFR defocuses (less power output than nominal one), the pump flow rate is fixed at the ORC nominal one, i.e. 0.22 kg/s;
- *OM0*: diathermic oil recirculates only in the LFR loop, at a constant flow rate of 1 kg/s, high enough to quickly homogenise the temperature gradients. This OM is activated if the LFR power is less than 15 kWth and the LFR outlet temperature is less than that required to charge LHTES.
- *OM1*: the oil flow rate through the LFR is adjusted proportionally in the range 0.11 ÷ 0.22 kg/s, when the collected solar power is between 15 kWth and 26 kWth respectively, assuring to the ORC a higher difference in temperature in the evaporator headers, than what it would have at 0.22 kg/s constant flow, thus increasing its electric efficiency;
- *OM2*: no sun is present, the pump is off, no electricity is generated;
- *OM3*: if the collected solar power by the LFR is lower than 15 kWth, the ORC unit can not operate efficiently. In this case, the storage system is charged (if  $T_{\text{LHTES}} < 215$  °C), and the LFR outlet flow rate is kept constant at 1 kg/s;
- *OM4*: when the output power from the solar field exceeds the nominal inlet power to the ORC (26 kWth), the extra power is used to charge the LHTES. The pump flow rate is proportionally adjusted in the range 0.22 -3 kg/s based on the collected power whose range is 26 kWth - 80 kWth.
- *OM5* when the LFR is off and the LHTES temperature is greater than 217 °C ( $T_{\text{ORC,on}}$ ), the LHTES runs the ORC till its temperature falls below 215 °C ( $T_{\text{ORC,off}}$ ). The pump flow rate is fixed at 3 kg/s enabling the LHTES to release as much power as possible;
- *OM6*: when the LFR power is lower than 26 kWth and the LHTES is charged, the LHTES is used together with the energy coming from the LFR to run the ORC unit. As it occurs in OM5 in order to release as much power as possible, the pump works at 3 kg/s.

because the low thermal conductivity of the solar salt, to assure better thermal performance of the storage, the temperature limits for the LHTES as:  $T_{\text{ORC,off}}$  and  $T_{\text{ORC,on}}$  (hysteresis interval) are chosen on the basis of the ability of the PCM to be charged and discharged quickly. Indeed, from fig. 6.14 it can be notice a greater power exchange occurs during the phase change in the temperature interval 216 - 223 °C, as a consequence the LHTES operation covers that rage. Instead, The maximum temperature limit derives from the heat pipes, because they can not sustain elevated pressures. Regarding the ORC operation, though is has a certain ability to work in part-load conditions, to avoid excessive efficiency reduction, the inlet power interval is fixed between 15 kWth and 26 kWth.

## Results and discussion

The annual simulations performed for the city of Lerida have shown a total electric energy production of  $2.32 \times 10^7$  kJ, equivalent to more than 6449 kWh (corresponding to about the electricity demand of two typical family houses), whilst the thermal energy may satisfy more than 4 dwelling needs.

The weather conditions in Lerida are characterized by a large DNI Vs *Global irradiance* ratio. This aspect increases the production of this kind of plants which are mainly driven by the direct irradiance [180]. The model framework may be utilised to improve the production performance of the plant by acting on its control logic. Indeed, rather than assessing the performance based on a deterministic approach (OM chosen a priori) a stochastic approach combined with optimization algorithms could be adopted enhancing the output of the plant. In the following histogram the operation modes distribution during a yearly simulation are shown excluding the OM2 (solar plant off) which alone totals 4280 h.

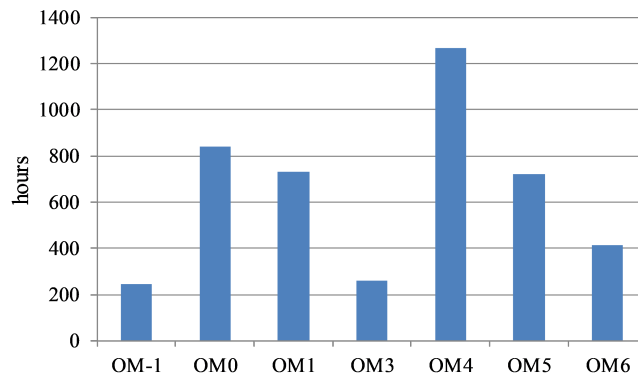


**Figure 7.2.** Total hours in the respective OM over a year.

As one can see from the histogram in fig. 7.2, OM0 occurs for a long time, just lower the OM4 mode. This behavior indicates that much care must be taken in evaluating the thermal losses since they are significant in this kind of plants. The LHTES is often at high temperature for most of the year, OM4 is promoted in summer because of high solar radiation, thus reducing OM3. Conversely, OM0 and OM1 take place mainly in winter time because the pipeline are cold (OM0), or the LFR outlet power  $P_{LFR,out}$  does not overcome the limit imposed to run the ORC equal to 15 kWth (OM1). Hence, the plant is able to produce electricity for 3384 h/year, which corresponds to 39 % of the yearly timespan; this goal is also achieved thanks to the big LHTES capacity. On the other hand, the LFR defocusing is not negligible, because of the high solar multiple with respect to the location under analysis.

The monthly overall energy balance of the system is shown in fig. 7.3. As expected, the input and output solar energy of the LFR solar field are much higher during summer and spring because of the higher DNI and hours of radiation. Despite the solar multiple of the plant, the surplus heat is limited. Most of the energy from the solar field indeed is used to supply the ORC unit and only a reduced amount flows into the TES. Although low, the electric energy production by the ORC is

significantly affected by the variable solar radiation during the year.

**Table 7.2.** Monthly average overall efficiency of the plant and of its main components.

Month	$\eta_{LFR}$	$\eta_{TES}$	$\eta_{ORC,el}$	$\eta_{ORC,th}$	heat losses	$\eta_{tot}$	$h_{ORC}$
Jan	27.8%	0.4%	7.85%	72.2%	60.8%	11.2%	71
Feb	34.6%	41.3%	7.87%	72.2%	47.0%	18.8%	157
Mar	40.4%	74.6%	7.91%	72.2%	40.7%	24.5%	301
Apr	43.1%	78.3%	7.92%	72.2%	39.5%	26.1%	336
May	44.5%	79.9%	7.92%	72.2%	38.2%	27.1%	396
Jun	43.4%	81.8%	7.93%	72.2%	36.6%	26.8%	445
Jul	42.7%	83.8%	7.93%	72.2%	36.5%	26.6%	484
Aug	43.9%	82.3%	7.92%	72.2%	37.1%	27.4%	441
Sep	41.6%	80.7%	7.92%	72.2%	38.8%	25.9%	359
Oct	36.2%	63.2%	7.89%	72.2%	44.2%	21.0%	225
Nov	29.2%	14.8%	7.83%	72.2%	54.7%	13.9%	99
Dec	25.3%	0.1%	7.70%	72.4%	63.7%	10.0%	61

Plant performance have been evaluated also in terms of monthly conversion efficiencies of the different subsystems as reported in table 7.2. The solar field efficiency ( $\eta_{LFR}$ ) is the ratio between the input solar energy and the output energy from the solar collector to the ORC unit and/or the TES, according to the operation mode. Because of the solar angles, which considerably affect the values of the IAM and the cosine effect, the solar field efficiency varies largely throughout the year. More precisely, it ranges from 25.3 % in December to 44.5 % in May with an annual average value of about 37.7 % which represents a satisfactory target. The thermal energy storage efficiency ( $\eta_{TES}$ ) is the ratio between the outlet thermal energy towards the ORC (discharging) and the inlet thermal energy from the LFR solar field (charging). On the basis of the control logic defined in the model (see subsection 7.1.1), OM5 and OM6 modes start when the TES temperature reaches 217 °C and stop as soon as the temperature is 215 °C. As already stated before, the TES discharging during the phase change of the storage medium is able to take advantage of higher heat transfer coefficient. On the other hand, the reduced discharging temperature range results in moderate annual operating hours of the system in OM5 and OM6 (see histogram 7.2). Moreover, this entails also low TES efficiencies during cold season, in January and December can be clearly seen. In winter, indeed, the DNI is usually not enough to supply adequate thermal power to the TES for its melting and the surplus energy from the solar field cannot be used during night time for most of the days.

However, in the real operation of the system this amount of thermal energy could be directly supplied to the final user for heating purposes thus significantly increasing the efficiency of the TES also in winter time. With regard to the ORC, its electric efficiency ( $\eta_{ORC,el}$ ), i.e. the ratio between the output electric energy and the inlet thermal energy to the ORC, remains almost constant throughout the year

and above 7.7 %, similarly to values shown in [171]. The results are very close each other since the control system is conceived to run the ORC at its nominal conditions, on the other hand, the electric efficiency is constant with an inlet temperature above 210 °C as shown in the section 6.17.

On the contrary, the thermal efficiency of the ORC ( $\eta_{ORC,th}$ ), defined as the ratio between the output and the inlet thermal energy of the ORC, is close to 70 % reaching the peak value of 72.4 % in December. Given the high solar radiation in summer and the corresponding collected thermal power from the LFR, the system shows a very interesting potential also as trigeneration plant. However, because of the further increase of its complexity and the reduction of its electric efficiency in case of solar cooling applications in summer, this configuration has not been investigated for the moment. As far as the total conversion efficiency of the plant ( $\eta_{tot}$ ) is concerned, namely the ratio between the output electric and thermal energy and the inlet solar energy, it varies because of the different solar field efficiency during the year and it ranges from 10.0 % in December to 27.1 % in summer. As reported in section 6.4, the model takes into account also the heat losses in the pipelines and in the main components (ORC and TES), the mean value globally accounts for more than 44 % of the available output thermal power from the LFR. In winter, the thermal losses in the TES account for about 20 % of the LFR thermal power. This is mainly due to: (i) the impossibility of supplying the ORC with TES energy because the TES temperature is below the melting point most of the time in winter, thus stored energy is not used; and to (ii) the reduced DNI in winter, which does not allow to run the ORC unit in OM1 and OM4 for long periods. Furthermore, the operating hours of the system in OM3 (TES charging) are by far higher in winter than in summer.

In terms of operating hours, the ORC unit is able to work more than 3374 h. Moreover the operating hours of the ORC unit could be sensibly increased by varying the set-point temperatures of the TES in OM5 and OM6, i.e. when the TES supplies the ORC. However, this would reduce the electric efficiency of the ORC and the overall energy production [53]. As far as the energy production is concerned, in the present configuration the ORC unit is able to generate about 6500 kWh/year and 58,800 kWhth/year, which represent a considerable amount of energy for household applications. Indeed, compared to the results presented by Calise et al. [9] for a 6 kWe solar-ORC set in an Italian location with a similar latitude, the proposed prototype plant can produce 30 % more thermal energy and 18 % more electric energy, despite the lower size of the ORC unit. The main purpose of this analysis is to evaluate how the ORC electric efficiency varies during plant operation and how it is affected by the operation modes of the implemented control strategy (see the operation modes in section 7.1.1). Therefore, the ORC performance data are evaluated on a monthly basis considering the operation modes when the ORC is on. On this purpose, table 7.3 reports the monthly average thermal input power, electric and thermal output power and efficiency of the ORC system during operation modes OM1, OM4, OM5 and OM6.

In general, since that the ORC unit does not exhibit variations in electric efficiency at varying of the OMs, this parameter has not been inserted in table 7.3.

Because of the set-point temperatures of the TES, the ORC is able to achieve high conversion efficiencies also in mode OM6, when both the LFR and TES supply

**Table 7.3.** ORC performance data: average thermal input power, average electric and thermal output power and average efficiency during each month for the different operation modes.

OM	$P_{ORC,out}(kW)$			$P_{ORC,in}(kW)$			$P_{ORC,el}(W)$					
	1	4	5	6	1	4	5	6	1	4	5	6
Month												
Jan	15.77	15.75	-	17.44	21.83	21.82	-	24.16	1723	1723	-	1917
Feb	16.19	18.65	14.84	15.57	22.39	25.85	20.57	21.58	2049	2049	1631	1711
Mar	16.30	18.79	15.7	17.03	22.55	26.04	21.76	23.6	2065	2065	1726	1872
Apr	16.09	18.8	15.89	17.97	22.28	26.05	22.02	24.9	2066	2066	1746	1975
May	16.19	18.79	16.03	17.62	22.42	26.04	22.22	24.42	2065	2065	1762	1936
Jun	16.38	18.81	15.74	18.32	22.70	26.07	21.82	25.38	2068	2067	1730	2013
Jul	16.35	18.81	15.79	18.27	22.65	26.06	21.88	25.32	2067	2067	1735	2007
Aug	16.27	18.8	16.00	17.94	22.53	26.05	22.18	24.86	2067	2067	1759	1972
Sep	16.27	18.8	15.91	18.20	22.52	26.05	22.04	25.22	2066	2066	1749	2000
Oct	16.05	18.77	15.26	16.92	22.20	26.01	21.15	23.44	2062	2062	1678	1857
Nov	16.11	17.7	14.69	15.79	22.29	24.52	20.36	21.88	1935	1936	1615	1734
Dec	15.75	14.89	-	-	20.56	21.77	-	-	1581	1581	-	-

power to the ORC. However, this operating mode is limited to about 411 h/year. Since high DNI and hours of radiation are needed to melt the PCM in the TES, OM6 and OM5 do not occur in December and in general such OMs are mainly present in summer season.

Finally, because of the limited output thermal power of the thermal storage in mode OM5, the ORC unit achieves an annual average output power of about 1.7 kWe, slightly less than other OMs. Indeed, even though the temperature interval for the TES discharging is chosen in the phase change range, the ability to run the ORC at its nominal point is not effective as in OM4 occurs. The defocusing in OM-1 is not shown in table 7.3, because the performances are the same of OM1.

In order to better appreciate how the plant switches from an operation mode to another, plant performance has been analysed also on an hourly basis. In particular, the power trends and the sequence of operation modes are evaluated for typical working days representative of the 4 seasons: 11 June, 11 October and 30 January are considered for the purpose. Fig. 7.4 show the daily trend of LFR and TES input and output power, ORC input thermal power and output electric power, during the different operation modes. Before analyzing the power trends, it is important to say that all the power signals are taken from the input and output enthalpies and flow rates of each subsystem (at the headers). Because of the time crossing delay introduced in the modeling and the thermal nodes of the LFR and pipeline network, some portions of the tube may be colder than others, therefore, when they travel in the active loops affect the calculated power signal introducing visible fluctuations. In other words, the temperature variations are not given by the inaccurate solution of the mathematical models, but they are a mere consequence of the applied method to record the above mentioned signals.

At first sight, the abundant solar radiation in summer seasons results in a prolonged operation of the plant at night time, in this summer day taken as a sample it works till 2 A.M. as shown in fig. 7.4a. As expected the TES achieves the maximum set point temperature causing the LFR defocusing cycling between OM4 and OM-1. 2 °C in the hysteresis set point allows the plant to connect the LFR

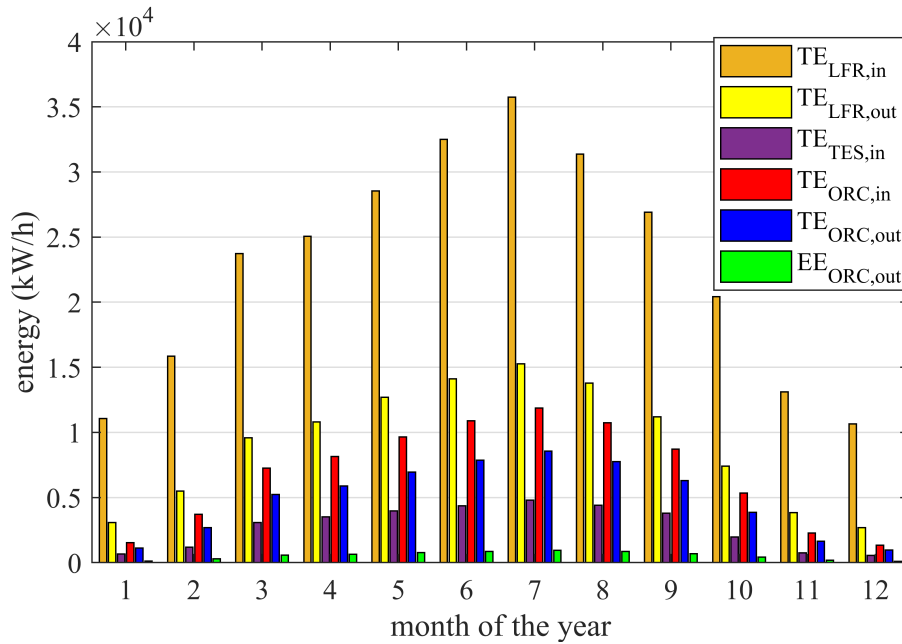
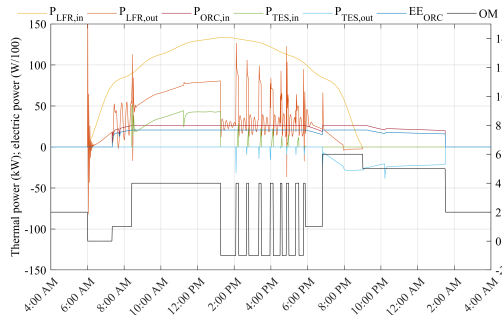


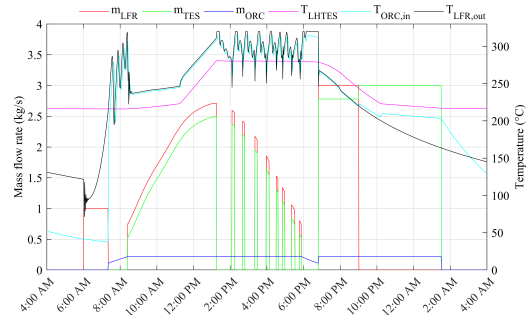
Figure 7.3

with the ORC (OM4) when it discharges because of the thermal losses, but as soon as it reaches again 280 °C the TES is immediately disconnected realizing again the defocusing configuration (OM-1). Another aspect concerns the very long discharging time of the TES (OM5), it releases not only the latent heat, but also the sensible one between its maximum temperature and the beginning of the solidification point. Because the solar plant is almost all the time at high temperature, it does not need of LFR recirculation (OM0), this operation mode is somewhat limited in summer. Despite the defocusing, fig. 7.4a shows also the maximum thermal power produced by the LFR equal to about 80 kWth, while the TES works nearby its maximum charging power of 40 - 50 kWth. As regard the power fluctuations mentioned before, these phenomena occurs especially during the OMs changing due to the connection and/or disconnection of different portion of the pipelines at dissimilar temperature levels, moreover this behavior is empathized at low flow rates, namely when the longitudinal thermal gradients become significant.

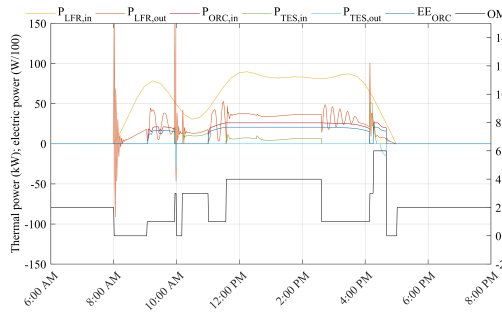
In fig. 7.4c the solar radiation in spring is variable during the day and it is not so high, with a maximum input power lower than 90 kW. This leads to a different schedule of the operation modes: first the LFR recirculates to warm up the pipeline network, then, the solar radiation increases enough to run the ORC (OM1), but a subsequent decrease in solar radiation does not have enough power to maintain the OM1, as a consequence only the TES can be supplied (OM3). As soon as the radiation increases significantly, both the TES and the ORC are supplied (OM4), finally it decreases again and only the ORC is supplied (OM1). Actually, the mid season day entails the TES discharging in the ORC (OM5) due to its temperature level, but it is supported by the LFR immediately after (OM6) because the state of charge is not sufficient.



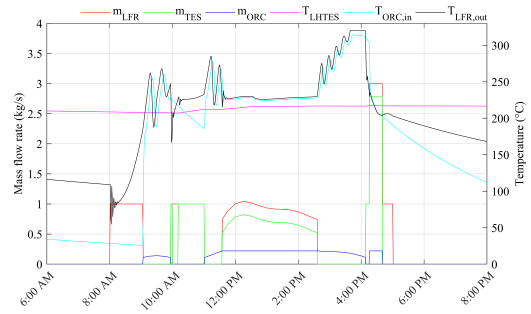
(a) Daily trends of the power in summer (11 June)



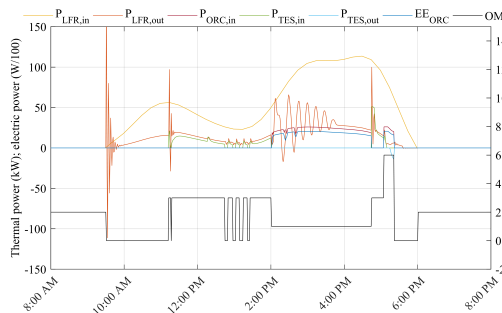
(b) Daily trends of the temperatures and flow rates in summer (11 June)



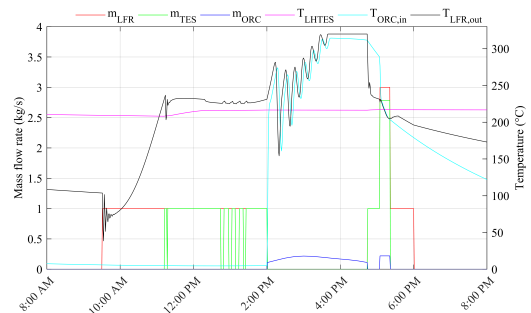
(c) Daily trends of the power in mid season (11 October)



(d) Daily trends of the temperatures and low rates in mid season (11 October)



(e) Daily trends of the power in winter (30 January)



(f) Daily trends of the temperatures and flow rates in winter (30 January)

**Figure 7.4.** The graphs represent also the operating mode (OM) of the plant, as specified in table 7.1.

During the considered winter day in fig. 7.4e, the energy stored in the TES is almost all the time low, as matter of fact the LFR is often forced to recharge it (OM3), but this action allows the TES temperature to be adequate to supply the ORC just the last part of the day.

Finally, figs. 7.4b, 7.4d and 7.4f report the daily trends of temperatures at the outlet of the LFR solar field, at the inlet of the ORC unit, i.e. the inlet oil temperature at the evaporator, and the average temperature of the PCM storage tank. Moreover, to facilitate the reader in recognizing the current subsystem supplied in the specified timespan, the respective flow rates are added in the graph.

Results show that in winter (fig. 7.4f) the collected thermal power allows to supply the ORC unit and to start the melting of the PCM material, however the upper bound of 217 °C to activate the OM5 phase is not reached at the beginning, as previously discussed. However, the intense solar radiation during the day end, enables the ORC to run just in OM6, after a little time in recharging the TES.

In autumn (fig. 7.4d) the trend is similar to the winter day, except for the OM4 established at noon, indeed the TES connection implies the maximum temperature at the LFR outlet and ORC inlet to be lower.

Finally, on the summer day (fig. 7.4b) it can be noticed a gradual increment in HTF flow rate as the solar radiation rises, indeed the pump is set to proportionally adjust the HTF flow rate to avoid overheating of some components. Despite this control, from figs. 7.4d and 7.4f the LFR defocuses, it is due to the excess of thermal power available that neither the TES or ORC can entirely accept.

Figures 7.4b, 7.4d and 7.4f highlight also the thermal inertia of the system. At the plant start up in the morning, the LFR outlet temperature rises at different slopes based on the current solar energy available. Consequently, the control strategy takes some time before the ORC inlet temperature increases as well. The same effect can be observed also in late afternoon or sunset. The residence time of the oil in the pipes and its thermal inertia are responsible for the heat losses discussed previously and reported in table 7.2.

The proposed model allows for a detailed energy analysis, thus evaluating any potential improvement in plant design and operation. Indeed, the low computational cost of the implemented code (of about 4 hours for a yearly simulation) enables the user to address either optimization strategies or parametric studies, thus supporting the system control designer to set for example the proportional-integral gains of all the devices. The reliability of the plant prototype is a crucial point, an extensive experimental tests campaign is needed to validate the developed models and its features. For example, the oscillations in the outlet power seen before may lead the controller to false alarms, because it reads high temperature values in some points, which instead are distributed in some little portions of the pipeline loop due to the temporarily non-steady state conditions of the plant.

## Conclusions

In this study, the overall performance of a micro solar CHP made up of a concentrated linear Fresnel reflectors solar field, a 2 kWe ORC unit coupled with a phase change material storage tank equipped with heat pipes has been investigated by means of a simulation analysis in Simulink. Ad hoc subroutines for the different subsystems

have been developed in order to better include the peculiarities of each system with respect to its actual design. The simulation analysis carried out has also provided useful information for the forthcoming assembly and testing of the future prototype plant. Indeed, according to the varying ambient conditions, the influence of the different operation modes of the micro CHP have been evaluated in terms of overall plant efficiency and power production, conversion efficiency of its main components, operating hours and working temperatures.

Main findings are summarized below:

- As expected, the overall conversion efficiency and the corresponding related power generation are considerably affected by ambient conditions and incident DNI. Therefore, the higher production is achieved in summer with a peak overall conversion efficiency of about 27.4 %. The electric efficiency of the organic Rankine cycle unit is almost constant throughout the year with a monthly average value higher than 7.8 %. However, more than 73 % of the annual operating hours of the ORC unit occur in the hot season in the period April-September with a peak monthly operation of more than 483 h in July. The annual operating hours of the ORC unit are more than 3374 h with an annual electric and thermal energy production of about 6500 kWh and 58,800 kWh respectively, which represent a considerable amount of energy for households.
- In terms of conversion efficiency and electric power production the system proves that the chosen operation strategy entails a flat ORC operation, thus the parameters remain approximately unaltered throughout the year. However, because of the set-point temperatures of the storage tank, the operating hours of the system are limited to 411 h/year in OM6. Operation modes OM1 (i.e. the solar field supplies directly the organic Rankine cycle unit and the storage tank is by-passed) and OM5 (only the storage supplies the organic Rankine cycle) allow to achieve a bit lower electric conversion efficiency than other OMs because of the limited input thermal power in the organic Rankine cycle unit and of intermittent operation of the system in such conditions.
- The integrated system has also shown a considerable amount of heat losses, which could be sensibly reduced by varying the storage operating temperature set-points or the control strategy of the plant. In winter, indeed, when the collected solar thermal power is not enough to melt the phase change material in the tank, the stored thermal power is then progressively lost to the ambient. This is a critical issue, because it is necessary to find the right trade-off between reducing thermal losses and increasing electric efficiency of the organic Rankine cycle when it is supplied directly from the storage. A solution could be to provide the low temperature heat not used directly to the final user for heating purposes, thus the heat losses of the system could be reduced and the energy storage efficiency not jeopardized.

Concluding, this work has given some insights into the influence of the design specifications and of the control strategy on the system performance. Therefore, the analysis could serve in the future as a general guide to understand the mutual interactions of the different subsystems in similar small-scale concentrated solar organic

Rankine cycle plants and, consequently, to choose the best operating conditions to improve the achievable production and overall efficiency.

### 7.1.2 Effect of the pipelines modeling

In this subsection four different detailed models of pipelines are proposed and compared to assess the thermal losses in small-scale concentrated solar combined heat and power plants. Indeed, previous numerical analyses revealed the high impact of pipelines on the performance of these plants because of their thermal inertia. Hence, in this work the proposed models are firstly compared to each other for varying temperature increase and mass flow rate. Such comparison shows that the one-dimensional (1 D) longitudinal model is in good agreement with the results of the more detailed two-dimensional (2 D) model at any temperature gradient for heat transfer fluid velocities higher than 0.1 m/s whilst the lumped model agrees only at velocities higher than 1 m/s. Then, the 1 D longitudinal model is implemented in a quasi-steady-state Simulink model of an innovative micro scale concentrated solar combined heat and power plant and its performances evaluated. Compared to the results obtained using the *Simscape* library model of the tube, the performances of the plant show appreciable discrepancies during the winter season. Indeed, whenever the longitudinal thermal gradient of the fluid inside the pipeline is high (as at part-load conditions in winter season), the lumped model becomes inaccurate with more than 20 % of deviation of the thermal losses and 30 % of the organic Rankine cycle electric energy output with respect to the 1 D longitudinal model. Therefore, the analysis proves that a hybrid model able to switch from a 1 D longitudinal model to a zero-dimensional (0 D) model with delay based on the fluid flow rate is recommended to obtain results accurate enough whilst limiting the computational efforts.

### Introduction

As stated in the past section, in particular referring to table 7.2, the numerical simulations reveal a large amount of thermal loss in the pipelines connecting the different subsystems. More precisely, the thermal inertia of the pipelines, the multiple-supply temperature levels of the transfer medium and the variability of the local renewable energy source entailed significant fluctuations of the plant operation also, according to [188]. Indeed, any shutdown and restart of the system as well as variations in the oil flow rate affect the ability of the solar field to generate thermal power or that of the TES to rise in temperature because of the thermal gradient along the pipe itself. Despite the significant influence of the pipeline behavior on the performance of small-scale solar CHP plants, none of the works on solar ORC reported in the literature have made use of advanced models to take into account the pipelines contribution. For this reason, in the present work different models of pipelines connected to the subsystems are investigated and their influence on the plant performance is assessed. Therefore, the main novelties of the work rely on: (i) the comparison of different numerical models to predict the thermal transient behavior of pipelines in small-scale concentrated solar ORC, based on the expected regime of operation; (ii) the evaluation of the performance of such CHP systems

when the pipeline behavior is taken into account and (iii) the impact of the different numerical models on the annual performance of the system. In Section 6.4 the three mathematical models implemented in Simulink are discussed in detail, while the Simscape model is introduced directly in this section. Therefore, the aforementioned analysis are carried out taking the Innova Microsolar plant as test case.

## Results

In order to better appreciate the influence of the different models of pipelines on the energy performance of small-scale concentrated solar plants, the case of the Innova Microsolar plant [21] has been considered. In particular, the system specifications are extensively discussed in [125] and section 4.1. The characteristics of the tubes (length, internal diameter and insulating material) are the same as in the Innova Microsolar, thus making possible in the future the comparison of the numerical simulations with the experimental data once the plant is in full operation.

Initially, a yearly dynamic simulation of the plant has been performed, aimed at assessing the most common HTF regimes in terms of temperature derivatives and flow velocities inside the pipelines during plant operation. The simulation is conducted for Lleida, Spain, where the plant is currently being built and the 1 D longitudinal model adopted to take into account the behavior of the pipelines and overcome the dumping effects derived from the 0 D model. More precisely, 20 thermal nodes are considered for each pipeline since they allow for a more reliable temperature derivative. Indeed, in a previous work, Vivian et al. [181] compared the same numerical methods here investigated with the experimental results of a buried, previously insulated pipe 470 m long, with an internal diameter of 312.7 mm, under a relative low flow rate of about 2.65 kg/s. They found that for explicit schemes there is an optimal Courant number  $< 1$  (this number indicates how fast the temperature information travels on the computational grid) beyond which the numerical scheme does not agree with experimental results. Furthermore, in their specific case study they obtained the best approximation of the temperature profile along the pipeline with the experimental data for a number of thermal nodes in the range 10–20.

As regards the global time step, it is fixed at 10 s, which allows to prevent any temperature leveling due to the thermal inertia of the pipelines. All the tubes have an internal diameter of 6 cm and a thickness of the insulating material of 3 cm. In order to limit the redundancy of the results, the fluid regimes are shown with reference to the following sections: (i) the outlet of the solar field (pipe 12 m long) and (ii) the outlet of the organic Rankine cycle system (pipe 5 m long). For both tubes the time derivative of the outlet temperature and the oil flow rate are calculated. Figures 7.5a and 7.5b report for both the sections previously mentioned the HTF regimes, in percent of the total time.

According to the contour plots depicted in figs. 7.5a and 7.5b, most of the operation occurs in a circumscribed region with  $rr < 1$  K/s and  $0.1$  m/s  $< u < 0.1$  m/s or  $u > 1$  m/s, depending on the considered section. Later on, the performance of the four models considered in this study are assessed and compared. The fluid is supposed to increase its temperature from 300 K up to 600 K inside a pipeline 10 m long. A sensitivity analysis is carried out by varying the slope of the temperature

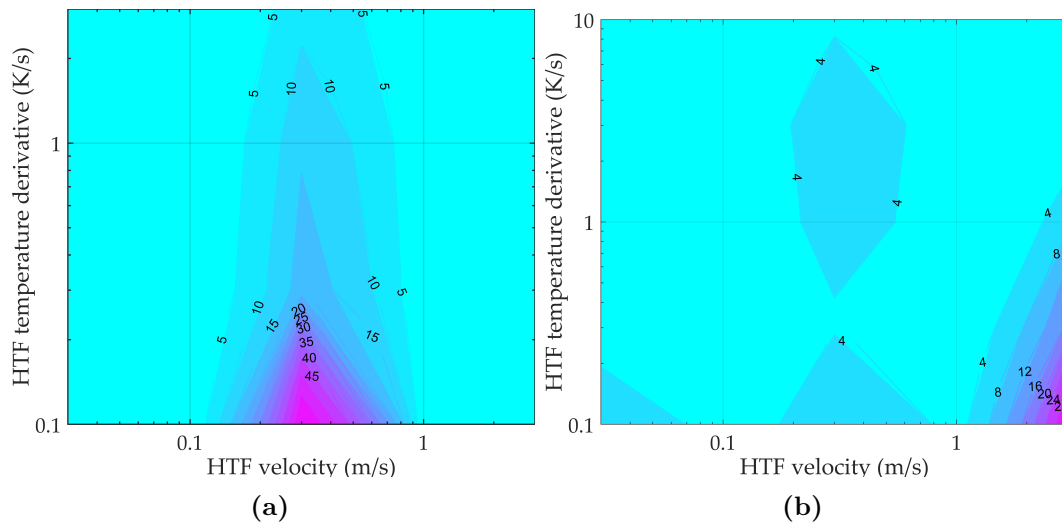


**Figure 7.5.** Fluid regime at ORC outlet (a) and at LFR outlet (b), in percent of total time for yearly simulation.

increase and the HTF velocity. Figure 7.6 shows an example of the response time of the four models under investigation with a  $rr = 1$  K/s and 0.5 m/s.

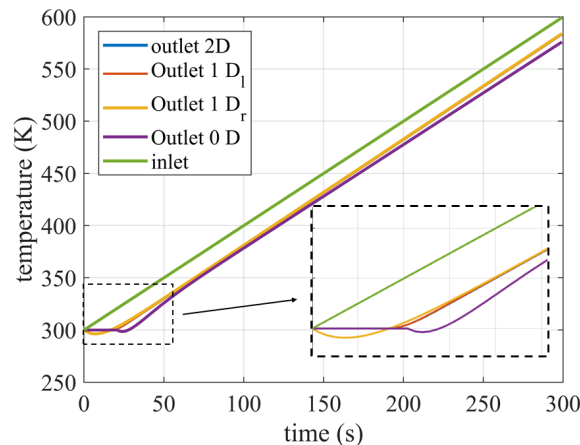


**Figure 7.6.** Response time test of the four models with  $rr = 1$  K/s and HTF velocity = 0.5 m/s.

It is worth noticing that the linear approximation of the temperature profile along the pipe length leads to a nonphysical decrement of the outlet temperature during the initial transitory for the 0 D and the 1 D radial model. In particular, this is more relevant with low flow rate and strong increase of the inlet temperature, or rather when the temperature gradient along the axial direction is high. On the basis of the results attained by the 2 D model, the deviations of the other models are evaluated as reported in figure 7.7. The good accuracy of the 1 D longitudinal model with the results of the 2 D model for HTF velocities than 0.1 m/s is evident at any temperature gradient as shown in figure 7.7a.

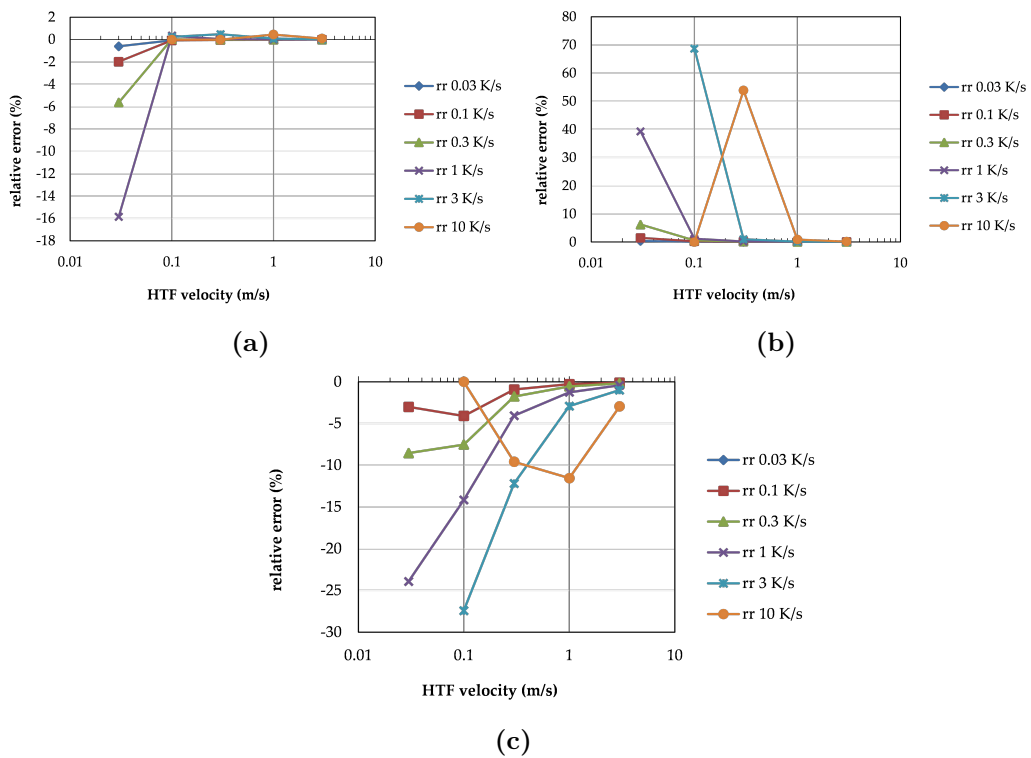


**Figure 7.7.** Relative error in the: 1 D longitudinal model (a), 1 D radial model(b) and 0 D model (c)

On the contrary, it cannot be stated the same for the 1 D radial model. In fact, for HTF velocities in the range 0.1-1 m/s significant deviations occur on the predicted output temperature when  $rr > 3$ , as reported in figure 7.7b. Hence, the assumption of a linear temperature distribution along the tube length causes a consistent error in the evaluation of the temperature profile. Eventually, the lumped model exhibits good accuracy only when the axial gradient is low, that is when the temperature increase is smooth and/or the fluid has a high velocity, as shown in figure 7.7c. Therefore, with reference to the operation of the Innova MicroSolar plant (see fig. 7.5)), characterized by  $rr < 1$  K/s and  $u > 0.1$  m/s for most of the time, only the lumped model does not agree with the results of the most detailed 2 D model, with the exception of HTF velocities  $> 1$  m/s. The 1 D radial model, instead, can lead to unrealistic values in the case of high temperature derivatives (rapid changes of DNI) at  $0.1 \text{ m/s} < u < 1 \text{ m/s}$ . Moreover, the latter one has no advantage in terms of CPU time with respect to the more accurate 1 D longitudinal model, as shown in fig. 7.8.

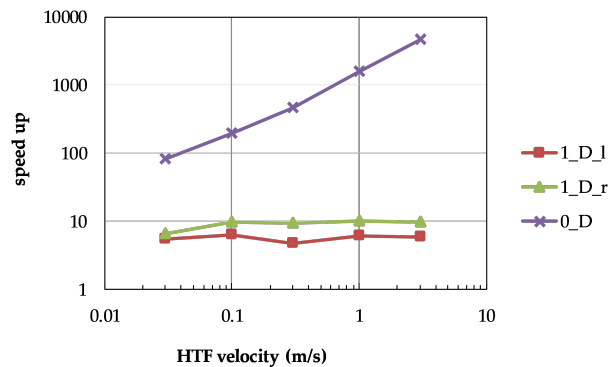


**Figure 7.8.** Speed-up Vs. 2 D model.

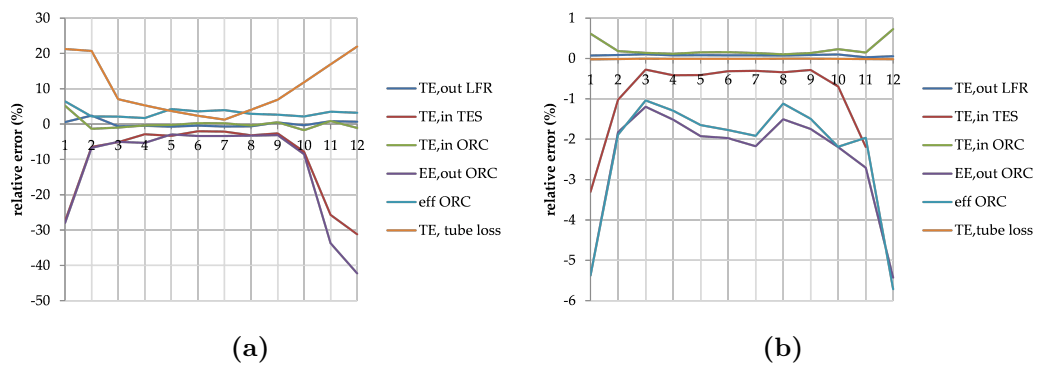
In light of this, the most suitable model for dynamic simulations of the pipelines in small-scale mid-temperature solar CHP plants is the 1 D longitudinal model. Therefore, in order to estimate the influence of the transient behavior of the pipelines on the dynamic simulation of small-scale concentrated solar CHP plants, this model is implemented for the case of the integrated Innova MicroSolar plant in the Simulink platform. Hence, the energy performances of the plant obtained by implementing the 1 D longitudinal model of the pipelines are compared with those considering the tube model of the Simscape library [28]. Compared to the Simscape library model of the tube, the proposed 1 D longitudinal model is able to adjust its internal time step based on the *Courant–Friedrich* condition calculated at the inlet of the tube and fixed at 0.8. However, in the case of high HTF flow rates such as at the nominal operating conditions of the linear Fresnel reflectors solar field (about 3 kg/s), the 1 D longitudinal model entails undesired computational efforts due to the significant decrease of the internal time step. Moreover, in the case of the 1 D longitudinal model, the performances of the integrated plant are evaluated both for one node and 20 nodes, thus assessing their impact on the annual energy results, as reported in table 7.4.

Since the Simscape library model of the tube is a simplified lumped model, some

**Table 7.4.** Annual energy results.

Parameter	Simscape	Simulink 1N	Simulink 20N
TE <sub>,out</sub> LFR (kJ)	$3.86 \cdot 10^8$	$3.87 \cdot 10^8$	$3.87 \cdot 10^8$
TE <sub>,loss</sub> LFR (kJ)	$7.96 \cdot 10^7$	$7.71 \cdot 10^7$	$7.73 \cdot 10^7$
TE <sub>,in</sub> TES (kJ)	$9.61 \cdot 10^7$	$1.00 \cdot 10^8$	$1.01 \cdot 10^8$
TE <sub>,in</sub> ORC (kJ)	$2.99 \cdot 10^8$	$2.99 \cdot 10^8$	$2.98 \cdot 10^8$
TE tube loss (kJ)	$6.58 \cdot 10^7$	$6.06 \cdot 10^7$	$6.11 \cdot 10^7$
EE <sub>,out</sub> ORC (kJ)	$1.78 \cdot 10^7$	$1.90 \cdot 10^7$	$1.93 \cdot 10^7$
Eff ORC (%)	6.65	6.44	6.58
Time on (s)	$1.09 \cdot 10^7$	$1.19 \cdot 10^7$	$1.19 \cdot 10^7$
CPU time (s)	$2.30 \cdot 10^4$	$3.01 \cdot 10^4$	$7.95 \cdot 10^4$

relevant discrepancies of the performances occur compared with those obtained using the 1 D Simulink model. In particular, in the case of the Simscape model the pipeline losses are 7.91 % higher, thus leading to a lower electric energy production of about 6.3 % ( $1.78 \times 10^7$  kJ compared to  $1.93 \times 10^7$  kJ of the Simulink 1N). This is mostly due to the lower running time of the plant (9.42 % lower). On the other hand, the ORC unit works most of the time at operating conditions having higher electrical efficiencies and as a result the mean electric efficiency is 3 % higher (6.65 % compared to 6.44 % of the Simulink 1N). The CPU time in Table 7.4 is measured on a workstation equipped with 32 GB of RAM and the *Intel Xeon E5530 @ 2.4 Ghz* processor whilst the code is able to use a single thread only. As regards the thermal discretization of the pipeline in the 1 D longitudinal model, it does not exhibit significant variation in the aggregated energy values. Indeed, all the annual results are within 1 % of deviation. However, the same cannot be said for the monthly average energies where significant relative differences occur, as depicted in figure 7.9b.

**Figure 7.9.** Simscape/Simulink 1 N monthly averaged energy variations (a); Simulink 1N/20N monthly averaged variations (b).

Indeed, during the winter period all the subsystems work at off-design conditions; the LFR solar field usually operates at low flow rates and in the case of high DNI, the longitudinal thermal gradient along the pipelines increases. This can be easily

appreciated in figure 7.10 which reports the HTF regime at ORC outlet (figure 7.10a) and LFR outlet (figure 7.10) for the winter month of December. Compared to the contour plots of fig. 7.5 that refer to the annual simulation, it can be noticed the lower fluid flow rates especially at the LFR outlet which affect the performance of the whole plant. In the case of low DNI, the oil from the LFR solar field often bypasses the TES and goes directly to the ORC unit, thus making the fluid regime at the ORC outlet and LFR outlet more similar (see figure 7.10).

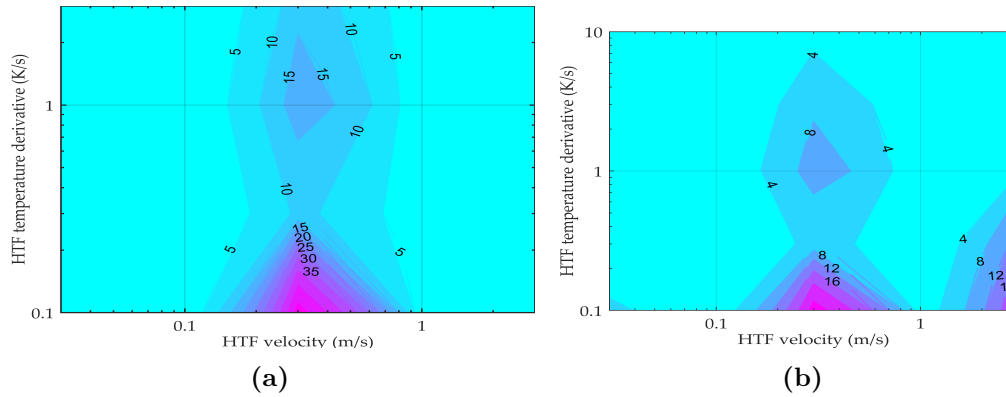
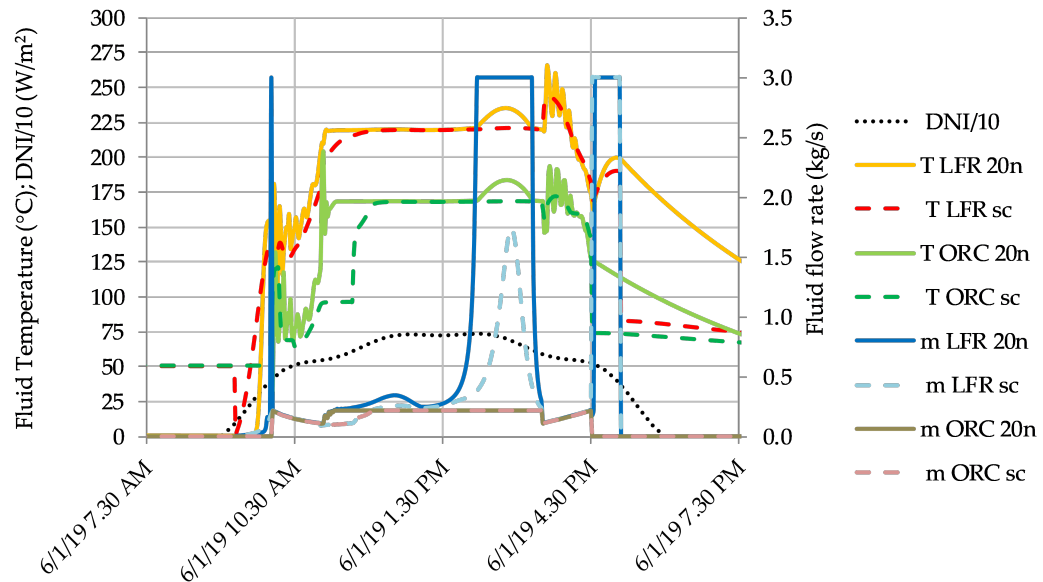


**Figure 7.10.** HTF regime at ORC outlet (a) and at LFR outlet (b) in percent of total time (December).

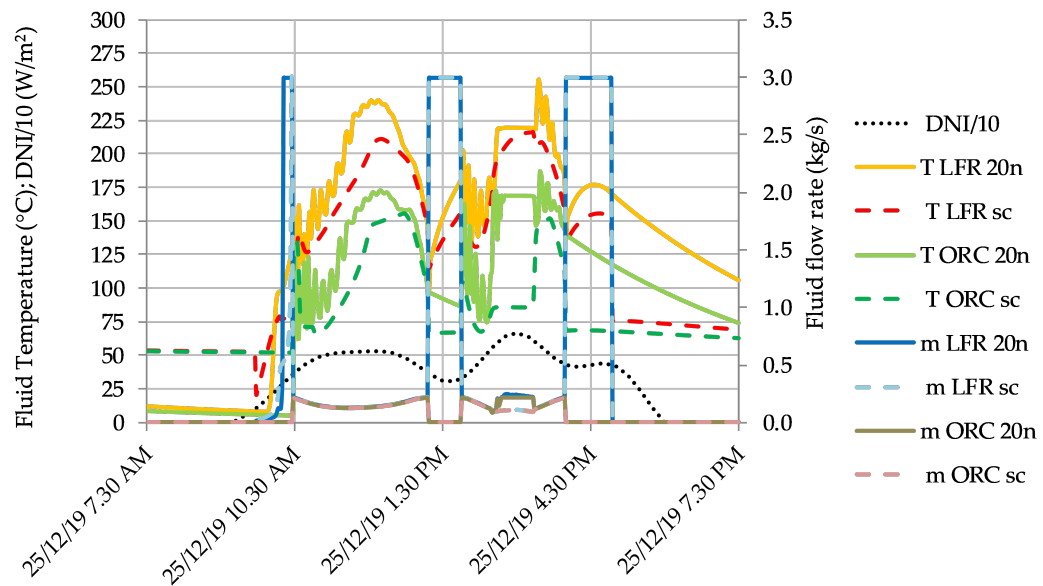
Eventually, the discrepancies of the plant performances between the 1 D longitudinal model with 20 thermal nodes and the simplified Simscape model are shown for typical days of operation in winter time. In particular, figure 7.11a shows the temperature and flow-rate profiles for a typical day in January while figure 7.11b shows December. In this case, the low solar radiation together with the very low oil flow rates cause higher longitudinal thermal gradients along the pipelines and as a consequence the discrepancies between the two models are more evident. According to the plant operation modes the high-mass flow rates (about 3 kg/s) occur when the TES is in operation (charging or discharging) depending on the solar radiation. For further details on the plant operation modes, interested readers are invited to see paper [79].

## Discussions

In general, the analysis confirms that the operation of a solar ORC system (in terms of operating hours and electric energy output) is significantly affected by the pipelines representation model. The developed thermodynamic model of the ORC unit limits the operation of the system at inlet thermal power below 25 kWth and fixes a minimum inlet temperature of about 130 °C. This means a continuous regulation of the input parameters to agree with the fixed constraints, especially at low flow rates. As a result, the higher spatial resolution of the thermal profile provided by the most accurate pipeline model determines greater fluctuations of the temperatures, as shown in figure 7.11. Moreover, the damping effects on the inlet parameters of the ORC subsystem typical of the lumped model disappear. Another implication in adopting an elevated number of thermal nodes is the consequent sharpness of the



(a)



(b)

Figure 7.11. Temperature and flow rate at the outlet of the LFR and ORC.

temperature fronts, as depicted in figure 7.11a. On the contrary, the presence of the crossing delay time cannot be appreciated here, also because of the high-mass flow rate of the HTF. Considering the monthly averaged energy values (figure 7.9), the solar CHP system works mainly at nominal conditions during the summer time when the energy production occurs for a prolonged time and as a consequence the influence of the thermal gradient can be neglected. On the contrary, in winter season the HTF regime reduces considerably and, despite this, it does not affect the thermal losses, as shown in Figure 7.9a; the sharpened fronts of the temperature profile have significant influence on the performance of the different subsystems, especially when their operation at off-design conditions is poor. For instance, the ORC system regulates often according to the changing inlet power and temperature and as a consequence it is subject to higher thermal gradients which result in reduced electric energy production. On the other hand, with the Simscape model of the tube the thermal losses of the pipelines are overestimated when compared with those of the Simulink 1N model (see figure 7.9b), for two reasons mainly: first, the external convective coefficient of the tube is fixed at  $20 \text{ W/m}^2\text{-K}$ , while in the Simulink models it depends also on the wind velocity (equations 6.59 and 6.64); second, the thermal conduction of the insulating material is fixed in the middle of the operating conditions, equal to  $0.07 \text{ W/m-K}$  (see table 6.13), whilst in the 1 D longitudinal model it depends on the mean temperature between the HTF and the external ambient for each thermal node, thus reflecting the real operating conditions of the tubes. Adding extra thermal nodes does not provide any gain in accuracy if the HTF flow rate is high, since it levels the temperature gradient in the axial direction. This behavior can be easily appreciated in figure 7.7c where the lumped model provides the same results as those of the 2D model for the case of HTF velocities higher than  $1 \text{ m/s}$  and a temperature gradient  $rr < 1 \text{ K/s}$ . In terms of computational efforts, the lumped model exhibits by far the best performance especially at high HTF velocities, as shown in figure 7.8. Indeed, it is basically independent from the mass flow rate, unlike the other models which need to adjust their internal time step. Despite the global computational time of the simulations depending not only on the model of the pipelines but also on those of the different subsystems (LFR, TES, ORC etc.), using the Simulink 20 N model the CPU time is more than twice the computational time of the simulations using the Simscape or the Simulink 1 N model, as shown in table 7.4. In conclusion, an hybrid model able to switch from a 1 D longitudinal model to a 0 D model with delay according to the fluid flow rate is the best compromise to obtain results accurate enough and to reduce the high computational effort due to the small internal time step at high flow rates in the case of 1 D models.

## Conclusions

Dynamic thermal distribution networks, as those in concentrated solar cogeneration and trigeneration plants, need an appropriate modeling of the pipelines network. In this study the comparison of four different mathematical models of the tubes is carried out on the basis of the fluid regime (in terms of temperature derivative at the inlet and flow velocity) typical of the Innova Microsolar plant. Such comparison shows that:

- the 1 D radial model entails significant deviations on the predicted output

temperature for HTF velocities in the range 0.1-1 m/s when  $rr > 3$  K/s;

- the 1 D longitudinal model is in good agreement with the results of the 2 D model at any  $rr$  for HTF velocities higher than 0.1 m/s;
- the lumped model agrees with the results of the 2 D model at HTF velocities  $> 1$  m/s.

Therefore, whenever high-longitudinal thermal gradients occur in the pipelines of complex energy systems, the calculated thermal losses as well as the dynamic response of the whole system can vary considerably based on the mathematical model used. With respect to the performances of the small-scale concentrated solar CHP plant of the Innova Microsolar project, the discrepancies of the predicted performances of the plant between the lumped model of the Simscape library and the 1 D longitudinal model become significant during winter season. In particular, due to the net temperature fronts obtained with the more accurate model of the pipelines, the ORC unit can better exploit the energy input. As a consequence, the annual electrical energy production of the ORC unit is more than 6 %. On the other hand, whenever the longitudinal thermal gradient inside the pipeline is negligible, a lumped model for dynamic simulations is accurate enough, thus significantly reducing the computational time without losing accuracy. Therefore, the analysis carried out has allowed assessment of the soundness of the different models of the tubes for small-scale concentrated solar ORC systems, and to conclude that an hybrid model able to switch from a 1 D longitudinal model to a 0 D model, with delay based on the fluid flow rate, is the best compromise to obtain results accurate enough whilst limiting the computational efforts.

### 7.1.3 Effect of the storage partialisation

Latent heat thermal energy storage (LHTES) systems allow to effectively store and release the collected thermal energy from solar thermodynamic plants; however, room for improvements exists to increase their efficiency when in operation. For this reason, in this work a smart management strategy of an innovative LHTES in a micro-scale concentrated solar combined heat and power plant is proposed and numerically investigated. The novel thermal storage system, as designed and built by the partners within the EU funded Innova MicroSolar project, is subdivided into six modules and consists of 3.8 tons of nitrate solar salt  $\text{KNO}_3/\text{NaNO}_3$  whose melting temperature is in the range 216 - 223 °C. In this study the partitioning of the storage system on the performance of the integrated plant is evaluated by applying a smart energy management strategy based on fuzzy logic approach. Compared to the single TES configuration, the proposed strategy allows reducing the storage thermal losses and improving the plant overall efficiency especially in periods with limited solar irradiance. The yearly dynamic simulations carried out show that the electricity produced by the combined heat and power plant is increased by about 5 %, while the defocus thermal losses in the solar plant are reduced by 30 %.

## Introduction

to improve the performance of the system over a more extended period an appropriate control logics are required. An interesting approach is represented by the TES conceptualization in several temperature levels, each one suitable for the respective section of the plant where it is installed. For example, Sebastian et al. [165] developed an innovative management strategy of a thermal storage system with molten salts for a solar plant with LFR conceived to reduce the part-load inefficiency due to the reorientation of the LFR solar field from NS to EW. The authors propose to divide the storage in three parts, each one working at a different temperature level, thus providing a wide range of possible operation strategies by combining them in series. In another study M. Horst et. al [133] reported experimental and numerical results from the investigation of cascade latent heat storages with alkali nitrate salts (i.e.  $\text{NaNO}_3$ ,  $\text{KNO}_3$ ) designed for a temperature range from 250 °C to 500 °C. Managing LHTES efficiently is a crucial point in optimizing the operation of solar energy based ORC systems. Indeed, an increase of the working fluid inlet temperature to the expander of the ORC unit entails higher electric conversion efficiency, but at the same time, it leads to higher thermal losses from the storage envelope to the ambient. Moreover, in case of LHTES, the collected thermal energy is more efficiently recovered in the melting temperature range of the phase change material and thus it is convenient limiting its proper operation in this interval. Before this study, the numerical investigation undertaken on the performance of a micro-solar CHP plant for residential applications with a LHTES in different seasons [80] revealed some weak points in the operation of the system, especially when working at low temperature levels because the low enthalpy energy stored was systematically lost. Considering this issue, it has been conceived a novel way to increase the storage efficiency of such LHTES by means of its subdivision in modules to be properly managed. Among all the possible control approaches, a fuzzy logic controller has been considered very suitable for the highlighted needs. Fuzzy logic control has been widely used in several applications, showing good results. For example it has been adopted for batteries in hybrid vehicles [126], for systems that store simultaneously sensible heat from solar and electric energy [117], for reducing the operating cost of microgrids by regulating the power output of energy storage [92], for prioritization of energy storage technologies [158] and in renewable energy systems in general [170]. The smart fuzzy logic control could potentially increase the overall annual performance of a micro-solar CHP plant, because it acts predominantly in reducing thermal losses. In particular a cascade fuzzy logic controller, which manages the thermal storage connections, has been considered for the micro solar plant already modeled. Some studies in literature already addressed the influence of TES subdivision [165, 125], as described above, but none of them referred to subdivided LHTES (sub-LHTES) operated with fuzzy logic control. Therefore, in this study this logic is applied to investigate the effects of the storage subdivision and its smart management on the performance of the overall plant. Hence, the main novelties of the work rely on: (i) the development of a fuzzy logic approach to sub-LHTES systems; (ii) the assessment of the influence of the smart management of the sub-LHTES on the performance of the small-scale integrated plant and its comparison with the system in its standard configuration.

### The fuzzy logic controller of the TES partialisation

The fuzzy logic controller has been implemented based on the following assumptions. First of all, to ensure an effective charging of the thermal storage, the LFR plant must supply oil at a temperature higher than the storage temperature to cover the thermal loss in the piping system (10 °C is the temperature difference assumed). Due to the different temperature of each module, the LFR checks the maximum temperature of the current connected sub-LHTES module and supplies all the connected modules with a temperature higher than that. Secondly, during the discharging phase, corresponding to OM5 and OM6 (tab. 7.8), the connected sub-LHTES must have a temperature suitable for the ORC supply, thereby the control system of the storage allows the connection only of the modules with a temperature higher than the temperature of the ORC inlet oil. Third, the oil flow rate is split equally among the sub-LHTES both in charging and discharging phase. The fuzzy logic controller has been designed according to a cascade approach to accomplish the following tasks: (i) select the number of modules to be connected with the plant; and (ii) manage each module based on a priority scale set out by the previous decision. In general, the performance of the plant can benefit from the subdivision of the LHTES. For example, when the solar radiation is high and the sub-LHTES is not fully charged, connecting a high number of modules allows mitigating the temperature overheating of the LFR solar field, thus avoiding the inefficient defocusing of some mirrors [165]. On the contrary, when the solar radiation is low it is convenient to connect and charge as less modules as possible so that the temperature of the storage medium is higher. Therefore, a close relationship exists between the outlet temperature of the diathermic oil from the LFR solar field and the number of modules to be connected. For this reason, a logarithmic function, shown in figure 7.12, has been chosen to correlate the diathermic oil outlet temperature from the solar field with the number of modules to be connected. The LFR outlet oil temperature ranges between 210 °C, corresponding to operation mode OM1, and 305 °C, i.e. the maximum allowed temperature before defocusing. The logarithmic function has been preferred since it leads to a low number of modules to be connected at low temperatures, whilst the number increases quickly at high temperatures to prevent the risk of defocusing.

The fuzzy logic decision criteria is based on the above-mentioned logarithmic function, used to define the membership functions (related in this case with the number of modules) as presented in figure 7.13: it provides as output a not integer value correlated with the final number of modules by varying the oil temperature.

Furthermore, in order to consider more accurately the changes in the diathermic oil temperature, a second parameter, i.e. its derivative with time, is included in the fuzzy logic. Therefore, the relative membership function of the controller adds a module if the derivative is positive ( $T_{LFR}$  derivative greater than 0.1 °C/min) or keeps the same number of modules if the derivative is zero, and finally it reduces the number of modules in case it is negative according to fig. 7.14.

Once the number of modules to be connected with the plant is assessed by the first fuzzy logic controller, a second fuzzy logic controller in cascade is applied in order to establish the working priority on the basis of the storage state of charge. The priority of charging has been chosen on the basis of the melting temperature range of the selected PCM, but also on the ORC turn on/off set points (OM5) and on

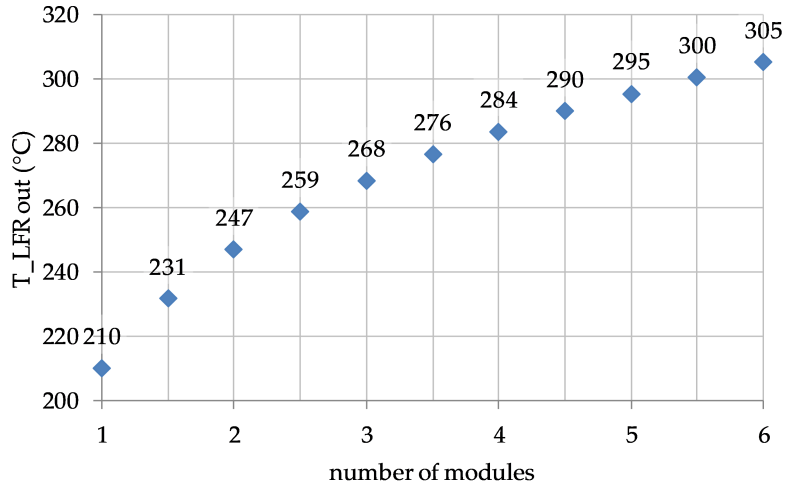


Figure 7.12. Logarithmic correlation between number of modules and LFR output temperature.

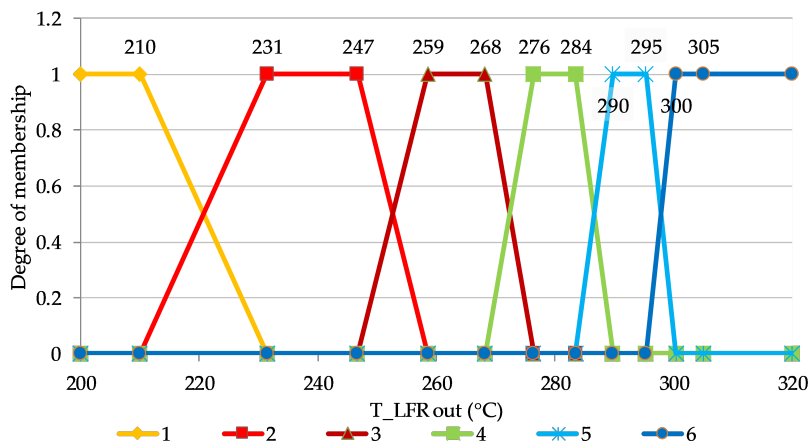
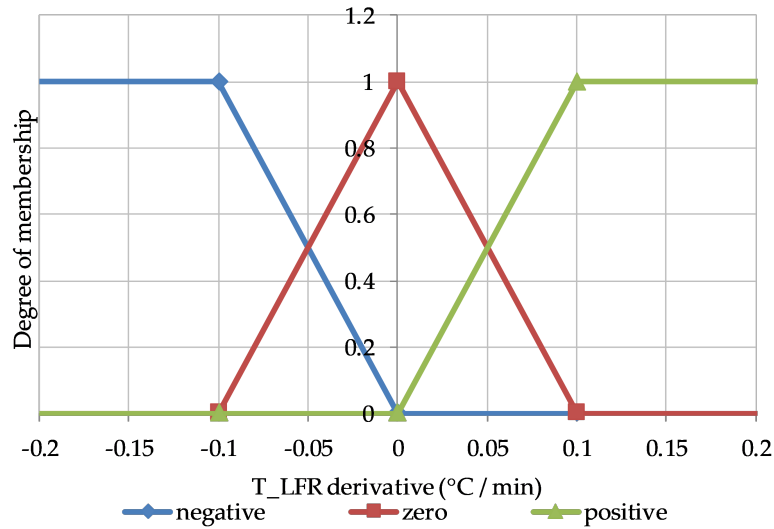


Figure 7.13. Number of working modules by varying the solar field output oil temperature.



**Figure 7.14.** Derivative component of the first fuzzy logic controller.

the heat exchange between heat pipes and modules of the sub-LHTES. The criteria for priority are as follows: (i) charging the thermal storage at low temperature is not convenient, even if the corresponding thermal losses are negligible, and at the same time the high difference in temperature between the PCM and the LFR outlet temperature facilitates the thermal exchange (preventing the defocusing). Indeed, rarely the received energy increases to the point that the sub-LHTES temperature is suitable for the ORC supply, while it is often lost. Thus, a low priority for this occurrence has been chosen. The low priority also occurs when the sub-LHTES is at high temperature, since the thermal losses are high, whilst the ORC unit does not benefit of this increase in temperature (there is a limit of the inlet temperature for preventing its damaging). Moreover, the sub-LHTES is less prone to receive thermal energy at high temperatures, because of the low temperature difference between the PCM and the oil and, therefore, a serious risk of LFR defocusing exists. (ii) the highest priority occurs whenever the sub-LHTES module has a temperature close to the melting temperature range of the PCM. In this case, indeed, the thermal energy input can be exploited to run the ORC unit in OM5 and OM6. (iii) when the sub-LHTES is at mid-high temperature, although the storage is near the melting phase with good thermal exchange properties, thermal losses are significant and the temperature difference between the PCM and the outlet temperature of the diathermic oil from the LFR is quite low, then it is not very convenient to charge the sub-LHTES. Therefore, a mid-priority is assigned to this condition. The membership functions of the second fuzzy logic controller depend on the above criteria and the charging of the sub-LHTES modules occurs with the priority shown in fig.7.15.

Therefore, according to the two fuzzy logic controllers in cascade described above, a matrix of identification of the modules to be connected with the plant and their priority is defined. All the identification codes are managed by an ad-hoc routine, which sorts the six outputs coming from the respective fuzzy logic controllers and

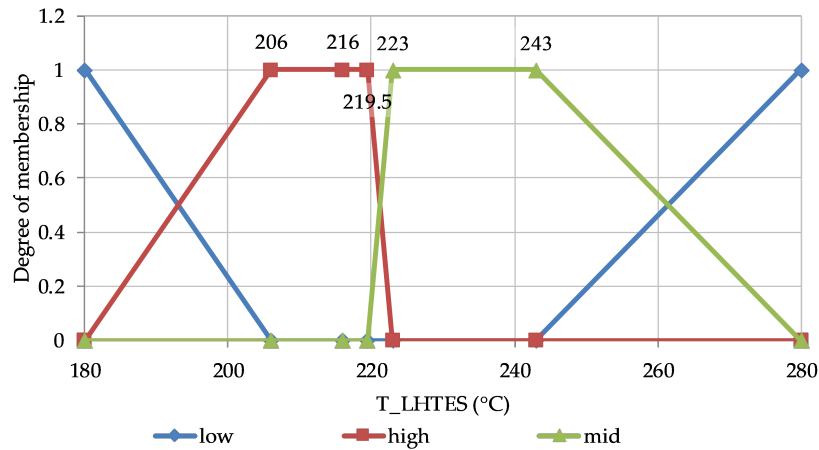


**Figure 7.15.** sub-LHTES charging priorities.

acts on the oil flow rate by directing it into the selected modules of the sub-LHTES.

## Results

In this section the performance of the system when the fuzzy logic controller is applied is investigated. The TES subdivided in modules (sub-LHTES) with the fuzzy logic controller is compared with the standard system where the single TES is operated following only the rules described in 7.8. Firstly, the performance of the two systems are analyzed during typical days of different seasons, i.e. summer, winter and mid-season, then the monthly and yearly behavior is evaluated. The figure 7.16 shows temperature and power trends for a typical summer day. In this case, because of the intense solar radiation when the storage reaches the maximum allowed temperature of 280 °C, the system is forced to defocus and it alternates the operation mode OM1 with OM4 to maintain the storage temperature level. It is evident that the sub-LHTES involves progressively the different modules on the basis of the thermal power coming from the LFR (figs. 7.16c and 7.16d). At the beginning only two modules (modules 2 and 3, chosen on the basis of the priority set by their initial temperature linked to the system dynamic the day ahead) are connected to the LFR and only later the whole storage is activated (figure 7.16c). This causes a longer time for the overall storage to reach the maximum temperature in comparison with the single TES (figure 7.16a), but on the other side a better management of the LFR power is possible. Indeed, the availability of some modules at lower temperature when the solar radiation rises allows reducing the defocus, as demonstrated by the trend of LFR losses in figure 7.16d compared to 7.16b. Nevertheless, the overall ORC performance in summer is similar with the two TES configuration, due to the huge amount of solar energy available that bring both storages in full charged mode.

In figure 7.17 a typical mid-season day is illustrated. In this case, due to the limited solar energy available, the sub-LHTES activates only two modules, which can reach a temperature slightly higher than the single- TES. Thanks to this small

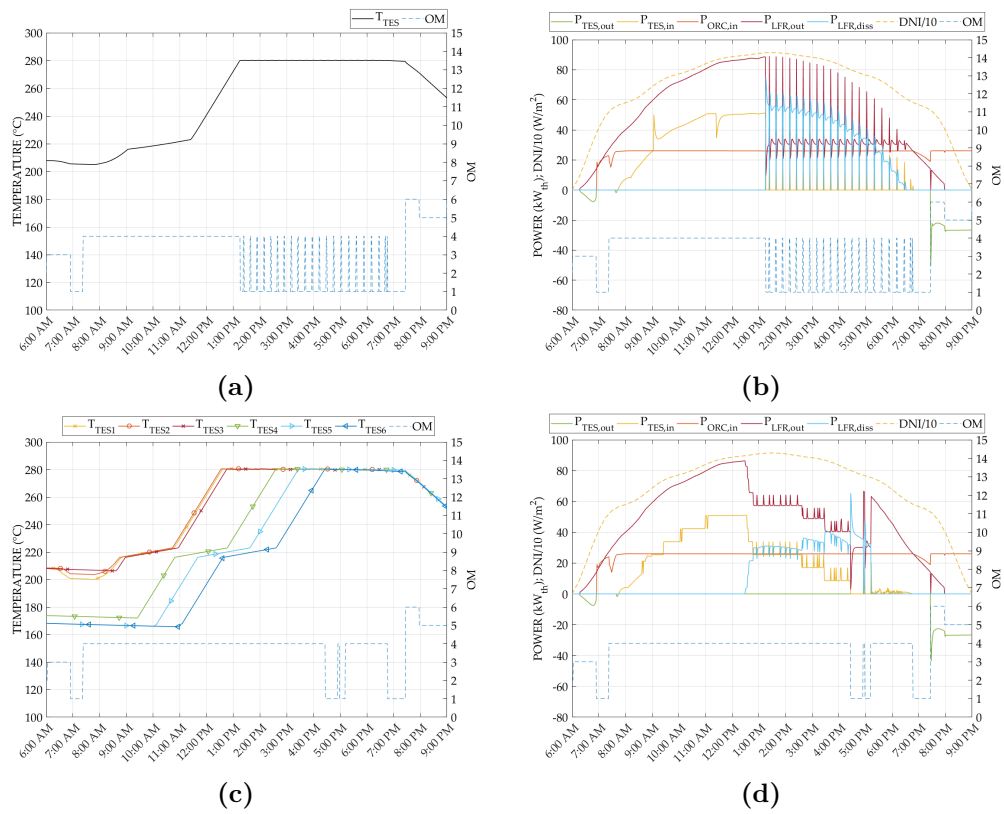


**Figure 7.16.** Daily temperatures (a) and power trends (b) of the LHTES compared with the daily temperature (c) and power trends (d) of the sub-LHTES for a typical summer season day (11 June). The graphs represent also the operating mode (OM) of the plant, as specified in table 7.8.

increase, the heated modules reach the melting stage and the TES can contribute to supply the ORC (the plant works in OM5 and OM6 between 4:30 pm and 6:00 pm). This behavior explains the longer duration of operating mode 5 and 6 in presence of sub-LHTES, as described later in the discussion on yearly results reported in table 7.5.

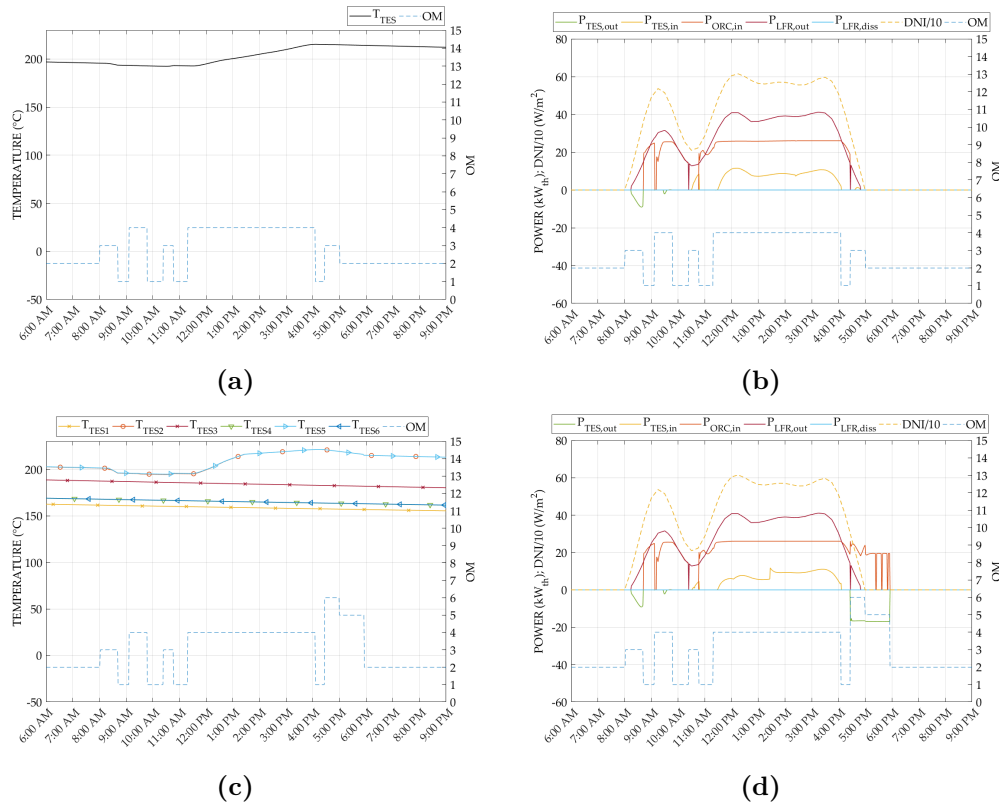


**Figure 7.17.** Daily temperatures (a) and power trends (b) of the LHTES compared with the daily temperature (c) and power trends (d) of the sub-LHTES for a typical mid-season day (11 October). The graphs represent also the operating mode (OM) of the plant, as specified in table 7.8.

Eventually, in figure 7.18 a typical winter day is shown. Even in this case it is possible to see that the sub-LHTES involves in the charging phase only two modules, which can increase significantly their temperature rather than the single TES, while the other modules remain cold ( $< 50$  °C, figure 7.18c). This effect causes the reduction of the heat stored in the thermal storage (see  $P_{TES,in}$  in figs. 7.18b and 7.18d). Nevertheless, the warm modules have a pretty high temperature, almost close to the melting condition. Thus, in case a bit more solar radiation would be available, the graphs demonstrate how easily the sub-LHTES could reach a sufficient temperature level to supply the ORC (switching on OM5 and OM6). This effect influences the better performance of the sub-LHTES in winter in comparison with the single TES, which experiences often too low temperature levels to discharge the stored heat towards the ORC.

On the basis of the priority schedule previously described in figure 7.15, the

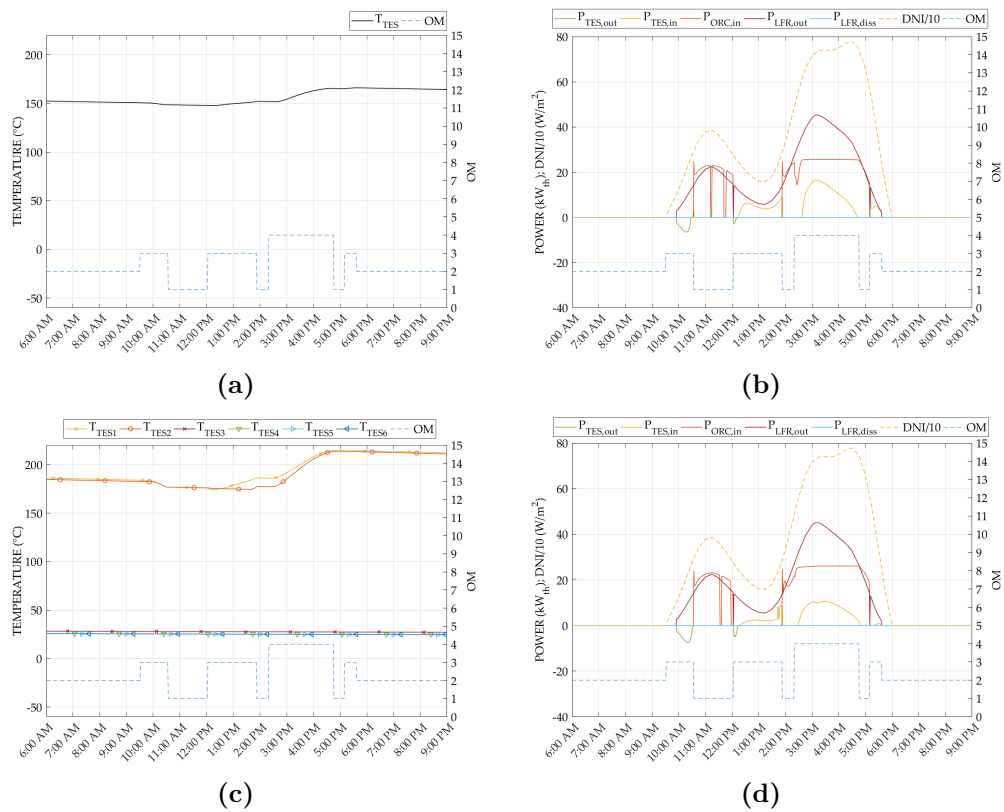


**Figure 7.18.** Daily temperatures (a) and power trends (b) of the LHTES compared with the daily temperature (c) and power trends (d) of the sub-LHTES for a typical winter day (30 January). The graphs represent also the operating mode (OM) of the plant, as specified in table 7.8.

module of the sub-LHTES with the highest priority should work more hours than the second one, the same behavior can be expected by the second module with respect to the third one and so on. Running a yearly dynamic simulation and recording the hours in which there is heat exchange between the  $n$ -th module and the transfer fluid, it is possible to draw the normalized histogram of figure 7.19a: only three modules are used most of the time. It is confirmed by the mean temperature level of the different modules of the sub-LHTES as shown in figure 7.19b. It is also possible to notice that during wintertime only a few modules work with a temperature above the average temperature of the single LHTES, while the others are cold and not involved in the charging phase, as already commented above.

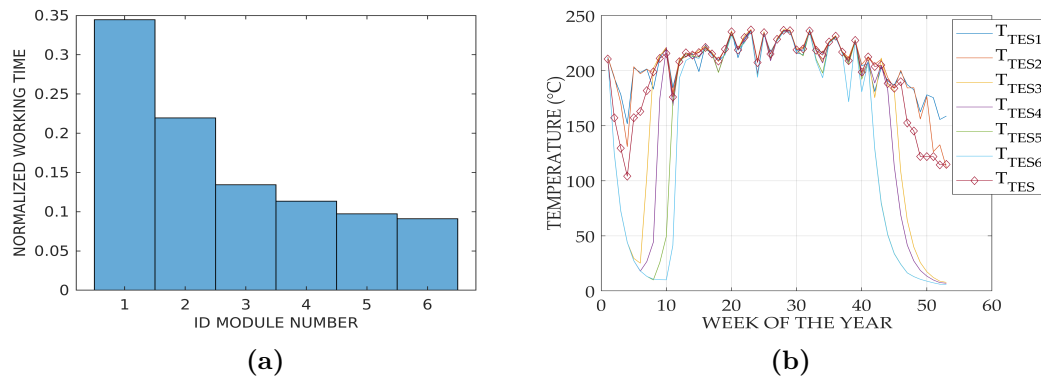


**Figure 7.19.** Normalized working time for each module (a); temperature trends of the six sub-LHTES modules and the single storage over the year (b).

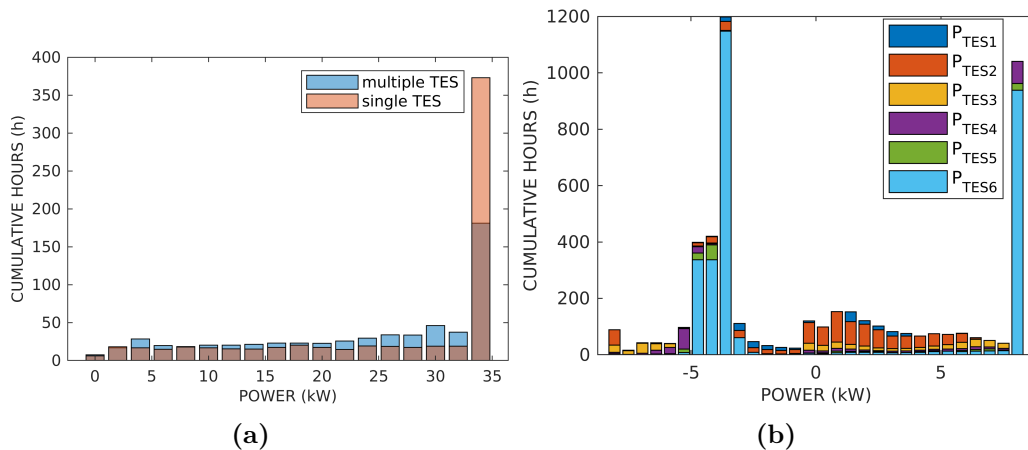
With the purpose of showing the influence of the developed cascade fuzzy logic control on the global performance of the plant, all the parameters of interest have been compared based on a yearly simulation with and without the storage smart management (table 7.5). It is evident that, thanks to a better management of the TES, its average temperature (considering the working modules) is increased in the sub-LHTES. Furthermore, even if less energy enters in the subdivided thermal storage, a higher amount of the stored energy is discharged to the ORC. These two aspects contribute to increase slightly the electric energy produced in the overall year (+4.7 %) and also the ORC electric efficiency (+1.8 %). This result is confirmed by the duration of operation mode OM5 and OM6 (i.e. when the TES discharges to the ORC, see table 7.8.), that are 11 % longer than for the single storage. Considering both the thermal losses due to the TES and to the pipelines, they compensate each other in the sub-LHTES configuration. Indeed the TES thermal losses are decreased due to the fact that less modules are involved in charging/discharging phases in case of limited energy available (thus less mass of the storage medium), while the pipelines thermal losses are bigger because the average oil temperature is higher (with less modules involved the charging phase is slower and the oil temperature tends to increase). Therefore also the wasted energy through pipelines is crucial for the whole plant performance and a good estimation of it, using accurate models, is paramount, as shown in [173].

Furthermore, the subdivision of the storage in modules allows a reduction of the solar plant defocusing (about -30 %): the thermal storage is better managed and

**Table 7.5.** Annual energy balance and performance of the plant with and without the smart fuzzy logic controller.

parameter	Single TES no fuzzy logic	sub-LHTES with fuzzy logic	Variation, % %
$TE_{TES, in}$ , (kJ)	$1.42 \cdot 10^8$	$1.37 \cdot 10^8$	-3.67
$TE_{TES, out}$ , (kJ)	$-1.15 \cdot 10^8$	$-1.14 \cdot 10^8$	-0.38
$TES_{eff}$ , (%)	65.73	73.97	12.53
$TE_{ORC, in}$ (kJ)	$3.38 \cdot 10^8$	$3.52 \cdot 10^8$	4.13
TES loss, (kJ)	$3.13 \cdot 10^7$	$2.72 \cdot 10^7$	-13.25
$t_{ORC, on}$ , (s)	$1.36 \cdot 10^7$	$1.41 \cdot 10^7$	3.74
LFR def, (kJ)	$4.75 \cdot 10^7$	$3.26 \cdot 10^7$	-31.39
$T_{TES, av}$ , ( $^{\circ}C$ )	199.60	210.70	5.56
$T_{ORC, in}$ , ( $^{\circ}C$ )	228.24	235.80	3.32
tube loss, (kJ)	$-5.45 \cdot 10^7$	$-5.97 \cdot 10^7$	9.56
$TE_{ORC, out}$ , (kJ)	$2.45 \cdot 10^8$	$2.55 \cdot 10^8$	4.09
$EE_{ORC, out}$ , (kJ)	$2.63 \cdot 10^7$	$2.75 \cdot 10^7$	4.68
$\eta_{el, ORC}$ , (%)	7.48	7.62	1.80

more volume at lower temperature is available to store the surplus of solar energy. In figure 7.20a it is interesting to notice that the sub-LHTES causes often defocusing at low LFR power generation compared to the single LHTES, because at low solar power less modules are connected to the plant. However, the single TES produces much more defocusing at higher LFR power generation and this causes the higher defocusing during the overall year. This behavior is supported by Figure 11b, where it is evident that modules 4, 5 and 6 work only at high power rate compared with the others (they are colder and work only when the LFR temperature is particularly high, i.e. in case of high temperature difference between the heat transfer fluid and the phase change material).

**Figure 7.20.** Normalized working time for each module (a); temperature trends of the six sub-LHTES modules and the single storage over the year (b).

The analysis based on the yearly averaged values does not clearly show the exact influence of the developed fuzzy control logic on the whole performance of the plant. Therefore, the monthly trends of the main performance parameters for the LHTES are shown in figure 7.21 and table 7.6.

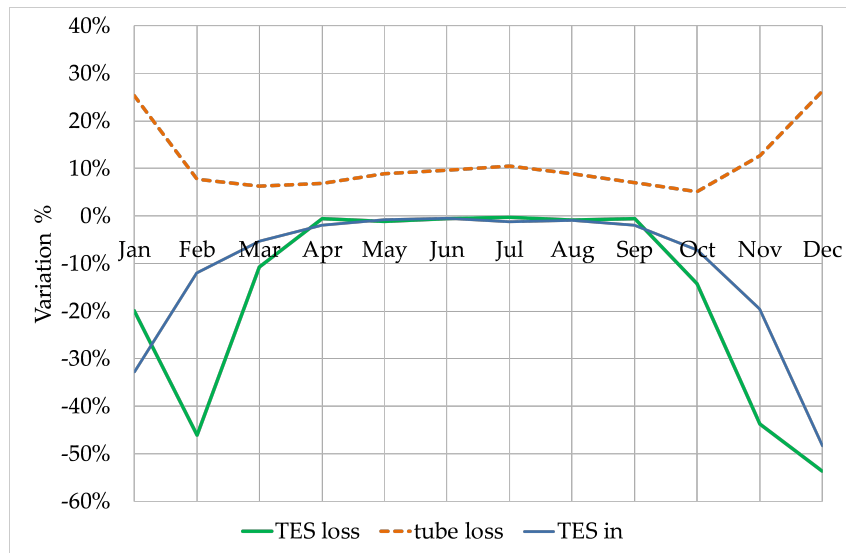


**Figure 7.21.** Relative variation of the TES thermal performance parameters between the configuration with and without fuzzy logic.

Figure 7.21 shows the monthly variation in percentage of the TES performance parameters in case of smart management compared to the standard control without fuzzy logic. During the winter period, the TES subdivision enables the LFR to produce oil at higher temperature, because it stores heat in a smaller amount of PCM. The low solar radiation entails a frequent operation in OM1 and OM3, the latter one occurs with an augmented temperature which in turn rises the pipeline thermal losses, as clearly shown in Figure 7.21. The mid-season is a particular period, in fact the temperature of several modules of the sub-LHTES is still higher than the single module, but the latter one has a stored energy reservoir not exploited (temperature below the melting point) accumulated during the past weeks. At this time, the exceeding solar energy can be easily stored and immediately released, while the sub-LHTES version uses this extra energy also to recharge the other modules that are not still in the right temperature range to run the ORC. The behavior described above affects the ORC efficiency and electricity production: a light decrease of the electricity production is observed especially in the mid-season months of March and October, while the system performs better in winter and as good as the plant with the single TES in summer.

## Conclusions

This study aims at evaluating the benefits provided in terms of thermal efficiency of a plant equipped with a thermal storage subdivided in several modules, while managing their operation by means of a smart fuzzy logic controller. In this case, the storage subdivision has been applied to an innovative micro-solar CHP plant

**Table 7.6.** Monthly performance of the ORC unit in presence of single TES or subdivided TES.

Month	Single TES no fuzzy logic				sub-LHTES with fuzzy logic			
	TE <sub>ORC,in</sub> GJ	$t_{ORC,on}$ h	EE <sub>ORC,out</sub> kWh	$\eta_{el,ORC}$ %	TE <sub>ORC,in</sub> GJ	$t_{ORC,on}$ h	EE <sub>ORC,out</sub> kWh	$\eta_{el,ORC}$ %
January	8.3	97.3	144.5	6.28	8.6	103.6	166.8	6.98
February	15.6	177.6	326.5	7.53	16.2	189.3	338.5	7.53
March	30.1	334.9	652.4	7.79	29.7	338.5	643.1	7.78
April	33.4	373.3	726.8	7.82	34.4	384.3	750.3	7.84
May	38.9	436.0	855.7	7.90	41.1	451.6	903.1	7.89
June	44.2	489.4	972.7	7.92	46.9	507.5	1032.7	7.91
July	48.1	533.3	1059.9	7.92	51.7	552.7	1139.8	7.92
August	43.3	481.5	950.2	7.88	45.6	499.5	998.4	7.87
September	35.6	395.2	780.3	7.89	36.5	409.4	800.7	7.88
October	22.9	260.9	497.5	7.80	23.1	270.6	497.3	7.74
November	10.7	124.9	210.8	7.10	11.3	136.1	235.0	7.51
December	7.0	81.8	114.8	5.99	7.0	84.6	127.8	6.58

used in residential applications. Six sub-LHTES modules have been used and their operation has been managed according to cascade fuzzy logic control. While the main control system of the plant is designed to maximize the annual electric energy production, this further control aims at managing the sub-LHTES system only, but, as a consequence, it affects the thermal and electric energy production of the whole plant over the year. Hence, the performance of the integrated plant has been evaluated on a monthly and yearly basis and compared to that of the plant with a single LHTES (without subdivision into modules and smart management). The main findings of the comparison highlight that the proposed smart management of the sub-LHTES contributes to:

- a significant increase in the storage efficiency during winter season, allowing a longer duration of the discharging phase of the storage towards the ORC, while the two TES configuration behaves in a similar way;
- an electric efficiency of the ORC unit, as well as the operating time, higher in winter which results in an increased yearly electric energy production (about 5 %);
- 30 % less thermal losses of the LFR solar field due to defocus;
- more than 9 % additional thermal losses due to the higher pipeline working temperature.

Concluding, the adoption of a smart control management of the sub-LHTES allows increasing the performance of an integrated micro-CHP unit powered by solar energy when the plant works in part-load conditions. Nevertheless, a further investigation is required to better estimate the exact potential of the proposed approach changing the priority ranges and a validation of the control strategy is desirable during the forthcoming experimental tests campaign.

## 7.2 System performance evaluation in building integration

### 7.2.1 Introduction

In Europe the building sector accounts for about 40 % of the final energy consumption and 36 % of CO<sub>2</sub> emissions [15]. In 2010 the Energy Performance of Buildings Directive and in 2012 the Energy Efficiency Directive have set the specifications for high energy performance buildings and for the adoption of energy efficiency measures within the EU. Among energy efficient technologies, combined heat and power (CHP) systems allow the reduction of primary energy consumptions and, as a consequence, limit CO<sub>2</sub> emissions. For this reason the European Directive 2004/8/EC [39] has encouraged European countries to develop combined heat and power systems and has supported their use in different sectors. Indeed, wherever thermal and electrical demands are simultaneous, CHP systems offer potential benefits. Going towards a decentralised energy production, small and micro-scale CHP units proved to be suitable for many industrial and civil applications, such as residential buildings. Although micro-CHP systems have a very interesting potential in households to curb CO<sub>2</sub> emissions [83], their adoption has been limited so far, because of the economic feasibility. Indeed, micro-CHP actual convenience strongly depends on the scenario in which they are expected to operate. Hence, a proper design of micro-CHP systems for heating supply to residential buildings is of paramount importance for their economic success [67]. Users energy demand, electricity and fuel tariffs as well as adequate incentives are the main factors affecting their profitability. In 2015, CHP fuel mix in Europe was mainly based on fossil fuels, whilst renewable sources accounted for about 20.6 % [6]. In order to meet the challenging targets set by the Paris Agreement, an increasing share of renewable energy sources (RES) was introduced in the last years in the power generation mix, supported by existing regulation and subsidies [41]. Furthermore, distributed generation technologies using renewable energy allow to increase the security of supply in developed countries and to provide access to safe, reliable, affordable and clean energy in rural areas of developing countries. Despite internal combustion engines are the most well-established prime movers for small and micro-scale CHP applications [136] and are already available in the market, some issues still need to be solved, such as the introduction of renewable fuels for their more environmentally-friendly operation. Hence, Martinez et al. [129] conducted an extensive literature review on micro-CHP systems based on renewable energies with particular focus on solar based technologies. Micro solar CHP units, indeed, are considered effective means to provide clean, efficient and secure energy to the building sector. At present, the most used technology for renewable thermal energy production at residential level is represented by evacuated tube solar panels, because of their ease of installation and absence of tracking mechanisms [71]. However, the use of medium and high temperature solar technologies in buildings is preferable for cogeneration applications and they can be competitive with evacuated tubes if the involved systems are properly designed [175]. In particular, Organic Rankine Cycle (ORC) systems are considered as one of the most common and competitive technologies to efficiently convert the solar energy into power [79]. Therefore, many researchers are paying attention on the development and optimization of

small-scale ORC systems. Furthermore, special interest exists for ORC coupled with different solar technologies. For example, Freeman et al. [94] evaluated the electrical performance of a domestic solar ORC using evacuated flat-plate solar collectors and investigated different solutions to optimize its operation in the UK climate. Baccioli et al. [56] carried out a dynamic simulation of a small-scale solar ORC power unit with rotary volumetric expander using compound parabolic collectors for different Italian locations. The control strategy proposed by the authors allowed operating without any storage system. Manfrida et al. [128], instead, first developed a mathematical model of a thermal energy storage system made of phase change material and then evaluated its application in a solar powered ORC using parabolic through collectors. The analysis shown that the proposed plant was able to produce electricity for almost 80 % of the investigated period with a weekly average overall efficiency of 3.9 % (solar-to-electricity). Taccani et al. [171] carried out laboratory and field tests of a prototypal solar ORC ( $< 10$  kWe) coupled with a 100 m<sup>2</sup> parabolic trough collectors (PTC) solar field obtaining a gross electrical efficiency of the ORC unit up to 8 %. In order to properly assess the actual potential of solar ORC in residential applications, their integration into the building needs to be accurately addressed. So far, most of the works in literature about micro solar CHP systems based on ORC units focused on the optimization of the different subsystems or of the whole plant, neglecting their exact interaction with the building. For example, Ramos et al. [155] performed a complete system optimisation considering the design parameters both of two different solar collector arrays and of a non-regenerative sub-critical ORC unit to be used in a domestic environment. In particular, the authors found that a 60 m<sup>2</sup> evacuated-tube solar field coupled with an ORC engine is able to deliver an electrical and thermal output of 3,605 kWh/year and 13,175 kWh/year respectively for the city of Athens with a levelised cost of energy close to that of PV systems. Calise et al. [9] carried out a dynamic simulation in *TRNSYS* of a 6 kWe ORC system coupled with a 73.5 m<sup>2</sup> solar field, consisting of novel flat-plate evacuated collectors and an auxiliary gas-fired heater to provide additional thermal energy to the ORC in case it is needed. The yearly output electrical and thermal energy by the ORC system was found to be 4,300 kWh and 41,200 kWh, respectively, with an additional heat input from the gas-fired burner of only 3,000 kWh. The issue of micro-CHP integration in building is, indeed, a relevant topic and it is confirmed by the fact that several studies in literature dealt with the coupling of different micro-CHP technologies, rather than solar, into buildings. For example, Fubara et al. [95] proposed a modelling framework to capture the impact of the adoption of solid oxide fuel cells, Stirling engines and internal combustion engines micro-CHP systems on the total primary energy usage in both generation and distribution by using as case study four different sizes of UK houses. Rosato et al. [160], instead, investigated in *TRNSYS* the energetic, economic and environmental performance of a 6 kWe micro-CHP unit based on internal combustion engine technology in a multi-family house in Naples. Fong and Lee [90] conducted, by means of *TRNSYS*, a year-round evaluation of trigeneration systems based on internal combustion engine technology subject to climatic conditions. In this case, prime movers under investigation were coupled with single-effect absorption chillers to satisfy the electrical, thermal and cooling energy demands of a 30-storey office. Four Asian cities with close longitudes and different latitudes were considered. The analysis revealed that a continental

climate with cold winter and hot summer is favourable to trigeneration, whilst a temperate climate results in a low energy-saving potential for such trigeneration systems. Therefore, renewable energy and solar technologies in particular could be of paramount importance to extend the energy profitability of cogeneration and trigeneration systems also in temperate climate zones. Hence, Rodriguez et al. [159] analysed the performance of several design configurations of a hybrid solar thermal/PV/micro-CHP system, composed of a natural gas internal combustion engine as micro-CHP unit, integrated into a building in different locations of Spain. Also Yang and Zhai [195] presented a simulation work of a solar hybrid cooling and combined heat and power plant in three building prototypes across seven climate zones. The buildings energy demand is obtained with models in Energy Plus and then used to optimize the design schemes of the plant, represented in a separate model in MATLAB. Instead, Martinez et al. [130] performed a numerical investigation on the performance of a micro solar CHP system consisting of a 46.5 m<sup>2</sup> PTC solar field, a single-cylinder steam engine working according to a Hirn cycle and an additional boiler integrated into a two-floors house in Chambéry. The simulation analysis developed in TRNSYS revealed that the volume of the water tank between the plant and the building has a huge impact on the operating hours of the plant. Garcia-Saez et al. [96] evaluated the economic and technical feasibility of solar ORC systems to cover the domestic hot water and electricity demand of residential buildings. They highlighted that the profitability is strictly related to the coverage of the energy demand. The authors claimed the need to develop dynamic simulation models to properly assess the interaction between demand and production. As regards ORC based cogeneration/trigeneration units, Zhang et al. [199] conducted different simulations of a prototype scale PTC-ORC system with a power output of 200 kW<sub>e</sub> and coupled with a single effect absorption chiller. In particular, the authors focused on different time-scale analyses to evaluate the functionality and the dynamic of the integrated technologies to provide electrical, thermal and cooling power to a baseline office building. According to mid-term simulations, the annual production of the optimized system under investigation was equivalent to 79.9 %, 95.9 % and 53.3 % of the cooling, heating and electrical energy demand of the building. However, the mutual interactions between the solar ORC system and the building is not analysed in detail, but heating and cooling curves are used. Such aspect cannot be neglected for a fair evaluation of the performance of micro solar ORC system. Indeed, Pereira et al. [146] highlighted how micro ORC systems in residential applications have the ability to face highly variable thermal demand loads with a short response time, nevertheless, just a few works in literature about solar ORC systems have already dealt with this topic taking into account the daily system dynamics and the mutual influence between energy demand and supply. Wang et al. [186] showed the potential of the integration of a combined heat and power unit and a concentrating solar power plant with buildings integrated with phase change materials. In particular they optimized the energy demand scheduling in order to maximize the energy efficiency of the system, which refers to large scale applications and relies on solar tower as concentrated solar power technology. In a previous paper Arteconi et al. [51], analysed the potential of a micro solar ORC system to provide space heating and domestic hot water in residential dwellings in different European countries. In this work a detailed evaluation at building level of the energy deployment of an

innovative micro solar ORC plant in residential dwellings is performed, but the influence on the production unit operation is neglected. The innovative micro solar ORC was presented in [79], where its operation and energy performance were also discussed. The plant is made up of a small-scale 2 kWe Organic Rankine Cycle system coupled with a concentrated solar Linear Fresnel Reflector plant and a phase change material thermal storage system equipped with reversible heat pipes, as proposed in the Innova MicroSolar EU project [21] led by Northumbria University [26]. The analysis highlighted that the plant is able to achieve a significant number of operating hours during the year with pretty good electric and thermal efficiencies. Moreover, the electric and thermal energy production is adequate to partially satisfy the energy demand of several dwellings. However, in order to better evaluate the useful energy production from the plant, which can effectively cover the thermal and electric demand of a building, a detailed dynamic simulation model for the integrated system (plant-building) was here developed, because the interaction in dynamic operation of energy demand and supply significantly affects the overall system performance. Purpose of the analysis is both understanding the influence of the integration on the ORC unit efficiency and also assessing the useful energy that can be recovered for the building needs. Furthermore an optimization of the integrated system is proposed. Hence, the main novelties of the work rely on: (i) the assessment of the performance of a novel micro-CHP system based on LFR solar field by means of an integrated model including both the dynamic behavior of the plant and of the building; (ii) the comparison of the overall system performance in case of using an integrated simulation model or a fixed ORC condensing temperature (i.e. a given load curve for the building energy demand) to quantify the impact of the real operation strategy. In particular, the latter aspect is not retrieved in other literature works, as highlighted in tab. 7.7 where the main features of the relevant literature studies analysed in the state of the art review are summarized. It is evident that there is a lot of research interest in the field, however different technologies are described in the listed papers, with different research targets and methodologies.

The study is organized as follows: in Section 7.2.2 the methodology of the analysis is presented, in Section 7.2.3 the system and simulation model are described, while in Section 7.2.4 the main results are discussed. Eventually Section 7.2.5 summarizes the main findings of the work.

**Table 7.7.** Summary of the main aspects of reported literature studies about solar CHP systems for buildings.

<b>Ref.</b>	<b>CHP plant</b>	<b>Size</b>	<b>Building representation</b>	<b>Objective of the study</b>
[94]	evacuated flat-plate solar collectors; ORC	Domestic size (electric annual average power about 100 W; solar collector area 15 m <sup>2</sup> )	N.A.	Optimal working fluid selection and configuration

[56]	compound parabolic collectors; ORC	N.A.	N.A.	Performance analysis
[128]	parabolic trough collectors; latent thermal storage; ORC	solar collector area $2600 m^2$	N.A.	Role of the latent thermal storage
[171]	parabolic trough collectors; ORC	$< 10kW_{el}$ ; solar collector area $100 m^2$	N.A.	Performance analysis in lab
[155]	flat-plate and evacuated-tube solar field; ORC	solar collector area $60 m^2$	N.A.	Performance analysis
[9]	flat-plate evacuated collectors, ORC	$6kW_{el}$ ; solar collector area $73.5 m^2$	N.A.	Performance analysis
[195]	hybrid system: PV and solar thermal panels; gas fueled CHP plant	Hospitals, hotels and offices application	load curve (obtained with a separated Energy Plus model)	Optimal design and performance analysis
[130]	parabolic trough collector; steam engine	Domestic application; solar collector area $46.5 m^2$ , dwelling of 4 users in Chambéry (France)	integrated TRN-SYS model	Role of the storage tank
[96]	flat collectors; ORC and reversible heat pump	solar collector area $40 m^2$ , dwelling of 4 users in Sanlucar and Santiago (Spain)	load curve	Economic and performance analysis

[199]	parabolic trough collector; ORC; absorption chiller	200kW <sub>el</sub> , office building, western region of China	load curve	Performance analysis
[186]	solar tower; absorption chiller	up to 40 MW, 5,000 households in China	RC model	Economic and performance analysis
[79]	linear Fresnel reflector solar collector; ORC	2 kW <sub>el</sub> ; solar collector area 146 m <sup>2</sup>	N.A.	Performance analysis
present work	linear Fresnel reflector solar collector; ORC; absorption chiller	2kW <sub>el</sub> ; solar collector area 146 m <sup>2</sup> , 4 dwellings in Spain	integrated TRNSYS model	Performance comparison in case of simulation model with or without integrated building

### 7.2.2 Methods and modeling

In this study the integration of a micro solar ORC plant with a residential building is investigated. The analysis is performed by means of a dynamic simulation model that represents both the plant and the building. First the ORC production is assessed considering an ideal thermal energy demand: the final user can use all the energy produced by the ORC and the condenser works at fixed temperature depending on the chosen configuration (i.e. cogeneration or trigeneration mode). Then the integrated operation of the ORC and the building is considered, taking into account the influence of the building demand on the ORC condensing temperature and thus on the ORC thermal and electric energy production and efficiency. Indeed the thermal interaction between the two systems is relevant for the performance of the ORC unit and a detailed analysis is required, while the corresponding electric energy produced is only compared with an assumed average electricity demand for the final user [12]. Eventually the heating and cooling system configuration in the building is optimized, in order to minimize the operational costs and the necessary final user energy demand to reduce the amount of wasted ORC thermal energy production. The plant is supposed to be located in Lerida (41° 37' 0" N, 0° 38' 0" E), very close to the Spanish city where the real prototype of the Innova Microsolar project has been built. The direct normal irradiance for this location is 2429 kWh/m<sup>2</sup> and the global horizontal irradiance 1882 kWh/m<sup>2</sup>. It is a place with typically cold winter and hot summer. A dynamic simulation model was set up using TRNSYS [35] to model the plant and the coupled building. The main components of the plants were included in the model in TRNSYS and ad-hoc subroutines were written in MATLAB [23] to represent the LFR solar field, the micro ORC plant and the PCM thermal energy storage tank equipped with reversible heat pipes. The weather data file was

obtained from Energy+ database [16] and a simulation time step of 10 minutes was assumed. In fig.7.22 the integrated plant-building system is represented and described in detail in the next Sections.

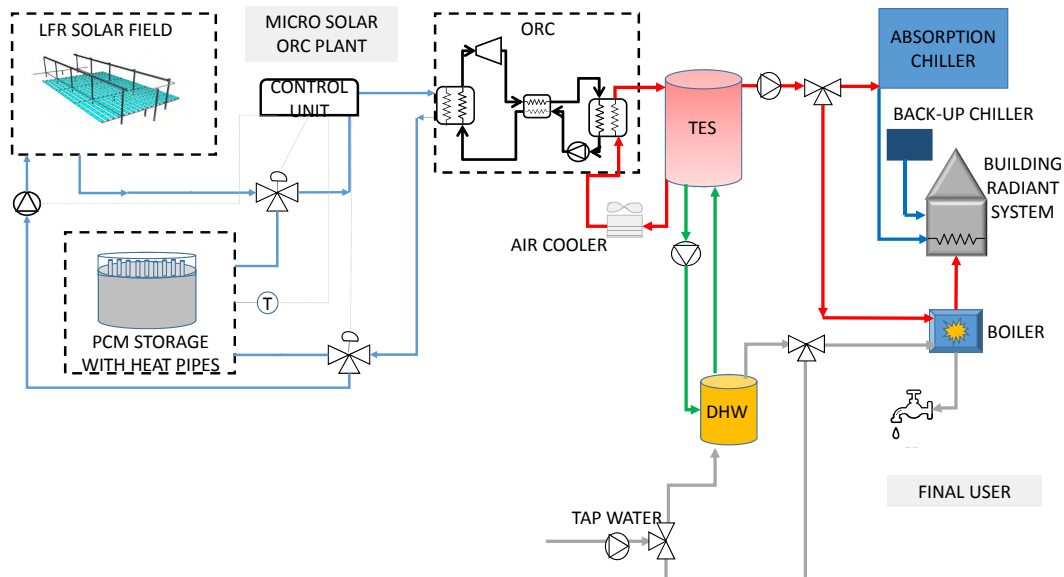


**Figure 7.22.** Integrated plant-building system schematics: the main components of the micro-solar Organic Ranking Cycle and the final user's heating and cooling devices are illustrated.

The thermal energy produced by the ORC is delivered to a thermal energy storage (TES) represented by a thermally stratified water tank (represented with Type 156 in TRNSYS, see fig.7.22), which decouples the energy production and demand from the final user, as better explained later on. In case the TES is fully charged, a back-up air cooler (modeled with Type 511 in TRNSYS) is switched on to cool the water return temperature to the condenser (outlet water temperature set-point at 40 °C).

The operation mode of the plant depends on the solar radiation and the state of charge of the PCM storage. The diathermic oil from the solar field flows to the PCM storage and/or directly to the ORC depending on its temperature and on the amount of power collected at the receiver. On the contrary, when the power produced by the solar field is low or zero and the average PCM storage temperature is within a given operating range ( $T_{ORC,on} = 217$  °C and  $T_{ORC,off} = 215$  °C), the thermal energy of the storage can be used to run the ORC unit and assure its operation for a maximum of 4 hours with no sun. tab.7.8 reports set-points and threshold values of each operation mode in accordance with the control system developed by S.TRA.TE.G.I.E. srl [30]. In particular, when the LFR supplies directly the ORC (OM1), the target oil temperature to be provided to the ORC for its operation

is 210 °C. In case there is a surplus of thermal power ( $>22$  kW), the solar field charges also the PCM storage (OM4) and in this case the oil temperature depends on the storage temperature (see tab. 7.8). In case the PCM storage temperature increases too much ( $>280$  °C), a defocusing of the LFR mirrors begins. Whereas if the LFR has not enough energy to run the ORC ( $< 15$  kW), it supplies only the PCM storage and the outlet oil temperature is set at 10 °C more than the average storage temperature. When, instead, the PCM storage supplies the ORC, it can provide oil with a temperature in the melting range of the phase change material.

**Table 7.8.** Operating conditions for the different operation modes of Innova Microsolar plant model.

Operation Mode	Description	Operating conditions
OM1	LFR supplies ORC	$T_{oil} = 210$ °C
OM2	System off	-
OM3	LFR supplies PCM storage	$T_{oil} = T_{PCM,av} + 10$ °C
OM4	LFR supplies PCM storage and ORC	$T_{oil} = 210$ °C if $T_{PCM,av} < 200$ °C or $T_{oil} = T_{PCM,av} + 10$ °C
OM5	PCM storage supplies ORC	oil flow rate 0.22 kg/s
OM6	PCM storage and LFR supply ORC	$T_{oil} = 210$ °C from LFR and tot oil flow rate 0.22 kg/s

The models of the main components of the plant were tested with available data from manufacturers. The Table 7.9 summarizes the main characteristics of the components represented in the simulation model of the solar ORC plant and integrated building. Further details about the solar ORC plant model can be found in [79].

### 7.2.3 Building specifications

Terraced houses built after 2010 were considered the most suitable final users for this analysis, as assessed in a previous study about potential application of the m-CHP plant [140]. In particular, a building composed of 4 dwellings was considered because it was demonstrated that it allows achieving the target set by the Innova Microsolar project of at least 50 % of the thermal energy demand coverage and 20 % energy costs savings [52]. The considered building was designed on the basis of the specifications for buildings thermal performance in place in Spain [55, 18], as reported in tab. 7.10. Each dwelling has a surface of 100 m<sup>2</sup> and a window area of at least 10 % of the wall surface. It was assumed about 30 m<sup>2</sup> per person providing an internal gain of 120 W each and a 0.5 ACH (air changes per hour) was modeled. A dynamic simulation model was developed and a schematic of the TRNSYS model is shown in fig.7.23.

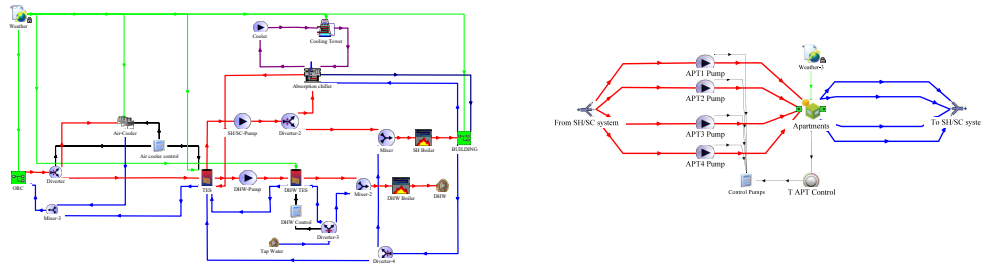
The best available technologies for *Space Heating* (SH), *Space Cooling* (SC) and *Domestic Hot Water* (DHW) production were taken into account in the evaluations. In winter the thermal energy produced by the ORC is stored in the thermal energy

**Table 7.9.** List of models description and mathematical formulation [35].

Component	Model description	Mathematical formulation
TES	A thermally stratified water storage tank with an immersed heat exchanger is used (Type 156). The tank is divided into isothermal temperature nodes, which interact between them for fluid conduction and movement.	Immersed heat exchanger: $\frac{n}{UA} = \frac{1}{h_o A_o} + R_W + \frac{1}{h_i A_i}$ where the outer surface heat transfer coefficient depends on: $Nu_D = C \cdot Ra^n$ and the inner surface heat transfer coefficient depends on: $Nu_{ax} = 0.023 Re_{hx}^{0.85} Pr_{hx}^{0.4} \left( \frac{d_i}{d_{coil}} \right)^{0.1}$
Building	TRNSYS Type 56 is used to represent the building with active layer for the radiant floor. It is an energy balance model where the air zone heat flux takes into account the thermal exchange by means of convection, infiltration, ventilation, solar radiation and internal gains.	Air zone energy balance: $\dot{Q}_{node} = \dot{Q}_{conv,surf} + \dot{Q}_{inf} + \dot{Q}_{vent} + \dot{Q}_{int,gains} + \dot{Q}_{solar,rad}$
Absorption chiller	TRNSYS Type 107 uses a normalized catalog data lookup approach to model a single-effect absorption chiller.	Heat capacity: $Capacity = f_{fullLoadCapacity} \cdot \dots$ $f_{NominalCapacity} \cdot \dots$ $Capacity_{rated}$
Cooling tower	TRNSYS Type 501 represents a closed loop cooling tower. It assesses the saturated air temperature as the temperature at the air-water interface and assumes it is also the temperature of the outlet fluid.	Saturated air enthalpy: $h_{sat}(T_{fluid,out}) = h_{air}(T_{air,in}) + \dots$ $\frac{\dot{Q}_{fluid,design}}{\dot{m}_{air} \left( 1 - \exp \left[ -\lambda \left( \frac{\dot{m}_{air}}{\dot{m}_{air,design}} \right)^{y-1} \right] \right)}$
Boiler	The model (Type 122) calculates the energy required to elevate the temperature of the liquid from its inlet value to the setpoint value.	Heat power transferred to the fluid: $\dot{Q}_{fluid} = \dot{m}_{fluid} c_{p,fluid} (T_{out,fluid} - T_{in,fluid})$
Dry cooler	TRNSYS Type 511 is used as dry fluid cooler in which air is blown across coils that contain a hot liquid. The liquid in the coils does not come into direct contact with the air. It is a single-pass, cross-flow heat exchanger represented with the $\epsilon$ -NTU method.	Heat exchangers efficiency: $\epsilon = \frac{1 - e^{-NTU(1-c_r)}}{1 - c_r e^{-NTU(1-c_r)}}$

**Table 7.10.** Building thermal specifications (U-values in W/m<sup>2</sup> K).

Location	Externalwalls	Roof	Floor	Windows
Lerida	0.74	0.46	0.62	3.1



(a) TRNSYS schematics of the integrated (b) detail of the building model with 4 model plant-building dwellings.

**Figure 7.23**

storage with a temperature set-point of 70 °C. The volume of the storage has a direct impact on the recovery efficiency of the ORC thermal energy, but it is also subject to space constraints in the installation. On the basis of the results from a previous study [53], a size of 1 m<sup>3</sup> per dwelling was considered as a good trade-off. Indeed in [53] a sensitivity analysis of the storage volume was conducted in case of ORC thermal production used only for DHW demand (the thermal energy was assumed given and the plant and building models were not integrated as in this work). The thermal power is used to supply space heating and, when it is not enough, a back-up boiler (*Type 122*) steps in (a capacity of 25 kW per dwelling was taken). Radiant floor is assumed as distribution system in the building, being the most efficient because of low working temperatures (it was modeled with *Type 56* with floor active layer). The inside temperature set-point was set at 20 °C ( $\pm 0.5$  °C) to be maintained 24 h per day with a continuous operation, typical control strategy for such distribution system. The water temperature supplied to the underfloor heating system is regulated on the basis of a linear compensation curve dependent on the outside ambient air temperature ( $T_{air}$ ):

$$T_{supply} = 20 + k_c(20 - T_{air}) \quad (7.1)$$

where  $k_c$  is 0.75. The water flow rate is designed to maintain 7 °C as temperature difference between inlet and outlet temperature to the floor and it is 500 kg/h. The thermal energy produced by the ORC is also retrieved from the TES tank and used for DHW production. A DHW tank of 300 l per dwelling is considered. The daily DHW tap profile is taken from the European standard *UNI EN 15316-3*, tap profile number 2, because the most representative of the average DHW use in Europe [40]. The back-up boiler is used when the DHW supply temperature is lower than the

target value required by the final user. In summer the TES tank is maintained at 90 °C, so that an absorption chiller can be supplied with the stored heat to produce the building cooling demand. A 17 kWc *Yazaki Energy System* [38] was used (modeled with *Type 107*), whose condenser is cooled by means of a cooling tower (*Type 510*) [32]. The same radiant distribution system is considered whilst the water supply temperature is set at 16 °C and the flow rate at 800 kg/h. A back-up chiller with an average coefficient of performance of 3 is included to supply the extra cooling demand not satisfied by the absorption chiller.

#### 7.2.4 Results and discussion

In this section the results obtained from the simulations are discussed. As previously anticipated they report:

- i the micro solar ORC plant performance without building integration (i.e. fixed operating temperatures at the condenser);
- ii the micro solar ORC plant performance for the integrated system (plant-building);
- iii the building heating system optimization in order to minimize the energy operational costs of the building.

##### Micro solar ORC plant performance without building integrations

The performance of the micro solar ORC plant is investigated during a whole year. It is assumed, as often done in literature, that the system can work at given reference conditions at the condenser and in particular all the produced energy can be used by a final user. Firstly, the cogeneration configuration is considered, because it is the simplest and corresponds to the prototype configuration of the Innova Microsolar project. In cogeneration mode, all the thermal energy produced by the ORC unit is used to supply space heating and domestic hot water production during the year, thus the return water temperature from the building entering the condenser is assumed at 60°C and the temperature difference equal to 10 °C with a fixed flow rate of 0.5 kg/s. In tab. 7.11 the main results of the micro solar ORC plant performance are summarized. It is possible to notice that, except for the winter months of December and January, the thermal power ( $P_{th,ORC}$ ) is always close to the design value (18 kW), while the average electric power output ( $P_{el,ORC}$ ) is always a bit lower than the design value (2 kW). The yearly electricity production ( $E_{el,ORC}$ ) is about 5,400 kWh and the yearly thermal energy ( $E_{th,ORC}$ ) production is about 56,330 kWh. Furthermore, as expected, both the thermal and electric energy present bigger production values during summer time, rather than in winter because the plant works for longer periods (duration of OM2, i.e. plant off, is more than double in winter time as reported in tab. 7.11). However, the electric efficiency of the plant is higher in winter period. This is mainly due to the control strategy of the plant. Indeed, as reported in tab. 7.12, in summer there is more solar radiation and the plant can store surplus energy in the PCM thermal storage and thus work also in operation modes OM5 and OM6 (i.e. the ORC is supplied by the PCM storage

**Table 7.11.** Micro solar ORC plant performance in cogeneration configuration: electric power ( $P_{el,ORC}$ ), thermal power ( $P_{th,ORC}$ ), inlet ( $T_{in,cond}$ ) and outlet ( $T_{out,cond}$ ) condenser temperature, electric energy ( $E_{el,ORC}$ ), thermal energy ( $E_{th,ORC}$ ), electric efficiency ( $\eta_{el,ORC}$ ), thermal efficiency ( $\eta_{th,ORC}$ ).

Month	$P_{el,ORC}$ kW	$P_{th,ORC}$ kW	$T_{in,cond}$ °C	$T_{out,cond}$ °C	$E_{el,ORC}$ kWh	$E_{th,ORC}$ kWh	$\eta_{el,ORC}$ %	$\eta_{th,ORC}$ %
January	1.59	15.83	60.0	67.6	131.9	1311.3	7.2%	78.0%
February	1.96	18.71	60.0	68.9	266.8	2550.8	7.6%	79.0%
March	1.84	18.64	60.0	68.9	455.9	4613.5	7.0%	81.5%
April	1.74	18.04	60.0	68.6	502.5	5217.3	6.8%	81.8%
May	1.69	17.99	60.0	68.5	614.0	6536.5	6.6%	82.1%
June	1.69	17.93	60.0	68.5	725.3	7693.0	6.6%	82.1%
July	1.64	17.65	60.0	68.4	792.3	8553.7	6.4%	82.3%
August	1.68	17.88	60.0	68.5	689.3	7325.8	6.6%	82.0%
September	1.69	18.05	60.0	68.5	558.5	5947.3	6.6%	82.0%
October	1.88	18.57	60.0	68.9	358.3	3530.5	7.3%	80.7%
November	1.79	17.26	60.0	68.2	191.3	1843.4	7.5%	78.1%
December	1.62	15.91	60.0	67.6	122.5	1206.3	7.3%	77.9%

or by the PCM storage and the LFR together, respectively). Being the electric efficiency of such configurations much lower than that in the other operation modes, this affects the overall electric efficiency of the system. Furthermore, in mid-season, when the solar radiation increases compared to the winter period, but the system still works in cogeneration mode (i.e. lower condensing temperature), the output thermal and electric power is higher than both winter and summer values.

From these results it is evident that the micro solar ORC plant can produce a huge amount of thermal energy, especially in summer, when the building thermal demand is represented only by domestic hot water if the cogeneration mode is assumed. This means that a lot of dwellings should be coupled to the plant to use all the produced thermal energy [53], while this plant was demonstrated to be particularly suitable for trigeneration applications [180]. For these reasons, the performance of the plant was also evaluated in trigeneration configuration, where during summer months the thermal energy is supplied to the TES at 90 °C in order to drive an absorption chiller for space cooling. tab. 7.13 reports the micro solar ORC plant performance during summer period for such configuration.

In trigeneration configuration (from May to September), the thermal efficiency is always higher than 84 % (against a maximum value of 82 % in cogeneration mode), while the higher condensing temperature in summer causes a drop of the electric efficiency of the ORC, which becomes almost half of the winter value. In July the average electric efficiency is 3.5%, whereas in cogeneration mode it reaches 6.4 %. As a consequence, the overall electricity production in summer is about 44 % less compared to cogeneration configuration, whilst the thermal energy production increases slightly. The electric and thermal efficiency of the ORC are, indeed, strictly connected to the condensation temperature, as shown in fig. 7.24. It is evident that, given the evaporating temperature, when the condenser inlet temperature increases, the electric efficiency decreases, because it is related to the temperature difference

**Table 7.12.** Operation modes duration and efficiency.

Month	OM1 h	OM2 h	OM3 h	OM4 h	OM5 h	OM6 h
January	28.8	515.3	124.3	72.8	2.5	0.0
February	25.5	430.3	86.5	129.5	0.0	0.0
March	22.0	396.7	79.0	200.0	41.7	4.5
April	24.2	310.3	99.2	212.3	63.3	10.5
May	25.2	264.2	99.0	252.0	94.2	9.5
June	16.8	211.8	69.7	294.0	103.7	24.0
July	18.7	192.2	57.0	315.2	131.8	29.2
August	29.7	267.0	51.0	279.3	104.3	12.7
September	17.3	303.0	73.2	230.3	87.7	8.5
October	27.7	435.5	96.7	166.0	16.2	1.8
November	27.8	474.5	121.5	96.0	0.0	0.0
December	20.7	509.0	147.5	66.7	0.0	0.0
$\eta_{el,ORC}$	7.5%			7.6%	3.8%	6.1%
$\eta_{th,ORC}$	79.5%			81.9%	80.2%	78.5%

**Table 7.13.** Micro solar ORC plant performance in cogeneration configuration: electric power ( $P_{el,ORC}$ ), thermal power ( $P_{th,ORC}$ ), inlet ( $T_{in,cond}$ ) and outlet ( $T_{out,cond}$ ) condenser temperature, electric energy ( $E_{el,ORC}$ ), thermal energy ( $E_{th,ORC}$ ), electric efficiency ( $\eta_{el,ORC}$ ), thermal efficiency ( $\eta_{th,ORC}$ ).

Month	$P_{el,ORC}$ kW	$P_{th,ORC}$ kW	$T_{in,cond}$ °C	$T_{out,cond}$ °C	$E_{el,ORC}$ kWh	$E_{th,ORC}$ kWh	$\eta_{el,ORC}$ %	$\eta_{th,ORC}$ %
May	0.96	18.13	80.0	88.7	343.5	6463.0	3.7%	84.7%
June	0.96	18.16	80.0	88.7	405.4	7669.5	3.6%	84.7%
July	0.93	17.93	80.0	88.6	437.5	8466.8	3.5%	84.9%
August	0.94	17.92	80.0	88.6	385.2	7347.5	3.6%	84.6%
September	0.94	18.02	80.0	88.6	311.2	5947.2	3.6%	84.6%

between the evaporator and the condenser. The thermal efficiency, instead, has an opposite trend with the condensing temperature than the electric efficiency and it increases by increasing the condenser temperature.

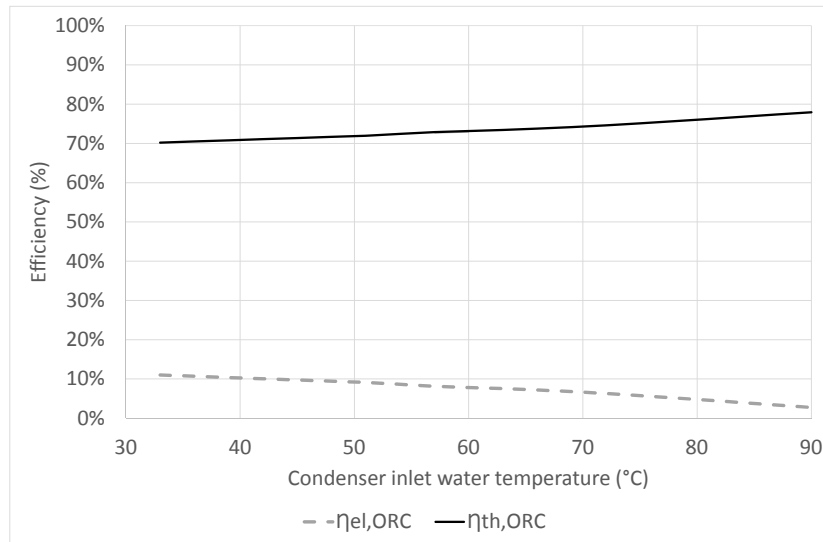


**Figure 7.24.** Electric ( $\eta_{el,ORC}$ ) and thermal ( $\eta_{th,ORC}$ ) efficiency of the ORC by varying the condensation temperature (the inlet oil temperature at the evaporator is assumed fixed at 210 °C).

### Integrated plant-building system

In this section the micro solar ORC plant is considered coupled to the building described in section 7.2.3, whose thermal demand affects the ORC condensation temperature. The trigeneration configuration is selected, because it allows a better exploitation of thermal energy produced in summer. Hence, the thermal energy produced by the ORC is collected in the thermal storage, whose maximum temperature set-point is at 70 °C in winter operation and at 90 °C in summer operation, delivered with a fixed water flow rate of 0.5 kg/s. With more detail, the operation strategy of the trigeneration unit is as follows: the micro CHP is operated on the basis of solar radiation availability (see conditions in tab. 7.8), while the ORC condensing temperature depends on the user's needs as specified above. The priority is given to the thermal energy production, meaning that the ORC condensing temperature depends on the demand and the electricity is a kind of by product. When there is too much thermal energy produced compared to the demand, an air cooler steps in to cool the water temperature down to 40 °C, favoring the electric energy production. Such control strategy allows the system to work a considerable number of working hours (compared to the total number of hours in presence of energy demand) during a year. In tab. 7.14 the performance of the micro-solar ORC plant when working in the integrated trigeneration configuration is summarized.

**Table 7.14.** Micro solar ORC plant performance in cogeneration configuration: electric power ( $P_{el,ORC}$ ), thermal power ( $P_{th,ORC}$ ), inlet ( $T_{in,cond}$ ) and outlet ( $T_{out,cond}$ ) condenser temperature, electric energy ( $E_{el,ORC}$ ), thermal energy ( $E_{th,ORC}$ ), electric efficiency ( $\eta_{el,ORC}$ ), thermal efficiency ( $\eta_{th,ORC}$ ), overall thermal efficiency of the integrated system  $\eta_{th,int}$ .

Month	$P_{el,ORC}$ kW	$P_{th,ORC}$ kW	$T_{in,cond}$ °C	$T_{out,cond}$ °C	$E_{el,ORC}$ kWh	$E_{th,ORC}$ kWh	$\eta_{el,ORC}$ %	$\eta_{th,ORC}$ %	$\eta_{th,int}$ %
January	2.20	15.97	36.9	44.5	195.9	1423.7	9.5%	75.7%	62.2%
February	2.31	18.20	45.8	54.5	331.6	2617.9	9.0%	77.1%	66.4%
March	2.26	18.68	47.0	55.9	554.6	4586.3	8.6%	79.6%	44.6%
April	2.37	18.02	40.5	49.1	654.8	4975.2	9.3%	79.7%	22.9%
May	1.98	18.78	55.6	64.5	594.7	5642.1	7.3%	80.9%	18.9%
June	1.41	18.29	69.2	78.0	551.7	7177.6	5.1%	83.1%	41.0%
July	1.00	17.97	77.0	85.5	460.8	8302.0	3.7%	84.2%	58.7%
August	0.88	18.20	80.9	89.6	346.6	7175.4	3.3%	84.1%	66.5%
September	1.18	18.19	74.1	82.8	368.0	5668.8	4.4%	83.5%	49.0%
October	2.33	18.19	45.4	54.1	453.4	3544.0	8.9%	78.0%	20.1%
November	2.26	17.19	42.4	50.6	253.3	1922.9	9.3%	76.4%	59.5%
December	2.28	16.08	35.6	43.3	182.0	1284.1	9.8%	75.3%	61.4%

The first evident difference with the results shown in the previous section is related to the inlet and outlet water temperatures at the ORC condenser. They are driven by the user thermal demand and are on average lower than the values for the reference condition without building integration. In winter the space heating can, indeed, be supplied with temperature also of 25 °C, depending on the outside air ambient temperature (see compensation curve, eq. 7.1), while the DHW is mostly demanded at temperatures lower than 45 °C. Also in summer the absorption chiller can work with slightly lower activation temperatures. During this season, the ORC thermal energy is used also to cover the DHW demand. Thus the heating supply strategy has a huge impact on the operation and performance of the generation plant, as demonstrated also by comparison with another study available in literature which shows a low energy demand coverage of a solar CHP plant in case of fixed and high supply temperature to the building [130]. The lower condensing temperatures on average allow achieving higher ORC electric efficiency and the electricity production is 26 % higher than the value obtained in the previous section with the trigeneration plant without building integration. Moreover, the electric power can even exceed the design value during the winter period. Looking at the ORC thermal efficiency, it does not change considerably in comparison with the trigeneration plant without building integrations. For the integrated trigeneration plant an overall thermal efficiency is also defined:

$$\eta_{th,int} = \frac{P_{th,net}}{P_{in,ORC}} = \frac{P_{th,ORC} - P_{waste} - P_{tank,loss}}{P_{in,ORC}} \quad (7.2)$$

where  $P_{th,net}$  is the *useful thermal power* delivered to the building, subtracting the *tank thermal losses* ( $P_{tank,loss}$ ) and the *thermal power dissipated* by the air cooler ( $P_{waste}$ ) when the tank is fully charged and cannot store more energy. As expected the thermal efficiency of the integrated system (ORC plus TES storage)

is lower than the ORC thermal efficiency (see tab. 7.14) and the lowest values are related to mid-season, because the thermal demand both for heating and cooling needs is limited. Indeed the reduction of the overall thermal efficiency is mostly due to the waste energy, which reaches about 60 % of the ORC output thermal energy in April, May and October. Whereas the tank thermal losses are pretty much constant during the year and account for about 10 % of the ORC thermal production (slightly higher values in winter and slightly lower values in summer, respectively 16 % and 7 %). From the building point of view, the monthly thermal energy demand breakdown can be seen in fig. 7.25. The graph shows that there is both a high thermal energy demand for space heating in winter and for space cooling in summer, while in mid-season the heating/cooling need is limited, as already pointed out. As a consequence the waste energy (i.e. the ORC thermal energy that the storage cannot collect because already fully charged and dissipated by the air cooler) is much higher during spring and autumn months, confirming the trend of the overall thermal efficiency above described. The boiler energy integration for DHW production is almost negligible as well as the back-up chiller production. On the contrary, the boiler integration for space heating, especially in January and December, is important.

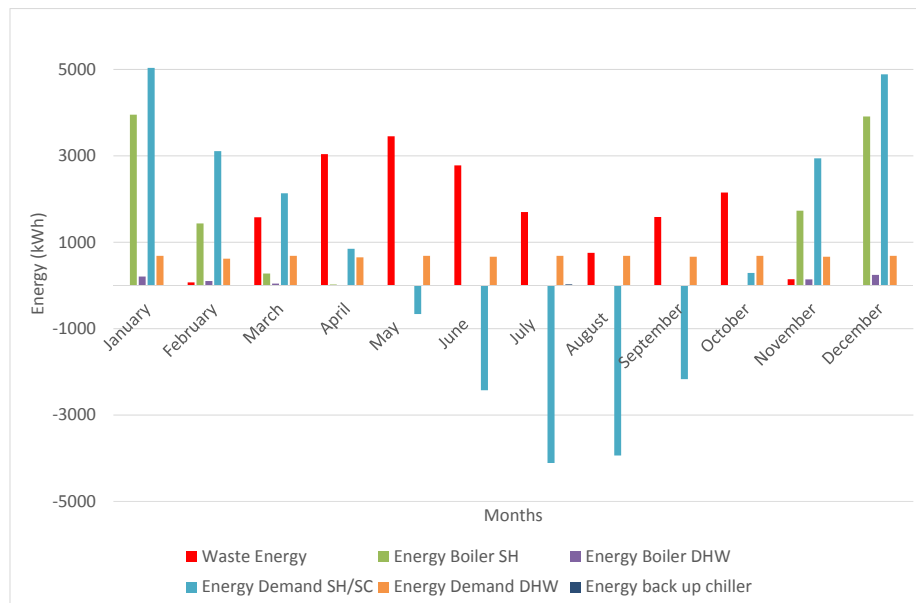


**Figure 7.25.** Monthly energy contributions for the considered building: energy demand for space heating (SH) and space cooling (SC), energy demand for domestic hot water (DHW), energy produced by the boiler to integrate the space heating or the domestic hot water, energy produced by the back-up chiller, energy dissipated by the air-cooler when the storage tank is fully charged (waste energy).

These results are confirmed by the demand coverage factors, defined as the

percentage of the corresponding energy demand which is satisfied by the energy produced by the micro-solar ORC without using the back-up generators or the electricity from the grid. They are the *space heating thermal energy demand coverage* ( $\text{Cov}_{\text{SH}}$ ), the *space cooling thermal energy demand coverage* ( $\text{Cov}_{\text{SC}}$ ), the *DHW thermal energy demand coverage* ( $\text{Cov}_{\text{DHW}}$ ), and the *total thermal energy demand coverage* ( $\text{Cov}_{\text{th}}$ ) as reported in tab. 7.15. The space cooling is almost completely driven by the ORC thermal energy production, with the exception of few hours during hot peak periods mainly in July. In summer also the DHW demand can be covered for more than 99 %, while a relevant share of energy is still wasted, because the production is much bigger than the user request. Some energy is also wasted in mid-season, while other energy needs to be produced by the boiler, because of a shifting in time between demand and production. Thus there are periods when the TES is fully charged and the air cooler has to step in, while in other periods the production is not enough to cover all the users requests. This aspect can be observed in fig. 7.26a, representing a typical mid-season day: in the morning the boiler steps in to cover the demand because there is not enough energy stored in the tank. When the micro-solar ORC plant starts working, it contributes to supply the building and re-charge the TES. In the evening when the TES reaches the temperature set-point and there is a low thermal energy demand, the ORC thermal energy cannot be used and it is dissipated through the air cooler. In fig. 7.26b, instead, a winter day is represented. The ORC works a limited number of hours in the afternoon. However the TES is initially partially charged and the heat stored is enough to run the low temperature SH distribution system in the early morning, then the boiler needs also to be switched on. During the considered winter day, the TES can never achieve the temperature set-point (70 °C). Furthermore the boiler has to switch on when the temperature of the DHW tank has a too low temperature level compared to the user's demand. Eventually in summer (fig. 7.26c), the TES temperature level is higher than in winter in order to run the absorption chiller. It can be observed that the boiler needs sometimes to step in anyway to satisfy an instantaneous high temperature DHW demand. The ORC thermal energy is produced also during night time, thanks to the ORC plant operating strategy, which is driven by the energy stored in the PCM thermal storage. The *electric energy demand coverage* ( $\text{Cov}_{\text{el}}$ ) was evaluated assuming for the electricity demand an average value per dwelling of 3,944 kWh/year, derived from available statistical data [12]. The obtained annual electric demand coverage is 31 %, while the total energy demand coverage ( $\text{Cov}_{\text{tot}}$ ) is 73 %.

**Table 7.15.** Monthly thermal coverage factors: space heating thermal energy demand coverage ( $\text{Cov}_{\text{SH}}$ ), space cooling thermal energy demand coverage ( $\text{Cov}_{\text{SC}}$ ), domestic hot water thermal energy demand coverage ( $\text{Cov}_{\text{DHW}}$ ), total thermal energy demand coverage ( $\text{Cov}_{\text{th}}$ ) and waste energy.

Month	Waste heat %	$\text{Cov}_{\text{SH}}$ %	$\text{Cov}_{\text{SC}}$ %	$\text{Cov}_{\text{DHW}}$ %	$\text{Cov}_{\text{th}}$ %
January	0.4%	21.5%	-	70.0%	70.0%
February	2.7%	53.9%	-	83.9%	83.9%

March	34.3%	87.2%	-	93.9%	93.9%
April	61.1%	97.6%	-	99.2%	99.2%
May	61.2%	-	100.0%	99.8%	99.8%
June	38.7%	-	99.8%	99.5%	99.5%
July	20.4%	-	99.4%	99.2%	99.2%
August	10.5%	-	99.8%	99.4%	99.4%
September	27.9%	-	100.0%	99.6%	99.6%
October	60.6%	99.9%	-	99.7%	99.7%
November	7.4%	41.2%	-	79.0%	79.0%
December	0.4%	20.0%	-	64.8%	64.8%
tot	31.7%	60.2%	99.8%	90.7%	90.7%

### Influence of design parameters on optimal building configuration

In this section the influence of the design parameters of the heating/cooling system in the building is investigated in order to minimize energy operational costs. In particular, it is investigated if there are different criteria than typical design practice to choose properly their values in an integrated system context. The thermal energy produced by the ORC is considered given and not affected in this case by the user demand itself, so to take into account in the analysis only the effect of the design configuration. The assumed performance for the micro solar ORC system is then that presented in subsection 7.2.4 for the plant in trigeneration condition. The design parameters that can be varied are:

- Volume of the thermal energy storage (TES) between the plant and the building;
- Volume of the DHW storage tank;
- Water flow rate of the heating system;
- Water flow rate of the cooling system;
- Compensation curve of the heating system.

Firstly, a sensitivity analysis of the influence of such parameters on the energy operational costs is performed. In tab. 7.16 the considered values of the parameters are reported: a technically feasible lower and higher value of the design value is assumed, in order to look for possible trends in their relationship with costs. The parameters are varied one by one in the dynamic simulation model, while the others are maintained fixed at the design value.

The operational costs include the electricity costs related to the energy use for the circulation pumps ( $E_{pumps}$ ), for the auxiliaries of the absorption chiller ( $E_{aux}$ ) and for the back-up chiller ( $E_{chiller}$ ) in summer and the natural gas cost for the back-up gas boiler for space heating and DHW (which has an efficiency  $\eta_{boiler}$ ). They are assessed as follows:

$$C_{tot} = (E_{pumps} + E_{aux} + E_{chiller})C_{el} + \frac{E_{boiler}}{\eta_{boiler}}c_{NG} \quad (7.3)$$

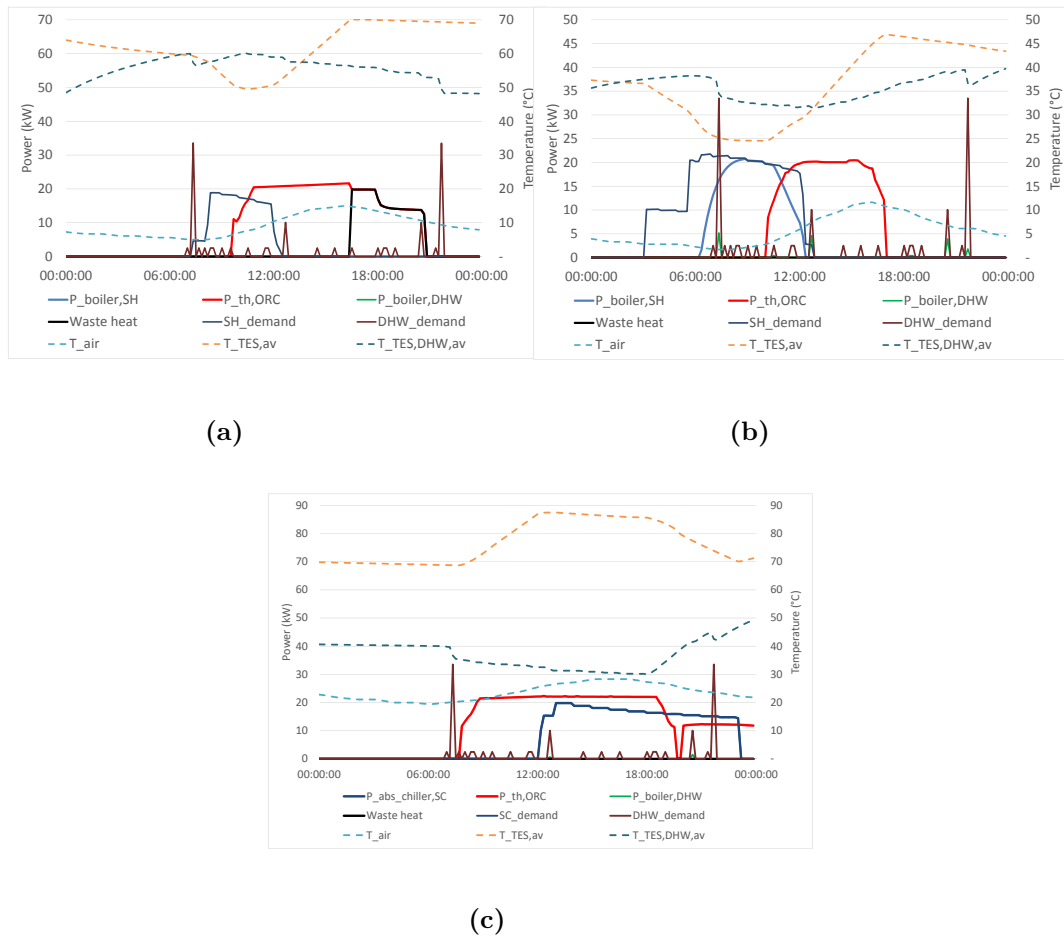


**Figure 7.26.** Daily energy flows related to the TES of the integrated system in different representative days: mid-season (a), winter (b), summer (c). The following variables are represented: the boiler power for space heating ( $P_{\text{boiler,SH}}$ ) and for domestic hot water ( $P_{\text{boiler,DHW}}$ ), the absorption chiller production ( $P_{\text{abs-chiller,SC}}$ ), the ORC thermal power ( $P_{\text{ORC}}$ ), the waste heat, the space heating ( $\text{SH}_{\text{demand}}$ ), the space cooling ( $\text{SC}_{\text{demand}}$ ) and the domestic hot water demand ( $\text{DHW}_{\text{demand}}$ ). The external ambient air temperature ( $T_{\text{air}}$ ) and the average temperature of the storage tank ( $T_{\text{TES,av}}$ ) and of the DHW tank ( $T_{\text{TES,DHW,av}}$ ) are also illustrated.

**Table 7.16.** Design parameters values used in the sensitivity analysis.

Parameter	Design value	Variations
Volume TES	4000 l	2000-10000 l
Volume DHW	1200 l	400-2000 l
Flow rate SH	500 kg/h	300-1000 kg/h
Flow rate SC	800 kg/h	500-1000 kg/h
kc	0.75	0.4-1

where  $c_{el}$  is the electricity price and  $c_{NG}$  is the natural gas price, whose values are assumed equal to 0.22 €/kWh and 18.52 €/GJ respectively, accordingly to the Spanish market prices [11, 24]. In fig. 7.27 the results of the sensitivity analysis are shown. The cost variation obtained by varying the design parameters is always lower than 2.5 %, corresponding to a maximum saving of about 30 €, meaning that their influence is very limited when they are considered separately. Looking at the trends, the operational costs reduction is favored by a water flow rate reduction for space heating, a water flow rate increase for space cooling, a reduction of the supply water temperature for space heating, an increase of the TES volume and a decrease of the DHW tank volume. In particular, a bigger TES volume allows the storage of more energy, limiting waste energy, and, as a consequence, less extra heating or cooling have to be produced with the back-up generators, while the influence of the DHW tank volume is very limited. Looking at the wasted energy, it drops from 42 % to 28 % when the TES volume passes from 2000 l to 10000 l. Instead, the lower value of the coefficient  $k_c$  for the compensation curve means that lower temperatures can be conveniently supplied to the radiant floor without any detriment to the internal comfort.

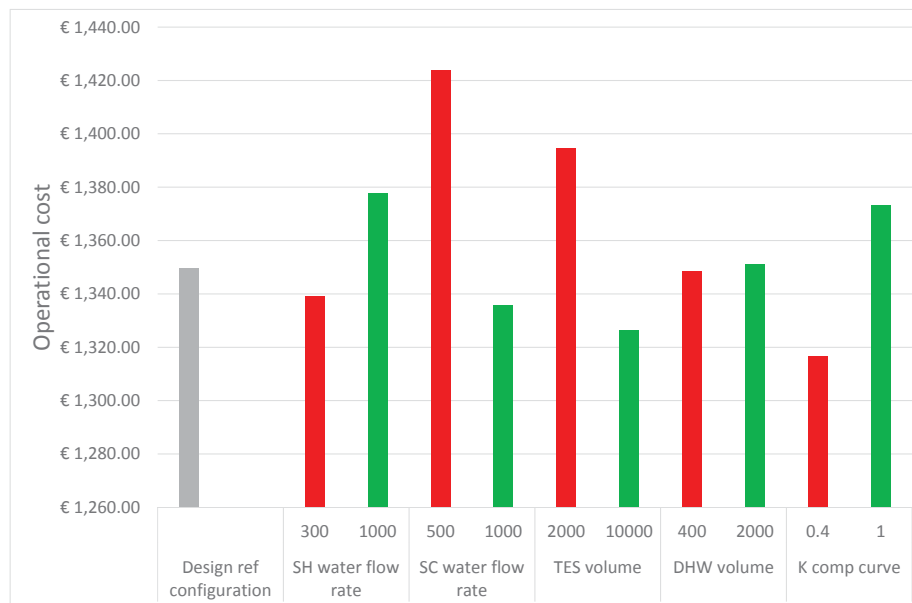


**Figure 7.27.** Electric (Operational costs variation on the basis of the selected design parameters: space heating and space cooling water flow rates, thermal energy storage volume and domestic hot water volume, compensation curve coefficient ( $k_c$ )).

Eventually, an optimization by means of *TRNOPT* [189] was performed in order to assess the influence of the simultaneous variation of all the considered parameters. *TRNOPT* is a dedicated *TRNSYS* interface for genetic optimization, *GenOpt*. The algorithm selected for the optimization process is Parametric Runs

on a Mesh [189]: this algorithm spans a multi-dimensional grid in the space of the independent parameters, and it evaluates the objective function at each grid point. The parameters considered are the same as those selected for the sensitivity analysis. However in this case they are all varied simultaneously in order to check all the possible combinations of values. The objective function of the optimization analysis is the operational costs minimization (as formulated in eq. 7.3). The comfort constraints for the indoor environment and for DHW are considered. The optimal configuration obtained by means of GenOpt optimization provides the best exploitation of the available ORC thermal energy, taking into account the costs for running all the auxiliaries and the natural gas costs when the boiler has to switch on. The optimal trade-off is represented by the following values of the parameters: space heating flow rate 300 kg/h, space cooling flow rate 1000 kg/h, TES volume 10,000 l, DHW tank volume 400 l,  $k_c$  value of compensation curve 0.4. The minimum total operational cost is 1230 €, which is about 9 % lower than the cost in the reference design condition.

### Influence of of final user demand on optimal building configuration

On the basis of the obtained results, it is evident that a building with 4 dwellings coupled with the considered micro solar ORC system still presents some wasted energy that cannot be recovered to satisfy the final users thermal demand. For this reason it was also evaluated the effect of coupling more dwellings on the wasted energy and final energy use demand coverage. Results are reported in tab. 7.17, where 4, 5, 6 and 10 dwellings are considered. The table shows also *primary energy variation* ( $PE_{var}$ ) and *energy cost variation* ( $Cost_{var}$ ) of the proposed micro solar CHP system in comparison with separate generation by means of traditional technologies. The primary energy use by taking the electricity from the grid, by producing thermal energy with a condensing boiler ( $\eta_{boiler}=110$  %) and cooling with an electrically driven chiller (*Coefficient Of Performance* 3) was assessed and compared with the *Primary Energy* (PE) use when the micro solar CHP system is introduced (2.5 and 1 were assumed as conversion factors for PE related with electricity and natural gas respectively).

**Table 7.17.** Energy coupling performance by varying the dwellings number: , waste energy,space heating thermal energy demand coverage ( $Cov_{SH}$ ), space cooling thermal energy demand coverage ( $Cov_{SC}$ ), domestic hot water thermal energy demand coverage ( $Cov_{DHW}$ ), total thermal and electrical energy demand coverage ( $Cov_{th}Cov_{el}$ ), primary energy variation respect to conventional technologies (PE), percent cost variation ( $Cost_{var}$  ) and absolute cost savings.

Dwellings	Waste heat %	$Cov_{SH}$ %	$Cov_{SC}$ %	$Cov_{DHW}$ %	$Cov_{el}$ %	$Cov_{Tot}$ %	$PE_{var}$ %	$Cost_{var}$ %	Cost saving €
4	36.7%	35.1%	99.7%	89.0%	22.5%	54.6%	43.3%	42.6%	2598.96
5	28.5%	31.6%	98.2%	87.4%	18.0%	52.4%	40.0%	39.2%	2911.18
6	22.7%	28.9%	92.9%	85.9%	15.0%	49.5%	36.7%	35.8%	3131.23
10	9.9%	20.9%	60.2%	82.3%	9.0%	37.0%	26.3%	25.0%	3464.23

By increasing the dwellings number from 4 to 10, the wasted energy drops down to 10 %. In turn, the energy share of the back-up generators increases, since the final

users demand grows more than the increased amount of energy recovered from the ORC. In particular a limitation is set by the space cooling coverage: the available thermal energy from the ORC in summer (in terms of quantity and temperature) is enough to run an absorption chiller with a cooling capacity of 17 kW. Thus if the number of dwellings is more than 6 the cooling supplied by the absorption chiller becomes much lower than the users cooling demand and the total energy coverage goes down to 50 %. Nevertheless, with 10 dwellings the energy cost reduction, compared to a traditional system, is still about 25 %. The performed analysis shows that the best number of dwellings to be coupled to the considered micro solar CHP depends also on the variable to be optimized (i.e. energy demand coverage, waste energy or costs).

### 7.2.5 Conclusions

In this section the effects of the integration of a novel micro-solar Organic Rankine Cycle system with residential buildings were investigated. In particular, the influence on the ORC electric and thermal performance of the final user dynamic energy demand was analysed by means of an integrated plant-building model. Furthermore the incidence of the design parameters of the building heating and cooling system on the energy operational costs was evaluated and an optimal configuration was proposed for the considered case study. Hence, the overall conclusions that can be drawn from the obtained results are:

- the system integration between the micro solar Organic Rankine Cycle plant and the building system cannot be neglected in order to assess properly the Organic Rankine Cycle performance and especially the electric efficiency and energy production. Indeed, the real user demand affects the Organic Rankine Cycle condensing temperature and this aspect has a very huge impact on the Organic Rankine Cycle electric efficiency, while it is limited on the Organic Rankine Cycle thermal production. The possibility of lowering the heating supply temperature has indeed a positive effect on the cogeneration unit and reduces storage thermal losses.
- The high amount of thermal energy produced by similar micro solar combined heat and power systems especially in summer makes such systems particularly suitable for trigeneration configurations, even if this aspect limits the electricity production.
- A bigger storage tank between the plant and the building helps to recover more effectively the thermal energy produced by the Organic Rankine Cycle, limiting wasted energy and energy production from back-up generators. However, space constraints and investment costs have to be taken into account in order to make a proper choice of the thermal energy storage size.
- The proposed micro solar Organic Rankine Cycle plant (2 kW<sub>el</sub>/ 18 kW<sub>th</sub>) is suitable to provide space heating, space cooling and domestic hot water to a number of 100 m<sup>2</sup> dwellings in the region of Lerida ranging from 4 to 6 in order to maintain the overall demand coverage higher than 50 % of the

building energy total demand, corresponding to operational cost savings of more than 35 %.

## 7.3 Wall temperature prediction of the LFR receiver tube

### 7.3.1 Material and methods

Referring to the wall treatment analysis described in the subsection 6.1.3, it is going to show the ability of the improved model to predict the wall temperature under various scenarios frequently occurring in a real plant operation. The importance of this aspect is twofold: firstly it concerns the structural integrity issues of the receiver tube due to the thermal stress. Indeed indeed the excessive differential thermal expansion in a side may cause a damaging. Secondly, it may improve the accuracy of the thermal model in predicting the global thermal efficiency, since this is strongly affected by the coating emissivity, which in turn depends by the wall temperature.

To quantitatively assess the benefits introduced by the wall treatment at expense of further computational burden, the wall temperature is analysed. Very high value of the internal oil-wall thermal resistance in the receiver tube can arise at low flow rates. Therefore, a new method to predict the wall temperature is needed not only to assess the thermal efficiency, but also to predict the tube response when the combination of the external conditions can entail excessive thermal stress on the absorber itself.

To simulate the problem taking into account the DNI intensity, fluid flow rate, inlet temperature, a new parameter has been conceived. More precisely, setting the model in steady state condition, the wall temperature is calculated resolving the thermal network at varying the inlet temperature  $T_{LFR,in}$  and the following parameter:

$$\frac{S_{mirr}DNI}{\dot{m}c_p} \quad (7.4)$$

the value got from eq. 7.4, here simply called as "load coefficient", compares the solar irradiation intensity collected by the LFR and its ability to collect heat from the sun, greater is this value and larger will be the wall temperature. Because the thermal properties of the diathermic oil change a lot over the LFR operating range, and the temperature difference between the inlet and outlet of the LFR is quite low (from few degrees Celsius to 20-30 °C), to appreciate the receiver behavior in all the conditions, its inlet temperature have to be also taken into account. The DNI is supposed to be in the range 200 - 1000 W/m<sup>2</sup> with intervals of 100 W/m<sup>2</sup>, while the oil velocity is assumed to change from 0.125 m/s to 1.5 m/s, the first value can be considered the extreme over which the thermal stress may deform the receiver definitely compromising it, whereas the second one is the design value provided by the manufacturer, but it can also be obtained by the ASHRAE indications [54]. Regarding the  $T_{LFR,in}$ , it is supposed to change from the winter external air temperature to the design one, thus a feasible range might be fixed between 0 °C and 300 °C (with steps of 30 °C). The ambient temperature and the wind speed are chosen 20 °C and 1 m/s respectively, the time interval for the simulation is long enough to assure a steady state condition, whereas the thermal nodes are varied to assess whether a grid dependence is present as shown in tab. 7.18.

**Table 7.18.** Grid dependence of the  $T_2$ .

number of thermal nodes	% of mean deviation
5	-0.1218
20	-0.0805
100	-

### 7.3.2 Results and discussion

At this point, all the elements for assessing the wall temperature  $T_2$  for the Forristall model and the improved version have been defined and the results are listed in the figures 7.29. For more details, the corresponding values of the contour plots are listed in appendix C. The grid points are the same utilised for the grid dependence in the previous section. It is important to point out  $T_2$  is evaluated at the LFR outlet (last thermal node) and each surface plot is related to HTF velocity of: 0.125, 0.25, 0.5, 1, 1.50 m/s, as a consequence the surface placed at the lower level in the figs. 7.28a and 7.29a, corresponds to 3 kg/s since the definition of the Reynolds number, conversely for fig. 7.28b and fig. 7.29b the upper surface corresponds to 0.125 kg/s, where the lower heat transfer coefficient inevitably rises the  $T_2$ .

At first sight, the graph in fig. 7.28b relative to the wall temperature computed with the Forristall model exhibits a temperature higher than the oil boiling point (333 °C), obviously this is a non physically behavior. The reason of that is attributable to several causes: because the implemented thermal oil characteristics into MATLAB code can not be evaluated outside that range, their value reach a saturation, but the heat flux is still intense throughout the receiver, on the other hand the latent heat of vaporization is not here considered, thus the thermal network solver is forced to increase the wall temperature to dissipate the excess of heat not received by the HTF due to its high convective resistance  $R_{12,conv}$ . On the contrary, the buoyancy driven flow in the improved model enhances the heat transfer at low flow rates, where the forced convection is negligible. In fact, from figure 6.11 is shown a Nusselt number above 40 almost throughout the map, thereby it is one order of magnitude more than the theoretical value of 4.36 assumed in the Forristall model in laminar conditions. The major influence is derived by the Grashof number, it is important to remember that it depends on the third power of the receiver's inner diameter.

As anticipated before, the goal of this study consists of predicting the wall temperature on the basis of the external environment/control conditions, to perform this task, it should be found an interdependence between these forcing parameters and the  $T_{LFR,in}$  derived from the previous analysis. For each flow rate and DNI (with step intervals of the previous analysis) the corresponding "Load Coefficient" (LC) is calculated. Peculiarity of this new parameter consists of depending by the inlet fluid properties and solar irradiation only (see equation 7.4). In the graph. 7.30 the results in the previous graphs (figs. 7.28b and 7.29b) are reprocessed and shown with respect to the load coefficient. One can see that as the load coefficient rises the wall temperature follow the same trend almost linearly. It is worth to point out that the slope of the hypothetical curve increases when the inlet temperature goes below 150 °C at high flow rates, in these conditions the HTF starts to increase

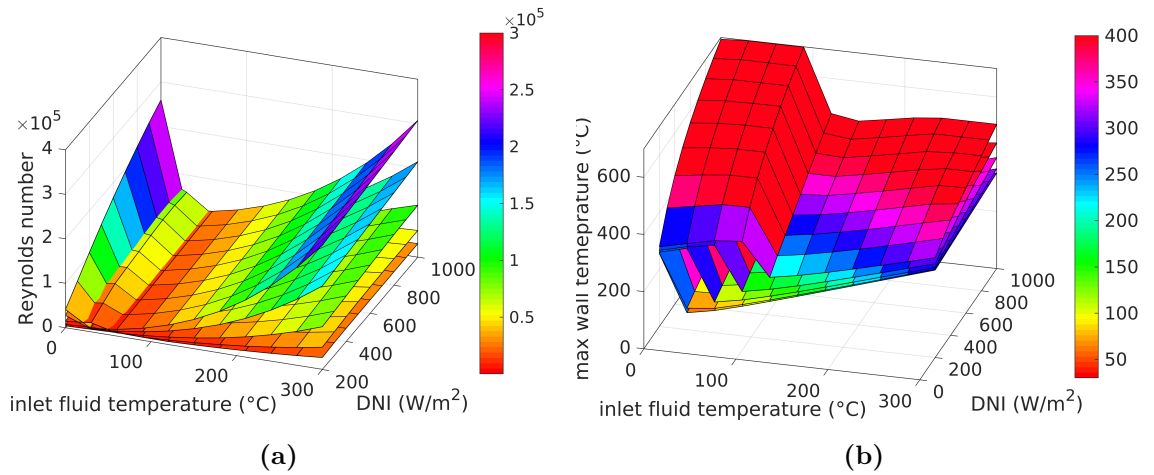


**Figure 7.28.** Reynolds number (a) and receiver wall temperature (b) from the Forristall model, for different mass flow rate.

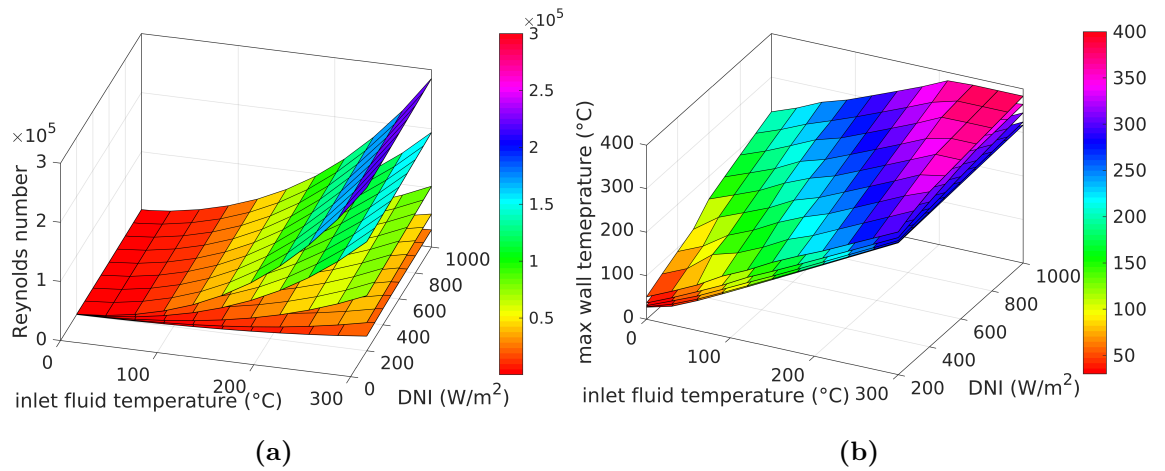


**Figure 7.29.** Reynolds number (a) and maximum receiver wall temperature (b) from the improved Forristall model, for different mass flow rate.

in viscosity and the thermophysical properties undergo a notable change. The same can not be said at low mass flow rate, in fact from the graph. 7.30, the slope of the curve seems not be affected by the inlet temperature, even if the load coefficient sharply changes (due to the lower denominator in the equation).

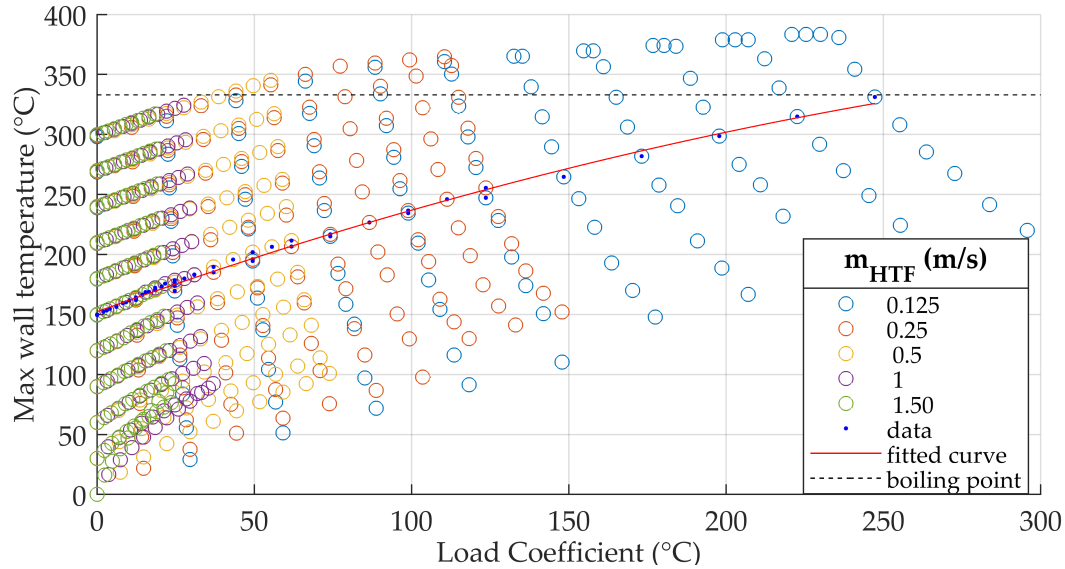


**Figure 7.30.** Correlation between the load coefficient (LC) and the wall temperature at different flow rates and inlet temperatures.

The scatter plot in 7.30 summarizes the results of several simulations of the receiver tube under a steady state condition. It is evident that many fitting curve can be drawn over the red line with the  $T_{LFR,in}$  of 150 °C, but just below 120 °C the working points no longer follow the same trend. According to this consideration, it is reasonable to assume a fitting curve for the wall temperature greater than 120 °C as best approximation for all the studied working conditions. Using a second degree of polynomial interpolation on the points aforementioned it is possible to have an R-square of 0.9961. The equation coefficients are the following:

$$\begin{aligned}
 T_2 &= p_1 \cdot LC^2 + p_2 \cdot LC + p_3 \\
 p_1 &= -976.5 \times 10^{-6} \\
 p_2 &= 0.9432 \\
 p_3 &= 152.3
 \end{aligned}
 \tag{7.5}$$

Where the LC term indicates the load coefficient at given  $T_{LFR,in}$ .

Just to clarify, it is worth saying that the radial conduction of the absorber tube mitigates the thermal gradient in the circumferential direction due to non-uniform flux distribution of the impinging solar radiation, but its action is not enough as shown in [139], Most likely, the results shown here underestimate the  $T_2$  of some tens of degrees in the laminar regime. This approximation can be overcome by means of a 3 D model using the real circumferential rays distribution. This degree of detail is needed when the wall temperature has to be precisely estimated, but from the control point of view, a rough estimation better than that of Forristall can

be considered adequate. Moreover, the computational cost of a 3 D model is not affordable in a dynamic solver and goes beyond the purpose of this dissertation.

### 7.3.3 Conclusions

In this section a novel thermal analysis of a solar receiver tube for PTC and LFR is presented. The study is aimed at showing the effect of the part-load operating conditions on the maximum internal wall temperature of receiver tubes. This task has to be addressed using a fast and robust mathematical model suitable for dynamic simulations. Wall temperature analysis arouses particular attention both in the scientific community and manufacturers, in the first case with regard to the room for improvements in thermal efficiency, on the other because the plant control could affect the thermal stress and thus the system reliability. Few scientific works deal with laminar flow in solar receiver tubes, many of them using Computational Fluid Dynamic models; in this dissertation instead, some correlations are adopted each one within their specific range of validity to entirely cover the Reynolds-Rayleigh map where the HTF works.

Main outcomes are summarized as follow:

- the HCEOI-12 receiver is more performing than the LS-2 one.
- The performance of the receiver does not depend on the HTF considered.
- With a  $\text{DNI} < 300 \text{ W/m}^2$  the efficiency of the HCEOI-12 receiver slightly drops thus limiting its potential in the foreseen CHP application.
- Because of the limited tube length, in case of high velocities of the fluid a small time-step of the simulation is required.
- The improved Forristall model exhibits a more trustable wall temperature at low HTF flow rates whichever DNI is applied. Even though the high oil viscosity at low inlet temperature reduces the heat transfer rate, the new model maintains a reasonable increment in temperature between the inlet and the maximum wall temperature. More precisely, within the Reynolds-Rayleigh map, the Nusselt number hardly any falls below 40, while the asymptotic value for constant heat flux and developed temperature and velocity profile accounts for 4.36, namely one order of magnitude below.
- If the resistances in the thermal network model change, the global solution is in turn affected, this means that a more accurate thermal model for the inner wall can improve the thermal efficiency evaluation making it more coherent with future experimental results.
- To properly operate the plant, particular attention must be paid to the thermal stress. Receiver tubes are one of the most critical components in solar power plants, an adequate heat transfer must be assured to avoid excessive overheating or heat disuniformity. Thanks to this study, a more accurate preliminary estimation of this issues is carried out under dynamic simulations, as a consequence the control system can be designed also to supervise this delicate element under any environmental conditions.

- A new correlation is developed to predict the wall temperature on the basis of the external parameters that can be simply monitored with sensors. A second order polynomial approximation can assure an R-square of 0.9961 over a wide range of the simulated data points. It goes without saying that on the basis of the correlation output, the pump of the solar field and/or the LFR mirrors can be properly adjusted to maintain the receiver tube within a safe operation region.

In conclusion, although an experimental test campaign is needed to better validate the proposed model regarding the non uniform effects on the local heat transfer coefficient, all in all the present analysis can adequately fulfill the LFR solar field performance assessments.

## 7.4 Hardware-In-the-Loop aided control design

In this section a *Hardware-in-the-Loop* (HiL) simulator of the micro combined heat and power system is presented and its use for control algorithm optimization is demonstrated and discussed. This methodology has been applied to a micro-CHP plant with the same characteristics of the Innova Microsolar plant. A smart control unit manages their integration and monitors the operation of each subsystem.

In order to support the optimization of the control algorithms and the definition of the best control strategy of the micro-CHP plant at different working conditions, a simulation framework based on MATLAB/Simulink has been developed and connected to the real control unit according to a HiL approach. In addition to the models of the different subsystems used in the past analysis, other models have been implemented, such as valves and variable speed pumps regulating the plant operation. The use of the HiL simulator permits to optimize the control logic of the integrated plant prior to its future commissioning, thus helping to overcome some of the technical and reliability issues occurring during the setup of the real system. In particular, the HiL has allowed: (i) to define the proportional and integral gains of the diverters in order to assure a robust and fast response of the plant during the switch among the different operation modes; (ii) to prove the limits of acting on the oil pump flow rate in assuring the nominal oil temperature at the inlet of the ORC unit, due to the inherent fluctuations caused by this control strategy; and (iii) to assess the best control strategy which is obtained by acting on the aperture of the diverter which controls the oil mass flow rate to the ORC unit. Hence, the scientific approach here proposed can be extended also to many other complex energy conversion systems in order to significantly reduce the potential critical issues during their commissioning.

### 7.4.1 Introduction

Broadly speaking, energy systems operation is always assisted by a control logic which assures the system integrity and a fine adjustment of the desired outputs. Basically, Proportional Integral-Derivative (PID) controllers are the most used in a broad variety of applications, but they need of a preliminary study in order to be used in practice on the basis of the dynamic effects on the adjusted variable and the mutual interaction with the others. When it is deal with energy systems, global efficiency is one of the most important parameter to be taken into account, controllers have a huge impact on it. For example Ni et al. [137] assessed the dynamic performances of a small-scale ORC plant driven by parabolic trough collectors under clear sky and cloudy sky conditions. Based on the response of the systems to the sky conditions, the authors found that the optimized system implementing a conventional PID control strategy can generate almost 20 % more energy than the system without control in a time span of 25,000 seconds during a cloudy sky day.

Independently from the solar ORC configuration, an adequate control logic and management of the integrated systems are of paramount importance to better exploit the collected solar energy and increase the conversion efficiency of such plants. However, generally speaking, the developing and testing of physical prototypes can be very expensive. Hence, use of powerful development tools is crucial to properly set

up complex energy systems, while minimizing the probability of errors, reducing the design time and the related costs. In order to minimize such costs, two approaches are commonly adopted: (i) simulation and (ii) hardware-in the-loop (HiL). In general the former allows to provide an estimation of the performance and of the main critical working conditions. However, when the dynamics of the systems need to be accurately taken into account, more powerful tools are required such those based on HiL approach. This approach, indeed, shows several interesting advantages, such as easy validation of control logic, discarding ineffective logics and optimizing the more promising ones. Therefore, once implemented in a simulator, the HiL technique allows reducing the required time for the development of the control algorithms of a real control system, since physical phenomena can be simulated and developers can concentrate most of their efforts directly on the control algorithms performances and optimization [78]. In literature, many researchers have addressed the use of the HiL technique to evaluate various optimizations of energy conversion systems operation. For example, Mohammadi et al. [135] developed an electromechanical emulator to study the behavior of wind turbines during faults, thus providing a useful tool to design more economical and higher performing wind turbines. Mehrfeld et al. [131] made use of the HiL concept to develop a new methodology to assess the annual performance of three energy conversion systems to be applied into buildings. In particular, a ground-source heat pump, an air-source heat pump and a Stirling engine mCHP system have been considered by the authors in their work finding good agreement between the simulated and the experimental tests results in terms of annual efficiencies. Huang et al. [105] developed an agent-based framework for HiL simulations to investigate the controller performance in buildings and the dynamics of major equipment. The potentiality of the developed HiL framework was then shown by controlling the speed of the supply fan in the air handling unit of a variable-air-volume building heating, ventilation and air-conditioning system, finding that a certain control sequence saved more than 50 % of the baseline fan energy consumption. Griese et al. [98] performed HiL simulations of an integrated energy system consisting of a biocatalytic methanation reactor, a photovoltaic park, a regenerative fuel cell and short-term storage units supporting the selection of the parts or process parameters prior to any potential realization of such a system at large scale. Mayyas et al. [141], instead, integrated the HiL and the model based design approach to evaluate the energy efficiency of hybridized powertrains and tune advanced energy management strategies for their operation. Eventually, Pugi et al. [149] applied the HiL approach to optimize the turbine bypass controllers and actuators used to regulate steam power plants during their transient operation. However, none of the works available in literature applies the HiL approach to energy conversion systems based on concentrated solar technologies. In a previous work [80], a proper control of the system was fundamental to optimize the operation of the different sub-systems with varying ambient conditions and user needs. Therefore in this work, is developed a smart HiL simulator of such a plant. The main novelty of the work relies on the use of the HiL approach for small-scale CSP-ORC plants able to perform the control algorithms and plant management optimization before its real operation in the field.

### 7.4.2 Methods and modeling

In this Section the main characteristics of the valves models and the pressure loss implemented in the tube models are described. Moreover, the methodology adopted to implement the HiL simulator is presented. Finally, the results adopting different gains for the PI regulators of the diverters are discussed in detail.

#### The integrated plant

As first instance, the Innova Microsolar prototype plant is used as sample to develop the HiL test. In order to assess the precise dynamic response of the subsystems to the diverters' adjustment, pressure drops have to be carefully modeled because the mass flow rate distribution over the hydraulic network depends on it. To do so, the characterization of the pipeline network is essential, length, diameter, roughness and number of bends have to be cataloged. For this purpose, the schematic in fig. 7.1 in the previous section is now modified in order to identify pipelines, diverters and tees, thereby the new schematic is depicted in fig. 7.31.

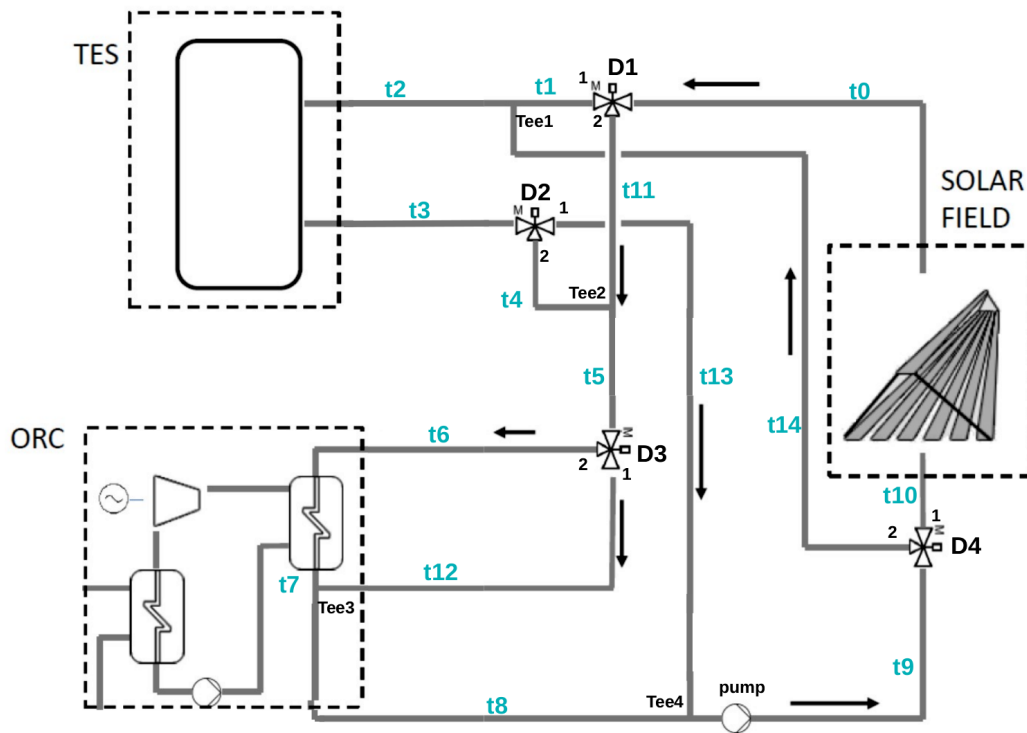


Figure 7.31. Scheme of the Innova Microsolar prototype plant.

As far as the Operation Modes concern, the chosen logic to switch from one OM to another one is the same described in the table 7.1 of Section 7.2.

#### The real control unit

The designed control unit has the aim both to monitor the overall system and to control and interact with the individual components (pre-operational checks,

start-up, operation monitoring, scheduling, controlled or emergency shut downs, monitoring charging and discharging of the thermal storage and on- and off-grid operation mode of the power plant). The control system has a specially developed built in software and its control algorithms have been designed to favor the use of the ORC system to cover the final user's energy demand and, in case of high DNI, to recharge as much as possible the thermal storage. In particular, the ORC thermal energy production should satisfy the domestic hot water and space heating demand, guaranteeing the highest possible energy and carbon savings.

The central control system does not have the internal control of the single subsystems, but collects information from them through a *field bus* connection. The control unit utilizes the collected information to achieve an efficient management and better integration of all subsystems. Indeed, the central control unit can manage the whole plant setup acting on the proportional valves ( $D_1$ ,  $D_2$ ,  $D_3$  and  $D_4$  of fig. 7.31) and on the main pump.

Control procedures are organized in two separate and parallel layers. The lower layer is responsible of system safety: if the system is not in a safe condition to operate, the control does not provide the enabling signal to the different subsystems, it blocks control procedures and deactivates supervision while, as soon as the system gets in a safe state, all functionalities are enabled again. The upper layer, instead, is responsible of the system control. The whole system can work in six different operating modes depending on the actual status of its sub-systems and the control logic switches between these admissible phases (see tab. 7.1).

The hardware architecture of the control system is reported in the following fig. 7.32 : an embedded PC is connected through the main switch to the external components (ORC and LFR) using *Modbus TCP-IP* open standard protocol. A *Wago* unit has been placed inside the control cabinet, connected to the field bus, with the aim of providing the management of digital and analog input/output.

### Models of the main subsystems

The mathematical models of the subsystems are the same reported in Section 6, for the pipelines, their dynamics is preliminary evaluated with varying mass flow rate and temperature of the oil. For the sake of clarity, the case of OM1 is shown in fig. 7.33. In this operation mode, according to fig. 7.31, tubes  $t_0$ ,  $t_5$ ,  $t_6$ ,  $t_7$ ,  $t_8$ ,  $t_9$ ,  $t_{10}$  and  $t_{11}$  are connected for a global length of about 37 m (based on the values reported later on in 7.20). As can be clearly noticed in fig. 7.33a, for a given inlet temperature (i.e. 250 °C), the oil takes a significant amount of time prior to rise in temperature at low mass flow rate. Specifically, more than 10 minutes are needed to achieve a steady state temperature in case of an oil mass flow rate of 0.22 kg/s and even a higher delay occurs for 0.11 kg/s. Moreover, in this case the peak temperature reached by the oil is reduced of about 15 °C, due to the significant thermal losses of the tubes. In particular, the overall time delay to reach 63 % of the peak value accounts to 1.56 mins, 7.03 mins and 13.98 min with 1 kg/s, 0.22 kg/s and 0.11 kg/s respectively. Instead, the dynamics of the tubes is not significantly influenced by the temperature of the oil as seen in fig. 7.33b, thus confirming that at 1 kg/s the delays are limited.

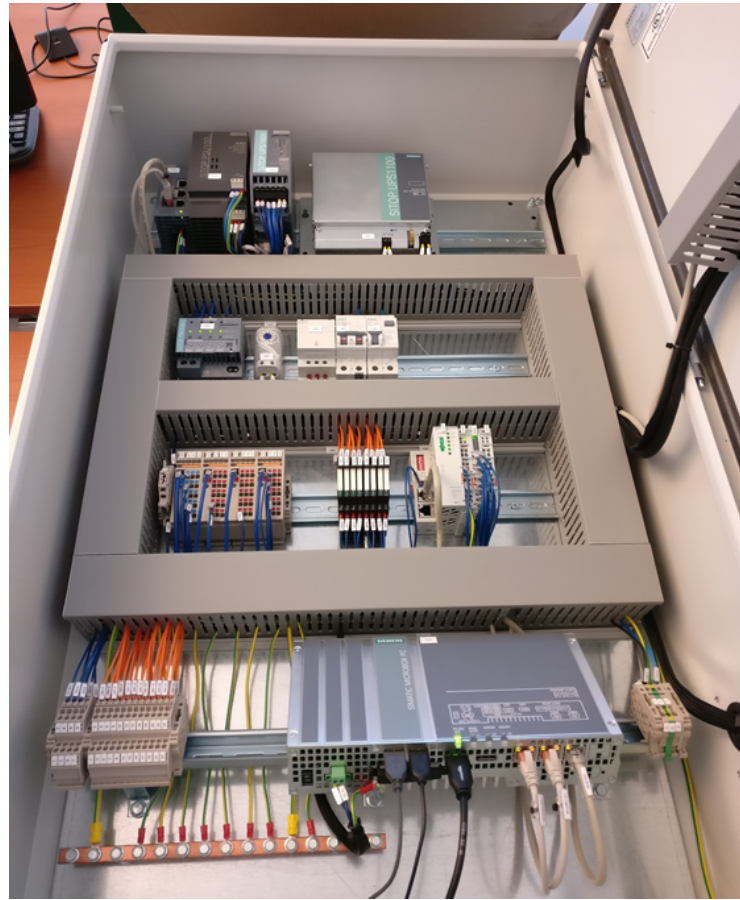


Figure 7.32. Real control unit cabinet.

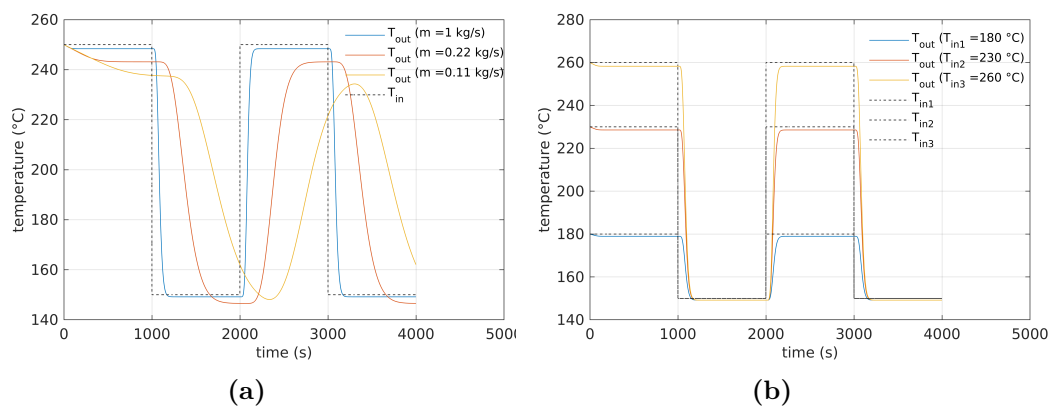


Figure 7.33. Dynamics of the pipelines in OM1 with varying: (a) oil mass flow rate and  $T_{in} = 250^{\circ}\text{C}$ ; (b) oil temperature and  $\dot{m} = 1 \text{ kg/s}$ .

### Model of the proportional valves

In order to properly simulate the actual operation of the plant at different OM, detailed models of the valves, namely the diverters, have been also included in MATLAB/Simulink. The real control unit, indeed, mainly acts on the diverters and the oil pump to control and adjust the operation of the integrated plant with varying ambient conditions and user needs. In the Innova Microsolar prototype plant the *SAMSON three-way valves 3535* (see the section in fig. 7.34) have been installed, whose main characteristics utilized in the dynamic simulation are reported in 7.19:

**Table 7.19.** Characteristic of the valves according to their datasheet [162].

Nominal diameter	50 mm
Seat diameter	40 mm
Rated travel	15 mm
$K_{vs}$	$32 \text{ m}^3/\text{s}$
Characteristic	Linear
Hysteresis	$\leq 1 \%$
Actuating time for rated travel	120 s
Position feedback signal	8 bit

In general, the behavior of a valve depends on the position of the stem, its previous condition and the amplitude of the received signal. These parameters may affect the stability of the control loop because of the non-linearity phenomena induced. Therefore, the model of the valve in MATLAB/Simulink (see fig. 7.35) contains several blocks which allow representing its actual behavior. In particular: (i) the saturation block, thus including into the model the input dead-band which does not result in any output; (ii) the derivative module related to the time for displacement of the stem, thus considering the time constant of the valve needed to be in place; (iii) a resolution block (8 bit) to take into account the resolution of the valve; and (iv) the backlash block to include the hysteresis of the valve assumed equal to 1 %. On the contrary, the stiction of the valve has been neglected, since it is not

reported in the datasheet of the valve and it needs to be evaluated experimentally. With reference to the Innova Microsolar plant, the Electric Actuator *Type 3374* [43] is installed. By using this actuator the stem of the valve takes about 120 s for the full movement of the stroke (15 mm) and the valve has a resolution of  $1/256 = 0.4$

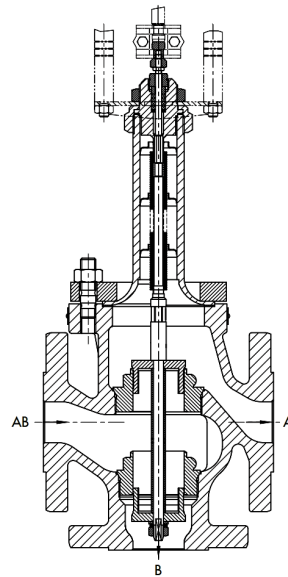


**Figure 7.34.** Section of the diverter (three-way valve) installed in the Innova Microsolar plant. This image appears in the datasheet of the manufacturer [162].

%

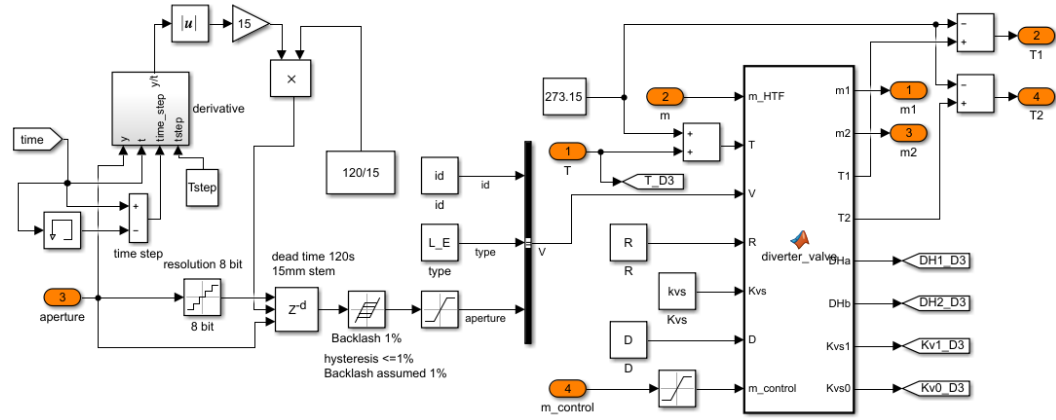


Figure 7.35. The valve block in MATLAB/Simulink.

The  $K_V$  values of the valve, which define the flow rate of the valve in each outlet generating a pressure drop of 1 bar, can be expressed as in eq. 7.6 and 7.7:

$$K_{v,1} = K_{vs} \left[ \frac{1}{R} + \left(1 - \frac{1}{R}\right) V_{ap} \right] \quad (7.6)$$

$$K_{v,2} = K_{vs} \left[ \frac{1}{R} + \left(1 - \frac{1}{R}\right) (1 - V_{ap}) \right] \quad (7.7)$$

where 1 represents the straight outlet, 2 the bended outlet,  $K_{vs}$  the flow rate that generates a pressure drop of 1 bar when the valve is opened at its maximum,  $R$  the rangeability of the valve, which is defined as the ratio of maximum to minimum flow controllable through the valve, and  $V_{ap}$  is the valve aperture, which ranges from 0 to 1. Furthermore, since the viscosity of the diathermic oil is highly affected by its temperature and in mid-temperature LFR plants the fluid is subject to significant temperature differences, a corrected  $K_{V,corr}$  value is considered according to *API standard 520* [2] as in eq. 7.8:

$$K_{v,corr} = \frac{1}{0.9935 + \frac{2.878}{Re_{seat}^{0.5}} + \frac{342.75}{Re_{seat}^{1.5}}} \quad (7.8)$$

where the Reynolds number evaluated in the seat is expressed as  $Re_{seat} = 4Q/P \cdot \nu_{oil}$ ,  $P = 2\pi D$ , with  $Q$  the volumetric flow rate,  $P$  the wetted perimeter of the cross sectional area  $A$  and  $\nu_{oil}$  the kinematic viscosity of the oil. This means that the Reynolds number depends only on the fluid dynamics of the oil through the valve. Hence, the  $K_{vs}$  values of the valve in each outlet can be assessed as:

$$K_{vs,1} = K_{v,1} \cdot K_{v,corr} \quad (7.9)$$

$$K_{vs,2} = K_{v,2} \cdot K_{v,corr} \quad (7.10)$$

whilst the corresponding pressure losses can be calculated as in equations 7.11 and 7.12:

$$\Delta p_{v,1} = \frac{K_1 \rho_{oil} V_{oil}^2}{2} + 10^5 \left( \frac{Q^2}{K_{vs,1}^2} \right) \quad (7.11)$$

$$\Delta p_{v,2} = \frac{K_2 \rho_{oil} V_{oil}^2}{2} + 10^5 \left( \frac{Q^2}{K_{vs,2}^2} \right) \quad (7.12)$$

where  $K_1$  e  $K_2$  are the additional pressure losses in the straight and bended outlet respectively,  $\rho_{oil}$  the oil density and  $v_{oil}$  the oil velocity which depends on the asymmetry of the valve and its regulation. For the sake of clarity, fig. 7.36 report the trends of the  $K_{vs}$  values and pressure drops with the aperture in case of a linear valve, as those installed in the prototype plant in Almatret. For those calculations, an inlet mass flow rate and temperature of the oil equal to 0.2 kg/s and 10 °C have been considered.

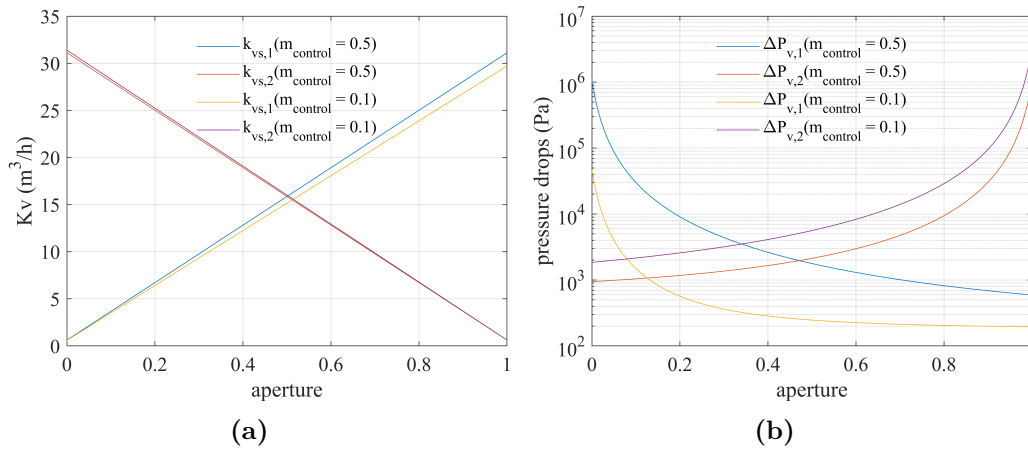


**Figure 7.36.**  $K_{vs}$  values (a) and pressure drops (b) with the aperture for a linear valve.

In a real plant, the balance of the mass flow rate in each part of the circuit depends not only on the pressure drops in the valves, but also on those in each tube. Hence, in the model also the latter are taken into account according to the following equation 7.13:

$$\Delta p_t = f \cdot \left[ \left( \frac{L}{D_{int}} \right) + 0.3 \cdot n_{90} \right] \rho_{oil} v_{oil}^2 / 2 \quad (7.13)$$

where  $D_{int}$  is the internal diameter of the tube,  $n_{90}$  is the number of bends at 90 degrees,  $\rho_{oil}$  and  $v_{oil}$  are the oil density and bulk velocity respectively and  $f$  the friction factor obtained according to [63] as in equation 7.14:

$$f = \left(\frac{64}{Re}\right)^a \left[0.75 \ln\left(\frac{Re}{5.37}\right)\right]^{2b(a-1)} \left[0.88 \ln\left(\frac{6.82D}{\epsilon}\right)\right]^{2(a-1)(1-b)} \quad (7.14)$$

$$a = \frac{1}{1 + \left(\frac{Re}{2712}\right)^{8.4}} \quad (7.15)$$

$$b = \frac{1}{1 + \left(\frac{Re\epsilon}{150D_{int}}\right)^{1.8}} \quad (7.16)$$

With  $\epsilon$  the roughness of the surface. In this case, the Reynolds number has been calculated based on the mean temperature and velocity of the fluid along the tube length, considering all the values of the thermal nodes. The ratio  $D/\epsilon$  is kept constant and equal to 500, which corresponds to a very smooth surface. Hence, according to the plant prototype installed in the city of Almatret, the following characteristics of the tubes connecting the different subsystems have been considered into the model (see fig. 7.31 for the acronyms of the tubes).

**Table 7.20.** Characteristics of the tubes modeled in MATLAB/Simulink.

Tube	Length (m)	Number of thermal nodes	$n_{90}$
t0	9.5	10	5
t1	0.25	2	0
t2	3	3	1
t3	3	3	2
t4	0.8	2	1
t5	2.5	3	3
t6	0.25	2	1
t7	0.25	2	0
t8	0.25	2	0
t9	2	2	1
t10	19.1	20	10
t11	3.4	4	2
t12	0.4	2	0
t13	1.5	2	1
t14	4.58	5	0

Hence, the hydraulic circuit is solved by applying the *Hardy Cross method* [167], which was originally proposed in 1936 to analyse the flow in conduits, according to an iterative procedure as summarized in fig. 7.37.

This method is applicable to closed-loop pipe networks. The outflows from the system are assumed to occur at the nodes, where a node is the end of each pipe. This assumption would therefore result uniform flow in the pipelines distribution systems. Consequently, the hydraulic solution is needed only when nodes are presents, for example in OM4 and OM6, whereas in the other operating modes the oil flows in a closed loop where the stream is not divided. When all the subsystems are connected, the pressure drops are completely unknown, thus the iterative procedure

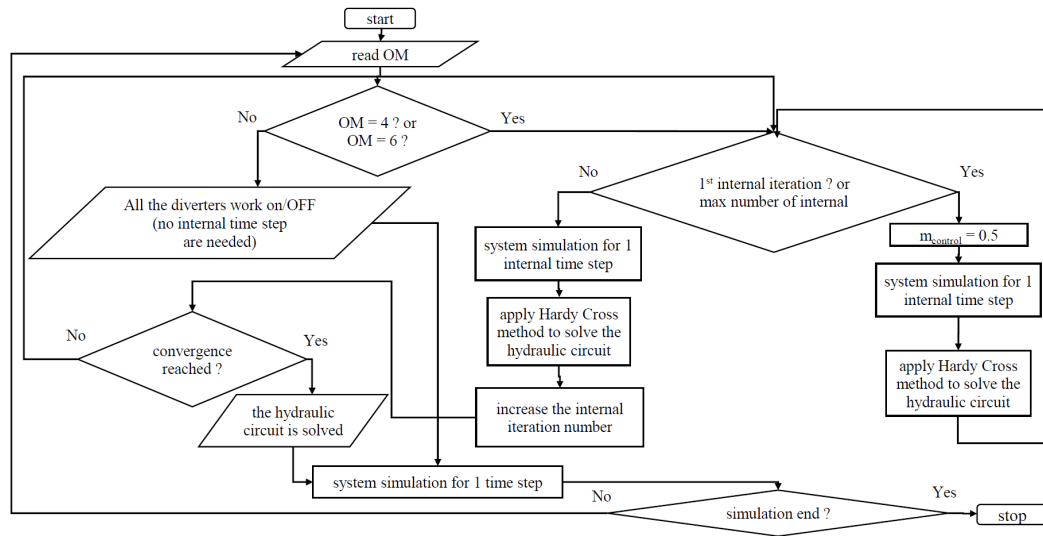


**Figure 7.37.** The iterative procedure to solve the hydraulic circuit.

starts with an initial guess value of the flow rate per each branch, by simulating the whole network (pipeline, tees, valves) the total pressure drops at the nodes can be calculated. At this point, assuming that the head loss have the simplified form, a first order correction factor to the flow rates is applied as follow:

$$\Delta Q = \frac{-\sum rQ^2}{\sum 2rQ} \quad (7.17)$$

where the numerator represents the total head loss in the specific loop (by subtracting the counter-clockwise head loss from the clockwise head loss), and the denominator is the first term of the Taylor expansion. After the correction have been applied to each pipe in a loop and to all loops, a second trial calculation is made for all loops. This procedure is repeated till the flow rate variation becomes negligible. The hydraulic network is solved within an internal time step, and the external control system can only see a perfect balanced network. The mass flow rate distribution of the diverter between the two outlets can be assumed equal to the volumetric flow rate since the fluid has the same density, thus it is calculated as:

$$\dot{m}_1 = \dot{m}_{oil} \cdot \dot{m}_{control} \quad (7.18)$$

$$\dot{m}_2 = \dot{m}_{oil} \cdot (1 - \dot{m}_{control}) \quad (7.19)$$

where  $m_{control}$  is the ratio between the mass flow rate from outlet 1 and the inlet mass flow rate to the valve.

### 7.4.3 The hardware-in-the-loop framework

Hence, the MATLAB/Simulink blocks have been designed in order to interact with the real control system running on an external *Programmable Logic Controller* (PLC). As already mentioned in section 7.4.2, the main control unit is responsible for the monitoring of the overall system, the actuation of the system-level control

procedures and the safety of the global plant. In the real system architecture this central control unit interacts in turn with the different subsystems, using a *Modbus TCP-IP* communication: the central controller can access all systems actuators and act as master agent. Hence, for these reasons the developed MATLAB/Simulink blocks emulate the subsystems control units or a part of them, following the same logic input/output as in the prototype plant. Therefore the HiL framework consists of a simulated plant model running on a standard PC and in a programmable and tunable control logic running on a PLC. Potentially, once the control logic has been validated, the same software could be used in the real system as it is, because the simulated model emulates exactly the real plant. However, one of the most critical aspect in a HiL system is the signal and data synchronization between components involved in the system. In particular, the simulation system (running on a standard PC) and the control system (running on a PLC) have to be synchronized. Despite the higher computational power, the former works with complex models, having configurable simulation step but no deterministic execution time. On the other hand, the second has lower computational power and processor frequency, but it is based on a deterministic cycle time.

Since the simulation time spent to complete one computational time step may differ from the hardware specification of the PC or with its actual load, a synchronization procedure is required as depicted in fig. 7.38:

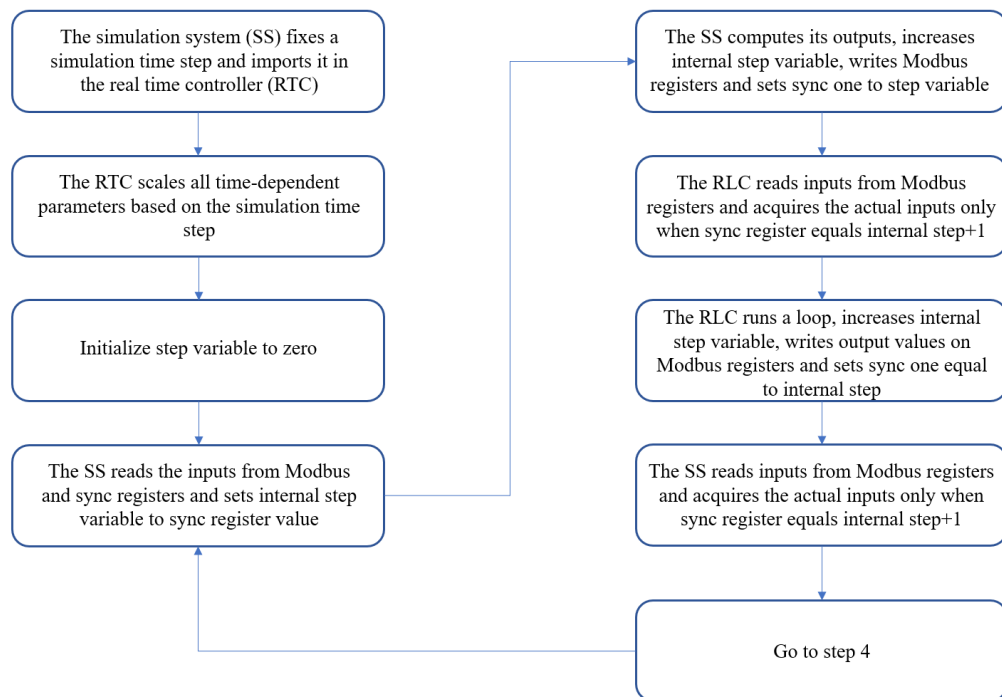


**Figure 7.38.** The sync procedure between the simulation system and the real time controller.

Therefore, according to the developed HiL approach, the Matlab/Simulink model interacts with the PLC controller with respect to the following list of input and

output parameters:

**Table 7.21.** List of parameters.

Input	Parameter	Specifications
Diverters	Aperture $V_{ap,D1}$ , $V_{ap,D2}$ , $V_{ap,D3}$ , $V_{ap,D4}$ ,	Discrete 1/50 range $0 \div 1$
Pump	Flow rate pump $\dot{m}_{pump}$	Continuous range $0 \div 3$ kg/s
Output	Parameter	Specifications
Diverters	Flow rate $\dot{m}_{D1}$ , $\dot{m}_{D2}$ , $\dot{m}_{D3}$ , $\dot{m}_{D4}$	Continuous range $0 \div 3$ kg/s
Linear Fresnel Reflector	Temperature $T_{LFR,out}$	Continuous $0 \div 320$ °C
	Flow rate LFR	Continuous range $0 \div 3$ kg/s
Direct solar irradiance	DNI	Continuous $W/m^2$
Thermal Energy Storage	Temperature $T_{TES,av}$	Continuous $0 \div 280$ °C
	Flow rate TES	Continuous range $0 \div 3$ kg/s
Organic Rankine Cycle	Flow rate ORC	Continuous range $0 \div 3$ kg/s
Operation Mode	$OM_{des}$	Discrete $-1 \div 6$

More precisely, the diverters are regulated by means of the  $V_{ap}$  parameter (eq. 7.6 and 7.7), according to their rangeability based on the datasheet of the manufacturers [162]. Another block of the valve receives as input from the PLC controller the value of its aperture, which range from 0 to 1.

#### 7.4.4 Results and discussion

In this section the potential of the HiL simulator is presented and some significant control algorithms scenarios are presented with respect to the management of the proportional valves ( $D_1$ ,  $D_2$ ,  $D_3$  and  $D_4$  of fig. 7.31) and of the main pump. Indeed, HiL technique allows to easily validate control logics, to discard ineffective approaches and to optimize the more promising ones.

First of all, the consistency of the HiL framework is verified with respect to the MATLAB/Simulink simulation in case of no interactions with the real control unit. More precisely, the performance of the plant in terms of thermal and electrical power output is assessed for a typical winter week. Weather data (i.e. solar radiation and ambient temperature) have been taken from Energy+ [16] database for the city of Lerida in Spain which is close to the town where the plant is located. Table 7.22 reports the cumulated thermal and electrical energy production and losses during the winter week under investigation, as well as the working hours of the system in the

different OM. Moreover, the performance of the HiL approach has been compared with the simulation model also in terms of computational time, as reported in 7.22. A time step of 10 s is considered and simulations run on a PC with *Intel® Core G840 2.8 GHz* processor.

**Table 7.22.** Comparison between HiL simulator and MATLAB/Simulink simulation model.

	<b>MATLAB/Simulink simulation</b>	<b>HiL simulator</b>
$E_{LFR,in}$ (kWh)	2606.6	2606.6
$E_{LFR,out}$ (kWh)	700	699.9
$E_{TES,in}$ (kWh)	73.0	71.9
$E_{ORC,in}$ (kWh)	512.0	552.6
$E_{ORC,out}$ (kWh)	378.5	410.6
$E_{ORC,el}$ (kWh)	31.8	32.1
$E_{TES,loss}$ (kWh)	147.3	148.1
$E_{tubes,loss}$ (kWh)	204.0	205.7
OM1 (h)	10.57	10.57
OM2 (h)	118.10	116.06
OM3 (h)	25.25	25.25
OM4 (h)	10.81	10.81
OM5 (h)	3.27	5.31
OM6 (h)	-	-
CPU time (min)	27.67	273.23

It is evident that the obtained performance is similar between the HiL simulator and the MATLAB/Simulink simulation, thus proving the conformity of the former with respect to the simulation system. In terms of computational efforts, about four hours and an half are needed to test the real control system, instead of a full week, without considering any system downtime or other mechanical or hydraulic problems that could even extend such period. At the same time, the MATLAB/Simulink simulation model takes 10 times less computational time than the HiL approach. The longer amount of time of the HiL architecture respect to the simulation model is mainly due to the following two factors: firstly the communication overhead introduced by *TCP-IP modbus* and secondly the minimum cycle time of the PLC-based control unit.

In order to better appreciate how the plant switches from an operation mode to another, figure 7.39 shows the trends of the power and the sequence of the operation mode for a typical winter day. For the day under investigation the plant works in OM1, OM3 and OM4 also. This means that even in winter time the solar field is able to supply both the ORC and TES when solar radiation is high enough. However in this case, the TES does not achieve its melting temperature and, as a consequence, does not supply the ORC when the solar radiation is low (OM5 and OM6).

Once verified the consistency of the adopted HiL technique, the HiL simulator is firstly used to optimize the control algorithms of the plant with respect to the diverters. In particular,  $D_1$ ,  $D_3$  and  $D_4$  (see fig. 7.31) are considered in the following analysis because of their relevance in the mass flow rate control during OM4 (LFR

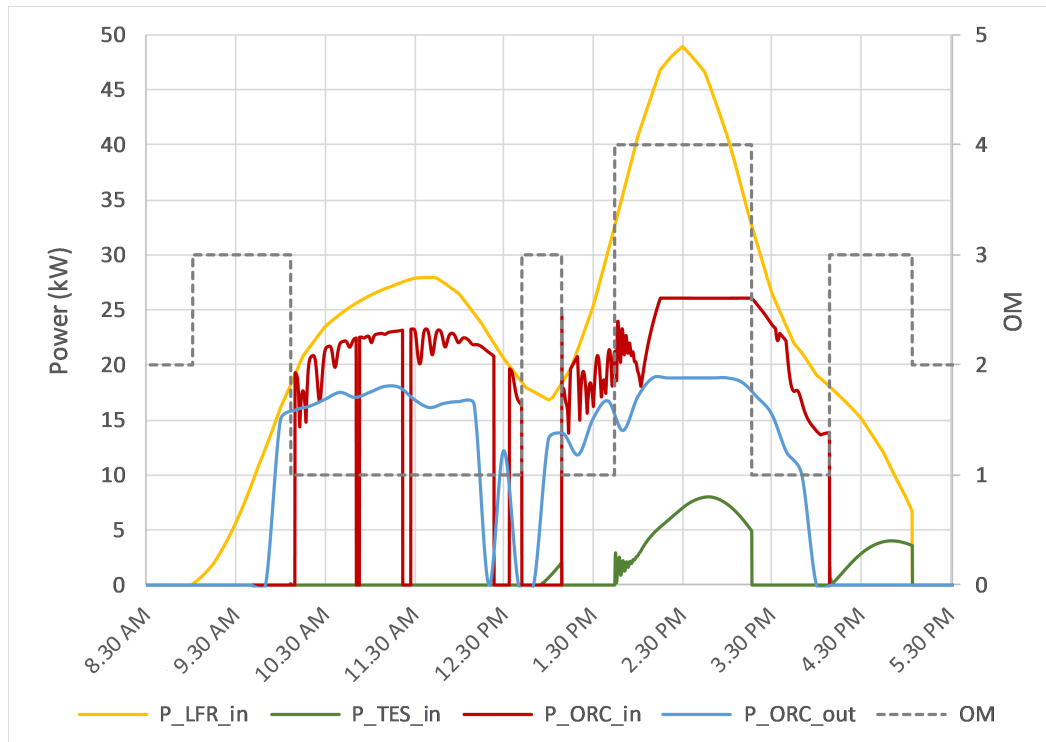


**Figure 7.39.** Plant operation in a typical winter day (04/01/20).

supplies both the LHTES and the ORC) and OM6 (both LHTES and LFR supply the ORC). A time step equal to 1 s is considered in this analysis in order to better appreciate any potential fluctuation of the flow rate. In particular, the optimal proportional and integral gains of the PI-based control are assessed during plant operation for a winter day. Hence, each PI-based controller is tuned, freezing the control output of the other controllers in order to avoid any negative interaction between the different controllers, and finally the whole system behavior is verified with all the controllers running in parallel. In the following, the tuning process of the controllers has been shown. HiL technique allows changing gains and parameters, appreciating immediately their effect.

Figs. 7.40 report the trend of the mass flow rates in the different subsystems of the plant with varying DNI and as a consequence OM. More precisely, trends of fig. 7.40a are obtained in case of small gains of the PI-based control, those of fig. 7.40b in case of high gains, while fig. 7.40c shows the trends in case of the optimal gains.

Figures 7.41a and 7.41b show in more detail the trend of the mass flow rates during the switch from OM1 to OM4, while figs. 7.41c and 7.41d the changes from OM1 to OM6 in case of small gains. In particular, figs. 7.41b and 7.41d focus on the obtained mass flow rates in the diverters under investigation with a comparison to the set-point values. As can be noticed, small gains of the integral PI-based control do not allow reaching steady state conditions in short time. Indeed, while switching from OM1 to OM4, part of the flow goes to the TES, but it takes some time prior to reach the set point ( $m_{1,D1}$ ). On the contrary, a higher amount flows to

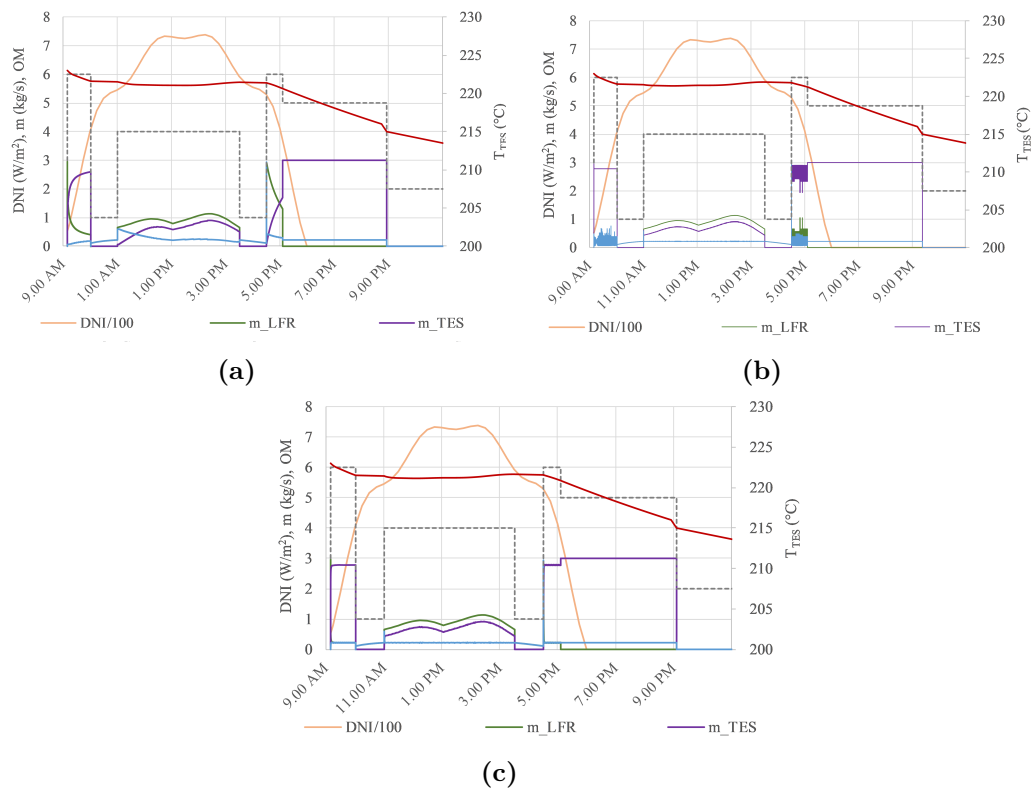


**Figure 7.40.** Trend of the mass flow rate with varying DNI and OM for (a) small gains; (b) high gains; (c) optimal gains (06/01/20).

the ORC unit at the beginning. Hence, in case of such gains the plant is not able to efficiently respond to the variation of the operating conditions due to changes in ambient conditions or user needs.

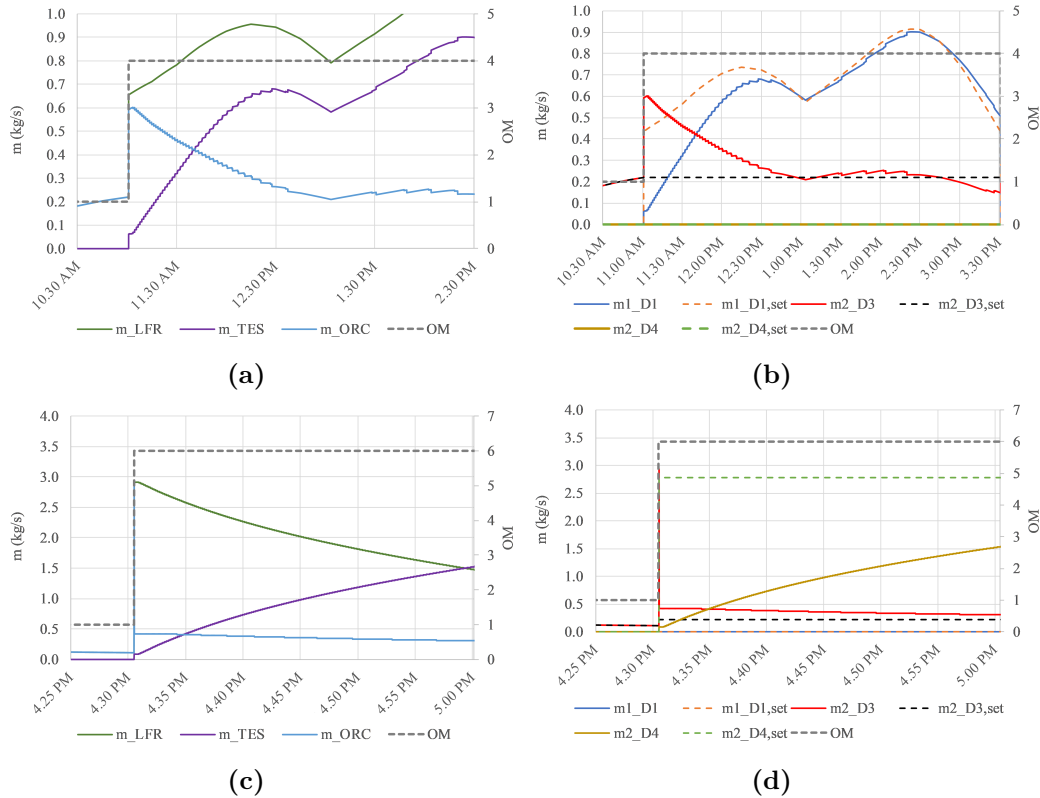


**Figure 7.41.** Details of the mass flow rates in the different subsystems (a, c) and in the diverters (b, d) during changes of the operation mode of the plant in case of small gains (06/01/20).

On the contrary, figs. 7.42 report the trend of the mass flow rates in the different subsystems and in the diverters in case of high gains. In this case, the system is too much sensitive to any change in the operating condition and tends to fluctuate around the set-point values in particular conditions. As can be seen in fig. 7.42d, this occurs especially in OM6, when the outlet of the diverters are almost fully opened or closed and, as a consequence, a small motion of the actuator corresponds to large change in the mass flow rate. Moreover, dynamic behavior often consists in overshooting phenomena. Therefore, also in this case the plant works in off-design conditions.

Therefore, the gains of the PI-based control have been modified until an optimum operation is achieved as reported in fig. 7.43. As can be clearly seen, in this case the plant achieves steady state conditions in very short time (order of magnitude of few minutes) thus proving its flexibility to varying input and constraints. During the switch from OM1 to OM4, the mass flow rate in the diverter  $D_3$  achieves the set point and, in order to comply with the small changes in the solar field, mass flow rate  $m_{2,D3}$  slowly fluctuates around this value due to hysteresis of the valve ( $<5\%$

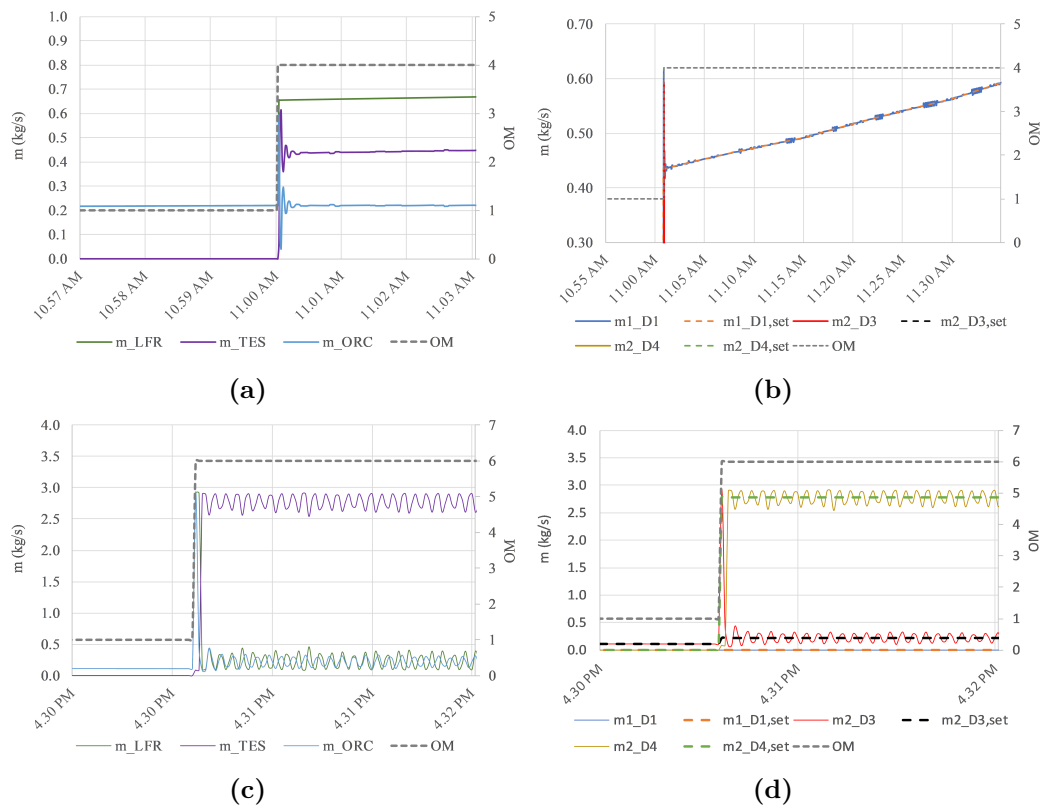


**Figure 7.42.** Details of the mass flow rates in the different subsystems (a, c) and in the diverters (b, d) during changes of the operation mode of the plant in case of high gains (06/01/20).

of set-point value). Analogously, during the switch from OM1 to OM6 the mass flow rate in the diverter  $D_4$  reaches the set point in short time. However, in this case the fluctuations around the set point are higher, since the diverter is adjusting the flow rate near the thresholds of its operating range (operating flow rate 2.8 kg/s on a maximum of 3 kg/s).

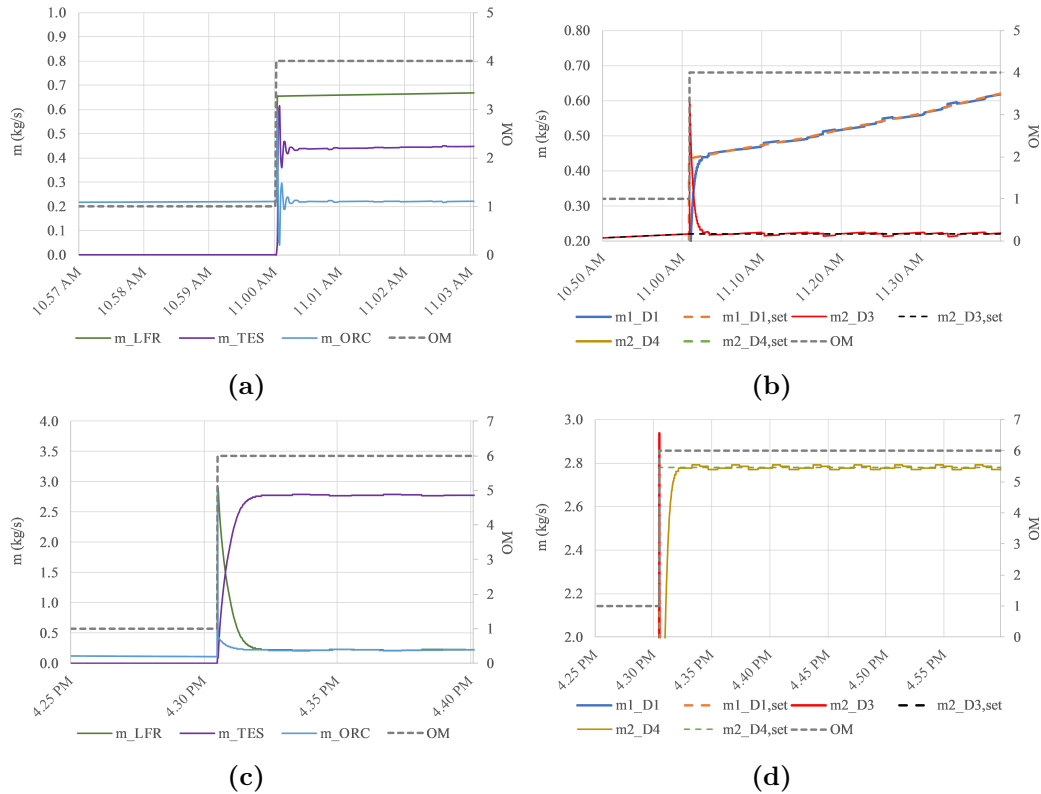


**Figure 7.43.** Details of the mass flow rates in the different subsystems (a, c) and in the diverters (b, d) during changes of the operation mode of the plant in case of optimal gains (06/01/20).

Eventually, the potential of the HiL framework is presented also with respect to the analysis of the best control strategy for the micro-CHP plant: different approaches have been tested in order to determine their pros and cons and to define the most performing one. In order to maximize the electrical power output from the ORC, the control strategy aims at assuring the nominal oil temperature of 210 °C at the inlet of the ORC unit. This set-point allows the ORC system working at its maximum electric conversion efficiency. In particular, three different control actions have been implemented: (i) acting on the oil pump to adjust the flow rate on the basis of the LFR outlet temperature; (ii) acting on the oil pump on the basis of the ORC inlet temperature; (iii) acting on the aperture of the  $D_3$  diverter on the basis of the ORC inlet temperature. For the scope of this analysis a DNI of 650 W/m<sup>2</sup> is considered, which causes the plant operation in OM1. In this operation mode, the mass flow rate of the oil ranges from 0.11 kg/s to 0.22 kg/s. Fig. 7.44 shows the mass flow rate of the oil and the trend of the temperatures by acting on the oil pump on the basis of the LFR outlet temperature in case of low proportional gains, low

integral gains and mid gains respectively. In the first control strategy, independently from the gains, at the beginning the mass flow rate is low and, because of the high thermal inertia of the plant (pipelines etc), the oil takes a consistent time to achieve the set-point temperature of 210 °C. Indeed, more than 10 mins are required to heat up the oil loop circuit (see the initial horizontal line of  $T_{LFR,out}$  in all the figures). Once achieved the set-point, the fluctuations of the temperatures of the oil are lower in case of low integral gains, but the pump flow rate is continuously adjusted, thus extending the transient operation of the plant. On the contrary, in case of mid gains, once the set-point temperature is achieved, the mass flow rate of the pump is reduced and achieves a steady state of about 0.14 kg/s. However, also in case of mid gains the oil achieves the nominal temperature of 210 °C at the inlet of the ORC unit with a certain delay compared to the outlet of the LFR solar field. Moreover, any change in the ORC temperature is slowly compensated, thus proving the deficiency of this control strategy in assuring the best operation of the ORC unit.

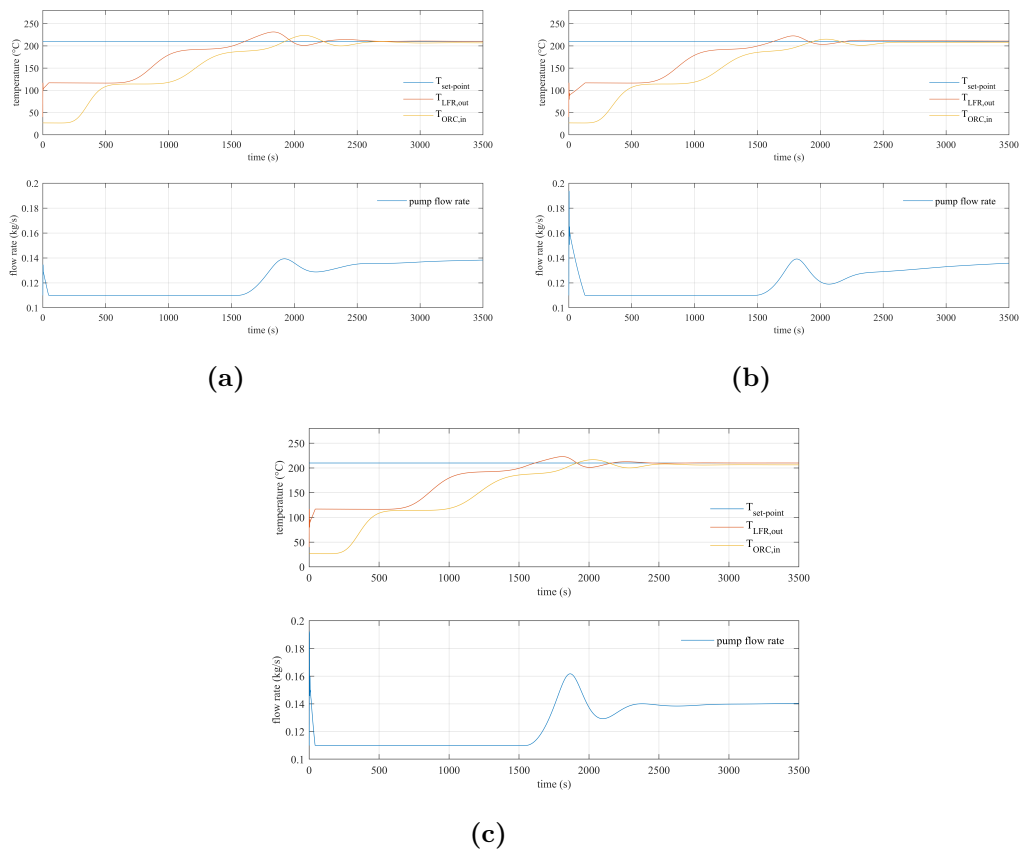


**Figure 7.44.** Control of the mass flow rate of the pump based on the outlet temperature of the oil from the solar field; **(a)** low proportional gains; **(b)** low integral gains; **(c)** mid gains.

In the second control strategy, instead, the mass flow rate of the pump is adjusted based directly on the signal of the inlet temperature to the ORC. However, any adjustment of the pump flow rate is reflected in a fluctuation of the inlet temperature of the oil to the ORC unit, thus requiring a longer time prior to reach the steady

state condition. In particular the distance between the sensor and the actuator can cause a delay in the action requested by the PLC, causing unwanted instability in the system. Hence, in this case a gain scheduling approach is applied once the oil achieves the set point temperature at the inlet of the ORC. More precisely, the proportional and integral gains are reduced by ten times. In this way the effect of the control action disturbs less the stability of the system, thus reducing the fluctuations in the mass flow rate of the pump and, as a consequence, those of the oil temperature.

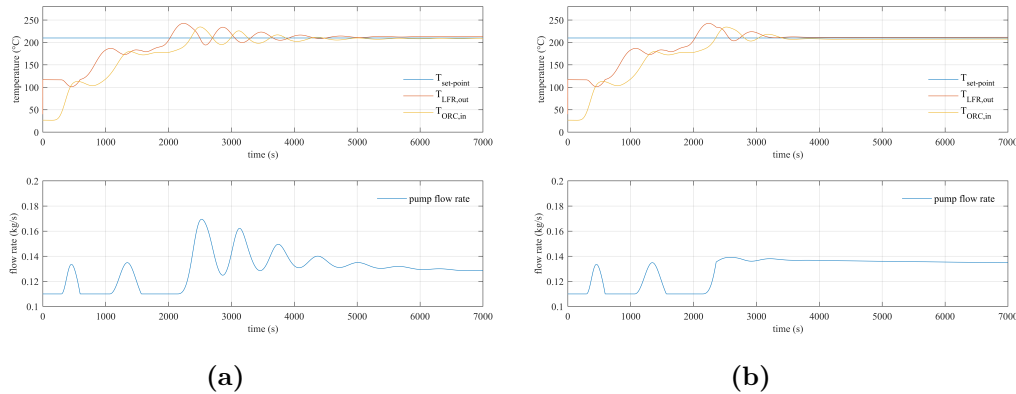


**Figure 7.45.** Control of the mass flow rate of the pump based on the inlet temperature of the oil to the ORC unit; (a) no gain scheduling; (b) gain scheduling.

Nevertheless, the results of both strategies highlight that an efficient and fast control of the inlet temperature of the oil to the ORC unit can not be performed by acting on the pump flow rate only. Hence, a third strategy is investigated and tuned according to which the ORC inlet temperature of the oil is controlled by acting on the aperture of the diverter  $D_3$ . The effectiveness of this control strategy is evaluated for different mass flow rate of the pump, as reported in figs. 7.46. More precisely, in case of fig. 7.46a a total mass flow rate of the oil of 1 kg/s is considered, while in case of fig. 7.46b of about 0.22 kg/s. This specific value is the maximum input flow that the ORC can manage: the pump works at fixed speed, while a proportional valve can act to modulated it. From these figures it can be clearly noticed that higher overall mass flow rates entail lower fluctuations of the oil temperature at the inlet of the ORC, but at the same time longer periods for heating up the fluid. Therefore, the optimum mass flow rate of the oil pump needs to be defined as a compromise between the better operation of the ORC unit at constant operating conditions and the lower electrical power consumption of the oil pump based on the ambient conditions and the states of the different subsystems of the m-CHP plant.

### 7.4.5 Conclusions

In this work a hardware-in-the-loop simulator of a novel micro combined heat and power system is presented and its potential in optimizing the control algorithms and the operation of the plant is shown.

In order to properly emulate the performance on a real mCHP system, the

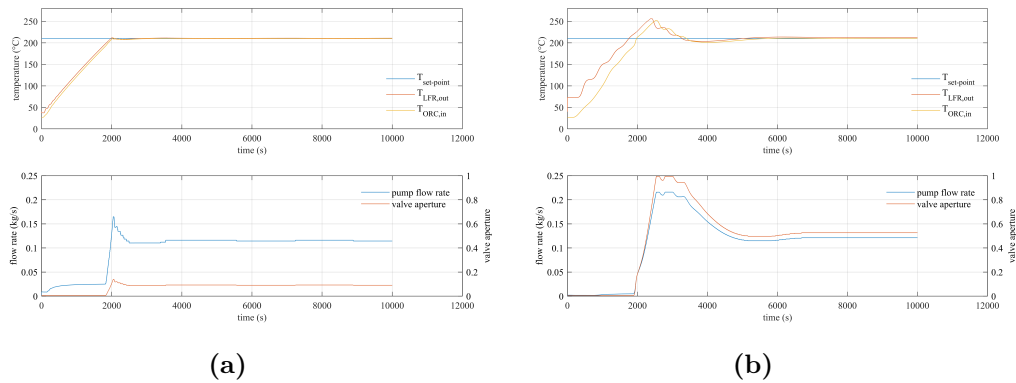


**Figure 7.46.** Control of the inlet temperature at the ORC unit based on D3 aperture; (a) total flow rate of 1 kg/s; (b) total flow rate of 0.22 kg/s.

HiL simulator has been accomplished with ad-hoc mathematical models of the main components developed in MATLAB/Simulink. The micro CHP of the Innova Microsolar project has been considered for testing the HiL approach. More precisely, the developed simulator is coupled with the real control unit of the plant in order to support the optimization of the control algorithms prior to the experimental tests campaign. The analysis carried out proves that such technique can be usefully and efficiently adopted to both perform the optimization of the control algorithms (PID control tuning) of the integrated system and analyse the best control strategy of the micro-CHP plant. More precisely, the analysis has shown:

- acting on the proportional and integral gains of the diverters, it is possible to find a configuration which assures a robust and fast response of the plant during the switch from the different operation modes. It confirms the relevance of a proper tuning of the PID parameters;
- acting on the oil pump to adjust the flow rate based on the LFR outlet temperature or the ORC inlet temperature does not properly assure the best operation of the ORC unit. Indeed, with these control strategies significant fluctuations of the inlet temperature of the oil to the ORC unit occur, which cause a longer time prior to reach the steady state condition;
- the best control strategy to assure the ORC unit operation at constant operating conditions consists in circulating higher amount of oil flow rate in the solar field loop and acting on the aperture of the D<sub>3</sub> diverter to assure the nominal ORC inlet temperature. However, the optimum mass flow rate of the oil pump needs to be defined as a compromise between the better operation of the ORC unit at constant operating conditions and the electrical power consumption of the oil pump.

Hence, the powerful effect of the developed HiL framework is demonstrated and confirmed also in case of novel configurations and integrated energy systems. In particular, the presented HiL has provided useful insights into the real operation of CSP-ORC plant with varying ambient conditions and operation modes. This

aspect can significantly reduce the potential critical issues during its commissioning, supporting a smoother implementation of the real plant.



## Chapter 8

# Conclusions and future works

### 8.1 Conclusions

The PhD research presented here, deals with a small scale solar CHP designed for dwellings. Goal of this research consists of developing a numerical framework of a micro solar cogenerator able to analyze: (i) thermal and electrical production, (ii) sensitivity of the outcomes from the mathematical models used, (iii) room for improvements adding a further storage management, (iv) the rapid control design reliability connecting the simulated environment to an external device.

In the dissertation several technologies are characterized and compared to spot out one of the best plant configuration in compliant with individual dwellings and small business residential buildings application. Obviously, performances and reliability have been taken into account on the basis of the current SoA. From this survey, a solar field with a *Linear Fresnel Reflector* (LFR) of 80 kWth can be adequately adopted to produce solar thermal energy at modest temperatures of 250-280 °C together with diathermic oil as Heat Transfer Fluid. The *Organic Rankine Cycle* (ORC) well fits the power block requirements, 2 kWe have been chosen as design power. Due to the significant solar multiple, and to assure greater flexibility in the demand request, a 4 hours thermal storage was needed. Compactness is mandatory in this kind of plants, so a latent heat storage was chosen to increase both the energy density and the thermal efficiency of the power block. Finally, to overcome the heat transfer issues in adopting *Phase Change Material* (PCM) as storage medium, a novel solution was thought: immersed heat pipes, in fact they assure a quick charging and discharging during the transients raising the thermodynamic performance of the plant.

As stated before, a preliminary investigation on the thermal and electrical production was performed in the city of Lerida (Spain), characterised by an intense solar radiation and clear sky conditions. The Organic Rankine cycle was allowed to reject heat from the condenser at fixed temperature of 60 °C (high temperature radiators supply) and performances were evaluated. In particular, although the annual peak overall conversion efficiency in summer is about 27.4 %, over the year, the ORC unit can work for more than 3374 h, producing electric and thermal energy for about 6,500 kWh and 58,800 kWh respectively. This first goal gives a preliminary estimation that two household electricity demand and four household

thermal demand can be fulfilled. Although the control strategy of the plant was aimed at maximizing the electric output, the designed ORC can provide a monthly average electric efficiency around 7.8 %. From this study other interesting matters had come up, first of all the considerable amount of heat losses in the pipeline network and the thermal storage.

Crucial point in Concentrated Solar Plants are the heat losses, they considerably affect the performances evaluations if no particular care is taken during the modeling of such part. On this purpose, four different mathematical models of the tubes were compared with varying fluid regime (in terms of temperature derivative "rr" at the inlet and flow velocity). The results revealed that lumped models lacks in accuracy especially in winter season, when the temperature gradients implies a more spatial detail in the analysis. On the other hand, whenever the longitudinal thermal gradient inside the pipeline is negligible, a lumped model for dynamic simulations is accurate enough, thus significantly reducing the computational time without losing accuracy. Quantifying, the 1 D radial model entails significant deviations on the predicted output temperature for *Heat Transfer Fluid* (HTF) velocities in the range 0.1-1 m/s when  $rr > 3$  K/s, whilst the 1 D longitudinal model is in good agreement with the results of the 2 D model at any rr for HTF velocities higher than 0.1 m/s. Finally, the lumped model agrees with the results of the 2 D model at HTF velocities beyond 1 m/s.

The performance assessments clearly shown considerable losses from the thermal energy storage (TES) derived by its control logic. Indeed, for maximizing the heat transfer in the oil-heat pipe- PCM loop, it has to be charged or discharged in the narrow "temperature window" spotted out by its phase change. In winter season, the weak solar radiation can not rise the TES temperature beyond which it can be exploitable by the ORC unit, as a result the TES is slightly charged and after that it wastes heat. In light of this issues, an innovative *Fuzzy Logic Controller* (FLC) was developed to manage a subdivided TES into six modules with the same capacity, called here sub-LHTES. The FLC establishes the modules to be connected realising a TES partialisation, in this way it is possible to charge less modules in winter, being at a adequate temperature, they can be exploited by the ORC, avoiding unwanted wasted heat. The FLC action revealed a significant increase in the storage efficiency during winter seasons, furthermore, the ORC electric efficiency, as well as the operating time, were higher in winter where the yearly electric energy production rises of about 5 %. An interesting result concerns the significant reduction in solar field defocusing, it totals 30 % less, on the other hand, the FLC pushes up the mean temperature of the pipeline network entailing more than 9 % of additional thermal losses.

Purpose of the micro CHP is the building integration, in this regard, by means of an integrated plant-building model was possible to asses the effects of the final user dynamic energy demand on the ORC electric and thermal performance. Furthermore, the incidence of the design parameters of the building heating and cooling system on the energy operational costs was evaluated and an optimal configuration was proposed for the considered case study. Since the ORC electric performance greatly affected by condenser inlet temperature, the past assumptions of 60 °C was taken off connecting the simulated plant to a building. The trigeneration version of the plant can exploit efficiently the large amount of thermal energy production especially in

summer. A bigger storage tank placed in bottoming to the ORC helps in increasing the demand coverage limiting wasted energy and energy production from back-up generators. On the other hand, space constraints and investment costs limit its dimensions. Concluding, the proposed micro solar Organic Rankine Cycle plant (2 kW<sub>el</sub>/ 18 kW<sub>th</sub>) can provide space heating, space cooling and domestic hot water to a number of 100 m<sup>2</sup> dwellings in the region of Lerida ranging from 4 to 6 in order to maintain the overall energy demand coverage higher than 50 %, corresponding to operational cost savings of more than 35 %.

To properly operate the plant, some parameters have to be carefully monitored both for energy performance and reliable reasons. A further research was carried out on the solar receiver tube for Parabolic Trough Collector (PTC) and LFR. Due to the variable solar source, the solar field is often forced to work in part-load conditions, thus a further study was addressed to quantify the effect on the receiver tube. Currently, the milestone of the thermal models for receiver tubes is the Forristall. It was designed only to evaluate the receiver thermal efficiency at nominal HTF flow rate (design point), despite its good accuracy, it can not estimate the internal wall temperature in contact with the HTF outside these conditions. This parameter is important to avoid excessive thermal stress of the receiver tube, thus a depth literature review was undertaken to characterize the thermal resistance to improve this existing thermal model. All the evaluations were accomplished with the optical and geometrical characteristics of the Innova Microsolar solar field, results shown that the HCEOI-12 receiver is more performing than the LS-2 (tested by Forristall). Moreover, unlike PTCs, the LFR geometry reduces the LFR ability to collect thermal energy under 300 W/m<sup>2</sup> of Direct Normal Irradiance (DNI). Nonetheless, the small size shortens the warm up time to 10 seconds (at nominal conditions). As regard the wall temperature, the new solver revealed a basic Nusselt number ten times higher than that considered by Forristall, this outcome has a huge impact on the performance and thermal stress. Finally, a new correlation was developed to preliminary estimate the internal wall temperature on the basis external parameters easily monitored by existing sensors.

Key feature of complex energy systems concerns control optimisation, to reduce the design time some ways can be undertaken, the Hardware-in-the-Loop is one of them. In this case, the micro CHP of the Innova Microsolar project was considered for testing the HiL approach. Thanks to the developed simulator, the real control unit of the plant can be properly tuned, testing control algorithms prior yet to the experimental tests campaign. A fast and robust diverters adjustment with Proportional and Integral (PI) gains was found. Moreover, the inlet temperature of the ORC was also regulated with both the pump speed of the plant and the inlet valve of the ORC evaporator. Results shown that at very part-load conditions, when the pump speed was adjusted, the large time delay between its regulation and the system response leads to inaccurate control, even with Gain Scheduling of the PI. Acting on the valve instead, the ORC inlet temperature quickly reaches the set-point showing better results than the other control set up.

## 8.2 Future works

The topics covered in this dissertation can be seen as a starting point for further analyses in the field of micro solar CHP. Despite the broad variety of scientific papers in CSP technologies, ORCs and latent heat thermal storages, some open-line of research are still present. Indeed, the system integration of these subsystems is a challenge, few studies investigate this matter, particularly at small scale. As regards possible future developments of this dissertation might be outlined by the following list:

- *system optimization*: the recently interests in *Artificial Intelligence* (AI), mainly driven by *Machine Learning*, could be very helpful to improve the developed control framework to decide when and to what extend working in an Operation Mode, rather than another one. Another alternative might be the *Dynamic Programming* since its ability to find the optimal solution when plenty of minimal or maximal points are possible under multiple states and variables. Additionally, the set-point values of the temperature and flow rate may follow different rules on the basis of the self learned effects on the plant. The *Moving Horizon Estimation* can help in this sense predicting the solar availability and the user demand to further optimize the system thermal management under a certain timeframe.
- *Predictive Controls*: may reduce as much as possible the transient time to achieve the new set-point values, thus enabling a fast transition to the new optimal Operation Mode established by an AI controller.
- *Latent heat thermal storage*: is still an open question the thermal characterization of the thermal storage filled with phase change material. Immersed heat pipes make the physical problem even more complex. The lumped model presented in the dissertation must be improved to better reproduce the transient response. In this regard, owing to the noticeable anisotropy of the physical problem either a 1 D or 2 D mathematical model have to be developed to replace the existent, but maintaining a reasonable CPU burden.
- *ORC off design*: the thermodynamic model has many room for improvement, the abundant plethora of models in literature can be useful to refine the electric and thermal output of the ORC in off design conditions still using a steady state model. In particular, results can gain from a more accurate Plate Heat Exchanger model, which takes into consideration the three phase flow.

## Appendix A

# Simulink models

This is the whole Simulink system of the micro Solar CHP in its basic version without implementing the Fuzzy logic controller or the Hardware In the Loop communication block.

As one can see the whether block sends all the variables to the LFR block, it supplies the network where the TES and the ORC are attached. The pipelines are colored in yellow-ochre, the tees are pink and the diverters are blue. On the basis of the plant state and the solar power available, the controller (green block) decides the correct Operation Mode, after that the valve control block (cyan color) adjusts each diverter to assure a correct flow rate throughout the subsystems.

The Solver works under discrete and fixed step conditions, thus a further time refinement can be carried out with internal time steps, as occurs in the TES, pipelines and LFR block. Under this settings the whole system can communicate with external programs, as matter of it is more simple to manage the communication between the two programs allowing to accomplish an HIL test as described in this dissertation.

The HTF properties are taken from the manufacturer datasheet, this means that heat capacity, viscosity, thermal conductivity are temperature dependent. This choice entails a careful managing of the energy inputs/outputs of each subsystem.

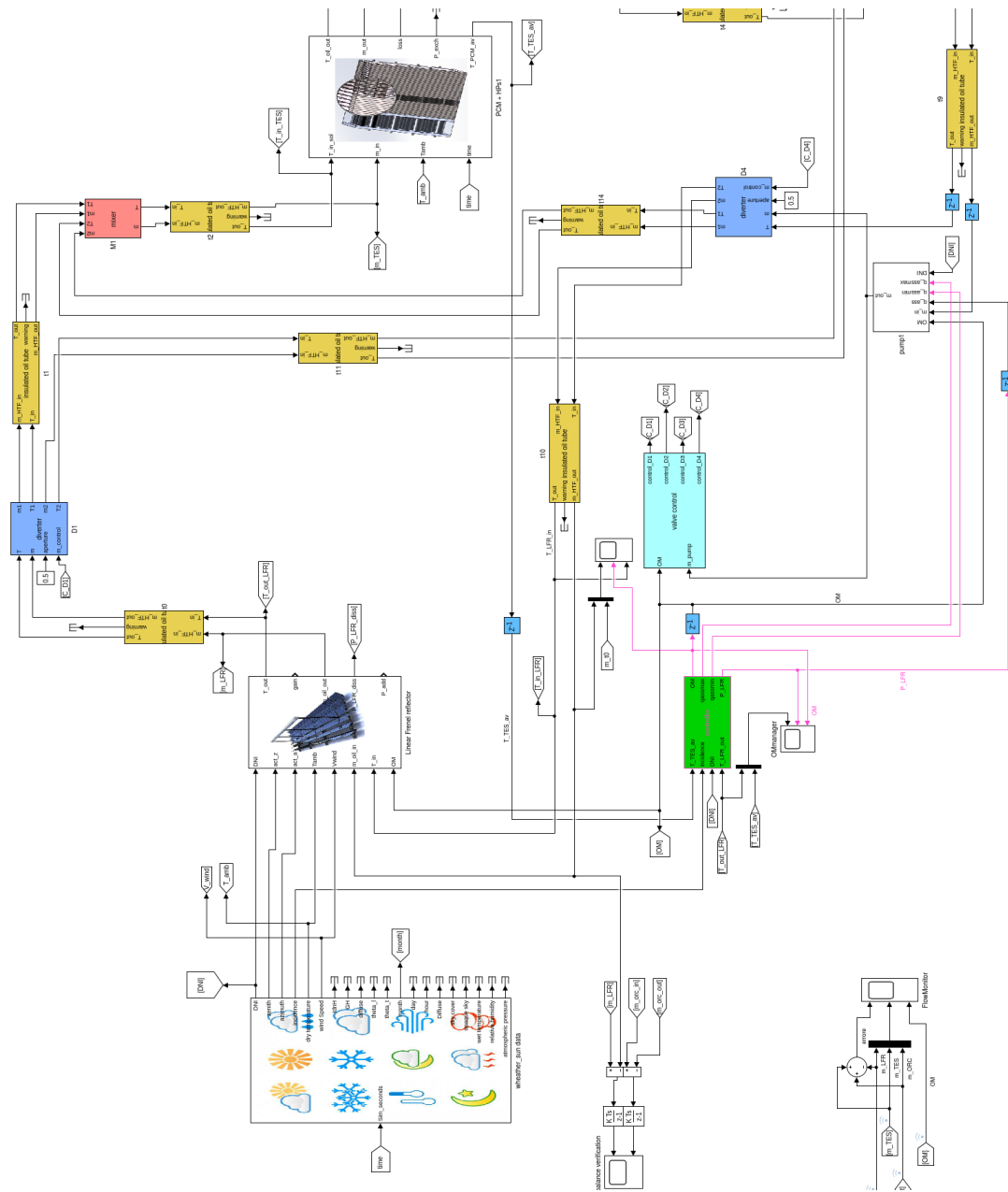


Figure A.1. The entire Simulink model part 1

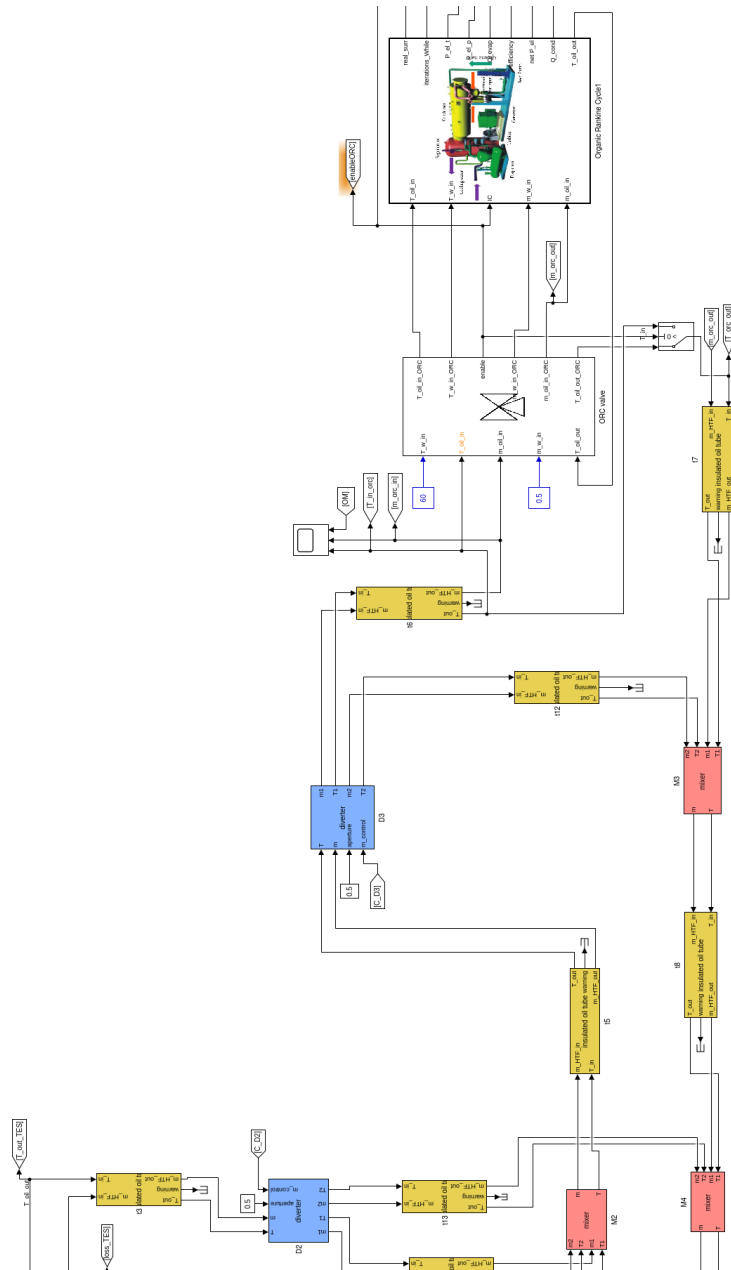


Figure A.2. The entire Simulink model part 2

## A.1 Solar generator

The weather data from the Energy+ database have been pre-processed (up-sampling) from a hourly sample rate to a quarter using a spline algorithm. In this way, a more real DNI variation is obtained, this aspect is important since that all the system dynamic is strongly affected by this parameter. To calculate with a best accuracy the solar position, an additional block has been developed (*SPA Bird Algorithm*), the algorithm comes from the NREL agency from US and it has been modified to

predict also the GHI and diffuse in clear sky conditions. It takes into account also of the surface (plain) orientation, thus it is able to simulate the LFR with N-S or and E-W orientation, in addition the slope of the ground can be considered as well.

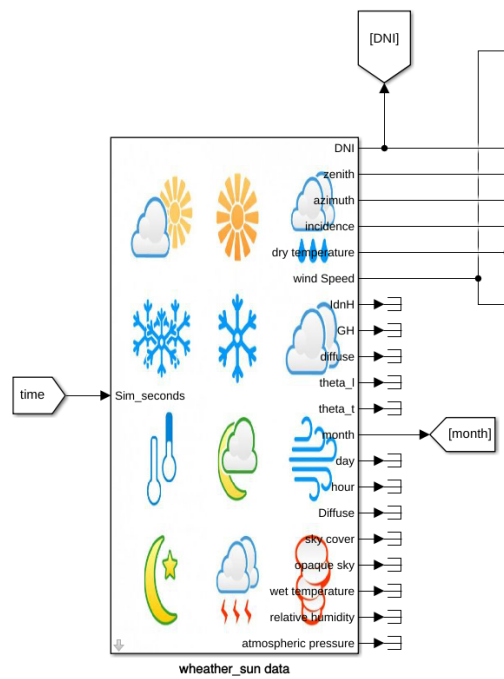


Figure A.3. The whether model

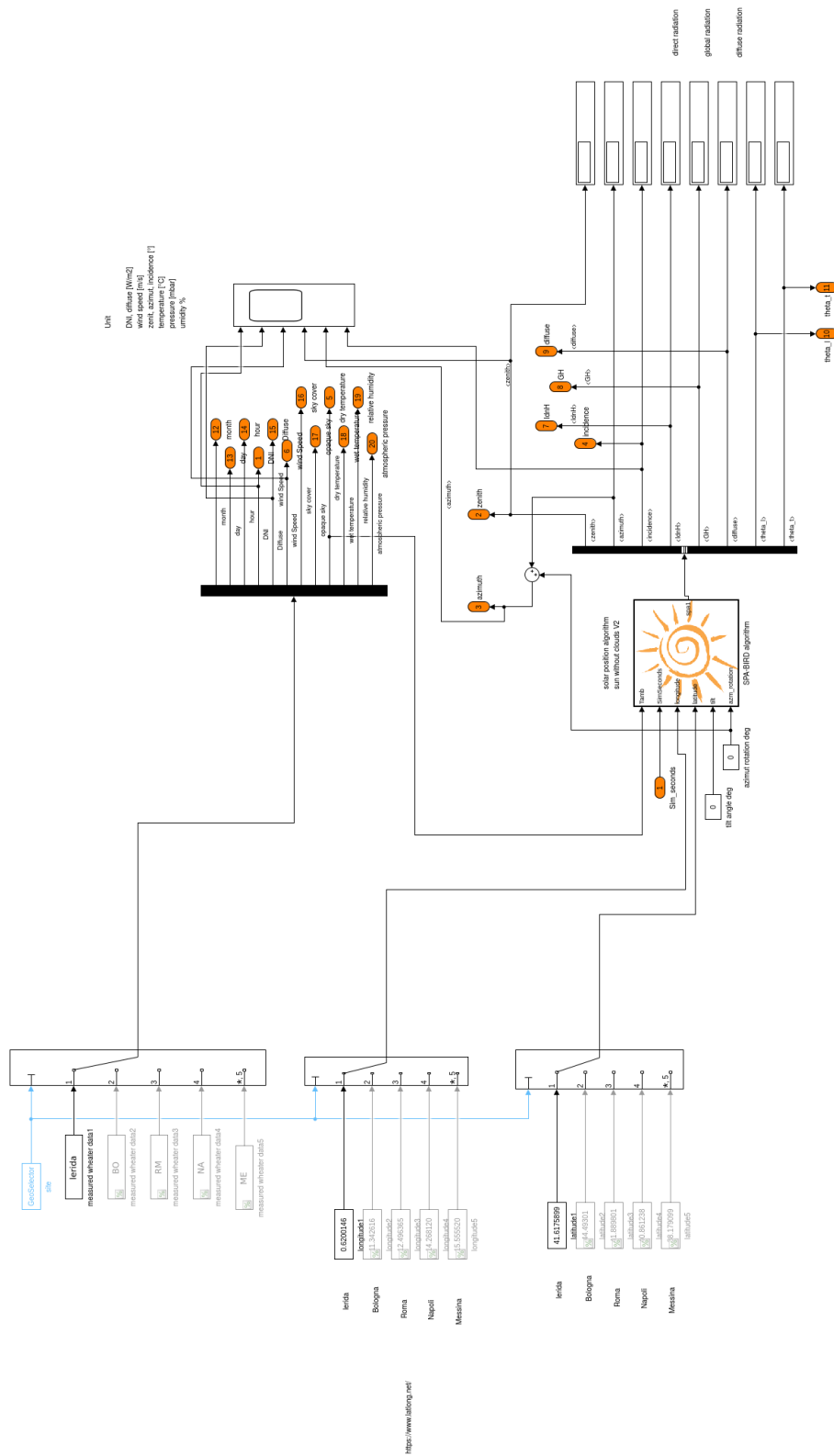


Figure A.4. Inside the weather block

## SPA MATLAB code

```

1
2
3 %%%%%%%%%%%%%%%%%%%%%%%%%%%%%%%%%%%%%%%%%%%%%%%%%%%%%%%%%%%%%%%%%%%%%%%%%
4 %
5 % Solar Position Algorithm (SPA) for Solar Radiation Application
6 %
7 % Measurement & Instrumentation Team Solar Radiation Research Laboratory
8 % National Renewable Energy Laboratory 1617 Cole Blvd, Golden, CO 80401
9 %
10 % Last modified: 2017/03/19 M. Mahooti
11 %
12 %%%%%%%%%%%%%%%%%%%%%%%%%%%%%%%%%%%%%%%%%%%%%%%%%%%%%%%%%%%%%%%%%%%%%%%%%
13 function spa1 = spa(Tamb,SimSeconds,longitude,latitude,tilt,azm_rotation)
14
15 [spa1.zenith,spa1.azimuth,spa1.incidence,spa1.IdnH,spa1.GH,spa1.diffuse,spa1.theta_l,spa1.theta_t] =
16 deal(0);
17
18 SPA_ALL = 3; %calculate all SPA output values
19 %-----
20 % example:
21 % SimSeconds= secondi simulazione Simulink
22 % C=datevec(SimSeconds/86400+datenum(2017,1,1))
23 %
24 % C =
25 %      2017      1      2      0      0      0
26 %-----
27 % SimSeconds= secondi simulazione Simulink input0
28 % VectorData=datevec(SimSeconds/86400+datenum(2017,1,1));
29 %Declare datevec as extrinsic altrimenti Simulink non la legge
30
31 coder.extrinsic('datevec');
32 VectorData=zeros(1,6); %con coder.extrinsic bisogna preallocare i dati
33 VectorData=datevec(floor(SimSeconds)/86400+736696);
34
35 % declare the SPA structure
36 % enter required input values into SPA structure
37 spa.year = VectorData(1);
38 % spa.year = 2017;
39 spa.month = VectorData(2);
40 spa.day = VectorData(3);
41 spa.hour = VectorData(4);
42 spa.minute = VectorData(5);
43 spa.second = VectorData(6);
44 spa.timezone = 1;
45 spa.delta_ut1 = 0;
46 spa.delta_t = 67;
47 spa.longitude = longitude;
48 spa.latitude = latitude;
49 spa.elevation = 30.14;
50 spa.pressure = 820;
51 spa.temperature = Tamb;
52 spa.slope = tilt;
53 spa.azm_rotation = azm_rotation;
54 spa.atmos_refract = 0.5667;
55 spa.function = SPA_ALL;
56
57
58 %-----
59 % inizializzazione strutture conti
60 [spa.jd,spa.jde,spa.jce,spa.jme,spa.l,spa.b,...
61 spa.x0,spa.x1,spa.x2,spa.x3,spa.x4,spa.jc,...
62 spa.theta,spa.theta_l,spa.theta_t] = deal(0);
63 %-----
64 [spa.beta,spa.epsilon0,spa.epsilon,spa.r,spa.del_tau,...
65 spa.lamda,spa.nu0,spa.nu,spa.alpha,spa.delta,spa.del,...
66 spa.del_epsilon,spa.del_psi,spa.h,spa.xi,spa.del_alpha,...
67 spa.delta_prime,spa.e,spa.e0,spa.azimuth_astro,spa.alpha_prime,...
68 spa.h_prime,spa.del_e,spa.zenith,spa.azimuth,spa.IdnH,spa.GH,...
69 spa.diffuse,spa.incidence,spa.srha,spa.ssha,spa.sta,spa.suntransi,...
70 spa.sunrise,spa.sunset,spa.eot] = deal(0);
71
72 [spa.beta,spa.epsilon0,spa.epsilon,spa.r,spa.del_tau,spa.lamda,spa.nu0,...
73 spa.nu,spa.alpha,spa.delta,spa.del,spa.del_epsilon,spa.del_psi,spa.h,...
74 spa.xi,spa.del_alpha,spa.delta_prime,spa.e,spa.e0,spa.azimuth_astro,spa.alpha_prime,...
75 spa.h_prime,spa.del_e,spa.zenith,spa.azimuth,spa.IdnH,spa.GH,spa.diffuse,spa.incidence,...
76 spa.srha,spa.ssha,spa.sta,spa.suntransit,spa.sunrise,spa.sunset,spa.eot] = deal(0);
77
78 %call the SPA calculate function and pass the SPA structure
79 [result, spa] = spa_calculate(spa);
80
81 if result == 0 %check for SPA errors
82 % %display the results inside the SPA structure
83 % fprintf('Julian Day: %.6f\n',spa.jd);
84 % fprintf('L: %.6e degrees\n',spa.l);
85 % fprintf('B: %.6e degrees\n',spa.b);
86 % fprintf('R: %.6f AU\n',spa.r);

```

```

87 % fprintf('H:           %.6f degrees\n',spa.h);
88 % fprintf('Delta Psi:   %.6e degrees\n',spa.del_psi);
89 % fprintf('Delta Epsilon: %.6e degrees\n',spa.del_epsilon);
90 % fprintf('Epsilon:     %.6f degrees\n',spa.epsilon);
91 % fprintf('Zenith:      %.6f degrees\n',spa.zenith);
92 % fprintf('Azimuth:    %.6f degrees\n',spa.azimuth);
93 % fprintf('Incidence:   %.6f degrees\n',spa.incidence);
94 spa1.zenith=spa.zenith; % zenith solare degrees
95 spa1.azimuth=spa.azimuth; % azimuth solare degrees
96 spa1.incidence=spa.incidence; % angolo di incidenza su superficie degrees
97 spa1.IdnH=spa.IdnH; % DNI W/m2
98 spa1.GH=spa.GH; % globale W/m2
99 spa1.diffuse=spa.diffuse; % diffusa W/m2
100 spa1.theta_l = spa.theta_l;
101 spa1.theta_t = spa.theta_t;
102
103 % min = 60*(spa.sunrise - floor(spa.sunrise));
104 % sec = 60*(min - floor(min));
105 % fprintf('Sunrise:     %2.2d:%2.2d:%2.2d Local Time\n', ...
106 % floor(spa.sunrise), floor(min), floor(sec));
107
108 % min = 60*(spa.sunset - floor(spa.sunset));
109 % sec = 60*(min - floor(min));
110 % fprintf('Sunset:      %2.2d:%2.2d:%2.2d Local Time\n', ...
111 % floor(spa.sunset), floor(min), floor(sec));
112 % fprintf('DNI W/m2 %.6f \n',spa.IdnH);
113 % fprintf('Global Radiation W/m2 %.6f \n',spa.GH);
114 % fprintf('Diffuse Radiation W/m2 %.6f \n',spa.diffuse);
115 else
116 % fprintf('SPA Error Code: %d\n', result);
117
118 end
119
120 %%%%%%%%%%%%%%%%%%%%%%%%%%%%%%%%%%%%%%%%%%%%%%%%%%%%%%%%%%%%%%%%%%%%%%%%%
121 % The output of this program should be:
122 %
123 %Julian Day:      2452930.312847
124 %L:              2.401826e+01 degrees
125 %B:              -1.011219e-04 degrees
126 %R:              0.996542 AU
127 %H:              11.105902 degrees
128 %Delta Psi:      -3.998404e-03 degrees
129 %Delta Epsilon:  1.666568e-03 degrees
130 %Epsilon:        23.440465 degrees
131 %Zenith:         50.111622 degrees
132 %Azimuth:        194.340241 degrees
133 %Incidence:      25.187000 degrees
134 %Sunrise:        06:12:43 Local Time
135 %Sunset:         17:20:19 Local Time
136 %
137 %%%%%%%%%%%%%%%%%%%%%%%%%%%%%%%%%%%%%%%%%%%%%%%%%%%%%%%%%%%%%%%%%%%%%%%%%
138
139 end
140
141 %%%%%%%%%%%%%%%%%%%%%%%%%%%%%%%%%%%%%%%%%%%%%%%%%%%%%%%%%%%%%%%%%%%%%%%%%
142
143 function limited = limit_degrees(degrees)
144
145 degrees = degrees/360;
146 limited = 360*(degrees-floor(degrees));
147
148 if (limited < 0)
149     limited = limited + 360;
150 end
151
152 end
153
154 %%%%%%%%%%%%%%%%%%%%%%%%%%%%%%%%%%%%%%%%%%%%%%%%%%%%%%%%%%%%%%%%%%%%%%%%%
155
156 function limited = limit_degrees180pm(degrees)
157
158 degrees = degrees/360;
159 limited = 360*(degrees-floor(degrees));
160
161 if(limited < -180)
162     limited = limited + 360;
163 elseif(limited > 180)
164     limited = limited - 360;
165 end
166
167 end
168
169 %%%%%%%%%%%%%%%%%%%%%%%%%%%%%%%%%%%%%%%%%%%%%%%%%%%%%%%%%%%%%%%%%%%%%%%%%
170
171 function limited = limit_degrees180(degrees)
172
173 degrees = degrees/180;
174 limited = 180*(degrees-floor(degrees));
175 if (limited < 0)
176     limited = limited + 180;

```

```

177 end
178
179 end
180
181
182 %%%%%%%%%%%%%%%%%%%%%%%%%%%%%%%%%%%%%%%%%%%%%%%%%%%%%%%%%%%%%%%%%%%%%%%%%
183 function limited = limit_zero2one(value)
184
185 limited = value - floor(value);
186 if (limited < 0)
187     limited = limited + 1;
188 end
189
190 end
191
192
193 %%%%%%%%%%%%%%%%%%%%%%%%%%%%%%%%%%%%%%%%%%%%%%%%%%%%%%%%%%%%%%%%%%%%%%%%%
194 function limited = limit_minutes(minutes)
195
196 limited = minutes;
197
198 if(limited < -20)
199     limited = limited + 1440;
200 elseif(limited > 20)
201     limited = limited - 1440;
202 end
203
204 end
205
206
207 %%%%%%%%%%%%%%%%%%%%%%%%%%%%%%%%%%%%%%%%%%%%%%%%%%%%%%%%%%%%%%%%%%%%%%%%%
208 function out = dayfrac_to_local_hr(dayfrac, timezone)
209
210 out = 24*limit_zero2one(dayfrac + timezone/24);
211
212 end
213
214
215 %%%%%%%%%%%%%%%%%%%%%%%%%%%%%%%%%%%%%%%%%%%%%%%%%%%%%%%%%%%%%%%%%%%%%%%%%
216 function out = third_order_polynomial(a, b, c, d, x)
217
218 out = ((a*x + b)*x + c)*x + d;
219
220 end
221
222
223 %%%%%%%%%%%%%%%%%%%%%%%%%%%%%%%%%%%%%%%%%%%%%%%%%%%%%%%%%%%%%%%%%%%%%%%%%
224 function out = validate_inputs(spa)
225 SPA_ALL=3;
226 SPA_ZA_INC=1;
227 % spa_const2
228
229 if ((spa.year < -2000) || (spa.year > 6000))
230     out = 1;
231     return
232 end
233 if ((spa.month < 1) || (spa.month > 12))
234     out = 2;
235     return
236 end
237 if ((spa.day < 1) || (spa.day > 31))
238     out = 3;
239     return
240 end
241 if ((spa.hour < 0) || (spa.hour > 24))
242     out = 4;
243     return
244 end
245 if ((spa.minute < 0) || (spa.minute > 59))
246     out = 5;
247     return
248 end
249 if ((spa.second < 0) || (spa.second >=60))
250     out = 6;
251     return
252 end
253 if ((spa.pressure < 0) || (spa.pressure > 5000))
254     out = 12;
255     return
256 end
257 if ((spa.temperature <= -273) || (spa.temperature > 6000))
258     out = 13;
259     return
260 end
261 if ((spa.delta_ut1 <= -1) || (spa.delta_ut1 >= 1))
262     out = 17;
263     return
264 end
265 if ((spa.hour == 24) && (spa.minute > 0))
266     out = 5;

```

```

267     return
268 end
269 if ((spa.hour      == 24 ) && (spa.second    > 0 ))
270     out = 6;
271     return
272 end
273
274 if (abs(spa.delta_t) > 8000 )
275     out = 7;
276     return
277 end
278 if (abs(spa.timezone) > 18 )
279     out = 8;
280     return
281 end
282 if (abs(spa.longitude) > 180 )
283     out = 9;
284     return
285 end
286 if (abs(spa.latitude) > 90 )
287     out = 10;
288     return
289 end
290 if (abs(spa.atmos_refract) > 5 )
291     out = 16;
292     return
293 end
294 if ( spa.elevation < -6500000)
295     out = 11;
296     return
297 end
298
299 if ((spa.function == SPA_ZA_INC) || (spa.function == SPA_ALL))
300     if (abs(spa.slope) > 360)
301         out = 14;
302         return
303     end
304     if (abs(spa.azm_rotation) > 360)
305         out = 15;
306         return
307     end
308 end
309
310 out = 0;
311
312 end
313
314
315 %%%%%%%%%%%%%%%%%%%%%%%%%%%%%%%%%%%%%%%%%%%%%%%%%%%%%%%%%%%%%%%%%%%%%%%%%
316 function julian_day = julian_day(year,month,day,hour,minute,second,dut1,tz)
317
318 day_decimal = day+(hour-tz+(minute+(second+dut1)/60)/60)/24;
319
320 if(month < 3)
321     month = month+12;
322     year = year-1;
323 end
324
325 julian_day = floor(365.25*(year+4716))+floor(30.6001*(month+1))+...
326             day_decimal-1524.5;
327
328 if (julian_day > 2299160)
329     a = floor(year/100);
330     julian_day = julian_day+(2-a+floor(a/4));
331 end
332
333 end
334
335
336 %%%%%%%%%%%%%%%%%%%%%%%%%%%%%%%%%%%%%%%%%%%%%%%%%%%%%%%%%%%%%%%%%%%%%%%%%
337 function out = julian_century(jd)
338
339 out = (jd-2451545)/36525;
340
341 end
342
343
344 %%%%%%%%%%%%%%%%%%%%%%%%%%%%%%%%%%%%%%%%%%%%%%%%%%%%%%%%%%%%%%%%%%%%%%%%%
345 function out = julian_ephemeris_day(jd, delta_t)
346
347 out = jd+delta_t/86400;
348
349 end
350
351
352 %%%%%%%%%%%%%%%%%%%%%%%%%%%%%%%%%%%%%%%%%%%%%%%%%%%%%%%%%%%%%%%%%%%%%%%%%
353 function out = julian_ephemeris_century(jde)
354
355 out = (jde-2451545)/36525;
356

```

```

357 end
358
359
360 %%%%%%%%%%%%%%%%%%%%%%%%%%%%%%%%%%%%%%%%%%%%%%%%%%%%%%%%%%%%%%%%%%%%%%%%%
361 function out = julian_ephemeris_millennium(jce)
362
363 out = (jce/10);
364
365 end
366
367 %%%%%%%%%%%%%%%%%%%%%%%%%%%%%%%%%%%%%%%%%%%%%%%%%%%%%%%%%%%%%%%%%%%%%%%%%
368 function out = earth_periodic_term_summation(terms,count,jme)
369 TERM_A = 1; TERM_B = 2; TERM_C = 3;
370 % spa_const2
371
372 sum = 0;
373
374 for i = 1:count
375 sum = sum + (terms(i,TERM_A)*cos(terms(i,TERM_B)+terms(i,TERM_C)*jme));
376 end
377
378 out = sum;
379
380 end
381
382 %%%%%%%%%%%%%%%%%%%%%%%%%%%%%%%%%%%%%%%%%%%%%%%%%%%%%%%%%%%%%%%%%%%%%%%%%
383 function out = earth_values(term_sum,count,jme)
384
385 sum = 0;
386
387 for i = 1:count
388 sum = sum + term_sum(i)*(jme^(i-1));
389 end
390
391 sum = sum/1e8;
392
393 out = sum;
394
395 end
396
397 %%%%%%%%%%%%%%%%%%%%%%%%%%%%%%%%%%%%%%%%%%%%%%%%%%%%%%%%%%%%%%%%%%%%%%%%%
398 function out = earth_heliocentric_longitude(jme)
399 L_COUNT = 6; L_subcount= [64,34,20,7,3,1];
400 % spa_const2
401
402 L_TERMS_1 = ...
403 [ 175347046.0,0,0;
404   3341656.0,4.6692568,6283.07585;
405   34894.0,4.6261,12566.1517;
406   3497.0,2.7441,5753.3849;
407   3418.0,2.8289,3.5231;
408   3136.0,3.6277,77713.7715;
409   2676.0,4.4181,7860.4194;
410   2343.0,6.1352,3930.2097;
411   1324.0,0.7425,11506.7698;
412   1273.0,2.0371,529.691;
413   1199.0,1.1096,1577.3435;
414   990,5.233,5884.927;
415   902,2.045,26.298;
416   857,3.508,398.149;
417   780,1.179,5223.694;
418   753,2.533,5507.553;
419   505,4.583,18849.228;
420   492,4.205,775.523;
421   357,2.92,0.067;
422   317,5.849,11790.629;
423   284,1.899,796.298;
424   271,0.315,10977.079;
425   243,0.345,5486.778;
426   206,4.806,2544.314;
427   205,1.869,5573.143;
428   202,2.458,6069.777;
429   156,0.833,213.299;
430   132,3.411,2942.463;
431   126,1.083,20.775;
432   115,0.645,0.98;
433   103,0.636,4694.003;
434   102,0.976,15720.839;
435   102,4.267,7.114;
436   99,6.21,2146.17;
437   98,0.68,155.42;
438   86,5.98,161000.69;
439   85,1.3,6275.96;
440   85,3.67,71430.7;
441   80,1.81,17260.15;
442   79,3.04,12036.46;
443   75,1.76,5088.63;

```

```

447      74,3.5,3154.69;
448      74,4.68,801.82;
449      70,0.83,9437.76;
450      62,3.98,8827.39;
451      61,1.82,7084.9;
452      57,2.78,6286.6;
453      56,4.39,14143.5;
454      56,3.47,6279.55;
455      52,0.19,12139.55;
456      52,1.33,1748.02;
457      51,0.28,5856.48;
458      49,0.49,1194.45;
459      41,5.37,8429.24;
460      41,2.4,19651.05;
461      39,6.17,10447.39;
462      37,6.04,10213.29;
463      37,2.57,1059.38;
464      36,1.71,2352.87;
465      36,1.78,6812.77;
466      33,0.59,17789.85;
467      30,0.44,83996.85;
468      30,2.74,1349.87;
469      25,3.16,4690.48];
470      L_TERMS_2 = [628331966747.0,0,0;
471      206059.0,2.678235,6283.07585;
472      4303.0,2.6351,12566.1517;
473      425.0,1.59,3.523;
474      119.0,5.796,26.298;
475      109.0,2.966,1577.344;
476      93,2.59,18849.23;
477      72,1.14,529.69;
478      68,1.87,398.15;
479      67,4.41,5507.55;
480      59,2.89,5223.69;
481      56,2.17,155.42;
482      45,0.4,796.3;
483      36,0.47,775.52;
484      29,2.65,7.11;
485      21,5.34,0.98;
486      19,1.85,5486.78;
487      19,4.97,213.3;
488      17,2.99,6275.96;
489      16,0.03,2544.31;
490      16,1.43,2146.17;
491      15,1.21,10977.08;
492      12,2.83,1748.02;
493      12,3.26,5088.63;
494      12,5.27,1194.45;
495      12,2.08,4694;
496      11,0.77,553.57;
497      10,1.3,6286.6;
498      10,4.24,1349.87;
499      9,2.7,242.73;
500      9,5.64,951.72;
501      8,5.3,2352.87;
502      6,2.65,9437.76;
503      6,4.67,4690.48];
504      L_TERMS_3 = [...
505      52919.0,0,0;
506      8720.0,1.0721,6283.0758;
507      309.0,0.867,12566.152;
508      27,0.05,3.52;
509      16,5.19,26.3;
510      16,3.68,155.42;
511      10,0.76,18849.23;
512      9,2.06,77713.77;
513      7,0.83,775.52;
514      5,4.66,1577.34;
515      4,1.03,7.11;
516      4,3.44,5573.14;
517      3,5.14,796.3;
518      3,6.05,5507.55;
519      3,1.19,242.73;
520      3,6.12,529.69;
521      3,0.31,398.15;
522      3,2.28,553.57;
523      2,4.38,5223.69;
524      2,3.75,0.98];
525      L_TERMS_4 = [...
526      289.0,5.844,6283.076;
527      35,0,0;
528      17,5.49,12566.15;
529      3,5.2,155.42;
530      1,4.72,3.52;
531      1,5.3,18849.23;
532      1,5.97,242.73];
533      L_TERMS_5 = [...
534      114.0,3.142,0;
535      8,4.13,6283.08;
536      1,3.84,12566.15];

```

```

537     L_TERMS_6 =[1,3.14,0];
538
539
540     sum = zeros(L_COUNT,1);
541     % coder.extrinsic('cell2struct');
542     % coder.extrinsic('cell2mat');
543     % L_TERMS_2 = cell2struct(L_TERMS,{'a','b','c','d','e','f'},2);
544     % L_TERMS_Names=zeros(6,1);
545     % L_TERMS_Names = cell2mat(fieldnames(L_TERMS_2));
546
547     for i = 1:L_COUNT
548         switch i
549             case 1
550                 sum(i) = earth_periodic_term_summation(L_TERMS_1, l_subcount(i), jme);
551             case 2
552                 sum(i) = earth_periodic_term_summation(L_TERMS_2, l_subcount(i), jme);
553             case 3
554                 sum(i) = earth_periodic_term_summation(L_TERMS_3, l_subcount(i), jme);
555             case 4
556                 sum(i) = earth_periodic_term_summation(L_TERMS_4, l_subcount(i), jme);
557             case 5
558                 sum(i) = earth_periodic_term_summation(L_TERMS_5, l_subcount(i), jme);
559             case 6
560                 sum(i) = earth_periodic_term_summation(L_TERMS_6, l_subcount(i), jme);
561         end
562         % prova=L_TERMS_2(L_TERMS_Names(i)); %tentativo andato male serve
563         % dichiarare le caratteristiche delle variabili extrinsic
564     end
565
566     %Original
567     % for i = 1:L_COUNT
568     %     L_TERM = cell2mat(L_TERMS(i));
569     %     sum(i) = earth_periodic_term_summation(L_TERM, l_subcount(i), jme);
570     % end
571
572     out = limit_degrees(rad2deg(earth_values(sum, L_COUNT, jme)));
573
574     end
575
576
577     %%%%%%%%%%%%%%%%%%%%%%%%%%%%%%%%%%%%%%%%%%%%%%%%%%%%%%%%%%%%%%%%%%%%%%%%%
578     function out = earth_heliocentric_latitude(jme)
579     B_COUNT = 2; b_subcount = [5,2];
580
581     % spa_const2
582
583     B_TERMS_1 =[ 280.0,3.199,84334.662;
584                 102.0,5.422,5507.553;
585                 80,3.88,5223.69;
586                 44,3.7,2352.87;
587                 32,4,1577.34];
588     B_TERMS_2 =[9,3.9,5507.55;
589                 6,1.73,5223.69];
590
591     sum = zeros(B_COUNT,1);
592     for i = 1:B_COUNT
593         switch i
594             case 1
595                 sum(i) = earth_periodic_term_summation(B_TERMS_1, b_subcount(i), jme);
596             case 2
597                 sum(i) = earth_periodic_term_summation(B_TERMS_2, b_subcount(i), jme);
598         end
599     end
600     %original code
601     % for i = 1:B_COUNT
602     %     B_TERM = cell2mat(B_TERMS(i));
603     %     sum(i) = earth_periodic_term_summation(B_TERM, b_subcount(i), jme);
604     % end
605
606     out = rad2deg(earth_values(sum, B_COUNT, jme));
607
608     end
609
610
611     %%%%%%%%%%%%%%%%%%%%%%%%%%%%%%%%%%%%%%%%%%%%%%%%%%%%%%%%%%%%%%%%%%%%%%%%%
612     function out = earth_radius_vector(jme)
613     R_COUNT = 5; r_subcount = [40,10,6,2,1];
614     % spa_const2
615
616     R_TERMS_1 =[ 100013989.0,0,0;
617                 1670700.0,3.0984635,6283.07585;
618                 13956.0,3.05525,12566.1517;
619                 3084.0,5.1985,77713.7715;
620                 1628.0,1.1739,5753.3849;
621                 1576.0,2.8469,7860.4194;
622                 925.0,5.453,11506.77;
623                 542.0,4.564,3930.21;
624                 472.0,3.661,5884.927;
625                 346.0,0.964,5507.553;
626                 329.0,5.9,5223.694;

```

```

627     307.0,0.299,5573.143;
628     243.0,4.273,11790.629;
629     212.0,5.847,1577.344;
630     186.0,5.022,10977.079;
631     175.0,3.012,18849.228;
632     110.0,5.055,5486.778;
633     98.0,0.89,6069.78;
634     86.5,69,15720.84;
635     86,1.27,161000.69;
636     65,0.27,17260.15;
637     63,0.92,529.69;
638     57,2.01,83996.85;
639     56,5.24,71430.7;
640     49,3.25,2544.31;
641     47,2.58,775.52;
642     45,5.54,9437.76;
643     43,6.01,6275.96;
644     39,5.36,4694;
645     38,2.39,8827.39;
646     37,0.83,19651.05;
647     37,4.9,12139.55;
648     36,1.67,12036.46;
649     35,1.84,2942.46;
650     33,0.24,7084.9;
651     32,0.18,5088.63;
652     32,1.78,398.15;
653     28,1.21,6286.6;
654     28,1.9,6279.55;
655     26,4.59,10447.39];
656 R_TERMS_2= [
657     103019.0,1.10749,6283.07585;
658     1721.0,1.0644,12566.1517;
659     702.0,3.142,0;
660     32,1.02,18849.23;
661     31,2.84,5507.55;
662     25,1.32,5223.69;
663     18,1.42,1577.34;
664     10,5.91,10977.08;
665     9,1.42,6275.96;
666     9,0.27,5486.78];
667 R_TERMS_3= [
668     4359.0,5.7846,6283.0758;
669     124.0,5.579,12566.152;
670     12,3.14,0;
671     9,3.63,77713.77;
672     6,1.87,5573.14;
673     3,5.47,18849.23];
674 R_TERMS_4= [
675     145.0,4.273,6283.076;
676     7,3.92,12566.15];
677 R_TERMS_5= [
678     4,2.56,6283.08];
679
680 sum = zeros(R_COUNT,1);
681
682 for i = 1:R_COUNT
683     % R_TERM = cell2mat(R_TERMS(i));
684     switch i
685     case 1
686         sum(i) = earth_periodic_term_summation(R_TERMS_1, r_subcount(i), jme);
687     case 2
688         sum(i) = earth_periodic_term_summation(R_TERMS_2, r_subcount(i), jme);
689     case 3
690         sum(i) = earth_periodic_term_summation(R_TERMS_3, r_subcount(i), jme);
691     case 4
692         sum(i) = earth_periodic_term_summation(R_TERMS_4, r_subcount(i), jme);
693     case 5
694         sum(i) = earth_periodic_term_summation(R_TERMS_5, r_subcount(i), jme);
695     end
696 end
697
698 out = earth_values(sum, R_COUNT, jme);
699
700 end
701
702
703 %%%%%%%%%%%%%%%%%%%%%%%%%%%%%%%%%%%%%%%%%%%%%%%%%%%%%%%%%%%%%%%%%%%%%%%%%
704 function theta = geocentric_longitude(l)
705
706 theta = l+180;
707
708 if (theta >= 360)
709     theta = theta-360;
710 end
711
712 end
713
714
715 %%%%%%%%%%%%%%%%%%%%%%%%%%%%%%%%%%%%%%%%%%%%%%%%%%%%%%%%%%%%%%%%%%%%%%%%%
716 function out = geocentric_latitude(b)

```

```

717
718 out = -b;
719
720 end
721
722
723 %%%%%%%%%%%%%%%%%%%%%%%%%%%%%%%%%%%%%%%%%%%%%%%%%%%%%%%%%%%%%%%%%%%%%%%%%
724 function out = mean_elongation_moon_sun(jce)
725
726 out = third_order_polynomial(1/189474,-0.0019142,445267.11148,297.85036,jce);
727
728 end
729
730
731 %%%%%%%%%%%%%%%%%%%%%%%%%%%%%%%%%%%%%%%%%%%%%%%%%%%%%%%%%%%%%%%%%%%%%%%%%
732 function out = mean_anomaly_sun(jce)
733
734 out = third_order_polynomial(-1/300000,-0.0001603,35999.05034,357.52772,jce);
735
736 end
737
738
739 %%%%%%%%%%%%%%%%%%%%%%%%%%%%%%%%%%%%%%%%%%%%%%%%%%%%%%%%%%%%%%%%%%%%%%%%%
740 function out = mean_anomaly_moon(jce)
741
742 out = third_order_polynomial(1/56250,0.0086972,477198.867398,134.96298,jce);
743
744 end
745
746
747 %%%%%%%%%%%%%%%%%%%%%%%%%%%%%%%%%%%%%%%%%%%%%%%%%%%%%%%%%%%%%%%%%%%%%%%%%
748 function out = argument_latitude_moon(jce)
749
750 out = third_order_polynomial(1/327270,-0.0036825,483202.017538,93.27191,jce);
751
752 end
753
754
755 %%%%%%%%%%%%%%%%%%%%%%%%%%%%%%%%%%%%%%%%%%%%%%%%%%%%%%%%%%%%%%%%%%%%%%%%%
756 function out = ascending_longitude_moon(jce)
757
758 out = third_order_polynomial(1/450000,0.0020708,-1934.136261,125.04452,jce);
759
760 end
761
762
763 %%%%%%%%%%%%%%%%%%%%%%%%%%%%%%%%%%%%%%%%%%%%%%%%%%%%%%%%%%%%%%%%%%%%%%%%%
764 function sum = xy_term_summation(i, x)
765 TERM_Y_COUNT=5;
766 % spa_const2
767 Y_TERMS = ...
768 [ 0,0,0,0,1;
769   -2,0,0,2,2;
770   0,0,0,2,2;
771   0,0,0,0,2;
772   0,1,0,0,0;
773   0,0,1,0,0;
774   -2,1,0,2,2;
775   0,0,0,2,1;
776   0,0,1,2,2;
777   -2,-1,0,2,2;
778   -2,0,1,0,0;
779   -2,0,0,2,1;
780   0,0,-1,2,2;
781   2,0,0,0,0;
782   0,0,1,0,1;
783   2,0,-1,2,2;
784   0,0,-1,0,1;
785   0,0,1,2,1;
786   -2,0,2,0,0;
787   0,0,-2,2,1;
788   2,0,0,2,2;
789   0,0,2,2,2;
790   0,0,2,0,0;
791   -2,0,1,2,2;
792   0,0,0,2,0;
793   -2,0,0,2,0;
794   0,0,-1,2,1;
795   0,2,0,0,0;
796   2,0,-1,0,1;
797   -2,2,0,2,2;
798   0,1,0,0,1;
799   -2,0,1,0,1;
800   0,-1,0,0,1;
801   0,0,2,-2,0;
802   2,0,-1,2,1;
803   2,0,1,2,2;
804   0,1,0,2,2;
805   -2,1,1,0,0;
806   0,-1,0,2,2;

```

```

807     2,0,0,2,1;
808     2,0,1,0,0;
809     -2,0,2,2,2;
810     -2,0,1,2,1;
811     2,0,-2,0,1;
812     2,0,0,0,1;
813     0,-1,1,0,0;
814     -2,-1,0,2,1;
815     -2,0,0,0,1;
816     0,0,2,2,1;
817     -2,0,2,0,1;
818     -2,1,0,2,1;
819     0,0,1,-2,0;
820     -1,0,1,0,0;
821     -2,1,0,0,0;
822     1,0,0,0,0;
823     0,0,1,2,0;
824     0,0,-2,2,2;
825     -1,-1,1,0,0;
826     0,1,1,0,0;
827     0,-1,1,2,2;
828     2,-1,-1,2,2;
829     0,0,3,2,2;
830     2,-1,0,2,2;
831
832
833     sum=0;
834
835     for j = 1:TERM_Y_COUNT
836         sum = sum + x(j)*Y_TERMS(i,j);
837     end
838
839 end
840
841
842
843 %%%%%%%%%%%%%%%%%%%%%%%%%%%%%%%%%%%%%%%%%%%%%%%%%%%%%%%%%%%%%%%%%%%%%%%%%
844 function [del_psi, del_epsilon] = nutation_longitude_and_obliquity(jce, x)
845 Y_COUNT = 63; TERM_PSI_A =1; TERM_PSI_B=2; TERM_EPS_C=3; TERM_EPS_D=4;
846 % spa_const2
847 PE_TERMS = ...
848 [ -171996,-174.2,92025,8.9;
849   -13187,-1.6,5736,-3.1;
850   -2274,-0.2,977,-0.5;
851   2062,0.2,-895,0.5;
852   1426,-3.4,54,-0.1;
853   712,0.1,-7,0;
854   -517,1.2,224,-0.6;
855   -386,-0.4,200,0;
856   -301,0,129,-0.1;
857   217,-0.5,-95,0.3;
858   -158,0,0,0;
859   129,0.1,-70,0;
860   123,0,-53,0;
861   63,0,0,0;
862   63,0.1,-33,0;
863   -59,0,26,0;
864   -58,-0.1,32,0;
865   -51,0,27,0;
866   48,0,0,0;
867   46,0,-24,0;
868   -38,0,16,0;
869   -31,0,13,0;
870   29,0,0,0;
871   29,0,-12,0;
872   26,0,0,0;
873   -22,0,0,0;
874   21,0,-10,0;
875   17,-0.1,0,0;
876   16,0,-8,0;
877   -16,0.1,7,0;
878   -15,0,9,0;
879   -13,0,7,0;
880   -12,0,6,0;
881   11,0,0,0;
882   -10,0,5,0;
883   -8,0,3,0;
884   7,0,-3,0;
885   -7,0,0,0;
886   -7,0,3,0;
887   -7,0,3,0;
888   6,0,0,0;
889   6,0,-3,0;
890   6,0,-3,0;
891   -6,0,3,0;
892   -6,0,3,0;
893   5,0,0,0;
894   -5,0,3,0;
895   -5,0,3,0;
896   -5,0,3,0;
897   4,0,0,0;

```

```

897     4,0,0,0;
898     4,0,0,0;
899     -4,0,0,0;
900     -4,0,0,0;
901     -4,0,0,0;
902     3,0,0,0;
903     -3,0,0,0;
904     -3,0,0,0;
905     -3,0,0,0;
906     -3,0,0,0;
907     -3,0,0,0;
908     -3,0,0,0;
909     -3,0,0,0];
910
911
912     sum_psi = 0;
913     sum_epsilon = 0;
914
915     for i = 1:Y_COUNT
916         xy_term_sum = deg2rad(xy_term_summation(i, x));
917         sum_psi = sum_psi + ( (PE_TERMS(i,TERM_PSI_A) + ...
918             jce*PE_TERMS(i,TERM_PSI_B))*sin(xy_term_sum) );
919         sum_epsilon = sum_epsilon + ( (PE_TERMS(i,TERM_EPS_C) + ...
920             jce*PE_TERMS(i,TERM_EPS_D))*cos(xy_term_sum) );
921     end
922
923     del_psi = sum_psi /36000000;
924     del_epsilon = sum_epsilon/36000000;
925
926     end
927
928
929     %%%%%%%%%%%%%%%%%%%%%%%%%%%%%%%%%%%%%%%%%%%%%%%%%%%%%%%%%%%%%%%%%%%%%%%%%
930     function out = ecliptic_mean_obliquity(jme)
931
932     u = jme/10;
933
934     out = 84381.448+u*(-4680.93+u*(-1.55+u*(1999.25+u*(-51.38 + ...
935         u*(-249.67+u*(-39.05+u*(7.12+u*(27.87+u*(5.79+u*2.45))))));
936
937     end
938
939
940     %%%%%%%%%%%%%%%%%%%%%%%%%%%%%%%%%%%%%%%%%%%%%%%%%%%%%%%%%%%%%%%%%%%%%%%%%
941     function out = ecliptic_true_obliquity(delta_epsilon, epsilon0)
942
943     out = delta_epsilon + epsilon0/3600;
944
945     end
946
947
948     %%%%%%%%%%%%%%%%%%%%%%%%%%%%%%%%%%%%%%%%%%%%%%%%%%%%%%%%%%%%%%%%%%%%%%%%%
949     function out = aberration_correction(r)
950
951     out = -20.4898/(3600*r);
952
953     end
954
955
956     %%%%%%%%%%%%%%%%%%%%%%%%%%%%%%%%%%%%%%%%%%%%%%%%%%%%%%%%%%%%%%%%%%%%%%%%%
957     function out = apparent_sun_longitude(theta, delta_psi, delta_tau)
958
959     out = theta + delta_psi + delta_tau;
960
961     end
962
963
964     %%%%%%%%%%%%%%%%%%%%%%%%%%%%%%%%%%%%%%%%%%%%%%%%%%%%%%%%%%%%%%%%%%%%%%%%%
965     function out = greenwich_mean_sidereal_time (jd, jc)
966
967     out = limit_degrees(280.46061837+360.98564736629*(jd-2451545)+ ...
968         jc*jc*(0.000387933 - jc/38710000));
969
970     end
971
972
973     %%%%%%%%%%%%%%%%%%%%%%%%%%%%%%%%%%%%%%%%%%%%%%%%%%%%%%%%%%%%%%%%%%%%%%%%%
974     function out = greenwich_sidereal_time (nu0, delta_psi, epsilon)
975
976     out = nu0 + delta_psi*cos(deg2rad(epsilon));
977
978     end
979
980
981     %%%%%%%%%%%%%%%%%%%%%%%%%%%%%%%%%%%%%%%%%%%%%%%%%%%%%%%%%%%%%%%%%%%%%%%%%
982     function out = geocentric_right_ascension(lamda, epsilon, beta)
983
984     lamda_rad = deg2rad(lamda);
985     epsilon_rad = deg2rad(epsilon);
986

```

```

987 out = limit_degrees(rad2deg(atan2(sin(lamda_rad)*cos(epsilon_rad) - ...
988     tan(deg2rad(beta))*sin(epsilon_rad), cos(lamda_rad))));
989
990 end
991
992
993 %%%%%%%%%%%%%%%%%%%%%%%%%%%%%%%%%%%%%%%%%%%%%%%%%%%%%%%%%%%%%%%%%%%%%%%%%
994 function out = geocentric_declination(beta, epsilon, lamda)
995
996 beta_rad = deg2rad(beta);
997 epsilon_rad = deg2rad(epsilon);
998
999 out = rad2deg(asin(sin(beta_rad)*cos(epsilon_rad) + ...
1000     cos(beta_rad)*sin(epsilon_rad)*sin(deg2rad(lamda))));
1001
1002 end
1003
1004
1005 %%%%%%%%%%%%%%%%%%%%%%%%%%%%%%%%%%%%%%%%%%%%%%%%%%%%%%%%%%%%%%%%%%%%%%%%%
1006 function out = observer_hour_angle(nu, longitude, alpha_deg)
1007
1008 out = limit_degrees(nu + longitude - alpha_deg);
1009
1010 end
1011
1012
1013 %%%%%%%%%%%%%%%%%%%%%%%%%%%%%%%%%%%%%%%%%%%%%%%%%%%%%%%%%%%%%%%%%%%%%%%%%
1014 function out = sun_equatorial_horizontal_parallax(r)
1015
1016 out = 8.794/(3600*r);
1017
1018 end
1019
1020
1021 %%%%%%%%%%%%%%%%%%%%%%%%%%%%%%%%%%%%%%%%%%%%%%%%%%%%%%%%%%%%%%%%%%%%%%%%%
1022 function [delta_alpha, delta_prime] = ...
1023     right_ascension_parallax_and_topocentric_dec(latitude, elevation, xi, h, delta)
1024
1025 lat_rad = deg2rad(latitude);
1026 xi_rad = deg2rad(xi);
1027 h_rad = deg2rad(h);
1028 delta_rad = deg2rad(delta);
1029 u = atan(0.99664719 * tan(lat_rad));
1030 y = 0.99664719 * sin(u) + elevation*sin(lat_rad)/6378140;
1031 x = cos(u) + elevation*cos(lat_rad)/6378140;
1032
1033 delta_alpha_rad = atan2(-x*sin(xi_rad)*sin(h_rad), ...
1034     cos(delta_rad)-x*sin(xi_rad)*cos(h_rad));
1035
1036 delta_prime = rad2deg(atan2((sin(delta_rad)-y*sin(xi_rad))* ...
1037     cos(delta_alpha_rad), cos(delta_rad)-x*sin(xi_rad)*cos(h_rad)));
1038
1039 delta_alpha = rad2deg(delta_alpha_rad);
1040
1041 end
1042
1043
1044 %%%%%%%%%%%%%%%%%%%%%%%%%%%%%%%%%%%%%%%%%%%%%%%%%%%%%%%%%%%%%%%%%%%%%%%%%
1045 function out = topocentric_right_ascension(alpha_deg, delta_alpha)
1046
1047 out = alpha_deg + delta_alpha;
1048
1049 end
1050
1051
1052 %%%%%%%%%%%%%%%%%%%%%%%%%%%%%%%%%%%%%%%%%%%%%%%%%%%%%%%%%%%%%%%%%%%%%%%%%
1053 function out = topocentric_local_hour_angle(h, delta_alpha)
1054
1055 out = h - delta_alpha;
1056
1057 end
1058
1059
1060 %%%%%%%%%%%%%%%%%%%%%%%%%%%%%%%%%%%%%%%%%%%%%%%%%%%%%%%%%%%%%%%%%%%%%%%%%
1061 function out = topocentric_elevation_angle(latitude, delta_prime, h_prime)
1062
1063 lat_rad = deg2rad(latitude);
1064 delta_prime_rad = deg2rad(delta_prime);
1065
1066 out = rad2deg(asin(sin(lat_rad)*sin(delta_prime_rad) + ...
1067     cos(lat_rad)*cos(delta_prime_rad) * cos(deg2rad(h_prime))));
1068
1069 end
1070
1071
1072 %%%%%%%%%%%%%%%%%%%%%%%%%%%%%%%%%%%%%%%%%%%%%%%%%%%%%%%%%%%%%%%%%%%%%%%%%
1073 function del_e = atmospheric_refraction_correction(pressure, temperature, ...
1074     atmos_refract, e0)
1075 % spa_const2
1076 SUN_RADIUS= 0.26667;

```





```

1257 function spa = calculate_geocentric_sun_right_ascension_and_declination(spa)
1258 TERM_X0 = 1; TERM_X1 = 2; TERM_X2=3; TERM_X3=4; TERM_X4=5; TERM_X_COUNT=5;
1259 % spa_const2
1260
1261 x = zeros(TERM_X_COUNT,1);
1262
1263 spa.jc = julian_century(spa.jd);
1264
1265 spa.jde = julian_ephemeris_day(spa.jd, spa.delta_t);
1266 spa.jce = julian_ephemeris_century(spa.jde);
1267 spa.jme = julian_ephemeris_millennium(spa.jce);
1268
1269 spa.l = earth_heliocentric_longitude(spa.jme);
1270 spa.b = earth_heliocentric_latitude(spa.jme);
1271 spa.r = earth_radius_vector(spa.jme);
1272
1273 spa.theta = geocentric_longitude(spa.l);
1274 spa.beta = geocentric_latitude(spa.b);
1275
1276 spa.x0 = mean_elongation_moon_sun(spa.jce);
1277 x(TERM_X0) = spa.x0;
1278 spa.x1 = mean_anomaly_sun(spa.jce);
1279 x(TERM_X1) = spa.x1;
1280 spa.x2 = mean_anomaly_moon(spa.jce);
1281 x(TERM_X2) = spa.x2;
1282 spa.x3 = argument_latitude_moon(spa.jce);
1283 x(TERM_X3) = spa.x3;
1284 spa.x4 = ascending_longitude_moon(spa.jce);
1285 x(TERM_X4) = spa.x4;
1286
1287 [spa.del_psi,spa.del_epsilon] = nutation_longitude_and_obliquity(spa.jce,x);
1288
1289 spa.epsilon0 = ecliptic_mean_obliquity(spa.jme);
1290 spa.epsilon = ecliptic_true_obliquity(spa.del_epsilon, spa.epsilon0);
1291
1292 spa.del_tau = aberration_correction(spa.r);
1293 spa.lamda = apparent_sun_longitude(spa.theta, spa.del_psi,spa.del_tau);
1294 spa.nu0 = greenwich_mean_sidereal_time (spa.jd, spa.jc);
1295 spa.nu = greenwich_sidereal_time (spa.nu0, spa.del_psi,spa.epsilon);
1296
1297 spa.alpha = geocentric_right_ascension(spa.lamda, spa.epsilon,spa.beta);
1298 spa.delta = geocentric_declination(spa.beta, spa.epsilon, spa.lamda);
1299
1300 end
1301
1302
1303 %%%%%%%%%%%%%%%%%%%%%%%%%%%%%%%%%%%%%%%%%%%%%%%%%%%%%%%%%%%%%%%%%%%%%%%%%
1304 % Calculate Equation of Time (EOT) and Sun Rise, Transit, & Set (RTS)
1305 %%%%%%%%%%%%%%%%%%%%%%%%%%%%%%%%%%%%%%%%%%%%%%%%%%%%%%%%%%%%%%%%%%%%%%%%%
1306 function spa = calculate_eot_and_sun_rise_transit_set(spa)
1307 JD_ZERO=2; JD_COUNT=4; SUN_TRANSIT = 1; SUN_RISE=2; SUN_SET=3; SUN_COUNT=4;
1308 SUN_RADIUS= 0.26667;
1309 % spa_const2
1310
1311 alpha = zeros(JD_COUNT,1);
1312 delta = zeros(JD_COUNT,1);
1313 m_rts = zeros(SUN_COUNT,1);
1314 nu_rts = zeros(SUN_COUNT,1);
1315 h_rts = zeros(SUN_COUNT,1);
1316 alpha_prime = zeros(SUN_COUNT,1);
1317 delta_prime = zeros(SUN_COUNT,1);
1318 h_prime = zeros(SUN_COUNT,1);
1319 h0_prime = -1*(SUN_RADIUS + spa.atmos_refract);
1320
1321 sun_rts = spa;
1322 m = sun_mean_longitude(spa.jme);
1323 spa.eot = eot(m, spa.alpha, spa.del_psi, spa.epsilon);
1324 sun_rts.hour = 0;
1325 sun_rts.minute = 0;
1326 sun_rts.second = 0;
1327 sun_rts.delta_ut1 = 0;
1328 sun_rts.timezone = 0;
1329
1330 sun_rts.jd = julian_day(sun_rts.year,sun_rts.month,sun_rts.day,sun_rts.hour, ...
1331 sun_rts.minute,sun_rts.second,sun_rts.delta_ut1,sun_rts.timezone);
1332
1333 sun_rts = calculate_geocentric_sun_right_ascension_and_declination(sun_rts);
1334 nu = sun_rts.nu;
1335
1336 sun_rts.delta_t = 0;
1337 sun_rts.jd = sun_rts.jd-1;
1338 for i = 1:JD_COUNT
1339 sun_rts = calculate_geocentric_sun_right_ascension_and_declination(sun_rts);
1340 alpha(i) = sun_rts.alpha;
1341 delta(i) = sun_rts.delta;
1342 sun_rts.jd = sun_rts.jd+1;
1343 end
1344
1345 m_rts(SUN_TRANSIT) = approx_sun_transit_time(alpha(JD_ZERO),spa.longitude,nu);
1346 h0 = sun_hour_angle_at_rise_set(spa.latitude,delta(JD_ZERO),h0_prime);

```

```

1347
1348 if (h0 >= 0)
1349     m_rts = approx_sun_rise_and_set(m_rts, h0);
1350     for i = 1:SUN_COUNT
1351         nu_rts(i) = nu + 360.985647*m_rts(i);
1352         n = m_rts(i) + spa.delta_t/86400;
1353         alpha_prime(i) = rts_alpha_delta_prime(alpha,n);
1354         delta_prime(i) = rts_alpha_delta_prime(delta,n);
1355         h_prime(i) = limit_degrees180pm(nu_rts(i)+spa.longitude-alpha_prime(i));
1356         h_rts(i) = rts_sun_altitude(spa.latitude,delta_prime(i),h_prime(i));
1357     end
1358
1359     spa.srha = h_prime(SUN_RISE);
1360     spa.ssha = h_prime(SUN_SET);
1361     spa.sta = h_rts(SUN_TRANSIT);
1362
1363     spa.suntransit = dayfrac_to_local_hr(m_rts(SUN_TRANSIT)- ...
1364         h_prime(SUN_TRANSIT)/360,spa.timezone);
1365
1366     spa.sunrise = dayfrac_to_local_hr(sun_rise_and_set(m_rts,h_rts, ...
1367         delta_prime,spa.latitude,h_prime,h0_prime,SUN_RISE),spa.timezone);
1368
1369     spa.sunset = dayfrac_to_local_hr(sun_rise_and_set(m_rts,h_rts, ...
1370         delta_prime,spa.latitude,h_prime,h0_prime,SUN_SET),spa.timezone);
1371
1372 else
1373     spa.srha = -99999;
1374     spa.ssha = -99999;
1375     spa.sta = -99999;
1376     spa.suntransit = -99999;
1377     spa.sunrise = -99999;
1378     spa.sunset = -99999;
1379 end
1380
1381 end
1382
1383
1384 %%%%%%%%%%%%%%%%%%%%%%%%%%%%%%%%%%%%%%%%%%%%%%%%%%%%%%%%%%%%%%%%%%%%%%%%%
1385 %{
1386 TRATTO DA Bird Clear Sky Model NREL
1387
1388     Richard E. Bird
1389     Clear Sky Broadband
1390     Solar Radiation Model
1391 From the publication "A Simplified Clear Sky model for Direct and Diffuse
1392 Insolation on Horizontal Surfaces" by R.E. Bird and R.L Hulstrom,
1393 SERI Technical Report SERI/TR-642-761, Feb 1991.
1394 Solar Energy Research Institute, Golden, CO.
1395
1396 The model is based on comparisons with results from rigorous radiative
1397 transfer codes. It is composed of simple algebraic expressions with 10 User
1398 defined inputs (green cells to left).
1399 Model results should be expected to agree within +/-10% with rigorous
1400 radiative transfer codes. The model computes solar radiation for every hour
1401 of the year, based on the 10 user input parameters.
1402 The graphical presentation includes diurnal clear sky radiation patterns
1403 for every day of the year.
1404 %}
1405 %%%%%%%%%%%%%%%%%%%%%%%%%%%%%%%%%%%%%%%%%%%%%%%%%%%%%%%%%%%%%%%%%%%%%%%%%
1406
1407 function spa=BIRD_algorithm(spa)
1408
1409 % INIZIO ALGORITMO
1410 % INPUT
1411 %lat=spa.latitude; % Enter Site Latitude, + for N and - for S of equator
1412 %Long=spa.longitude; % Enter site Longitude, - for W of 0 (Greenwich), + for E.
1413 %TZ=spa.timezone; % Enter Time Zone for site, - for W of Greenwich, + for E
1414 %Zenith_angle=topocentric_zenith_angle(spa.e); % da algoritmo SPA NREL
1415 %Pressure=spa.pressure; % Enter the station pressure in milliBars for site. Sea level = 1013 mB
1416 %doy=spa.day; % Day Of Year
1417 %HR=spa.hour; % Hour of day
1418
1419
1420 %Ozone=0.3; % Enter the total column Ozone thickness in cm. Values range from .05 to .4
1421 %H2O=1.5; % Enter the total column water vapor in cm. Values range from 0.01 to 6.5 typically
1422 %AOD500nm=0.1; %values range from 0.02 to 0.5. Values>0.5 represent clouds and volcanic dust, etc.
1423 %AOD380nm=0.15; % Optical Depth at 0.380 um (380 nm). Typical values range from 0.1 to 0.5
1424 %Ba=0.85; %proportion of scattered radiation is sent off in the same direction as the
1425 %incoming radiation ("forward scattering"). Bird recommends a value of 0.85 for rural
1426 %aerosols
1427 %Albedo=0.2; %albedo. Used to compute effect of multiple reflections between the ground and the sky.
1428 %Typical value for earth is 0.2, snow 0.9, vegetation 0.2
1429
1430 %-----
1431 % INIZIO ELABORAZIONI
1432 %-----
1433
1434 % Beam intensity, W/m2, corrected for earth-sun distance variations, for DOY
1435 ETR=1367*(1.00011+0.034221*cos(2*pi*(doy-1)/365)+...
1436     0.00128*sin(2*pi*(doy-1)/365)+0.000719*cos(2*(2*pi*(doy-1)/365))+...

```

```

1436         +0.000077*sin(2*(2*pi*(doy-1)/365)) );
1437     % risultati intermedi codice
1438     %Zenith angle fo Sun, complement of solar elevation
1439
1440     % Air Mass
1441     if Zenith_angle<89.999
1442         M_air=1/(cos(Zenith_angle/(180/pi))+0.15/(93.885-Zenith_angle)^1.25);
1443     else
1444         M_air=0;
1445     end
1446     %coalcoli intermedi modello Bird Clear Sky Model NREL
1447     if M_air>0
1448         T_rayliegh=exp(-0.0903*(Pressure*M_air/1013)^0.84*(1+Pressure*M_air/1013-(Pressure*M_air/1013)
1449             ^1.01));
1450         T_ozone=1-0.1611*(Ozone*M_air)*(1+139.48*(Ozone*M_air))^(-0.3034)-...
1451             0.002715*(Ozone*M_air)/(1+0.044*(Ozone*M_air)+0.0003*(Ozone*M_air)^2);
1452         T_gases=exp(-0.0127*(M_air*Pressure/1013)^0.26);
1453         T_water=1-2.4959*M_air*H20/((1+79.034*H20*M_air)^0.6828+6.385*H20*M_air);
1454         Taua=0.2758*AOD380nm+0.35*AOD500nm;
1455         T_aerosol=exp(-(Taua^0.873)*(1+Taua-Taua^0.7088)*M_air^0.9108);
1456         TAA=1-0.1*(1-M_air+M_air^1.06)*(1-T_aerosol);
1457         rs=0.0685+(1-Ba)*(1-T_aerosol/TAA);
1458         id=0.9662*ETR*T_aerosol*T_water*T_gases*T_ozone*T_rayliegh;
1459         Ias=ETR*cos(Zenith_angle/(180/pi))*0.79*T_ozone*T_gases*T_water*TAA*...
1460             (0.5*(1-T_rayliegh)+Ba*(1-(T_aerosol/TAA)))/(1-M_air+(M_air)^1.02);
1461         if cos(deg2rad(spa.incidence)) > 0
1462             spa.IdnH = id*cos(deg2rad((spa.incidence)));
1463         else
1464             spa.IdnH = 0;
1465         end
1466         spa.GH=(spa.IdnH+Ias)/(1-Albedo*rs);
1467     else
1468         % T_rayliegh=0;
1469         spa.GH=0; spa.IdnH = 0;
1470     end
1471     spa.diffuse=spa.GH-spa.IdnH;
1472     % spa.IdnH = BIRD_algorithm(spa.zenith,spa.pressure,spa.day);
1473
1474 end%-----
1475
1476 %%%%%%%%%%%%%%%%%%%%%%%%%%%%%%%%%%%%%%%%%%%%%%%%%%%%%%%%%%%%%%%%%%%%%%%%%%%%%%%
1477 % Calculate all SPA parameters and put into structure
1478 % Note: All inputs values (listed in header file) must already be in structure
1479 %%%%%%%%%%%%%%%%%%%%%%%%%%%%%%%%%%%%%%%%%%%%%%%%%%%%%%%%%%%%%%%%%%%%%%%%%%%%%%%
1480 function [result, spa] = spa_calculate(spa)
1481 SPA_ALL=3;
1482 SPA_ZA_RTS=2;
1483 SPA_ZA_INC=1;
1484 % spa_const2
1485
1486 result = validate_inputs(spa);
1487
1488 if (result == 0)
1489
1490     spa.jd = julian_day(spa.year,spa.month,spa.day,spa.hour,spa.minute, ...
1491         spa.second, spa.delta_ut1, spa.timezone);
1492
1493     spa = calculate_geocentric_sun_right_ascension_and_declination(spa);
1494
1495     spa.h = observer_hour_angle(spa.nu, spa.longitude, spa.alpha);
1496     spa.xi = sun_equatorial_horizontal_parallax(spa.r);
1497
1498     [spa.del_alpha, spa.delta_prime] = ...
1499         right_ascension_parallax_and_topocentric_dec(spa.latitude, ...
1500             spa.elevation,spa.xi,spa.h,spa.delta);
1501
1502     spa.alpha_prime = topocentric_right_ascension(spa.alpha, spa.del_alpha);
1503     spa.h_prime = topocentric_local_hour_angle(spa.h, spa.del_alpha);
1504
1505     spa.e0 = topocentric_elevation_angle(spa.latitude, spa.delta_prime, spa.h_prime);
1506     spa.del_e = atmospheric_refraction_correction(spa.pressure, ...
1507         spa.temperature,spa.atmos_refract, spa.e0);
1508     spa.e = topocentric_elevation_angle_corrected(spa.e0, spa.del_e);
1509
1510     spa.zenith = topocentric_zenith_angle(spa.e);
1511     spa.azimuth_astro = topocentric_azimuth_angle_astro(spa.h_prime, ...
1512         spa.latitude,spa.delta_prime);
1513     spa.azimuth = topocentric_azimuth_angle(spa.azimuth_astro);
1514
1515     if ((spa.function == SPA_ZA_INC) || (spa.function == SPA_ALL))
1516         spa.incidence = surface_incidence_angle(spa.zenith, ...
1517             spa.azimuth_astro,spa.azm_rotation,spa.slope);
1518         [spa.theta_l,spa.theta_t] = surface_incidence_angle_l_t(spa.zenith, ...
1519             spa.azimuth_astro,spa.azm_rotation,spa.slope);
1520     end
1521     if ((spa.function == SPA_ZA_RTS) || (spa.function == SPA_ALL))

```

```

1525     spa = calculate_eot_and_sun_rise_transit_set(spa);
1526     end
1527     spa=BIRD_algorithm(spa);
1528 end
1529
1530
1531 end

```

## A.2 LFR

This is the 1 D LFR block developed with the specifications of the HCEOI-12 receiver. It is coded using the Finite Difference Method and it has an internal time step with fixed thermal nodes decided at priory before the simulation (using a mask).

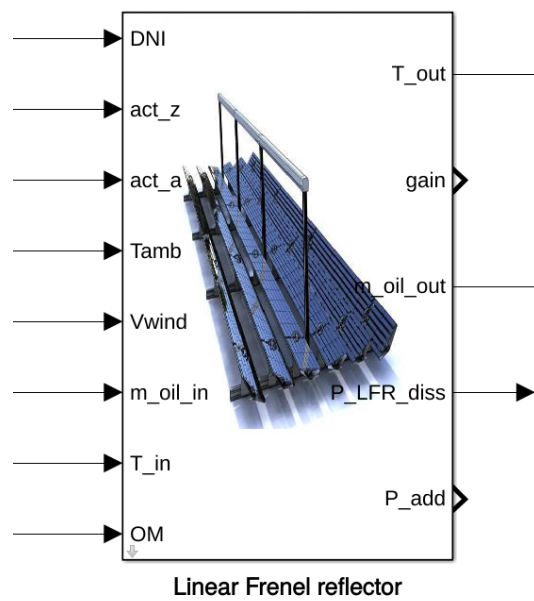


Figure A.5. The LFR block

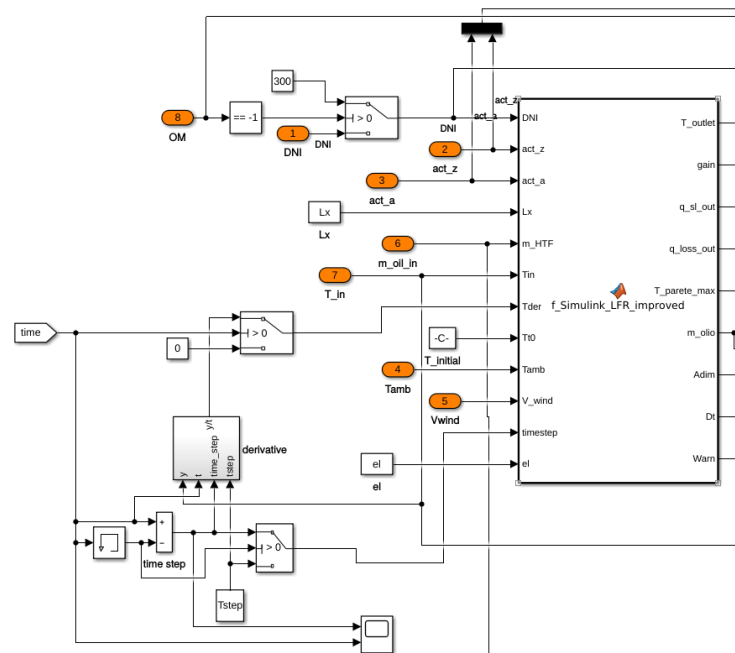


Figure A.6. Inside the LFR block

## LFR MATLAB code

```

1 function [T_outlet, gain, q_sl_out, q_loss_out, T_parete_max, m_olio, Adim, Dt, Warn] = ...
2   f_Simulink_LFR_improved(DNI, act_z, act_a, Lx, m_HTF, Tin, Tder, Tt0, Tamb, V_wind, timestep, el)
3 % DNI = 400; act_z=70; act_a=160; Lx=20; m_HTF=0.1; Tin=100; Tder=0; Tt0=100; Tamb=30; V_wind=1; timestep=100; el
4   =10;
5 % ricevitore elianto funzione
6 coder.extrinsic('pwd', 'fullfile');
7 % coder.extrinsic('warning');
8 % boundary conditions
9 global D22 D3 D4 D5 windSpeed Pa L...
10 epsilon4 epsilon5 eta_env alpha_env IAM q_sl tau_env alpha_abs
11
12 persistent T_receiver T167 T2 T3 T4 T4p T5 Tx T_out var Reflectivity...
13   Shadowing TrackingError GeomEffects ...
14   Rho_mirror_clean Dirt_mirror Dirt_HCE Error Warning tab gas
15
16
17 if isempty(T_receiver)
18   %loading of oil properties
19   tab = inzialization(); %creating the fields before to fill them
20   tab = load((fullfile(pwd, 'data', 'oil_Table2.mat')));
21   [-] = f_app(tab);
22   % oilVp1 = load('oil_Table.mat'); % serve per evitare di ricambiare tutto il codice (funzioni
23     comprese)
24   % cambiati, olio, T iniziale, T amb, q_sl, V_HTF, IAM, DNI
25   T_receiver = ones(el + 1, 1) * Tt0; %initial temperature of the whole receiver
26   D22 = 66e-3; % [m] inside diameter of the absorber pipe
27   D3 = 70e-3; % [m] absorber outside diameter
28   D4 = 119e-3; % [m] glass internal tube diameter
29   D5 = 125e-3; % [m] glass external tube diameter
30   L = Lx; % [m] length of the receiver tube
31
32   T1 = T_receiver + 273; % [K] mean (bulk) temperature of the HTF
33   T2 = T_receiver + 273; % [K] inside surface temperature of absorber pipe
34   T3 = T_receiver + 273; % [K] absorber outside surface temperature
35   T4 = (T_receiver + Tamb)/2 + 273; % [K] inner glass envelope surface temperature
36   T4p = T4 + 1; % [K] intermid glass envelope temperature
37   T5 = ones(el + 1, 1) * Tamb + 30 + 273; % [K] outer glass envelope surface temperature
38   T6 = ones(el + 1, 1) * Tamb + 273; % [K] Ambient temperature
39   T7 = ones(el + 1, 1) * (0.0552 * (Tamb)^(3/2) + 273); % [K] Sky Temperature Swinbank (1963)
40   T167 = [T1 T6 T7]; % to avoid global variables
41   % Tbase = 25 + 273; % [K] temperature at base of bracket
42   % T6brac = 273 + (Tbase - 273 + T6 - 273)/3; % estimate average bracket temperature
43
44   % epsilon3 = 0.2; % Absorber selective coating emissivity
45   epsilon4 = 0.86; % glass envelope emissivity

```

```

45     epsilon5 = 0.86; % emissivity of the glass envelope outer surface
46     Reflectivity = 0.9; % Solar Weighted Mirror Reflectivity
47     Shadowing = 0.974;
48     TrackingError = 0.994;
49     GeomEffects = 0.98;
50     Rho_mirror_clean = 0.935;
51     Dirt_mirror = Reflectivity/Rho_mirror_clean;
52     Dirt_HCE = (1+ Dirt_mirror)/2;
53     Error = 0.96;
54     Pa = 0.0001*0.75; % [Torr] anular gas pressure
55     gas = 'air'; % type of gas in vaccum tube
56 end
57 %warnings settings to 0
58 [Warning.PrCorr,Warning.WindCorr,Warning.TurbCorr,Warning.OilTemp,Warning.lambdaAir,Warning.Iter] =
    deal (0);
59
60 IAM = optical_efficiency(act_z,act_a); % Incident Angle Modifier
61 eta_env = (Shadowing*TrackingError*GeomEffects*Rho_mirror_clean*Dirt_mirror*Dirt_HCE*Error)*IAM; %
    shadowing, tracking error, dirt, unaccounted
62 alpha_env = 0.02; % The solar absorption in the glass envelope (Touloukian and DeWitt 1972)
63 alpha_abs = 0.96; % The solar absorption on the absorber layer, Cermet coating emittance
64 tau_env = 0.969; %0.98 - alpha_env; % transmittance of the glass envelope
65 windSpeed = V_wind; % wind speed [m/s]
66 % V_HTF = 47e-3/60/(pi*D22^2/4); % heat transfer fluid speed [m/s]
67 rho_oil = interp1(tab.oil.T,tab.oil.rho,Tin + 273); % [kg/m3]
68 V_HTF = m_HTF/rho_oil/(pi*D22^2/4);
69 V_HTF0 = V_HTF; % variabile appoggio
70 Adim = zeros(5,1);
71 T_out = zeros(size(T2,1),5);
72 % assert(Tin > Tamb,'inlet LFR temperature < Tamb');
73 q_sl = 4.05*DNI; % W/m
74 if timestep == 0
75     T_outlet = T_receiver(end);
76     [gain,q_sl_out,q_loss_out,T_parete_max,m_olio,Dt] = deal(0);
77     % q_loss = q_loss_m; %store the prevoius solution to assure output variable during the code
    bypass
78
79 else % code bypass for the hydraulic network balancing
80     %% Solve the 1D heat eq.
81     % Input Parameters
82     Dx = Lx/el;%0.29; % m, el = elements
83     Dt = Dx/V_HTF*0.7; % [s] Courant Friedrichs Lewy condition
84     tt = timestep; %[s] total simulation time = simulink timestep (simulink)
85     step = round(tt/Dt); % number of internal timestep (Courant stability)
86     if step < 2 || isnan(step) % because of low V_HTF
87         Dt = tt/4; % assure at least 2 internal time step
88     end
89     tt = linspace(0,timestep,round(timestep/Dt)+1); % [s] internal simulation time +1 because of
    step 0
90     Dt = tt(2) - tt(1); % new timestep to have the last time exactly
91     l_t = length(tt);
92     l_x = el + 1;
93     %% code non linear inside fsolve
94     T2x = T2;
95     Tmid = [T2x T3 T4 T4p T5];
96     if isempty(Tx) % <<-- esecuzione solo all'innescio per ottimizzare !
97         [T_out,var] = Dy_ThermalCircuitSolve4_vec_E(Tmid,Warning,tab,T167,gas,V_HTF*ones(l_x,1));
98     end
99     T_out(:,1) = T2;
100    T_out(:,2) = T3;
101    T_out(:,3) = T4;
102    T_out(:,4) = T4p;
103    T_out(:,5) = T5;
104    Tx = 0;
105    epsilon3 = var(:,1); phi3 = var(:,2); phi4p = var(:,3); r13 = var(:,4); k21 = var(:,5);
106    k2phi3 = var(:,6); k2phi4 = var(:,7); k2a = var(:,8); k2sky = var(:,9); q_loss = var(:,10); q_gain
    = var(:,11);
107
108    %% 2 points formula (1st order)
109
110    % preallocation
111    T = zeros(l_x,l_t);
112    Tmx2 = ones(l_x,l_t,5);
113    addQ_loss = T; addQ_gain = T;
114    [cp_oil,rho_oil,V_HTFil] = deal(zeros(l_x,1));
115    % initaial conditions
116    Tmx2(:,1,:) = T_out;
117    %BC's
118    T(1,:) = Boundary(Tder,Tin + 273,timestep,numel(T(1,:)),tab); % inlet Celsius
119    T(2:end,1) = T_receiver(2:end) + 273; % t = 0 T = ... Celsius everywhere
120
121    A = pi*D22^2/4; % m2
122    rho_oil_in = interp1(tab.oil.T,tab.oil.rho,T(1,1));
123    % tic
124    for kk = 1:l_t-1
125        % for ii = 2:length(x)
126            if kk==1
127                T(:,kk) = stability(T(:,kk),tab);
128                cp_oil = 1000*interp1(tab.oil.T,tab.oil.cp,T(:,kk)); % [J/kgk]
129                rho_oil = interp1(tab.oil.T,tab.oil.rho,T(:,kk));

```

```

130     else
131         T(:,kk) = stability(T(:,kk),tab);
132         cp_oil = 1000*interp1(tab.oil.T,tab.oil.cp,T(:,kk-1)); % [J/kgk]
133         rho_oil = interp1(tab.oil.T,tab.oil.rho,T(:,kk-1)); % [kg/m3]
134     end
135     V_HTFi = rho_oil_in./rho_oil*V_HTF0; % variation of velocity along the pipe
136
137     a = 1/Dt;
138     b = -1/Dt + V_HTFi/Dx - (k21 - 1)./(cp_oil.*rho_oil*A.*r13);
139     c = -V_HTFi/Dx;
140     d = 1./(rho_oil.*cp_oil.*A.*r13).*(k2phi3.*phi3 + k2phi4.*phi4p + k2a.*T167(:,2) + k2sky.*T167
141         (:,3));
142     T(2:end,kk+1) = 1/a*(d(2:end) - b(2:end).*T(2:end,kk) - c(2:end).*T(1:end-1,kk));
143     T(2:end,kk+1) = stability(T(2:end,kk+1),tab);
144
145     T167(:,1) = T(:,kk+1);
146     %sol verso l'esterno
147     newT = reshape(Tmx2(:,kk,:),size(Tmx2,1),size(Tmx2,3));
148     [T_out,var] = Dy_ThermalCircuitSolve4_vec_E(newT,Warning,tab,T167,gas,V_HTFi);
149     epsilon3 = var(:,1); phi3 = var(:,2); phi4p = var(:,3); r13 = var(:,4); k21 = var(:,5);
150     k2phi3 = var(:,6); k2phi4 = var(:,7); k2a = var(:,8); k2sky = var(:,9); q_loss = var(:,10);
151     q_gain = var(:,11);
152     % Re_D2 = R_e_value(V_HTFi,T167(:,1),Tmx2(:,end,2),D22,tab);
153     Tmx2(:,kk+1,:) = T_out;
154
155     addQ_loss(:,kk+1) = q_loss; % thermal loss storing
156     addQ_gain(:,kk+1) = q_gain; % thermal gain storing
157     T_receiver = T(:,end) - 273; %store the previous solution for the new initialization
158     % disp(['totale esecuzione ',num2str(kk/(length(time)-1)*100)]);
159
160     end
161     [Re_D2,Gr_D2,Pr_D2,Ra_D2,Gz_D2,-,-,-,-,-,-,-] = Ad_numbers(V_HTFi,T167(:,1),Tmx2(:,end,2),D22,L
162         );
163     Adim = [Re_D2,Gr_D2,Pr_D2,Ra_D2,Gz_D2]';
164
165     % toc
166     T_receiver = stability(T_receiver,tab);
167
168     q_sl_out = q_sl;
169     q_loss_out = sum(addQ_loss(:,end)); % total Watts wasted
170     T_parete_max = max(Tmx2(:,end,2)) - 273;
171     m_olio = m_HTF;
172     gain = m_HTF*sum(cp_oil(2:end).*(T(2:end,end)-T(1:end-1,end))); % total Watt gained
173     T_outlet = T(end,end) - 273;
174
175     end
176     Warn = manageWarning(Warning);
177 end
178
179 function T = stability(TT,tab)
180 TT(isnan(TT)) = tab.oil.T(end);
181 TT(TT > tab.oil.T(end)) = tab.oil.T(end);
182 TT(TT < tab.oil.T(1)) = tab.oil.T(1);
183 T = TT;
184 end
185
186 function T_1st_row = Boundary(Tder,Tin,time,n_col,tab)
187
188 if Tder == 0 % the inlet derivative of the previous step fixes the inlet T variation during time
189     T_1st_row = Tin*ones(1,n_col);
190 else % it finds the correct time spacng to get the final time properly
191     T_1st_row = linspace(Tin,(Tin + Tder*time),n_col);
192     % T(1,:) = Tinf_i:r*Dt:(Tinf_i + r*time); % [K] inlet temperature variation during the timestep
193     % add lower bound
194     T_1st_row = tab.oil.T(1).*(T_1st_row < tab.oil.T(1)) + T_1st_row.*(T_1st_row >= tab.oil.T(1));
195     % add upper bound
196     T_1st_row = tab.oil.T(end).*(T_1st_row > tab.oil.T(end)) + T_1st_row.*(T_1st_row <= tab.oil.T(end))
197     ;
198 end
199
200 end
201
202 function [Tmid,var] = Dy_ThermalCircuitSolve4_vec_E(Tmid_in,Warning,tab,T167,gas,V_HTF)
203 global D22 D3 D4 D5 windSpeed Pa...
204 epsilon4 epsilon5 eta_env alpha_env q_sl tau_env alpha_abs
205 persistent W f_conv %NN T2_ck T3_ck T4_ck T4p_ck T5_ck
206
207 if isempty(W)
208     W = Warning;
209 % [T2_old,T3_old,T4_old,T4p_old,T5_old,T2_ck,T3_ck,T4_ck,T4p_ck,T5_ck,NN] = deal(ones(size(Tmid_in
210     (:,1))));
211 f_conv = @(Tnew,Told,relax)Tnew*(relax) + Told*(1 - relax);
212 end
213
214 % elianto version
215 T1 = T167(:,1); T6 = T167(:,2); T7 = T167(:,3);
216 T2 = Tmid_in(:,1);
217 T3 = Tmid_in(:,2);
218 T4 = Tmid_in(:,3);
219 T4p = Tmid_in(:,4);
220 T5 = Tmid_in(:,5);
221 T2_old = T2; T3_old = T3; T4_old = T4; T4p_old = T4p; T5_old = T5;

```

```

215 toll = 1e-3; % (K) tollerance on the temperatures
216 girimax = 200; % max loops
217 Tmid = Tmid_in;
218 giri = 0; % loops
219 err = 1; % initial convergence error
220 i_m = 1;
221 k = 6; % number of samples to do the mean when the network does not converge
222 r12_old = -ones(numel(Tmid_in(:,1)),k); % it does the weighted mean of last k values when the solution
      oscillates
223 % preallocation:
224 [epsilon3, phi3, phi4p, r13, k21, k2phi3, k2phi4, k2a, k2sky, q_loss, q_gain] = deal(T3);
225 while max(abs(err)) > toll && giri < girimax
226     % Absorber selective coating emissivity
227     % epsilon3 = (2.2e-7)*(T3 - 273).^2 + 7.513e-2; % Archimede cermet (Elianto)
228     epsilon3 = 1.8333e-04.*(T3 - 273) + 0.0117; % (da datasheet 0.03 at 100 degrees e 0.0855 at 400
      Celsius degrees )
229     Ta = T6; Tsky = T7;
230
231     [r12, Nu] = R_12conv(V_HTF, T1, T2, D22, Warning, tab);
232     [-, -, -, -, -, Re, Gr, Pr, Ra, Gz, -, -, -, lambda_b] = Ad_numbers(V_HTF, T1, T2, D22, L);
233     % Re
234     % Ra
235     % Pr
236
237     if sum(r12_old > 0) > 0
238         r12 = mean(r12_old, 2);
239     % r12 = (r12_m*k + r12)/(k + 1);
240     end
241     r23 = R_23cond(T3, T2, D3, D22);
242     r34r = R_34rad(epsilon3, epsilon4, D3, D4, T3, T4);
243     r34c = R_34conv(T3, T4, gas, D3, D4, Pa, Warning);
244     r45 = ones(numel(T2), 1) .* R_45cond(D4, D5);
245     r7 = R_57rad(epsilon5, D5, T5, T7);
246     r6 = R_56conv(windSpeed, D5, T5, T6, Warning);
247     % [r12(end); r23(end); r34r(end); r34c(end); r45(end); r7(end); r6(end)]
248
249     phi3 = ones(numel(T2), 1) .* J_3solabs(eta_env, tau_env, q_sl, alpha_abs);
250     phi4p = ones(numel(T2), 1) .* J_5solabs_glass(eta_env, alpha_env, q_sl);
251
252     r13 = r12 + r23; r34 = (r34r .* r34c) ./ (r34r + r34c);
253     d5 = 2 ./ r45 + 1 ./ r6 + 1 ./ r7;
254     k54 = (2 ./ r45) ./ d5; k5a = (1 ./ r6) ./ d5; k5sky = (1 ./ r7) ./ d5;
255     T5 = k54 .* T4p + k5a .* Ta + k5sky .* Tsky;
256
257     d4p = 2 - k54; k44 = 1 ./ d4p;
258     k4phi = (r45 ./ 2) ./ d4p; k4a = k5a ./ d4p; k4sky = k5sky ./ d4p;
259     T4p = k44 .* T4 + k4phi .* phi4p + k4a .* Ta + k4sky .* Tsky;
260
261     d4 = 1 ./ r34 + 2 ./ r45 - 2 * k44 ./ r45;
262     k33 = (1 ./ r34) ./ d4; k3phi = (2 * k4phi ./ r45) ./ d4; k3a = (2 * k4a ./ r45) ./ d4; k3sky = (2 * k4sky ./ r45) ./ d4;
263     T4 = k33 .* T3 + k3phi .* phi4p + k3a .* Ta + k3sky .* Tsky;
264
265     d3 = 1 ./ r13 + 1 ./ r34 - k33 ./ r34;
266     k21 = (1 ./ r13) ./ d3; k2phi3 = 1 ./ d3; k2phi4 = (k3phi ./ r34) ./ d3;
267     k2a = (k3a ./ r34) ./ d3; k2sky = (k3sky ./ r34) ./ d3;
268     T3 = k21 .* T1 + k2phi3 .* phi3 + k2phi4 .* phi4p + k2a .* Ta + k2sky .* Tsky;
269
270     T2 = (r23 .* T1 + r12 .* T3) ./ (r12 + r23);
271
272     % error evaluation
273     E = [T2 T3 T4 T4p T5] - Tmid;
274     q_loss = (T3 - T5) ./ (r45 + r34);
275     q_gain = (T3 - T1) ./ r13;
276
277     relax_f = 0.9;
278     if giri > 6 && giri < 20
279         relax_f = 0.7;
280     elseif giri > 20 && giri < 50
281         relax_f = 0.5;
282     % Nu(abs(E(:,1))) == max(abs(E(:,1))))
283     elseif giri > 50
284         relax_f = 1;
285         i_m = i_m + 1;
286         if i_m > numel(r12_old(1,:))
287             i_m = 1;
288         end
289         r12_old(:, i_m) = r12;
290     % Nu(abs(E(:,1))) == max(abs(E(:,1))))
291     end
292
293     T2 = f_conv(T2, T2_old, relax_f);
294     T3 = f_conv(T3, T3_old, relax_f);
295     T4 = f_conv(T4, T4_old, relax_f);
296     T4p = f_conv(T4p, T4p_old, relax_f);
297     T5 = f_conv(T5, T5_old, relax_f);
298
299     %update Tmid
300     Tmid(:, 1) = T2;
301     Tmid(:, 2) = T3;
302     Tmid(:, 3) = T4;

```

```

303 Tmid(:,4) = T4p;
304 Tmid(:,5) = T5;
305
306 err = max(max(abs(E)));
307 T2_old = T2; T3_old = T3; T4_old = T4; T4p_old = T4p; T5_old = T5;
308
309 giri = giri + 1;
310 % ck = 1;
311 % T2_ck(giri) = T2(ck); T3_ck(giri) = T3(ck); T4_ck(giri) = T4(ck);
312 % T4p_ck(giri) = T4p(ck); T5_ck(giri) = T5(ck); NN(giri) = Nu(ck);
313 end
314 if giri == girimax
315 % err
316 % x_ax = 1:1:numel(T2_ck);
317 % plot(x_ax,T2_ck,x_ax,T3_ck,x_ax,T4_ck,x_ax,T4p_ck,x_ax,T5_ck,x_ax,NN)
318 if giri >= girimax
319 % assert(err < 5,'thermal network does not converge')
320 disp('thermal network does not converge')
321 end
322 W.Iter = 1;
323 end
324 manageWarning(W);
325 var = [epsilon3 phi3 phi4p r13 k21 k2phi3 k2phi4 k2a k2sky q_loss q_gain];
326 end
327
328 % function OptEff = optical_efficiency_V2(theta_l,theta_t,incidence)
329 % % costruzione polinomio su base dati Elianto
330 % persistent IAM_trasv IAM_long d_theta % opt_eff zenith azimuth
331 %
332 % if isempty(IAM_trasv)
333 % % zenith = (5:10:75); % 0°C sunrise/sunset others maximum = midday
334 % % azimuth = (0:10:90); % 0° = suth; 90° = West/est
335 % % IAM for 0:5:90 degrees
336 % d_theta = 0:5:90;
337 % IAM_trasv = [0.795 0.795 0.795 0.795 0.787 0.777 0.767...
338 % 0.759 0.741 0.724 0.706 0.683 0.623 0.544 0.447...
339 % 0.338 0.227 0.112 0];
340 % IAM_long = [0.776 0.776 0.776 0.776 0.752 0.727 0.687...
341 % 0.648 0.606 0.559 0.508 0.448 0.386 0.323 0.253...
342 % 0.185 0.123 0.064 0];
343 %
344 % end
345 %
346 % Kbl = interp1(d_theta,IAM_long,abs(theta_l));
347 % Kbt = interp1(d_theta,IAM_trasv,abs(theta_t));
348 % OptEff = Kbl*Kbt;%*cos(deg2rad(incidence));
349 % OptEff(OptEff<0) = 0;
350 % end
351
352 function OptEff = optical_efficiency(act_z,act_a)
353 % costruzione polinomio su base dati Elianto
354 persistent opt_eff zenith azimuth
355
356 if isempty(opt_eff)
357 zenith = (5:10:75); % 0°C sunrise/sunset others maximum = midday
358 azimuth = (0:10:90); % 0° = suth; 90° = West/est
359 opt_eff=[
360 %restricted data;
361 %restricted data;
362 %restricted data;
363 %restricted data;
364 %restricted data;
365 %restricted data;
366 %restricted data;
367 %restricted data;
368 %restricted data;
369 %restricted data;
370 ];
371 % permutation to ensure monotonic x y using interp2
372 idx2 = [8 7 6 5 4 3 2 1];
373 B2 = opt_eff(:,idx2); %variabile appoggio e permutazione matrice
374 opt_eff = B2;
375 end
376 % 0° <= azimuth <= 360°
377 % 0° <= zenith <= 90°
378 % change of convention
379 act_z = abs(act_z - 90);% sunrise, 90° for sunset/sunrise <90° = day
380 act_a = act_a - 90; % azimuth <90°, >270° = night
381 if act_a > 180
382 act_a = 180;
383 elseif act_a < 0
384 act_a = 0;
385 end
386 act_a = abs(act_a - 90); % 90° = suth, 0°-90°, 90°-180° = East/West
387
388 if act_z >75
389 act_z=75; % to be into the given polinomial IAM
390 end
391 OptEff = interp2(zenith,azimuth,opt_eff,act_z,act_a);
392 OptEff(isnan(OptEff) || OptEff < 0) = 0;

```

```

393 if act_z < 5
394     OptEff = 0; % to be into the given polinomial IAM
395 end
396 end
397
398 function J_5solabs = J_5solabs_glass(eta_env,alpha_env,q_sl)
399 %Solar Irradiation Absorption in the Glass Envelope
400 % the solar absorption into the glass envelope is treated as a heat flux to simplify
401 % the model. Physically this is not true. The solar absorption in the glass envelope is a heat
402 % phenomenon and is a function of the glass thickness. However, this assumption introduces minimal
403 % error
404 % since the solar absorptance coefficient is small for glass
405
406 % q_si --> solar irradiation per receiver length (W/m)
407 % eta_env --> effective optical efficiency at the glass envelope
408 % alpha_env --> absorptance of the glass envelope (Pyrex glass)
409 % IAM --> incident angle modifier
410 J_5solabs = q_sl*eta_env*alpha_env; % [W/m]
411 end
412
413 function J_3solabs = J_3solabs(eta_env,tau_env,q_sl,alpha_abs)
414 % Solar Irradiation Absorption in the Absorber
415
416 % The solar energy absorbed by the absorber occurs very close to the surface;
417 %therefore, it is treated as a heat flux
418
419 % q_si --> solar irradiation per receiver length (W/m)
420 % eta_env --> absorptance of absorber
421 % tau_env --> transmittance of the glass envelope
422 eta_abs = eta_env*tau_env;
423 J_3solabs = q_sl*(eta_abs*alpha_abs); % [W/m]
424 end
425
426 function [Re,Gr,Pr,Ra,Gz,Reb_v,Gr_v,Prb_v,Rab_v,Gzb_v,mu_w,mu_b,Prw_v,lambda_b] = Ad_numbers(V_HTF,T1,
427     T2,D22,L)
428 % oil properties evaluation to find all the adimensional numbers needed for
429 % processing the heat exchange
430 % b = bulk, w = wall
431 persistent tab Oldv_out oldv_out old_in
432 if isempty(tab)
433     %loading of oil properties
434     tab = inizialization(); %creating the fields before to fill them
435     tab = f_app(tab);
436     Oldv_out = zeros(size(T1,1),9);
437     oldv_out = zeros(1,5);
438     old_in = zeros(size(T1,1),3);
439 end
440
441 % bypass code if no call is needed
442 if any(any(old_in ~= [V_HTF,T1,T2])) % does the input change ?
443     Re = oldv_out(1);
444     Gr = oldv_out(2);
445     Pr = oldv_out(3);
446     Ra = oldv_out(4);
447     Gz = oldv_out(5);
448     Reb_v = Oldv_out(:,1);
449     Gr_v = Oldv_out(:,2);
450     Prb_v = Oldv_out(:,3);
451     Rab_v = Oldv_out(:,4);
452     Gzb_v = Oldv_out(:,5);
453     mu_w = Oldv_out(:,6);
454     mu_b = Oldv_out(:,7);
455     Prw_v = Oldv_out(:,8);
456     lambda_b = Oldv_out(:,9);
457 else
458     % Tmean = (T1+T2)/2;
459     % Tb = stability(T1,tab); % <<----- metti minore di T max
460     % Tw = stability(T2,tab); % <<----- metti minore di T max
461     Tmax = max(tab.oil.T); % max oil temperature degrees
462     T1(T1>Tmax) = Tmax; T2(T2>Tmax) = Tmax; % <<----- metti minore di T max
463     Tb = T1;
464     Tw = T2;
465
466     ni_b = interp1(tab.oil.T,tab.oil.ni,Tb)*10^-6; % [m2/s]
467     cp_b = 1000*interp1(tab.oil.T,tab.oil.cp,Tb); % [J/kgk]
468     lambda_b = interp1(tab.oil.T,tab.oil.lambda,Tb); % [W/K m]
469     rho_b = interp1(tab.oil.T,tab.oil.rho,Tb); % [kg/m3]
470
471     Reb_v = V_HTF.*D22./ni_b;
472     Re = mean(Reb_v);
473
474     beta = 0.001; % 1/°C therminol 62
475     g = 9.81; % accelerazione di gravità [m/s2]
476     Gr_v = (beta*g*abs(Tb - Tw)*(D22)^3)./(ni_b.^2); %calcolato tramite il teorema di Buckingham
477     Gr = mean(Gr_v);
478
479     mu_b = rho_b.*ni_b;
480     Prb_v = (cp_b.*mu_b)./lambda_b;
481     Pr = mean(Prb_v);

```

```

480
481 Rab_v = Gr_v.*Prb_v;
482 Ra = mean(Rab_v);
483
484 Gzb_v = D22/L*Reb_v.*Pr;
485 Gz = mean(Gzb_v);
486
487 ni_w = interp1(tab.oil.T,tab.oil.ni,Tw)*10^-6; % [m2/s]
488 rho_w = interp1(tab.oil.T,tab.oil.rho,Tw); % [kg/m3]
489 lambda_w = interp1(tab.oil.T,tab.oil.lambda,Tw); % [W/K m]
490 cp_w = 1000*interp1(tab.oil.T,tab.oil.cp,Tw); % [J/kgk]
491 mu_w = rho_w.*ni_w;
492 Prw_v = (cp_w.*mu_w)./lambda_w;
493
494 end
495 Oldv_out = [Reb_v,Gr_v,Prb_v,Rab_v,Gzb_v,mu_w,mu_b,Prw_v,lambda_b];
496 oldv_out = [Re,Gr,Pr,Ra,Gz];
497 old_in = [V_HTF,T1,T2];
498 end
499
500 %% thermal resistances
501
502 function [R_12conv,Nu] = R_12conv(V_HTF,Tb,Tw,D22,Warning,tab)
503 % convention HTF(therminol62)/absorber
504
505 % Pr1 = Prandtl number evaluated at the HTF temperature, T1
506 % Pr2 = Prandtl number evaluated at the absorber inner surface
507
508 if max(Tb) > tab.oil.T(end) || max(Tw) > tab.oil.T(end) % oil is boiling
509 % fprintf('warning out of range tab.oil polynomial curve T2_max = %4.2f °C\n',max(max(T1),max(T2)))
510 ;
511 % fix the maximum temperature artificially
512 Tb = tab.oil.T(end)*(Tb > tab.oil.T(end)) + Tb.*(Tb <= tab.oil.T(end));
513 Tw = tab.oil.T(end)*(Tw > tab.oil.T(end)) + Tw.*(Tw <= tab.oil.T(end));
514 Warning.OilTemp = 1; % to display externally of the simulink model
515 end
516 if min(Tb) < tab.oil.T(1) || min(Tw) < tab.oil.T(1) % oil is boiling
517 % fix the minimum temperature artificially
518 Tb = tab.oil.T(1)*(Tb < tab.oil.T(1)) + Tb.*(Tb >= tab.oil.T(1));
519 Tw = tab.oil.T(1)*(Tw < tab.oil.T(1)) + Tw.*(Tw >= tab.oil.T(1));
520 Warning.OilTemp = 1; % to display externally of the simulink model
521 end
522 if any(isnan(Tb)) || any(isnan(Tw))
523 Warning.OilTemp = 1; % to display externally of the simulink model
524 end
525 Nu = mapTw(Tb,Tw,V_HTF);
526
527 lambda_b = interp1(tab.oil.T,tab.oil.lambda,Tb); % [W/K m]
528 h1 = Nu.*lambda_b/D22; % [W/m2-K] HTF convection heat transfer coefficient at T1
529 R_12conv = 1./(h1*D22*pi); % (T2 - T1) [K/W*m]
530 manageWarning(Warning);
531 end
532
533 function R_23cond = R_23cond(T3,T2,D3,D22)
534 % Conduction Heat Transfer through the Absorber Wall
535
536 T23 = 0.5*(T3 + T2);
537 k23 = 0.013*T23 + 15.2; % [W/m-K] absorber thermal conductance at the average absorber
538 % temperature (T2+T3)/2 stainless steel Davis (2000)
539 % if is chosen SS 321H we have 0.0153*T23 + 14.775
540 R_23cond = log(D3/D22)./(2*pi*k23); % (T2- T3) [K/W*m]
541 end
542
543 function R_34conv = R_34conv(T3,T4,gas,D3,D4,Pa,Warning)
544 % Heat Transfer from the Absorber to the Glass Envelope
545 % Convection Heat Transfer
546
547 p11 = -2.709e-05;
548 p12 = 0.09021;
549 p13 = 1.71;
550
551 T34 = (T3 + T4)/2;
552 % - 50 °C + 412 °C range of validity
553 lambda34 = (p11*T34.^2 + p12*T34 + p13)*1e-3; % air thermal conductivity [W/m K]
554 if min(T34) < 223 || max(T34) > 685
555 % fprintf('warning out of polynomial curve of R34 conv T34_max = %4.2f °C\n',max(T34));
556 Warning.lambdaAir = 1;
557 end
558 switch gas
559 case 'air'
560 csi = 3.53e-8; % cm
561 %Gamma = cp34/cv34;
562 Gamma = -1.5e-7*T34.^2 + 4.5e-5*T34 + 1.402; % 300-600K
563 case 'hydrogen'
564 csi = 2.4e-8; % cm
565 Gamma = 1.293e-7*T34.^2 - 1.455e-4*T34 + 1.437; % 300-600K
566 case 'argon'
567 csi = 3.8e-8; % cm --> controlla unità di misura
568 Gamma = 1.6667; % 300-600K

```

```

569     otherwise
570     % 'gas name only: air, hydrogen, argon'
571     csi = 3.53e-8; % cm % to avoid variable definition errors in Simulink
572     %Gamma = cp34/cv34;
573     Gamma = -1.5e-7*T34.^2 + 4.5e-5*T34 + 1.402; % 300-600K % to avoid variable definition errors
           in Simulink
574 end
575 A = 2.331*10^(-20)*T34/(Pa*csi^2); % [cm] C1*10^(-20) [mmHg*cm^3/K]
576 b = (9*Gamma - 5)/(2*Gamma + 2);
577 gamma34conv = lambda34./(D3/2*log(D4/D3) + b.*A/100*(D3/D4 + 1)); % A/100 from [cm] to [m]
578 % for high pressure anular gas When the HCE annulus loses vacuum (pressure > -1 torr)
579 % beta34 = 1/T34; % [1/K]
580 % Rad3 = (g*beta34*abs(T3-T4)*D3^3)/(alpha34*ni34); % Rayleigh number
581 %q32conv = 2.425*k34*((T3 - T4)/(1+(D3/D4)^0.6)^1.25)*(Pr34*Rad3/(0.861 + Pr34))^0.25; % [W/m] Bejan
           (1995)
582 R_34conv = 1./(pi*D3*gamma34conv); % (T3- T4) [K/W*m]
583 manageWarning(Warning);
584 end
585
586 function R_34rad = R_34rad(epsilon3,epsilon4,D3,D4,T3,T4)
587 % Radiation Heat Transfer
588 % Incropera and DeWitt (1990)
589 sigma = 5.670e-8; % [W/m2-K4] Stefan-Boltzmann constant
590 gamma34rad = sigma*(T3 + T4).*(T3.^2 + T4.^2)/...
591     (1./epsilon3 + D3/D4*(1/epsilon4 - 1));
592 R_34rad = 1./(pi*D3.*gamma34rad); % (T3^4 - T4^4) [K/W*m]
593 end
594
595 function R_45cond = R_45cond(D4,D5)
596 % Conduction Heat Transfer through the Glass Envelope
597
598 k45 = 1.04; % (Pyrex glass) [Touloukian and DeWitt 1972].
599 R_45cond = log(D5/D4)/(2*pi*k45); % (T4- T5) [W/m]
600 end
601
602 function R_56conv = R_56conv(windSpeed,D5,T5,T6,Warning)
603 % Heat Transfer from the Glass Envelope to the Atmosphere
604 % Convection Heat Transfer
605
606 p1 = -5.615e-10;
607 p2 = 1.056e-06;
608 p3 = -0.000611;
609 p4 = 0.8106;
610
611 pa1 = 0.0001343;
612 pa2 = 0.05606;
613 pa3 = -6.195;
614
615 pn1 = 7.92e-06;
616 pn2 = 0.004698;
617 pn3 = -0.5507;
618
619 pb1 = -4.132e-08;
620 pb2 = 7.138e-05;
621 pb3 = -0.0436;
622 pb4 = 11.13;
623
624 pc1 = -2.709e-05;
625 pc2 = 0.09021;
626 pc3 = 1.71;
627 g = 9.81; % (m/s2) gravitational constant
628
629 T56 = 0.5.*(T5 + T6);
630 % range of validity air -100°C + 300°C
631 Pr5 = p1*T5.^3 + p2*T5.^2 + p3*T5 + p4;
632 Pr6 = p1*T6.^3 + p2*T6.^2 + p3*T6 + p4;
633
634 % range of validity air -100°C + 300°C
635 alpha56 = (pa1*T56.^2 + pa2*T56 + pa3)*1e-06; % thermal diffusivity for air at T56 (m2/s)
636
637 % range of validity air -23°C + 423°C
638 ni56 = (pn1*T56.^2 + pn2*T56 + pn3)*1e-05; % kinematic viscosity for air (m2/s)
639 Re_D5 = windSpeed*D5./ni56;
640 Pr56 = p1*T56.^3 + p2*T56.^2 + p3*T56 + p4;
641
642 % range of validity air -75°C + 412°C
643 beta56 = (pb1*T56.^3 + pb2*T56.^2 + pb3*T56 + pb4)*1e-03; % volumetric thermal expansion coefficient (
           ideal gas) (1/K)
644 lambda56 = (pc1*T56.^2 + pc2*T56 + pc3)*1e-3; % air thermal conductivity [W/m K]
645
646 C = 0.75.*(Re_D5 < 40) + ...
647     0.51.*(Re_D5 >= 40 & Re_D5 < 1000) + ...
648     0.26.*(Re_D5 >= 1000 & Re_D5 < 2e5) + ...
649     0.076.*(Re_D5 >= 2e5 & Re_D5 < 1e6);
650 m = 0.4.*(Re_D5 < 40) + ...
651     0.5.*(Re_D5 >= 40 & Re_D5 < 1000) + ...
652     0.6.*(Re_D5 >= 1000 & Re_D5 < 2e5) + ...
653     0.7.*(Re_D5 >= 2e5 & Re_D5 < 1e6);
654 if max(Re_D5) >= 1e6

```

```

655 % disp('Warning : wind Speed is out of range with regard the external tube convection correlation')
656 ;
657 Warning.WindCorr = 1; % to display externally of the simulink model
658 end
659 if windSpeed == 0 % No Wind Case
660 Rad5 = (g*beta56.*abs(T5 - T6)*D5^3)/(alpha56.*ni56); % Rayleigh number
661 Nu_d5 = (0.6 + (0.387*Rad5.^(1/6))./((1+(0.559./Pr56).^(9/16)).^(8/27))).^2; % Nusselt number,
        Incropera and DeWitt (1990)
662 else
663 if max(Pr6) > 500 || min(Pr6) < 0.7
664 % disp('Warning : the calculated Prantdl Number in external glass envelope is out of range');
665 Warning.PrCorr = 1; % to display externally of the simulink model
666 n = 0.37; % to avoid variable definition errors in Simulink
667 else
668 n = 0.37.*(Pr6 <=10) + 0.36.*(Pr6 > 10);
669 end
670
671 Nu_d5 = C.*Re_D5.^m.*Pr6.^n.*(Pr6./Pr5).^0.25; % The Nusselt number in this case is estimated with
        Zhukauskas°
672 %correlation for external forced convection flow normal to an
673 %isothermal cylinder [Incropera and DeWitt (1990)
674 end
675 h_56 = Nu_d5.*lambda56/D5; % [W/m2-K] convection heat transfer coefficient for air at (T5 ° T6)/2
676 R_56conv = 1./(h_56*pi*D5); %(T5 - T6) [K/W*m]
677 manageWarning(Warning);
678 end
679
680 function R_57rad = R_57rad(epsilon5,D5,T5,T7)
681 % Radiation Heat Transfer
682 % The net radiation
683 % transfer between the glass envelope and sky becomes [Incropera and DeWitt 1990]
684 % epsilon5 = emissivity of the glass envelope outer surface
685
686 sigma = 5.670e-8; % [W/m2-K4] Stefan-Boltzmann constant
687
688 R_57rad = 1./((T5 + T7).*(T5.^2 + T7.^2)*(sigma*D5*pi*epsilon5)); %(T5^4 - T7^4) [K/W*m]
689 end
690
691 %% functions for constant heat flux R12
692
693 function Nu = mapTw(Tb,Tw,V_HTF)
694 persistent f29 f30 f31 f32
695 global D22 L
696 if isempty(f29)
697 f29 = @(x)1730.9*x.^0.0549; % Re_cr
698 f30 = @(x)3056.4*x.^0.0217; % Re_qt
699 f31 = @(x)2.73*10^9*x.^-1.39 + 75.5;
700 f32 = @(x)-3.338*10^4*x.^-0.3112 + 3839;
701 end
702 [-,-,-,-,Re,Gr,Pr,Ra,Gz,-,-,-,-] = Ad_numbers(V_HTF,Tb,Tw,D22,L);
703 Nu = -ones(size(Re));
704
705 % for i=1:numel(X(:,1)) % Ra variation
706 % % for j = 1:numel(Y(1,:))
707 % Y Re
708 % X Ra
709 % X2 PR
710 % X3 Gr
711 % X4 Gz
712 % (Re,Pr,Gr,Gz,D,L)
713
714 MeyerC = meyerCond(Re,Pr,Gr,Gz);
715 err_f = zeros(size(MeyerC));
716
717 if any(MeyerC)
718 C_1 = Re < f29(Ra) & Re < f31(Ra);
719 C_2 = Re < f30(Ra) & ...
720 Re > f29(Ra) & ...
721 Re > f32(Ra);
722 C_3 = Re > f30(Ra);
723
724 if any(C_1) % Re < Re_cr
725
726 [Nu(C_1),err_f(C_1)] = meyer(Tb(C_1),Tw(C_1),V_HTF);
727 if any(err_f(C_1))
728 % val.meyer(C_1 & err_f) = -1;
729 % [val.ghajar(C_1 & err_f),val.gnielinski(C_1 & err_f),...
730 % val.ludovisi(C_1 & err_f),val.strikland(C_1 & err_f)] = id_eq(n_eq,Nu
        (C_1 & err_f),err_f);
731 end
732 % valx(C_1) = 10; % eq. 34
733 end
734 if any(C_2) % Re < Re_qt
735
736 [Nu(C_2),err_f(C_2)] = meyer(Tb(C_2),Tw(C_2),V_HTF);
737 if (err_f(C_2))
738 % val.meyer(C_2 & err_f) = -1;
739 % [val.ghajar(i,C_2 & err_f),val.gnielinski(i,C_2 & err_f),...

```

```

740         %           val.ludovisi(i,C_2 & err_f),val.strikland(i,C_2 & err_f)] = id_eq(
741         end
742         %           valx(i,C_2) = 30; % eq. 36
743     end
744     if any(C_3) % Re > Re_qt
745
746         [Nu(C_3),err_f(C_3)] = meyer(Tb(C_3),Tw(C_3),V_HTF);
747         %           valx(i,C_3) = 20; % eq. 37
748     end
749 end
750 if any(MeyerC == 0)
751     C_4 = MeyerC == 0;
752     %     if size(V_HTF) ~= size(C_4)
753     %     V_HTF = V_HTF*ones(size(C_4));
754     %     end
755     [Nu(C_4),n_eq,err_f(C_4)] = classicMap(Tb(C_4),Tw(C_4),V_HTF);
756     %     [val.ghajar(i,:),val.gnielinski(i,:),val.ludovisi(i,:),val.strikland(i,:)] = id_eq(n_eq,
757     %     Nu(i,:),err_f);
758     %     Ri_map2(i,:) = Gr./Re.^2;
759 end
760 %     end
761 assert(any(Nu>0),'error Nussel evaluation');
762 end
763 function MeyerC = meyerCond(Re,Pr,Gr,Gz)
764 % definition of the meyer limits
765 laminarC = Pr >= 3 & Pr <= 7.4 &...
766 Gr >= 30 & Gr <= 2.49*10^5 &...
767 Re >= 467 & Re <= 3217 &...
768 Gz >= 2.6 & Gz <= 5589; % laminar flow regime --> Re < Rec
769 turbulentC = Pr >= 5.5 & Pr <= 6.9 &...
770 Gr >= 8.9*10^2 & Gr <= 1.4*10^4 &...
771 Re >= 2804 & Re <= 9787; % Quasi-turbulent & turbulent --> Re > Reqt
772 transitionC = Pr >= 5.4 & Pr <= 6.8 &...
773 Gr >= 2.8*10^4 & Gr <= 3.2*10^4 &...
774 Re >= 2520 & Re <= 3361; % transitional --> Rec < Re < Reqt
775
776 MeyerC = laminarC & transitionC & turbulentC;
777 end
778
779 function [Nu,n_eq,err_f] = classicMap(Tb,Tw,V_HTF)
780 % this function manages all the available heat transfer models for single
781 % phase fluid in the forced-mixed-free convection regions
782 global D22 L
783
784 D = D22;
785 % n_eq = 0 infinity long laminar
786 % n_eq = 1 ghajar
787 % n_eq = 2 gnielinski
788 % n_eq = 3 ludovisi
789 % n_eq = 4 Strickland
790
791 % initialization
792 Nu = 4.364*ones(size(Tb));
793 n_eq = zeros(size(Tb));
794 err_f = zeros(size(Tb));
795 [Nu_gni,Nu_hwa,Nu_lud,Nu_gha,Nu_str] = deal(Nu);
796 [err_f_gni,err_f_hwa,err_f_lud,err_f_gha,err_f_str] = deal(err_f);
797
798 [-,-,-,-,Re,Gr,Prb,Ra,-,mu_w,mu_b,Prw,-] = Ad_numbers(V_HTF,Tb,Tw,D22,L);
799
800 Ri = Gr./Re.^2; % Richardson number buoyancy/flow shear
801 Forced = Ri <= 0.1;
802 Free = Ri >= 10;
803
804 if any(Forced) % F = forced
805     c0 = Forced & ((Re < 280) | (Gr == 0 & Re < 2300));
806     if any(c0) % fully developed laminar
807         %     Nu_new = 4.364; % infinity long laminar regime
808         n_eq(c0) = 0;
809         %     Nu(c0) = 4.36;
810
811     %     c00 = Gr == 0 | Ra < 10^3;
812     if any(Gr == 0 | Ra < 10^3)
813         Nu(c0) = 4.36;
814     else
815         [Nu_gni(c0),err_f_gni(c0)] = gniwang(Re(c0),Prb(c0)...
816         ,Prw(c0),Ra(c0));
817         [Nu_hwa(c0),err_f_hwa(c0)] = Hwang(Ra(c0));
818         err_f(c0) = (err_f_gni(c0) + err_f_hwa(c0)) > 0;
819
820         Nu(c0) = (Nu_gni(c0) - Nu_hwa(c0))./(0.1-1).*(Ri(c0) - 1) + Nu_hwa(c0); % range Ri 0.1 -1
821         [Nu_gni,Nu_hwa] = deal(4.364*ones(size(Tb)));
822         [err_f_gni,err_f_hwa] = deal(zeros(size(Tb)));
823     end
824 end
825 if any((Re < 49000) & c0 == 0) % fully developed transitional + turbulent
826     c1 = Forced & Re >= 280 & Re < 49000 & c0 == 0;
827     n_eq(c1) = 1;

```

```

828     [Nu(c1),err_f(c1)] = ghajar(Re(c1),Prb(c1),Gr(c1),D,L,mu_b(c1),mu_w(c1));
829
830     if any(err_f(c1))
831         % Forced convection heat transfer in the transition
832         % region between laminar and turbulent flow for a
833         % vertical circular tube (D. Huber and H. Walter) ISBN: 978-960-474-211-0
834         logic1 = err_f & c1;
835         logic1_trans = logic1 & Re < 10000;
836         logic1_turb = logic1 & Re >= 10000;
837         if any(logic1_trans)
838             [Nu(logic1_trans),err_f(logic1_trans)] = gniwang(Re(logic1_trans),Prb(logic1_trans),...
839                 Prw(logic1_trans),Ra(logic1_trans));
840         end
841         if any(logic1_turb)
842             [Nu(logic1_turb),err_f(logic1_turb)] = gnielinski(Re(logic1_turb),Prb(logic1_turb),Prw(
843                 logic1_turb));
844         end
845         n_eq(logic1) = 2; % id failed equation
846     end
847     if any(Re >= 49000 & c0 == 0) % fully turbulent
848         c2 = Forced & Re >=49000 & c0 == 0;
849         [Nu(c2),err_f(c2)] = gnielinski(Re(c2),Prb(c2),Prw(c2));
850         n_eq(c2) = 2;
851     end
852 end
853
854 if any(Free) % % N = natural
855     [Nu(Free),err_f(Free)] = ludovisi(Ra(Free),Prb(Free));
856     n_eq(Free) = 3;
857 end
858 cmixfree = Ri >= 1; % free convection boundary
859 cmixforce = Ri < 1; % forced convection boundary
860
861 if any(Free ~= 1 & Forced ~= 1) % M = mixed
862     if any(Re <= 10700)
863         c3 = Re <= 10700 & Free ~= 1 & Forced ~= 1;
864         % ghajar mixed free
865         c3free = c3 & cmixfree;
866         if any(c3free)
867             [Nu_lud(c3free),err_f_lud(c3free)] = ludovisi(Ra(c3free),Prb(c3free));
868             [Nu_gha(c3free),err_f_gha(c3free)] = ghajar(Re(c3free),Prb(c3free),Gr(c3free),D,L,mu_b(
869                 c3free),mu_w(c3free));
870             err_f(c3free) = (err_f_lud(c3free) + err_f_gha(c3free)) > 0;
871
872             Nu(c3free) = (Nu_gha(c3free) - Nu_lud(c3free))./(1-10).*(Ri(c3free) - 10) + Nu_lud(c3free)
873                 ;
874             [Nu_lud,Nu_gha] = deal(4.364*ones(size(Tb)));
875             [err_f_lud,err_f_gha] = deal(zeros(size(Tb)));
876         end
877         % ghajar mixed forced
878         c3forc = c3 & cmixforce;
879         if any(c3forc)
880             [Nu(c3forc),err_f(c3forc)] = ghajar(Re(c3forc),Prb(c3forc),Gr(c3forc),D,L,mu_b(c3forc),mu_w
881                 (c3forc));
882         end
883         n_eq(c3) = 1;
884         if any(err_f(c3)) % i.e. ghajar fails
885             logic3 = err_f & c3 & Re <= 2300; % forced/free and mixed boundary all laminar
886             logic2 = err_f & c3 & Re > 2300; % forced/free and mixed boundary all turbulent
887
888             % mixed/free laminar boundary all laminar
889             log3free = logic3 & cmixfree;
890             if any(c3free)
891                 [Nu_hwa(log3free),err_f_hwa(log3free)] = Hwang(Ra(log3free));
892                 [Nu_lud(log3free),err_f_lud(log3free)] = ludovisi(Ra(log3free),Prb(log3free));
893                 err_f(log3free) = (err_f_hwa(log3free) + err_f_lud(log3free)) > 0;
894
895                 Nu(log3free) = (Nu_hwa(log3free) - Nu_lud(log3free))./(1-10).*(Ri(log3free) - 10) +
896                     Nu_lud(log3free); % range Ri 1 -10
897                 [Nu_lud,Nu_hwa] = deal(4.364*ones(size(Tb)));
898                 [err_f_lud,err_f_hwa] = deal(zeros(size(Tb)));
899             end
900             % mixed/forced boundary all laminar
901             log3forc = logic3 & cmixforce;
902             if any(log3forc)
903                 [Nu_gni(log3forc),err_f_gni(log3forc)] = gniwang(Re(log3forc),Prb(log3forc)...
904                     ,Prw(log3forc),Ra(log3forc));
905
906                 [Nu_hwa(log3forc),err_f_hwa(log3forc)] = Hwang(Ra(log3forc));
907                 err_f(log3forc) = (err_f_gni(log3forc) + err_f_hwa(log3forc)) > 0;
908
909                 Nu(log3forc) = (Nu_gni(log3forc) - Nu_hwa(log3forc))./(0.1-1).*(Ri(log3forc) - 1) +
910                     Nu_hwa(log3forc); % range Ri 0.1 -1
911                 [Nu_gni,Nu_hwa] = deal(4.364*ones(size(Tb)));
912                 [err_f_gni,err_f_hwa] = deal(zeros(size(Tb)));
913             end
914         end
915         % mixed/forced boundary all turbulent

```

```

912     log2forc = logic2 & cmixforce;
913     if any(log2forc)
914         [Nu_gni(log2forc),err_f_gni(log2forc)] = gniwang(Re(log2forc),Prb(log2forc)...
915             ,Prw(log2forc),Ra(log2forc));
916         [Nu_str(log2forc),err_f_str(log2forc)] = Strickland(Re(log2forc),Prb(log2forc));
917         err_f(log2forc) = (err_f_gni(log2forc) + err_f_str(log2forc))> 0;
918
919         Nu(log2forc) = (Nu_gni(log2forc) - Nu_str(log2forc))./(0.1-1).*(Ri(log2forc) - 1) +
920             Nu_str(log2forc); % range Ri 0.1 -1
921         [Nu_gni,Nu_str] = deal(4.364*ones(size(Tb)));
922         [err_f_gni,err_f_str] = deal(zeros(size(Tb)));
923     end
924
925     % mixed/free boundary all turbulent
926     log2free = logic2 & cmixfree;
927     if any(log2free)
928         [Nu_lud(log2free),err_f_lud(log2free)] = ludovisi(Ra(log2free),Prb(log2free));
929         [Nu_str(log2free),err_f_str(log2free)] = Strickland(Re(log2free),Prb(log2free));
930         err_f(log2free) = (err_f_lud(log2free) + err_f_str(log2free))> 0;
931
932         Nu(log2free) = (Nu_str(log2free) - Nu_lud(log2free))./(1-10).*(Ri(log2free) - 10) +
933             Nu_lud(log2free);
934         [Nu_lud,Nu_str] = deal(4.364*ones(size(Tb)));
935         [err_f_lud,err_f_str] = deal(zeros(size(Tb)));
936     end
937
938     %             [Nu(logic2),err_f(logic2)] = Chen(Re(logic2),Pr(logic2),Gr(logic2),mu_b(
939         logic2),mu_w(logic2),D,L);
940     %             [Nu(logic2),err_f(logic2)] = Mon(Re(logic2),Pr(logic2),Gr(logic2));
941     n_eq(logic2) = 4; % id failed equation
942 end
943
944 if any(Re > 10700)
945     c4 = Free == 1 & Forced == 1 & Re > 10700;
946     % mixed/free boundary all turbulent
947     c4free = c4 & cmixfree;
948     if any(c4free)
949         [Nu_lud(c4free),err_f_lud(c4free)] = ludovisi(Ra(c4free),Prb(c4free));
950         [Nu_str(c4free),err_f_str(c4free)] = Strickland(Re(c4free),Prb(c4free));
951         err_f(c4free) = (err_f_lud(c4free) + err_f_str(c4free))> 0;
952
953         Nu(c4free) = (Nu_str(c4free) - Nu_lud(c4free))./(1-10).*(Ri(c4free) - 10) + Nu_lud(c4free)
954             ;
955         [Nu_lud,Nu_str] = deal(4.364*ones(size(Tb)));
956         [err_f_lud,err_f_str] = deal(zeros(size(Tb)));
957     end
958
959     % mixed/forced boundary all turbulent
960     c4forc = c4 & cmixforce;
961     if any(c4forc)
962         [Nu_gni(c4forc),err_f_gni(c4forc)] = gnielinski(Re(c4forc),Prb(c4forc),Prw(c4forc));
963         [Nu_str(c4forc),err_f_str(c4forc)] = Strickland(Re(c4forc),Prb(c4forc));
964         err_f(c4forc) = (err_f_gni(c4forc) + err_f_str(c4forc))> 0;
965
966         Nu(c4forc) = (Nu_gni(c4forc) - Nu_str(c4forc))./(0.1-1).*(Ri(c4forc) - 1) + Nu_str(c4forc)
967             ; % range Ri 0.1 -1
968         [Nu_gni,Nu_str] = deal(4.364*ones(size(Tb)));
969         [err_f_gni,err_f_str] = deal(zeros(size(Tb)));
970     end
971     n_eq(c4) = 4;
972 end
973 end
974
975 function [Nu,err] = Hwang(Ra)
976 % laminar flow mixed convection constant T wall
977 err = zeros(size(Ra));
978
979 Nu = 0.626*Ra.^0.269;
980 if any(Ra >= 5*10^8)
981     % disp('Hwang correlation: Re fails');
982     err(Ra >= 5*10^8) = 1;
983 end
984 end
985
986 function [Nu,err] = gniwang(Re,Prb,Prw,Ra)
987 % this function does a linear interpolation for transitional turbulent flow
988 % where gnielinski fails
989
990 % Forced convection heat transfer in the transition
991 % region between laminar and turbulent flow for a
992 % vertical circular tube (D. Huber and H. Walter) ISBN: 978-960-474-211-0
993 Nu = -ones(size(Re));
994 err = zeros(size(Re));
995 lam = Re < 2300;
996 tur = Re >= 2300;
997 if any(lam)
998     [Nu(lam),err(lam)] = Hwang(Ra(lam));
999 end
1000 if any(tur)

```

```

997     gamma = (Re(tur) - 2300)/(10^4 - 2300);
998     [Nu_hwa,err_f2] = Hwang(Ra(tur));
999     [Nu_gni,err_f1] = gnielinski(10000,Prb(tur),Prw(tur));
1000    %For the transition region of 2300 < Re < 104 the following interpolation function should be used
        according
1001    % to V. Gnielinski, V., "A new calculation procedure for the heat transfer in
1002    % the transition region between laminar and turbulent pipe flow (Ein neues
1003    % Berechnungsverfahren fur die Wärmeübertragung im Übergangsbereich
1004    % zwischen laminarer und turbulenter Rohrströmung)," Forschung im
1005    % Ingenieurwesen, vol. 61, no. 9, pp. 240-248, 1995.
1006    Nu(tur) = (1 - gamma).*Nu_hwa + gamma.*Nu_gni;
1007    err(tur) = (err_f1 + err_f2) > 0;
1008 end
1009 end
1010
1011 function [Nu,err] = ludovisi(Ra,Pr)
1012 % NATURAL CONVECTION HEAT TRANSFER IN HORIZONTAL CYLINDRICAL
1013 % CAVITIES: A COMPUTATIONAL FLUID DYNAMICS (CFD) INVESTIGATION
1014 % Proceedings of the ASME 2013 Power Conference; Daniele Ludovisi,Ivo A. Garza
1015 % (constant temperature BC)
1016
1017 err = zeros(size(Ra));
1018 Nu = 1.15*Ra.^0.22;
1019
1020 if any(Ra <= 3*10^4 | Ra >= 10*10^10)
1021 % disp('natural correlation: Ra fails');
1022 err(Ra <= 3*10^4 | Ra >= 10*10^10) = 1;
1023 end
1024 if any(Pr <= 1 | Pr>= 20) % 15 is the right one
1025 % disp('natural correlation: Pr fails');
1026 err(Pr <= 1 | Pr>= 20) = 1;
1027 end
1028 end
1029
1030 function [Nu,err] = ghajar(Re,Pr,Gr,D,L,mu_b,mu_w)
1031 % mean value of nusselt in mixed/forced transition Horizontal tube under
1032 % constant uniform flux
1033 % ref Transitional Heat Transfer in Plain Horizontal Tubes,LAP MOU TAM, AFSHIN J. GHAJAR
1034 % Heat Transfer Engineering, 27(5):23-38, 2006
1035
1036 err = zeros(size(Re));
1037 [Nu,Nu_l,Nu_t] = deal(-1*ones(size(Re)));
1038 mu_r = mu_b./mu_w;
1039 % Nu_l = 1.24*((Re.*Pr*D/L) + 0.025*(Gr.*Pr).^0.75).^(1/3).*(mu_r).^0.14;
1040 % Nu_t = 0.023*Re.^0.8.*Pr.^0.385*(L/D).^(-0.0054).*(mu_r).^0.14;
1041 a = 2617; b = 207; c = -0.95; % Inlet geometry Square-edged
1042
1043 laminarC = (Re >= 280 & Re <= 3800 & Pr >= 40 & Pr <= 160 & ...
1044 Gr >= 1000 & Gr <= 28000 & mu_r >= 1.2 & mu_r <= 3.8);
1045 turbulentC = (Re >= 7000 & Re <= 49000 & Pr >= 4 & Pr <= 34 & ...
1046 mu_r >= 1.1 & mu_r <= 1.7);
1047 transitionC = (Re >= 1600 & Re <= 10700 & Pr >= 5 & Pr <= 55 & ...
1048 Gr >= 4000 & Gr <= 250000 & mu_r >= 1.2 & mu_r <= 2.6);
1049
1050 if any(laminarC)
1051 Nu(laminarC) = 1.24*((Re(laminarC).*Pr(laminarC)*D/L) + ...
1052 0.025*(Gr(laminarC).*Pr(laminarC)).^0.75).^(1/3).*(mu_r(laminarC)).^0.14;
1053 end
1054
1055 if any(turbulentC)
1056 Nu(turbulentC) = 0.023*Re(turbulentC).^0.8.*Pr(turbulentC).^0.385...
1057 *(L/D).^(-0.0054).*(mu_r(turbulentC)).^0.14;
1058 end
1059
1060 if any(transitionC)
1061 Nu_l(transitionC) = 1.24*((Re(transitionC).*Pr(transitionC)*D/L) + ...
1062 0.025*(Gr(transitionC).*Pr(transitionC)).^0.75).^(1/3).*(mu_r(transitionC)).^0.14;
1063 Nu_t(transitionC) = 0.023*Re(transitionC).^0.8.*Pr(transitionC).^0.385...
1064 *(L/D).^(-0.0054).*(mu_r(transitionC)).^0.14;
1065 Nu(transitionC) = Nu_l(transitionC) + (exp((a - Re(transitionC))/b) + Nu_t(transitionC).^c).^c;
1066 % if it is out of range Re number establishes the correlation regardless the range
1067 end
1068
1069 if any((laminarC + turbulentC + transitionC) == 0)
1070 err((laminarC + turbulentC + transitionC) == 0) = 1;
1071 end
1072
1073 % if any(err) == 1
1074 % if any(Re >= 7000 & Re <= 49000) % turbulent
1075 % if any(Pr <= 4 | Pr >= 34)
1076 % disp('ghajar correlation: Pr fails (turbulent flow)');
1077 % elseif any(mu_r <= 1.1 | mu_r >= 1.7)
1078 % disp('ghajar correlation: mu_b/mu_w fails (turbulent flow)');
1079 % end
1080 % end
1081 % if any(Re >= 1600 & Re <= 10700) % transitional
1082 % if any(Pr <= 5 | Pr >= 55)
1083 % disp('ghajar correlation: Pr fails (transitional flow)');
1084 % elseif any(Gr <= 4000 | Gr>= 250000)
1085 %

```

```

1086 %         disp('ghajar correlation: Gr fails (transitional flow)');
1087 %         elseif any(mu_r <= 1.2 | mu_r >= 2.6)
1088 %             disp('ghajar correlation: mu_b/mu_w fails (transitional flow)');
1089 %         end
1090 %     end
1091 %     if any(Re >= 280 & Re <= 3800) % laminar
1092 %         if any(Pr < 40 | Pr > 160)
1093 %             disp('ghajar correlation: Pr fails (laminar flow)');
1094 %         elseif any(Gr < 1000 | Gr > 28000)
1095 %             disp('ghajar correlation: Gr fails (laminar flow)');
1096 %         elseif any(mu_r < 1.2 | mu_r > 3.8)
1097 %             disp('ghajar correlation: mu_b/mu_w fails (laminar flow)');
1098 %         end
1099 %     end
1100 % end
1101 end
1102
1103 function [Nu,err] = gnielinski(Re,Prb,Prw)
1104 % turbulent flow Gnielinsky [1976] and Incropera and DeWitt (1990)
1105 % b = bulk
1106 % w = wall
1107
1108 err = zeros(size(Re));
1109 % developing flow
1110 % f = (1.82*log(Re) - 1.64).^(-2);
1111 % Nu = ((f/8.*(Re - 1000).*Prb)*(1 + (D/L)^(2/3))...
1112 %       ./ (1 + 12.7*sqrt(f/8).*(Prb.^(2/3) - 1))).*(Prb./Prw).^0.11;
1113
1114 % developed flow
1115 % f = (1.58*log(Re) - 3.28).^(-2);
1116 % Nu = ((f/2.*(Re - 1000).*Prb)./(1 + 12.7*sqrt(f/2).*(Prb.^(2/3) - 1))).*(Prb./Prw).^0.11;
1117
1118 if any(Re > 5*10^6 | Prb < 0.5 | Prb > 2000)
1119 %     disp('gnielski correlation: out of range');
1120 %     err(Re > 5*10^6 | Prb < 0.5 | Prb > 2000) = 1;
1121 end
1122 end
1123
1124 function [Nu,err_f] = meyer(Tb,Tw,V_HTF)
1125 %{
1126 Single-phase mixed convection of developing and fully developed flow
1127 in smooth horizontal circular tubes in the laminar and transitional
1128 flow regimes; J.P. Meyer , M. Everts;
1129 International Journal of Heat and Mass Transfer 117 (2018) 1251-1273
1130
1131 Flow regime maps for smooth horizontal tubes at a constant heat flux
1132 M. Everts and J. P. Meyer* Department of Mechanical and Aeronautical
1133 Engineering, University of Pretoria, Pretoria, 0002, South Africa,
1134 %}
1135 global D22 L
1136 [-,-,-,-,Re,Gr,Prb,-,-,Gz,-,-,-] = Ad_numbers(V_HTF,Tb,Tw,D22,L);
1137
1138 lx = L*ones(size(Re));
1139 [Nu_new,Nu1,Nu2] = deal(30*ones(size(Re))); % preallocation
1140 err_f = zeros(size(Re)); % warning function error
1141 Nu = 30*ones(size(Re)); % guess value
1142 % Gr_m = Gr; % guess value
1143 loop = 0; % iteration number
1144 err = ones(size(Re));
1145 toll = 0.01;
1146
1147 while any(abs(err) > toll) && loop < 50
1148     Gr_m = Gr.*Nu;
1149     % conditions of validity
1150     laminarC = Prb >= 3 & Prb <= 7.4 &...
1151         Gr_m >= 541 & Gr_m <= 4.01*10^6 &...
1152         Re >= 467 & Re <= 3217 &...
1153         Gz >= 2.6 & Gz <= 5589; % laminar flow regime --> Re < Rec
1154     turbulentC = Prb >= 5.5 & Prb <= 6.9 &...
1155         Gr_m >= 5.9*10^4 & Gr_m <= 3.6*10^5 &...
1156         Re >= 2804 & Re <= 9787; % Quasi-turbulent & turbulent --> Re > Reqt
1157     transitionC = Prb >= 5.4 & Prb <= 6.8 &...
1158         Gr_m >= 6.1*10^4 & Gr_m <= 3.7*10^5 &...
1159         Re >= 2520 & Re <= 3361; % transitional --> Rec < Re < Reqt
1160
1161     if any(laminarC)
1162         LtMCD = 2.1*Re(laminarC).*Prb(laminarC).^0.6*D22./Gr_m(laminarC).^0.45;
1163         LtMCD(LtMCD > lx) = lx;
1164
1165         Nu1(laminarC) = (-0.84*Prb(laminarC).^(-0.2)*LtMCD + 0.72*(Re(laminarC)*D22).^0.54...
1166             .*Prb(laminarC).^0.34.*LtMCD(laminarC).^0.46)/lx;
1167         Nu2(laminarC) = (0.202*Gr_m(laminarC).^0.254 - 1.23).*Prb(laminarC).^0.39...
1168             .* (Re(laminarC)*D22).^(-0.06.*(lx - LtMCD(laminarC)))/lx;
1169
1170         Nu_new(laminarC) = 4.36 + Nu1(laminarC) + Nu2(laminarC);
1171     end
1172
1173     if any(transitionC)
1174
1175

```

```

1176     Nu_new(transitionC) = (0.00087*Re(transitionC) - 2.01)...
1177     .*Gr_m(transitionC).^(-0.01.*Prb(transitionC).^2);
1178 end
1179
1180 if any(turbolentC)
1181
1182     Nu_new(turbolentC) = (0.417*(Re(turbolentC) - 1000).^0.499...
1183     - 8.2).*Prb(turbolentC).^0.42;
1184 end
1185 if any(laminarC ~=1 & transitionC ~= 1 & turbolentC ~= 1)
1186     Nu_new(laminarC ~=1 & transitionC ~= 1 & turbolentC ~= 1) = -1;
1187     err_f(laminarC ~=1 & transitionC ~= 1 & turbolentC ~= 1) = 1;
1188 end
1189 loop = loop + 1;
1190 err = (Nu - Nu_new)./Nu_new*100;
1191 Nu = Nu_new;
1192 end
1193
1194
1195 % if any(Nu_new == -1)
1196 %     if any(~laminarC & Re(~laminarC) <= 2520)
1197 %         if any(Prb(laminarC) <= 3 | Prb(laminarC) >= 7.4)
1198 %             disp('meyer correlation laminar: Prb fails');
1199 %         end
1200 %         if any(Gr_m(laminarC) <= 541 | Gr_m(laminarC) >= 4.01*10^6)
1201 %             disp('meyer correlation laminar: Gr* fails');
1202 %         end
1203 %         if any(Re(laminarC) <= 467 | Re(laminarC) >= 3217)
1204 %             disp('meyer correlation laminar: Re fails');
1205 %         end
1206 %         if any(Gz(laminarC) <= 2.6 | Gz(laminarC) >= 5589)
1207 %             disp('meyer correlation laminar: Gz fails');
1208 %         end
1209 %     end
1210 %     if any(~transitionC & Re >= 2520 & Re <= 3361)
1211 %         if any(Prb(transitionC) <= 5.4 | Prb(transitionC) >= 6.8)
1212 %             disp('meyer correlation transition: Prb fails');
1213 %         end
1214 %         if any(Gr_m(transitionC) <= 6.1*10^4 | Gr_m(transitionC) >= 3.7*10^5)
1215 %             disp('meyer correlation transition: Gr* fails');
1216 %         end
1217 %         if any(Re(transitionC) <= 2520 | Re(transitionC) >= 3361)
1218 %             disp('meyer correlation transition: Re fails');
1219 %         end
1220 %     end
1221 %     if any(~turbolentC & Re >= 3361 & Re <= 9787)
1222 %         if any(Prb(turbolentC) <= 5.5 | Prb(turbolentC) >= 6.9)
1223 %             disp('meyer correlation turbulent: Prb fails');
1224 %         end
1225 %         if any(Gr_m(turbolentC) <= 5.9*10^4 | Gr_m(turbolentC) >= 3.6*10^5)
1226 %             disp('meyer correlation turbulent: Gr_m fails');
1227 %         end
1228 %         if any(Re(turbolentC) <= 2804 | Re(turbolentC) >= 9787)
1229 %             disp('meyer correlation turbulent: Re fails');
1230 %         end
1231 %     end
1232 %     if any(laminarC ~=1 & transitionC ~= 1 & turbolentC ~= 1)
1233 %         disp('meyer correlation fails');
1234 %     end
1235 % end
1236 end
1237
1238 function [Nu,err] = Strickland(Re,Pr)
1239 % D.T. Strickland, Heat transfer measurements in the transition region for a horizontal
1240 % circular tube with a square-edged entrance, Masters dissertation, Oklahoma State University,
1241 % Stillwater, 1990.
1242 % used for mixed region only, contant flux, fully developed
1243 err = zeros(size(Re));
1244 % Re 281 50529
1245 % Pr 3 - 157.8
1246 % Nu 12-239
1247 if any(Pr <= 3 | Pr >= 157.8)
1248     disp('Strickland correlation: Pr fails');
1249     err(Pr <= 3 | Pr >= 157.8) = 1;
1250 end
1251 if any(Re <= 281 | Re >= 50000)
1252     disp('Strickland correlation: Re fails');
1253     err(Re <= 281 | Re >= 50000) = 1;
1254 end
1255
1256 f = 1./(2.21*log(Re/7));
1257 Nu_l = 14.5;
1258 Nu_t = 6.3 + (0.079*f.*Re.*Pr)./(1 + Pr.^0.8).^5/6;
1259 Nu = Nu_l + ((exp(2311 - Re)/533.7)./Nu_l.^2 + 1./Nu_t.^2).^(-0.5;
1260 end
1261
1262 %% other auxiliary functions
1263
1264 function Warn = manageWarning(Warning)
1265 % this function share the variable Warning among other funtions

```

```

1266 persistent W
1267 if isempty(W)
1268     [W.PrCorr,W.WindCorr,W.TurbCorr,W.OilTemp,W.lambdaAir,W.Iter] = deal (0);
1269 end
1270 W.PrCorr     = Warning.PrCorr + W.PrCorr;
1271 W.WindCorr   = Warning.WindCorr + W.WindCorr;
1272 W.TurbCorr   = Warning.TurbCorr + W.TurbCorr;
1273 W.OilTemp    = Warning.OilTemp + W.OilTemp;
1274 W.lambdaAir  = Warning.lambdaAir + W.lambdaAir;
1275 W.Iter       = Warning.Iter + W.Iter;
1276 % W = Warning;
1277 Warn = [W.PrCorr,W.WindCorr,W.TurbCorr,W.OilTemp,W.lambdaAir,W.Iter];
1278 end
1279 function tab = f_app(tab)
1280 % temporary memory store
1281 persistent tab_app
1282 if isempty(tab_app)
1283     tab_app = inzialization(); %creating the fields before to fill them
1284     tab_app = tab;
1285 end
1286 tab = tab_app;
1287 end
1288
1289 function out = inzialization()
1290 %inialization of fluid properties structure
1291 out = struct(...
1292     'oil',struct(...
1293         'T',zeros(38,1),...
1294         'rho',zeros(38,1),...
1295         'cp',zeros(38,1),...
1296         'r',zeros(38,1),...
1297         'h',zeros(38,1),...
1298         'lambda',zeros(38,1),...
1299         'ni',zeros(38,1),...
1300         'vap_press',zeros(38,1),...
1301         'u',zeros(38,1))...
1302     );
1303 end

```

## A.3 TES

The Thermal Energy storage block is a lumped model, it has internal time steps to increase the results accuracy during the changing of the PCM enthalpy in case of too long global time step.

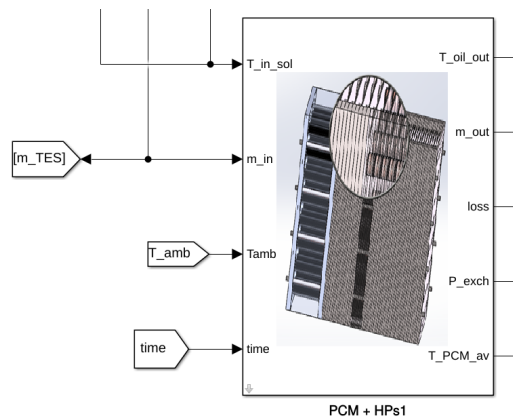


Figure A.7. The TES block

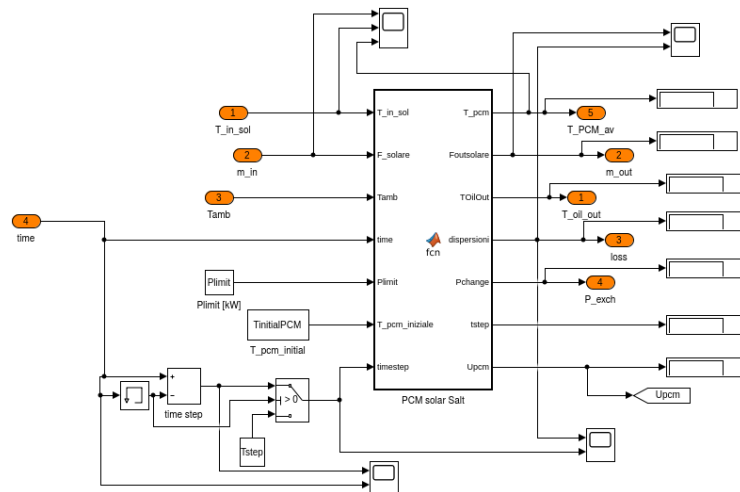


Figure A.8. Inside the TES block

## TES MATLAB code

```

1 function [T_pcm,Foutsolare,TOilOut,dispersioni,Pchange,tstep,Upcm] = fcn(T_in_sol,F_solare,Tamb,time,
2     Plimit,T_pcm_iniziale,timestep)
3 persistent L V A disp P_limite sogli1 sogli2 P_loss T_oil_out P...
4     lambdaSol lambdaLiq giri cpHigh cpLow...
5     beta g ni Gr Pr Ra Nu cp_oil rho M exit Tpcm
6
7 % global t1 Tpcm
8 %f
9 modello semplificato heat pipes pi\`u PCM
10 ipotesi semplificative:
11 - dT HP min=5°C al di sotto non si ha scambio termico
12 - PCM isotropo
13 - assenza di isteresi e sottoraffreddamento
14 - limitazione allo scambio termico dovuta al contatto tra HP e
15 PCM, supposto scambio termico conduttivo e convettivo, a questo si aggiunge
16 la limitazione in potenza imposta con P_limite dalle HPs stesse
17 %}
18
19 %condizioni di lavoro iniziali
20 if isempty(A)
21     P_loss = 0; T_oil_out = 0; P = 0;
22     Tpcm = T_pcm_iniziale + 273; %[K] di prima iterazione
23     %inizializzazione PCM
24     %caratteristiche PCM
25     sogli1 = 216 + 273; %[K]
26     sogli2 = 223 + 273; %[K]
27     M = 3800; %massa [kg] %corrispondente a 100kWh accumulati
28     L = 0.3; % lunghezza caratteristica scambio termico interno [m]
29     rho = 1.96*1000; %densità PCM kg/m3
30     V = (M/rho); % volume PCM [m3]
31     % 6 moduli da dimensioni: lph 0.6626*1.069+(0.476+0.161) [m]
32     %posizionati 3 coppie affiancate
33     A = 1.069*0.6626*3*2+1.609*(0.476+0.161)*2*2+0.6626*3*(0.476+0.161)*2*2;
34     disp = 0.4; % dispersioni termiche per m2 di superficie [W/m2K]
35     lambdaSol = 0.4; %[W/mK] conducibilità termica PCM solido
36     lambdaLiq = 0.55; %[W/mK] conducibilità termica PCM liquido
37     cpLow = 1.5; % J/gK calore specifico PCM in assenza di cambiamento di fase
38     cpHigh = 95/(sogli2-sogli1); % J/gK calore specifico PCM in cambiamento di fase
39     beta=1*10^(-4); % https://thermalfluidscentral.org/encyclopedia/index.php/Thermophysical_Properties
40     :_Phase_Change_Materials
41     g=9.81; % accelerazione di gravità [m/s2]
42     p1 = -1.843733103e-06;
43     p2 = 0.003715432304844;
44     p3 = 1.012291903694753;
45     cp_oil = (p1*T_in_sol^2 + p2*T_in_sol + p3)*1000; % calore specifico olio diatermico [kJ/kgK]
46 end
47
48 %-----
49 % INPUT
50 T_in_sol = T_in_sol+273; %temperatura in ingresso all'HP dell'olio dal solare [K]
51
52 Tamb = Tamb+273; % temperatura ambiente [K]
53
54 %-----
55 % timestep = time-t1; %estrapolazione timestep
56 % t1 = time;

```

```

54 TSTEP = timestep/20; % Simulink timestep diviso timestep interni
55 % TSTEP=30; % Simulink timestep diviso timestep interni
56 stopSim = timestep+time; %stop simulazione [s]
57 inizioSim = time; % inizio simulazione [s]
58 P_limite = Plimit; %kW massimi gestibili dal sistema
59 %-----
60
61 giri=1; giri2 = 1;
62
63 exit=0; %uscita dal ciclo che impedisce si superare la Q_limite
64 % iterazioni=(stopSim-inizioSim)/TSTEP;
65 tstep=0;
66 if (time > 0) && (TSTEP > 0)
67     iterazioni=length(inizioSim:TSTEP:stopSim);
68     [P_loss,Tpcm_new,dTpcm,T_oil_out,E_step,Q,P,Q_loss] = deal(zeros(floor(iterazioni+1),1));
69     dt = 0;
70     TpipeInPCM = 0;
71     toll = 10^-3;
72
73     % for i=inizioSim:TSTEP:(stopSim-TSTEP)
74     for j = 1:iterazioni-1
75         err = 1;
76         while err>toll && giri2<100
77             %-----
78             %calcolo cp [kJ/kgK] e lambda funzione dello stato termodinamico
79             %-----
80             while 1
81                 [cp_pcm,lambda,mu] = PCMstat(cpLow,cpHigh,soglia1,soglia2,lambdaSol,lambdaLiq,Tpcm);
82                 %-----
83                 %calcolo temperatura ai capi del Pipe
84                 %-----
85                 if j==1
86                     p1 = -1.843733103e-06;
87                     p2 = 0.003715432304844;
88                     p3 = 1.012291903694753;
89                     cp_oil = (p1*T_in_sol^2 + p2*T_in_sol + p3)*1000; % calore specifico olio
90                         diatermico [kJ/kgK]
91                     cp_oil_old = cp_oil;
92                     err = abs((cp_oil_old - cp_oil)/cp_oil*100);
93                     if giri==1
94                         if T_in_sol-5>=Tpcm % calore dall'olio al PCM
95                             TpipeInPCM=T_in_sol-5; %calcolo temperatura del pipe a contatto col PCM [K]
96                             dT=TpipeInPCM-Tpcm; %differenza di temperatura all'interno del PCM [K]
97                         else
98                             if Tpcm>=T_in_sol+5 % calore dal pcm all'olio
99                                 TpipeInPCM=T_in_sol+5;
100                                 dT=-TpipeInPCM+Tpcm;
101                                 % else
102                                 % T_pcm_new=Tpcm; %se la diff di T ai capi
103                                 % del pipe non supera i 5°C
104                                 %il PCM non scambia calore.
105                             end
106                         end
107                     else
108                         cp_oil_old = cp_oil;
109                         cp_oil = int_cp(T_in_sol,T_oil_out(j-1))*1000;
110                         err = abs((cp_oil_old - cp_oil)/cp_oil*100);
111                     end
112
113             %-----
114             %calcolo scambio termico HP/PCM
115             %-----
116             ni = mu/rho;
117             Gr = (beta*g*dt*(L)^3)/((ni)^2);%calcolato tramite il teorema di Buckingham
118             Pr = (cp_pcm*mu)/lambda;
119             Ra = Gr*Pr;
120             Nu = 0.046*Ra^(1/3); %valida per 10^6<Ra<10^9 1<altezza/ampiezza<40 delle cavità
121             % lambdaeEff=lambda*Nu; % conducibilità termica effettiva da inserire per tener
122             % conto della convezione ?
123             Pr=(cp_pcm*mu)/lambda; %seconda iterazione
124             Ra=Gr*Pr;
125             Nu=0.046*Ra^(1/3);
126             h = 20*Nu*lambda/L;
127             Q_loss(j) = A*disp*(Tpcm - Tamb)*TSTEP; % energia dispersa in ambiente [W*subTimestep]
128             P_loss(j) = Q_loss(j)/TSTEP; % potenza dispersa in ambiente [W]
129             if F_solare > 0
130                 Tpcm_new(j) = TpipeInPCM - (TpipeInPCM-Tpcm)*exp(-(TSTEP*F_solare*cp_oil*...
131                     (1 - exp(-(h/(F_solare*cp_oil)))))/(V*rho*cp_pcm)); % in condizioni adiabatiche
132                 % calcolo della temperatura dell'olio in uscita
133                 T_oil_out(j)=-((Tpcm_new(j)-Tpcm)*M*cp_pcm)/(cp_oil*F_solare*TSTEP)+T_in_sol;
134                 % la Tpcm nella prossima iterazione terrà in conto
135                 % delle perdite per il bilancio della T_oil_out riga su
136                 Tpcm_new(j) = Tpcm_new(j) - Q_loss(j)/(M*cp_pcm);
137             else
138                 T_oil_out(j) = T_in_sol;
139                 Tpcm_new(j) = Tpcm - Q_loss(j)/(M*cp_pcm);
140             end
141             dTpcm(j)=Tpcm_new(j)-Tpcm;
142             %-----
143             % Calcolo outputs

```

```

141 %-----
142 if j>1
143     Q(j) = dTpcm(j)*M*cp_pcm; % energia scambiata tra olio e PCM [J]
144     %calcolo temperatura olio uscita scambiatore di calore [K]
145     % T_oil_out(j)=-Q(j)/(cp_oil*F_solare*TSTEP)+T_in_sol;
146     P(j) = Q(j)/(TSTEP*1000); % potenza scambiata tra olio e PCM [kW]
147     Q(j) = Q(j-1) + Q(j);
148     Q_loss(j) = Q_loss(j) + Q_loss(j-1);
149     E_step(j) = Q(j)/1000; %kJ accumulati dal PCM
150 else
151     Q(j) = dTpcm(j)*M*cp_pcm;
152     Q_loss(j) = 0;
153     P(j) = Q(j)/(TSTEP*1000); % potenza scambiata [kW]
154     if F_solare > 0
155         T_oil_out(j) = -Q(j)/(cp_oil*F_solare*TSTEP) + T_in_sol;
156     else
157         T_oil_out(j) = T_in_sol;
158     end
159 end
160
161 if abs(P(j))>=P_limite
162     if T_in_sol - 5 >=Tpcm
163         if abs(P(j)) >= P_limite + 5 % per ottimizzare
164             TpipeInPCM = TpipeInPCM - abs(P(j))/P_limite;
165         else
166             TpipeInPCM = TpipeInPCM - 0.1;
167         end
168         dT = TpipeInPCM - Tpcm;
169     else
170         if Tpcm >= T_in_sol + 5 % calore dal pcm all'olio
171             if abs(P(j)) >= P_limite + 5 % per ottimizzare
172                 TpipeInPCM = TpipeInPCM + abs(P(j))/P_limite;
173             else
174                 TpipeInPCM = TpipeInPCM + 0.1;
175             end
176             dT = - TpipeInPCM + Tpcm;
177         end
178     end
179 else
180     exit=1;
181     if T_in_sol - 5 >= Tpcm % calore dall'olio al PCM
182         TpipeInPCM = T_in_sol - 5; %calcolo temperatura del pipe a contatto col PCM [K]
183         dT = TpipeInPCM - Tpcm; %differenza di temeperatura all'interno del PCM [K]
184     else
185         if Tpcm >= T_in_sol + 5 % calore dal pcm all'olio
186             TpipeInPCM = T_in_sol + 5;
187             dT = - TpipeInPCM + Tpcm;
188         end
189     end
190 end
191 giri = giri + 1;
192
193 % T_c(giri)=TpipeInPCM;
194 if exit == 1
195     break
196 end
197
198 exit = 0;
199 Tpcm = Tpcm_new(j);
200 giri2 = giri2 + 1;
201 % j = j + 1; % \\'e necessario qui per gestire le iterazioni quando la P eccede il valore
202     max
203 end
204 Foutsolare = F_solare;
205 % dispersioni = Q_loss(j-1)/timestep;
206 dispersioni = P_loss(j-1);
207 % T0ilOut=-E_step(j-1)*1000/(cp_oil*F_solare*stopSim)+T_in_sol-273;
208 T0ilOut = T_oil_out(j-1) - 273;
209 Pchange = P(j-1);
210 T_pcm = Tpcm - 273;
211 timestep = stopSim - inizioSim;
212 if F_solare == 0
213     T0ilOut = T_in_sol - 273;
214 end
215 else
216 if time <= 0
217     T_pcm = T_pcm_iniziale;
218     Foutsolare = 0;
219     dispersioni = 0;
220     T0ilOut = 0;
221     Pchange = 0;
222 else
223     Foutsolare = F_solare;
224     dispersioni = P_loss(end);
225     % T0ilOut=-E_step(j-1)*1000/(cp_oil*F_solare*stopSim)+T_in_sol-273;
226     T0ilOut = T_oil_out(end) - 273;
227     % [cp_pcm,-,-] = PCMstat(cpLow,cpHigh,soglia1,soglia2,lambdaSol,lambdaLiq,Tpcm);
228     % Q_loss = A*disp*(Tpcm - Tamb)*TSTEP; % energia dispersa in ambiente [W*subTimestep]
229     % Pchange = Q_loss/TSTEP; % potenza dispersa in ambiente [W]

```

```

230     % Tpcm_new = Tpcm - Q_loss/(M*cp_pcm);
231     T_pcm = Tpcm - 273;
232     Pchange = P(end);
233 end
234 end
235 Upcm = internalEnergy(Tpcm,cpLow,cpHigh,soglia1,soglia2,M);
236 end
237
238 function Upcm = internalEnergy(Tpcm,cpLow,cpHigh,soglia1,soglia2,M)
239 % internal energy stored, 0 degrees as reference
240
241 if Tpcm < soglia1
242     Upcm = M*cpLow*Tpcm; % [kJ]
243 elseif Tpcm < soglia2
244     Upcm1 = M*cpLow*soglia1; % [kJ]
245     Upcm2 = M*cpHigh*(Tpcm - soglia1); % [kJ]
246     Upcm = Upcm1 + Upcm2;
247 else
248     Upcm1 = M*cpLow*soglia1*1000; % [kJ]
249     Upcm2 = M*cpHigh*(soglia2 - soglia1); % [kJ]
250     Upcm3 = M*cpLow*(Tpcm - soglia2); % [kJ]
251     Upcm = Upcm1 + Upcm2 + Upcm3;
252 end
253 end
254
255 function cp_int_mean = int_cp(T1,T2)
256 % correct estimation of cp using integration between the two temperatures
257 k = [-0.000001843733103 0.003715432304844 1.012291903694753];
258 if T1==T2
259     cp_int = k(3)*(T2 - T1) + k(2)*(T2^2 - T1^2)/2 + k(1)*(T2^3 - T1^3)/3;
260     cp_int_mean = cp_int/(T2-T1);
261 else
262     cp_int_mean = k(3) + k(2)*T1 + k(1)*T1^2;
263 end
264 end
265
266 function [cp_pcm,lambda,mu] = PCMstat(cpLow,cpHigh,soglia1,soglia2,lambdaSol,lambdaLiq,Tpcm)
267 persistent f_mu
268 if isempty(f_mu)
269     f_mu = @(T) 0.07543937-2.77*10^(-4)*T+3.49*10^(-7)*T^2-1.47*10^(-10)*T^3;
270 end
271 if Tpcm <= soglia1
272     cp_pcm = cpLow*1000;
273     lambda = lambdaSol;
274 else
275     if Tpcm <= soglia2
276         cp_pcm = cpHigh*1000;
277         lambda = lambdaSol+((lambdaLiq-lambdaSol)/(soglia2-soglia1))*(Tpcm-soglia1); % [W/mK]
278     else
279         cp_pcm = cpLow*1000;
280         lambda = lambdaLiq;
281     end
282 end
283 mu = f_mu(Tpcm);
284 end

```

## A.4 ORC

The ORC block works with a thermodynamic cycle with imposed boundary conditions explained in the modeling chapter. The fluid properties have been got with CoolProp over a large range with a logarithmic grid spacing enabling a better precision for the creation of the lookup tables. These tables, as well as the HTF properties are loaded in the MATLAB function only during the first initialisation, after that the internal while loop evaluates all the thermodynamic points iteratively to reach the desired conditions and stops when the convergence is achieved. To increase the computational efficiency, in addition to the lookup tables, also the previous solution is stored to be used in the next iteration as guess value, this "trick" sometimes fails because the value does not fit well the new input conditions, thus a reset of the all guess values to the design ones is carried out in the feedback network. Moreover, an interposed block at the ORC inlet is placed to assure a correct supplying temperature to the evaporator (it can not exceed 220 °C).

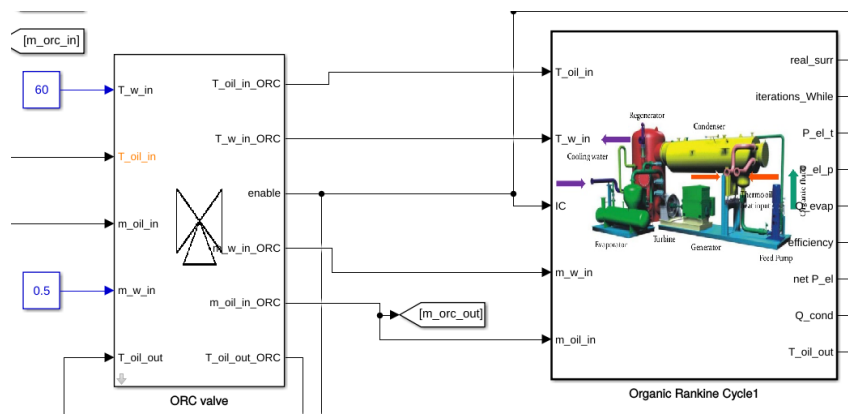


Figure A.9. The ORC block

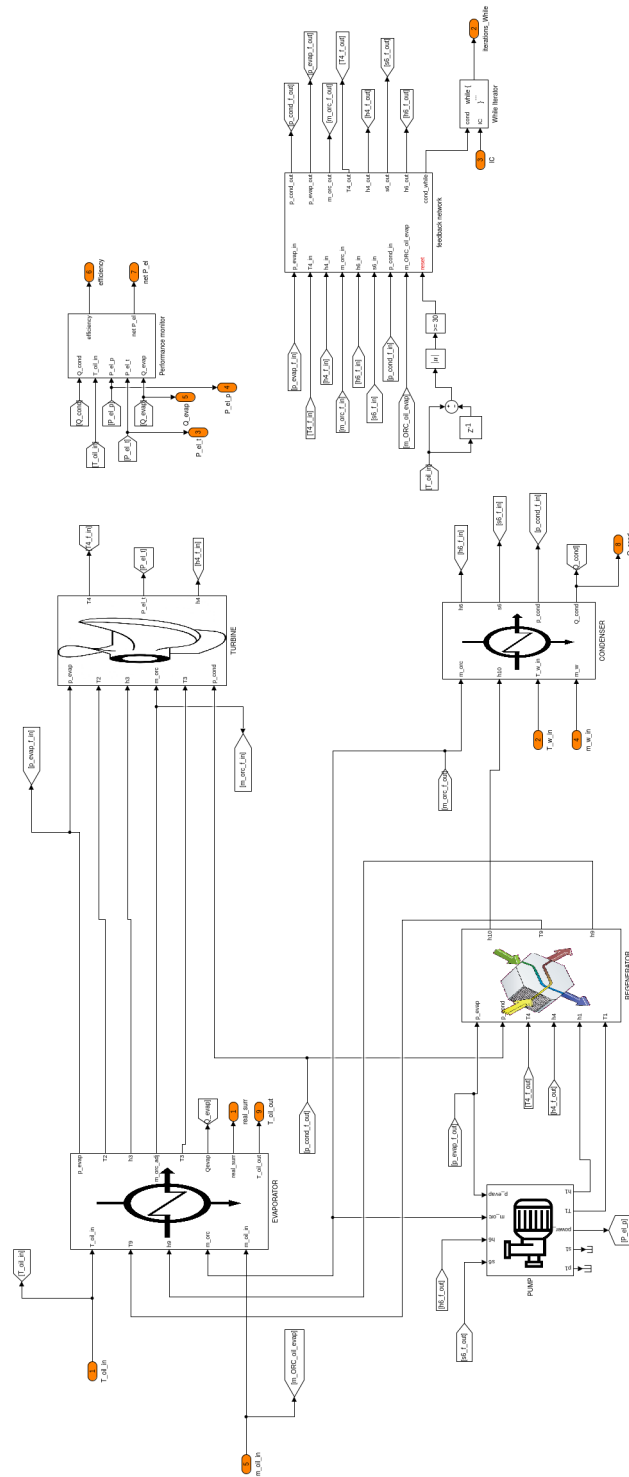


Figure A.10. Inside the ORC block

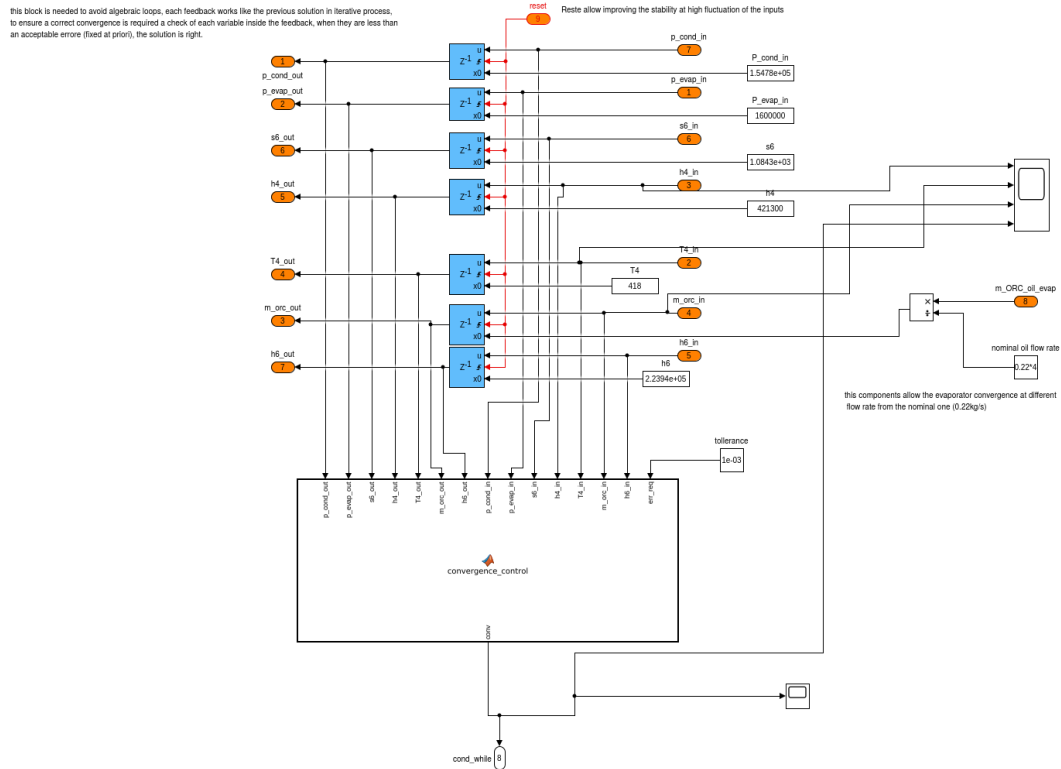


Figure A.11. The ORC feedback block

## ORC condenser MATLAB code

```

1 function [T_w_out,Q_cond,p_cond,s6,h6] = condenser(effCond,m_orc,h10,m_w,T_w_in)
2
3 dTpp_cond = 12;
4 T6 = dTpp_cond + T_w_in;
5 if T6>=380
6     T6 = 380; %first guess relaxation
7 end
8 % p6=CoolProp.PropsSI('P','T',T6,'Q',0,'Novec649');
9 p6 = p_T_sat(T6,1);
10 p_cond=p6;
11 % h6= CoolProp.PropsSI('H','P',p6,'Q',0,'Novec649');
12 h6 = H_p_sat(p6,1);
13 % s6= CoolProp.PropsSI('S','H',h6,'P',p_cond,'Novec649');
14 s6 = S_p_H(p_cond,h6,1);
15 %-----
16
17 c_p_w = 4.1849e+03;
18 %Poiché il sistema prende in input la temperatura di ritorno dell'utenza,
19 %si fissa la T_w_in, così come la portata m_w
20 Q_cond=m_orc*(h10 - h6)*effCond;
21 T_w_out=Q_cond/(c_p_w*m_w)+ T6 - dTpp_cond;
22
23 end

```

## ORC evaporator MATLAB code

```

1 function [T2,p_evap,h3,T3,mOilOut,T_oil_out,m_orc_adj,Qevap,c_p_oil,iterazioni] = evaporator(T_oil_in,
2     T9,h9,surr,mOilIn,m_orc,Q_evap_max)
3 persistent h3_int Q_evap TOutold
4 if isempty(h3_int)
5     h3_int = 4.525e+05; % J/kg di prima iterazione
6     Q_evap = Q_evap_max;
7     TOutold = T_oil_in;
8 end
9 %CALCOLO UA SCAMBIATORI
10 dT1_evap = 200+273-(170+273); %Tce-Tfu
11 dT2_evap = 170.35+273-(89+273); %Tcu-Tfe

```

```

12 DTML_evap = (dT1_evap-dT2_evap)/(log(dT1_evap/dT2_evap));
13 UA_evap = Q_evap_max/DTML_evap;
14
15 c_p_oil = int_cp(T_oil_in,TOutold)*1000;
16
17 Tcr = 441.8;
18 dTpp_evap_design=34;          dTpp_evap= dTpp_evap_design;
19 if(T_oil_in - dTpp_evap > Tcr - 5)
20     dTpp_evap = T_oil_in-Tcr + 5; %blocco per Tcr altrimenti il codice da errore
21     %attenzione perché se la T_oil_in supera molto il valore di design il
22     %dTpp_evap alto riduce parecchio il rendimento per questo il secondo if fa
23     %ritornare la condizione pari a quella di design
24 else
25     if T_oil_in - Tcr + 5 <= dTpp_evap_design
26         dTpp_evap = dTpp_evap_design;
27     end
28 end
29 T2 =T_oil_in - dTpp_evap;
30 p2=p_T_sat(T2,1);
31 p_evap=p2;
32 %% evaluation of heat exchanged
33 err = 1; toll = 1e-5;
34 h3 = h3_int;
35 T3 = T_p_H(p_evap,h3,0);
36 iterazioni = 0;
37 while abs(err) > toll && iterazioni<100
38     if (((h3-h9)/(T3-T9))*m_orc >= c_p_oil*mOilIn)
39         c_min_evap=c_p_oil*mOilIn;
40         c_max_evap=((h3-h9)/(T3-T9))*m_orc;
41     else
42         c_max_evap=c_p_oil*mOilIn;
43         c_min_evap=((h3-h9)/(T3-T9))*m_orc;
44     end
45     c_r_evap=c_min_evap/c_max_evap;
46     NTU_evap= (UA_evap)/c_min_evap;
47     epsilon_evap= (1-exp(-NTU_evap*(1-c_r_evap)))/(1-c_r_evap*exp(-NTU_evap*(1-c_r_evap)));
48     Q_evap = epsilon_evap*c_min_evap*(T_oil_in - T9);
49     h3 = h9 + Q_evap/m_orc;
50     %          T3=CoolProp.PropsSI('T','P',p_evap,'H',h3,'Novec649');
51     T3 = T_p_H(p_evap,h3,0);
52     err = abs(h3_int - h3)/h3;
53     h3_int = h3;
54     iterazioni = iterazioni + 1;
55 end
56 assert(iterazioni<100,'evaporatore ORC non converge');
57 %% output evaluation
58 mOilOut = mOilIn;
59 T3_surr_design = T2 + surr;
60 % m_orc_adj = (m_orc + m_orc*((T3)/T3_surr_design))/2;
61 m_orc_adj = m_orc + (T3 - T3_surr_design)/T3_surr_design;
62 % controller saturation
63 if m_orc_adj>5
64     m_orc_adj = 5;
65 elseif m_orc_adj<0.22/50
66     m_orc_adj = 0.22/50;
67 end
68 % T_oil_out = T_oil_in_new - Q_evap/(mOilOut*c_p_oil);
69 T_oil_out = T_oil_in - Q_evap/(mOilOut*c_p_oil);
70 TOutold = T_oil_out; % save prev T to calculate cpmed
71 Qevap = Q_evap;
72 h3 = h9 + Q_evap/m_orc_adj;
73 T3 = T_p_H(p_evap,h3,0);
74 h3_int = h3;
75 end
76
77 function cp_int_mean = int_cp(T1,T2)
78 % correct estimation of cp using integration between the two temperatures
79 k =[-0.000001843733103  0.003715432304844  1.012291903694753];
80 if T1==T2
81     cp_int = k(3)*(T2 - T1) + k(2)*(T2^2 - T1^2)/2 + k(1)*(T2^3 - T1^3)/3;
82     cp_int_mean = cp_int/(T2-T1);
83 else
84     cp_int_mean = k(3) + k(2)*T1 + k(1)*T1^2;
85 end
86 end
87 %% calls for Lookup Tables
88
89 function out = fluid(in1,in2,ID)
90 coder.extrinsic('scatteredInterpolant','pwd','fullfile')
91 persistent T_p_U_1 T_p_U_v S_p_U_1 S_p_U_v H_p_U_1 H_p_U_v D_p_U_1 D_p_U_v S_p_H_1 ...
92     S_p_H_v H_p_S_1 H_p_S_v H_p_T_1 H_p_T_v T_p_H_1 T_p_H_v S_p_T_1 S_p_T_v tab
93 if isempty(T_p_U_1)
94     tab = inizialization();
95     tab = load((fullfile(pwd, 'data', 'fluidTables.mat')));
96     T_p_U_1 = scatteredInterpolant(tab.pLiquid(:),tab.fluidTables.liquid.u(:),tab.fluidTables.liquid.T
97         (:));
98     T_p_U_v = scatteredInterpolant(tab.pVapor(:),tab.fluidTables.vapor.u(:),tab.fluidTables.vapor.T(:))
99     ;
100     S_p_U_1 = scatteredInterpolant(tab.pLiquid(:),tab.fluidTables.liquid.u(:),tab.fluidTables.liquid.S

```

```

100     ());
101     S_p_U_v = scatteredInterpolant(tab.pVapor(:),tab.fluidTables.vapor.u(:),tab.fluidTables.vapor.S(:))
102     ;
103     H_p_U_l = scatteredInterpolant(tab.pLiquid(:),tab.fluidTables.liquid.u(:),tab.fluidTables.liquid.H
104     ());
105     H_p_U_v = scatteredInterpolant(tab.pVapor(:),tab.fluidTables.vapor.u(:),tab.fluidTables.vapor.H(:))
106     ;
107     D_p_U_l = scatteredInterpolant(tab.pLiquid(:),tab.fluidTables.liquid.u(:),tab.fluidTables.liquid.D
108     ());
109     D_p_U_v = scatteredInterpolant(tab.pVapor(:),tab.fluidTables.vapor.u(:),tab.fluidTables.vapor.D(:))
110     ;
111     S_p_H_l = scatteredInterpolant(tab.pLiquid(:),tab.fluidTables.liquid.H(:),tab.fluidTables.liquid.
112     S_p_H(:));
113     S_p_H_v = scatteredInterpolant(tab.pVapor(:),tab.fluidTables.vapor.H(:),tab.fluidTables.vapor.S_p_H
114     ());
115     H_p_S_l = scatteredInterpolant(tab.pLiquid(:),tab.fluidTables.liquid.S(:),tab.fluidTables.liquid.
116     H_p_S(:));
117     H_p_S_v = scatteredInterpolant(tab.pVapor(:),tab.fluidTables.vapor.S(:),tab.fluidTables.vapor.H_p_S
118     ());
119     H_p_T_l = scatteredInterpolant(tab.pLiquid(:),tab.fluidTables.liquid.T(:),tab.fluidTables.liquid.
120     H_p_T(:));
121     H_p_T_v = scatteredInterpolant(tab.pVapor(:),tab.fluidTables.vapor.T(:),tab.fluidTables.vapor.H_p_T
122     ());
123     T_p_H_l = scatteredInterpolant(tab.pLiquid(:),tab.fluidTables.liquid.H(:),tab.fluidTables.liquid.
124     T_p_H(:));
125     T_p_H_v = scatteredInterpolant(tab.pVapor(:),tab.fluidTables.vapor.H(:),tab.fluidTables.vapor.T_p_H
126     ());
127     S_p_T_l = scatteredInterpolant(tab.pLiquid(:),tab.fluidTables.liquid.T(:),tab.fluidTables.liquid.
128     S_p_T(:));
129     S_p_T_v = scatteredInterpolant(tab.pVapor(:),tab.fluidTables.vapor.T(:),tab.fluidTables.vapor.S_p_T
130     ());
131 end
132 switch ID
133 case 1
134     out = T_p_U_l(in1,in2);
135 case 2
136     out = T_p_U_v(in1,in2);
137 case 3
138     out = S_p_U_l(in1,in2);
139 case 4
140     out = S_p_U_v(in1,in2);
141 case 5
142     out = H_p_U_l(in1,in2);
143 case 6
144     out = H_p_U_v(in1,in2);
145 case 7
146     out = D_p_U_l(in1,in2);
147 case 8
148     out = D_p_U_v(in1,in2);
149 case 9
150     out = S_p_H_l(in1,in2);
151 case 10
152     out = S_p_H_v(in1,in2);
153 case 11
154     out = H_p_S_l(in1,in2);
155 case 12
156     out = H_p_S_v(in1,in2);
157 case 13
158     out = H_p_T_l(in1,in2);
159 case 14
160     out = H_p_T_v(in1,in2);
161 case 15
162     out = T_p_H_l(in1,in2);
163 case 16
164     out = T_p_H_v(in1,in2);
165 case 17
166     out = S_p_T_l(in1,in2);
167 case 18
168     out = S_p_T_v(in1,in2);
169 case 19
170     out = interp1(tab.fluidTables.liquid.T_sat,tab.fluidTables.p,in1);
171 case 20
172     out = interp1(tab.fluidTables.vapor.T_sat,tab.fluidTables.p,in1);
173 case 21
174     out = interp1(tab.fluidTables.p,tab.fluidTables.liquid.H_sat,in1);
175 case 22
176     out = interp1(tab.fluidTables.p,tab.fluidTables.vapor.H_sat,in1);
177 end
178 end
179 function T = T_p_U(p,U,liq)
180 T = 0; % Define output as a scalar of type double for code generation

```

```

174 if liq==1
175     T = fluid(p,U,1);
176 else
177     T = fluid(p,U,2);
178 end
179 end
180 %-----
181 function S = S_p_U(p,U,liq)
182 S = 0; % Define output as a scalar of type double for code generation
183 if liq==1
184     S = fluid(p,U,3);
185 else
186     S = fluid(p,U,4);
187 end
188 end
189 %-----
190 function H = H_p_U(p,U,liq)
191 H = 0; % Define output as a scalar of type double for code generation
192 if liq==1
193     H = fluid(p,U,5);
194 else
195     H = fluid(p,U,6);
196 end
197 end
198 %-----
199 function D = D_p_U(p,U,liq)
200 D = 0; % Define output as a scalar of type double for code generation
201 if liq==1
202     D = fluid(p,U,7);
203 else
204     D = fluid(p,U,8);
205 end
206 end
207 %-----
208 function S = S_p_H(p,H,liq)
209 S = 0; % Define output as a scalar of type double for code generation
210 if liq==1
211     S = fluid(p,H,9);
212 else
213     S = fluid(p,H,10);
214 end
215 end
216 %-----
217 function H = H_p_S(p,S,liq)
218 H = 0; % Define output as a scalar of type double for code generation
219 if liq==1
220     H = fluid(p,S,11);
221 else
222     H = fluid(p,S,12);
223 end
224 end
225 %-----
226 function H = H_p_T(p,T,liq)
227 H = 0; % Define output as a scalar of type double for code generation
228 if liq==1
229     H = fluid(p,T,13);
230 else
231     H = fluid(p,T,14);
232 end
233 end
234 %-----
235 function T = T_p_H(p,H,liq)
236 T = 0; % Define output as a scalar of type double for code generation
237 if liq==1
238     T = fluid(p,H,15);
239 else
240     T = fluid(p,H,16);
241 end
242 end
243 %-----
244 function S = S_p_T(p,T,liq)
245 S = 0; % Define output as a scalar of type double for code generation
246 if liq==1
247     S = fluid(p,T,17);
248 else
249     S = fluid(p,T,18);
250 end
251 end
252 %-----
253 function p = p_T_sat(T,liq)
254 if liq==1
255     p = fluid(T,0,19);
256 else
257     p = fluid(T,0,20);
258 end
259 end
260 %-----
261 function H = H_p_sat(p,liq)
262 if liq==1
263     H = fluid(p,0,21);

```

```

264 else
265     H = fluid(p,0,22);
266 end
267 end
268
269 function out = inzialization()
270 %inizialization of fluid properties structure
271 out = struct(...
272     'fluidTables',struct(...
273         'uMin',0,'uMax',0,...
274         'pMin',0,'pMax',0,...
275         'p',zeros(1,60),...
276         'liquid',struct(...
277             'unorm',zeros(25,1),...
278             'u_sat',zeros(1,60),...
279             'T_sat',zeros(1,60),...
280             'H_sat',zeros(1,60),...
281             'u',zeros(25,60),...
282             'T',zeros(25,60),...
283             'S',zeros(25,60),...
284             'H',zeros(25,60),...
285             'D',zeros(25,60),...
286             'H_p_S',zeros(25,60),...
287             'H_p_T',zeros(25,60),...
288             'S_p_H',zeros(25,60),...
289             'S_p_T',zeros(25,60),...
290             'T_p_H',zeros(25,60),...
291             ),...
292         'vapor',struct(...
293             'unorm',zeros(25,1),...
294             'u_sat',zeros(1,60),...
295             'T_sat',zeros(1,60),...
296             'H_sat',zeros(1,60),...
297             'u',zeros(25,60),...
298             'T',zeros(25,60),...
299             'S',zeros(25,60),...
300             'H',zeros(25,60),...
301             'D',zeros(25,60),...
302             'H_p_S',zeros(25,60),...
303             'H_p_T',zeros(25,60),...
304             'S_p_T',zeros(25,60),...
305             'S_p_H',zeros(25,60),...
306             'T_p_H',zeros(25,60),...
307             ),...
308         'pLiquid',zeros(25,60),...
309         'pVapor',zeros(25,60),...
310     );
311 end

```

## ORC pump MATLAB code

```

1 %% Pump model using Novec649
2 function [p1,h1,s1,T1,powerIn] = pump(s6,h6,eta_p,p_evap,eta_m,eta_g,m_orc)
3 p1 = p_evap;
4 % h1is = CoolProp.PropsSI('H','P',p_evap,'S',s6,'Novec649');
5 h1is = H_p_S(p_evap,s6,1);
6 h1 = h6 + (h1is - h6)/ eta_p;
7 % s1 = CoolProp.PropsSI('S','H',h1,'P',p_evap,'Novec649');
8 s1 = S_p_H(p_evap,h1,1);
9 % T1 = CoolProp.PropsSI('T','H',h1,'P',p_evap,'Novec649');
10 T1 = T_p_H(p_evap,h1,1);
11 powerIn = m_orc*(h1-h6)/(eta_m*eta_g);
12 end

```

## ORC regenerator MATLAB code

```

1 function [T10,h10,s10,s9,T9,h9] = regenerator(p_cond,p_evap,T4,h4,T1,h1,E)
2
3 T10 = T4 - E*(T4 - T1);
4 h10 = 0; s10 = 0; p10 = 0;
5 h9 = 0; s9 = 0; T9 = 0; p9 = 0;
6
7 if T4 <= T1 %questa situazione anomala non si dovrebbe verificare !!!
8     h10=h4-E*(h4 - h1); %il rigeneratore condensa !!!
9     s10 = S_p_H(p_cond,h10,0);
10    p10 = p_cond;
11    E = 0;
12    T4 = T1;
13    h9 = h1;
14    T9 = T1;
15    s9 = S_p_H(p_evap, h9,0);
16 else
17    h10 = H_p_T(p_cond,T10,0);
18    s10 = S_p_H(p_cond,h10,0);
19    p10 = p_cond;
20    h9 = h4 - h10 + h1;

```

```

21     s9 = S_p_H(p_evap, h9,0);
22     T9 = T_p_H(p_evap,h9,0);
23     % T9 = (T9 + T9)/2; %soluzione progressiva
24     p9 = p_evap;
25     end
26     end

```

## ORC turbine MATLAB code

```

1 function [T4,h4,s4,T8,beta,eta_t,P_el_t] = turbine(T2,T3,h3,m_orc,p_evap,p_cond,eta_m,eta_g)
2 if T3<=T2+0.001 %se T3=T2 non può trovare l's perché sta evaporando...
3     % s3= CoolProp.PropsSI('S','H',h3,'P',p_evap,'Novec649');
4     s3 = S_p_H(p_evap,h3,0);
5     % k=2;
6     px = 1; %verifica qui errore !!!!
7     % break
8 else %calcolato così da la soluzione più accurata
9     % s3= CoolProp.PropsSI('S','T',T3,'P',p_evap,'Novec649');
10    s3 = S_p_T(p_evap,T3,0);
11    px = 0;
12 end
13 %%%%%%%%%%%%%%%%%%%%%%%%%%%%%%%%%%%%%%%%%%%%%%%%%%%%%%%%%%%%%%%%%%%%%%%%%
14 p3 = p_evap;
15
16 % h8= CoolProp.PropsSI('H','P',p_cond,'S',s3,'Novec649');
17 h8 = H_p_S(p_cond,s3,0);
18 s8 = s3;
19 % T8= CoolProp.PropsSI('T','H',h8,'P',p_cond,'Novec649');
20 T8 = T_p_H(p_cond,h8,0);
21 p8 = p_cond;
22 beta = p_evap/p_cond;
23 if beta<=2
24     eta_t = 0; %sotto 2 la turbina non lavora bene, rendimento iso nullo
25 else
26     if beta>=10
27         beta = 10;
28     end
29     eta_t = 0.000110756689704*(beta)^4-0.000428259200189*(beta)^3-0.031787169945064*(beta)
30         ^2+0.362514029180695*(beta)-0.479949874686716;
31 end
32 h4 = h3-(h3-h8)*eta_t;
33 % s4= CoolProp.PropsSI('S','H',h4,'P',p_cond,'Novec649');
34 s4 = S_p_H(p_cond,h4,0);
35 % T4= CoolProp.PropsSI('T','H',h4,'P',p_cond,'Novec649');
36 T4 = T_p_H(p_cond,h4,0);
37 p4 = p_cond;
38 P_el_t= m_orc*(h3-h4)*(eta_m*eta_g);
39 end

```

## A.5 Pipeline

The pipeline code has the same internal framework of the LFR, furthermore are implemented also the friction losses. This other contribution allows to solve the hydraulic network to find the correct mass flow rate in each thermal node, tee and diverters add additional pressure losses to the circuit as well.

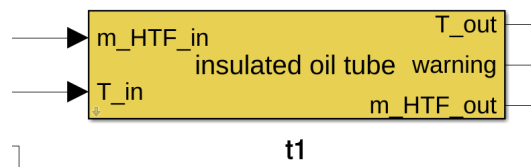


Figure A.12. The pipe block

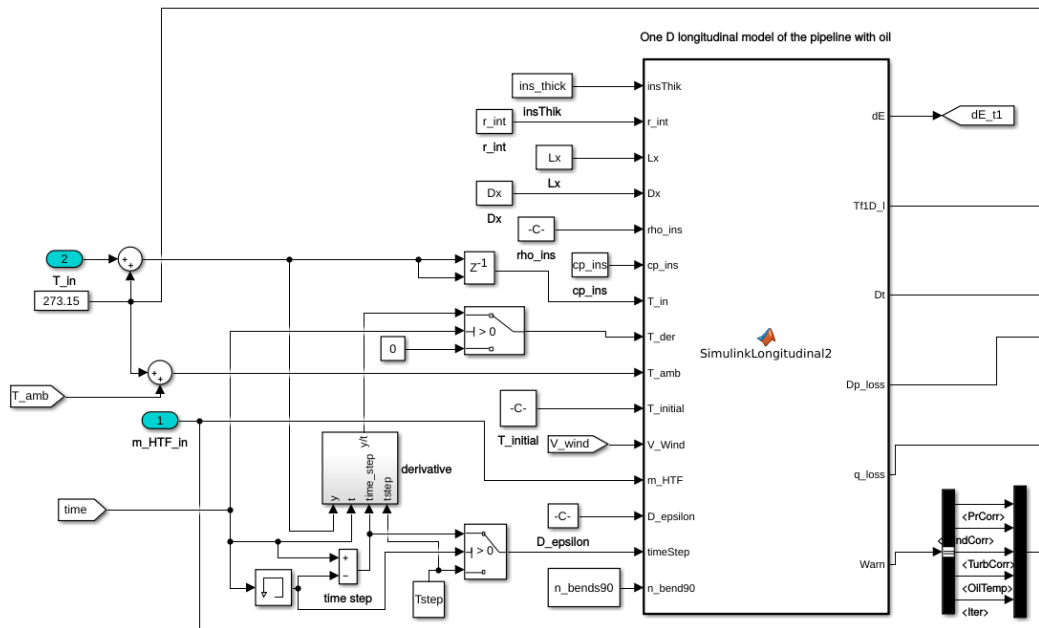


Figure A.13. Inside the pipe block

## pipe MATLAB code

```

1 function [dE,Tf1D_l,Dt,Dp_loss,q_loss,Warn] = SimulinkLongitudinal2(insThick,r_int,Lx,Dx,rho_ins,cp_ins,
2 ...
3 T_in,T_der,T_amb,T_initial,V_Wind,m_HTF,D_epsilon,timeStep,n_bend90)
4 %% unsteady 1D longitudinal oil tube model vectorialized (Simulink version)
5 %%this model refers to a generic tube with oil flow inside
6
7 % SimulinkLongitudinal2(0.03,0.03,10,1,100,840,...
8 % 300,0.1,300,300,0,0.1,100)
9 %-----
10 coder.extrinsic('pwd','fullfile');
11 global time r Tinf_i Tmax re ri windSpeed D2 s
12
13 persistent T_tube lambdaV tab Warning q_loss_m
14
15 if isempty(T_tube)
16     T_tube = ones(Lx/Dx+1,1)*T_initial; %initial condition
17     q_loss_m = 0; %initial condition
18     lambdaV = @(T)5.714e-07.*T.^2 + -0.0002619.*T + 0.0671; % [W/m2 K ] thermal conductivity
19     tab = load('oil_Table2.mat');
20     %loading of oil properties
21     tab = inzialization(); %creating the fields before to fill them
22     tab = load((fullfile(pwd,'data'),'oil_Table2.mat'));
23     % tab.oilVP1= temp.oil; % to pass from one oil characteristics to another one
24 end
25 assert(m_HTF>=0,'flow rate t1 is negative');
26 assert(isnan(insThick+r_int+Lx+Dx+rho_ins+cp_ins+...
27     T_in+T_der+T_amb+T_initial+V_Wind+m_HTF+D_epsilon+timeStep+n_bend90)==1,'t1 model NaN inputs');
28
29 %wanrings settings to 0
30 [Warning.PrCorr,Warning.WindCorr,Warning.TurbCorr,Warning.OilTemp,Warning.Iter] = deal (0);
31 dE = zeros(4,1);
32 % Bc's
33 % lavoro con rampa in ingresso, T all'interno all'istante 0 = T dell'olio
34 % in ingresso al tubo
35 %-----
36 Tinf_i = T_in; % oil T inlet and t=0; all length
37 Tinf_e = T_amb; % ambient T
38 %V_HTF = 0.3; % [m/s] oil flow velocity
39 r = T_der; % [°C/s] ramp value
40 time = timeStep; %[s] total simulation time = simulink timestep (simulink)
41 %-----
42 Tmax = tab.oil.T(end); %fixed by polynomial curve of the oil
43 windSpeed = V_Wind; % [m/s]

```

```

44 D2 = 2*ri;
45 A = pi*D2^2/4; % [m2]
46 rho_oil_in = interp1(tab.oil.T,tab.oil.rho,T_in);
47 V_HTF0 = m_HTF/(rho_oil_in*A);
48 cp_oil_f = @(T)1000*interp1(tab.oil.T,tab.oil.cp,T); % [J/kgK]
49 rho_oil_f = @(T)interp1(tab.oil.T,tab.oil.rho,T); % [kg/m3]
50 V_HTF_f = @(T)rho_oil_in./rho_oil_f(T).*V_HTF0; % variation of velocity along the pipe
51 if timeStep ==0
52     Tf1D_l = T_tube(end,end);
53     Dt = 0;
54     q_loss = q_loss_m; %store the prevoius solution to assure output variable during the code bypass
55 else % code bypass for the hydraulic network balancing
56
57     s = insThik; % [m] insulation thickness
58     ri = r_int; % [m] internal radius
59     re = ri + s; % [m] external radius
60     % rockwool parameters
61     cp = cp_ins; % [kJ/kg K] specific heat
62     % lambda = @(T)5.714e-07*T^2 + -0.0002619*T + 0.0671; % [W/m2 K ] thermal conductivity
63     rho = rho_ins; % [kg/m3] density insulant
64     % Lx = 10; % [m] total length
65     % discretisation Dx = [m] spatial discretization
66     if isnan(rho_oil_in)
67         rho_oil_in = 1000;
68     end
69     % m_is = rho*pi*(re^2 - ri^2);
70     m_is = rho*pi*(re^2 - ri*re)*0; % <----- to change
71     %-----
72     %-----
73
74     Dt = Dx/V_HTF0*0.7; % Courant-Friedrichs-Lewy condition
75     step = round(time/Dt); % number of internal timestep (Courant stability)
76     if step < 2 || isnan(step) % because of low V_HTF
77         Dt = time/4; % assure at least 2 internal time step
78     end
79
80     % discretisation
81     xx = 0:Dx:Lx;
82     tt = linspace(0,time,round(time/Dt)+1); % +1 because of step 0
83     Dt = tt(2) -tt(1); % new timestep to have the last time exactly
84
85     % preallocation
86     l_t = numel(tt);
87     l_x = numel(xx);
88     T = ones(l_x,l_t)*Tinf_e;
89     T(:,1) = T_tube; % starts from the prevoious T solution
90     q_loss_t = zeros(l_t-1,1);
91     % Telaps = 0;
92
93     if r==0 % the inlet derivative of the previous step fixes the inlet T variation during time
94         T(1,:) = Tinf_i;
95     else % it finds the correct time spacng to get the final time properly
96         T(1,:) = linspace(Tinf_i,(Tinf_i + r*time),numel(T(1,:)));
97         % T(1,:) = Tinf_i:r*Dt:(Tinf_i + r*time); % [K] inlet temperature variation during the
98             timestep
99         % add lower bound
100        T(1,:) = tab.oil.T(1).*(T(1,:)< tab.oil.T(1)) + T(1,:).*(T(1,:)>= tab.oil.T(1));
101        % add upper bound
102        T(1,:) = tab.oil.T(end).*(T(1,:)> tab.oil.T(end)) + T(1,:).*(T(1,:)<= tab.oil.T(end));
103    end
104
105    %l_t = sum(T(1,:) <= Tmax);
106    % tic
107
108    kx_f = @(T,Tinf_e,lambdaV,V_HTF_f,l_x) 1./((rho_oil_f(T).*cp_oil_f(T)*A).*TpiTpe(T,Tinf_e,lambdaV,
109        V_HTF_f,l_x,tab,Warning));
110
111    for kk = 1:l_t-1 % tempreature solution
112        %preallocation
113        cost = kx_f(T(2:end,kk),Tinf_e,lambdaV,V_HTF_f,l_x);
114        rho_c = rho_oil_f(T(2:end,kk));
115        cp_oil_c = cp_oil_f(T(2:end,kk));
116        V_HTF_c = V_HTF_f(T(2:end,kk));
117        q_loss_t(kk) = -sum(cost.*(T(2:end,kk) -Tinf_e).*(rho_c.*cp_oil_c*A))*Dx; % [W] tube loss per
118            time step
119
120        T(2:end,kk+1) = Dt./(1+(m_is*cp)./(rho_c.*cp_oil_c*A)).*...
121            ((-cost + 1./Dt - V_HTF_c./Dx + (m_is*cp)./(rho_c.*cp_oil_c*A*Dt)).*T(2:end,kk) +...
122            (V_HTF_c./Dx).*T(1:end-1,kk) + cost*Tinf_e);
123    end
124
125    % %computation of total simulation time (seconds)
126    % Telaps = toc;
127    mass_i = A*Lx*rho_oil_f(T(2:end,1))/numel(T(2:end,1));
128    mass_f = A*Lx*rho_oil_f(T(2:end,end))/numel(T(2:end,1));
129    mass_mid = (mass_i+ mass_f) /2;
130    U_i = mass_mid.*interp1(tab.oil.T,tab.oil.u,T(2:end,1)); % initial internal energy [kJ]
131    U_f = mass_mid.*interp1(tab.oil.T,tab.oil.u,T(2:end,end)); % initial internal energy [kJ]
132
133    Tf1D_l = T(end,end);
134    T_tube = T(:,end); %store the prevoius solution for the new initialization

```

```

131     q_loss = Dt/time*sum(q_loss_t);
132     q_loss_m = q_loss; %store the previous solution to assure output variable during the code bypass
133     ddT = T(end,end) - T(1,end);
134     cpp = cp_oil_f((T(end,end) + T(1,end))/2);
135
136     e_InOut = -m_HTF*cpp*ddT;
137     dU = sum(U_f - U_i)*1000/time;
138     dE(1) = e_InOut;
139     % dE(1) = Dt/time*sum(e_InOut);
140     dE(2) = q_loss;
141     dE(3) = -dU;% energy balance
142     dE(4) = sum(U_f);
143 end
144 if (V_HTF0 ==0)
145     Dp_loss = 0;
146 else
147     Tmean = mean(T_tube(2:end));
148     V_HTFmean = V_HTF_f(Tmean);
149     Dp_loss = Pdrop(Tmean,tab,V_HTFmean,Lx,D2,D_epsilon,n_bend90);
150 end
151 Warn = manageWarning(Warning);
152
153 %% % return
154 %% %% temperature visualization
155 % delta = 2; % time step visualization
156 % figure()
157 % hold on
158 % grid on
159 % xlabel('length [m]', 'FontSize',18)
160 % ylabel('Temperature [K]','FontSize',18)
161 % title('temperature distribution along the length 1 D longitudinal model','FontSize',16);
162 %
163 % for kk = 1:delta:l_t-1
164 %     plot(T(:,kk))
165 %     grid on
166 %     pause(0.2)
167 % end
168 end
169
170 %%
171 function [sumR] = TpiTpe(T,Tinf_e,lambdaV,V_HTF_f,l_x,tab,Warning)
172 global re ri windSpeed D2 s
173 persistent Tpi Tpe W
174
175 [R_cond, R_ci, R_ce] = deal(ones(1_x,1));
176
177 %initial guess
178 if isempty(Tpe)
179     Tpi = T - 2;
180     Tpe = Tinf_e*ones(size(Tpi));
181     W = Warning;
182 end
183 % loop initialization
184 toll = 1e-3; giri = 0; err = 1;
185
186 while err>=toll && giri<100
187
188     R_cond = log(re/ri)/(2*pi*lambdaV((Tpi + Tpe)/2));
189     R_ci = R_int_conv(V_HTF_f,T,Tpi,D2,tab,Warning);
190     R_ce = R_ext_conv(windSpeed,D2 + s,Tpe,Tinf_e,Warning);
191
192     q = (T - Tinf_e*ones(size(Tpi)))/(R_cond + R_ci + R_ce);
193     Tpe_new = Tinf_e*ones(size(Tpi)) + q.*R_ce;
194     Tpi_new = T - q.*R_ci;
195
196     err1 = (abs(Tpe - Tpe_new)./Tpe_new)*100;
197     err2 = (abs(Tpi - Tpi_new)./Tpi_new)*100;
198     Tpe = Tpe_new;
199     Tpi = Tpi_new;
200
201     err = max(max(max(err1)),max(max(err2)));
202     giri = giri + 1;
203 end
204
205 if giri >= 100
206     W.Iter = 1;
207 end
208 sumR = R_ci + R_ce + R_cond;
209
210 manageWarning(W);
211 end
212
213
214 %%
215 function R_12conv = R_int_conv(V_HTF_f,T1,T2,D2,tab,Warning)
216 % convection HTF(therminol62)/absorber
217
218 % Pr1 = Prandtl number evaluated at the HTF temperature, T1
219 % Pr2 = Prandtl number evaluated at the absorber inner surface
220

```

```

221 if max(T1) > tab.oil.T(end) || max(T2) > tab.oil.T(end)
222 % fprintf('warning out of range oilVp1 polynomial curve',max(T1,T2));
223 % fix the maximum temperature artificially
224 T1 = tab.oil.T(end)*(T1 > tab.oil.T(end)) + T1.*(T1 <= tab.oil.T(end));
225 T2 = tab.oil.T(end)*(T2 > tab.oil.T(end)) + T2.*(T2 <= tab.oil.T(end));
226 Warning.OilTemp = 1; % to display externally of the simulink model
227 elseif min(T1) < tab.oil.T(1) || min(T2) < tab.oil.T(1) % oil is boiling
228 % fix the minimum temperature artificially
229 T1 = tab.oil.T(1)*(T1 > tab.oil.T(1)) + T1.*(T1 <= tab.oil.T(1));
230 T2 = tab.oil.T(1)*(T2 > tab.oil.T(1)) + T2.*(T2 <= tab.oil.T(1));
231 Warning.OilTemp = 1; % to display externally of the simulink model
232 elseif any(isnan(T1)) || any(isnan(T2))
233 Warning.OilTemp = 1; % to display externally of the simulink model
234 end
235
236 cp_oilT1 = 1000*interp1(tab.oil.T,tab.oil.cp,T1); % [J/kgK] T [K]
237 cp_oilT2 = 1000*interp1(tab.oil.T,tab.oil.cp,T2); % [J/kgK] T [K]
238
239 rhoT1 = interp1(tab.oil.T,tab.oil.rho,T1); % [kg/m3]
240 rhoT2 = interp1(tab.oil.T,tab.oil.rho,T2); % [kg/m3]
241
242 ni_oilT1 = rhoT1.*interp1(tab.oil.T,tab.oil.ni,T1)*10^-6;
243 ni_oilT2 = rhoT2.*interp1(tab.oil.T,tab.oil.ni,T2)*10^-6;
244
245 lambda_oilT1 = interp1(tab.oil.T,tab.oil.lambda,T1); % [W/K m]
246 lambda_oilT2 = interp1(tab.oil.T,tab.oil.lambda,T2); % [W/K m]
247
248 Pr1 = ni_oilT1.*cp_oilT1./lambda_oilT1;
249 Pr2 = ni_oilT2.*cp_oilT2./lambda_oilT2;
250 ni_oil = interp1(tab.oil.T,tab.oil.ni,T1)*10^-6; % [m2/s]
251 Re_D2 = V_HTF_f(T1)*D2./ni_oil;
252
253 if max(Re_D2) > 5e+6 || min(Pr1) < 0.5 || max(Pr1) > 2000
254 % warning('turbulent correlation HTF/absorber tube is out of range')
255 Warning.TurbCorr = 1; % to display externally of the simulink model
256 end
257 % turbulent flow Gnielinsky [1976] and Incropera and DeWitt (1990) laminar (no anular flow)
258 f2 = (1.82*log(Re_D2.*(Re_D2 > 2300)) - 1.64).^(-2);
259 Nu_D2 = ((f2/8.*(Re_D2 - 1000).*Pr1)./(1 + 12.7*sqrt(f2/8)).*(Pr1.^(2/3) - 1)).*(Pr1./Pr2).^0.11...
260 + 4.36*(Re_D2 <= 2300);
261
262
263 % Nu_D2 = 0.023*Re_D2^0.8*Pr1^0.4; % dittus bolter for testing
264 h1 = Nu_D2.*lambda_oilT1/D2; % [W/m2-K] HTF convection heat transfer coefficient at T1
265 R_12conv = 1./(h1*D2*pi); % (T2 - T1) [K/W*m]
266
267 manageWarning(Warning);
268 end
269
270
271 %%
272 function R_56conv = R_ext_conv(windSpeed,D5,T5,T6,Warning)
273 % Heat Transfer from the Glass Envelope to the Atmosphere
274 % Convection Heat Transfer
275
276 p1 = -5.615e-10;
277 p2 = 1.056e-06;
278 p3 = -0.000611;
279 p4 = 0.8106;
280
281 pa1 = 0.0001343;
282 pa2 = 0.05606;
283 pa3 = -6.195;
284
285 pn1 = 7.92e-06;
286 pn2 = 0.004698;
287 pn3 = -0.5507;
288
289 pb1 = -4.132e-08;
290 pb2 = 7.138e-05;
291 pb3 = -0.0436;
292 pb4 = 11.13;
293
294 pc1 = -2.709e-05;
295 pc2 = 0.09021;
296 pc3 = 1.71;
297 g = 9.81; % (m/s2) gravitational constant
298
299 T56 = 0.5.*(T5 + T6);
300 % range of validity air -100°C + 300°C
301 Pr5 = p1*T5.^3 + p2*T5.^2 + p3*T5 + p4;
302 Pr6 = p1*T6.^3 + p2*T6.^2 + p3*T6 + p4;
303
304 % range of validity air -100°C + 300°C
305 alpha56 = (pa1*T56.^2 + pa2*T56 + pa3)*1e-06; % thermal diffusivity for air at T56 (m2/s)
306
307 % range of validity air -23°C + 423°C
308 ni56 = (pn1*T56.^2 + pn2*T56 + pn3)*1e-05; % kinematic viscosity for air (m2/s)
309 Re_D5 = windSpeed*D5./ni56;
310 Pr56 = p1*T56.^3 + p2*T56.^2 + p3*T56 + p4;

```

```

311
312 % range of validity air -75 °C + 412 °C
313 beta56 = (pb1*T56.^3 + pb2*T56.^2 + pb3*T56 + pb4)*1e-03; % volumetric thermal expansion coefficient (
      ideal gas) (1/K)
314 lambda56 = (pc1*T56.^2 + pc2*T56 + pc3)*1e-3; % air thermal conductivity [W/m K]
315
316 C = 0.75.*(Re_D5 < 40) + ...
317     0.51.*(Re_D5 >= 40 & Re_D5 < 1000) + ...
318     0.26.*(Re_D5 >= 1000 & Re_D5 < 2e5) + ...
319     0.076.*(Re_D5 >= 2e5 & Re_D5 < 1e6);
320 m = 0.4.*(Re_D5 < 40) + ...
321     0.5.*(Re_D5 >= 40 & Re_D5 < 1000) + ...
322     0.6.*(Re_D5 >= 1000 & Re_D5 < 2e5) + ...
323     0.7.*(Re_D5 >= 2e5 & Re_D5 < 1e6);
324 if max(Re_D5) >= 1e6
325     % disp('Warning : wind Speed is out of range with regard the external tube convection
      correlation');
326     Warning.WindCorr = 1; % to display externally of the simulink model
327 end
328
329 if windSpeed == 0 % No Wind Case
330     Rad5 = (g*beta56.*abs(T5 - T6)*D5^3)./(alpha56.*ni56); % Rayleigh number
331     Nu_d5 = (0.6 + (0.387*Rad5.^(1/6))./((1+(0.559./Pr56).^(9/16)).^(8/27))).^2; % Nusselt number,
      Incropera and DeWitt (1990)
332 else
333     if max(Pr6) > 500 || min(Pr6) < 0.7
334         % disp('Warning : the calculated Prantdl Number in external envelope is out of range');
335         Warning.PrCorr = 1; % to display externally of the simulink model
336         n = 0.37.*(Pr6 <=10) + 0.36.*(Pr6 > 10);
337     else
338         n = 0.37.*(Pr6 <=10) + 0.36.*(Pr6 > 10);
339     end
340
341     Nu_d5 = C.*Re_D5.^m.*Pr6.^n.*(Pr6./Pr5).^0.25; % The Nusselt number in this case is estimated with
      Zhukauskas
342     %correlation for external forced convection flow normal to an
343     %isothermal cylinder [Incropera and DeWitt (1990)
344 end
345 h_56 = Nu_d5.*lambda56/D5; % [W/m2-K] convection heat transfer coefficient for air at (T5 + T6)/2
346 R_56conv = 1./(h_56*pi*D5); % (T5 - T6) [K/W*m]
347
348 manageWarning(Warning);
349 end
350
351 function Dp_loss = Pdrop(Tmean,tab,V_HTF,L,D,D_epsilon,n_bend90)
352 % this model is got by the following formula:
353 % Dp_loss = f*(L/D)*(rho*u^2/2)
354 %
355 % Dp_loss = major (friction) pressure loss in fluid flow (Pa)
356 % f = Darcy-Weisbach friction coefficient
357 % L = length of duct or pipe (m)
358 % u = velocity of fluid (m/s)
359 % D = hydraulic diameter (D)
360 % rho = density of fluid (kg/m^3)
361 % n_bend90 = number of bends of 90 degrees
362 %
363 % where f is got by:
364 % Friction Modeling of Flood Flow Simulations
365 % Vasilis Bellos; Ioannis Nalbantis; and George Tsakiris
366 ni_oil = interp1(tab.oil.T,tab.oil.ni,Tmean)*10^-6; % [m2/s]
367 rho = interp1(tab.oil.T,tab.oil.rho,Tmean); % [kg/m3]
368 Re = V_HTF*D/ni_oil;
369
370 a = 1/(1+(Re/2712)^8.4); % Re = Reynolds
371 b = 1/(1+(Re/(150*D_epsilon))^1.8); % roughnes = epsilon
372
373 f = (64/Re)^a*...
374     (0.75*log(Re/5.37))^(2*b*(a-1))*...
375     (0.88*log(6.82*D_epsilon))^(2*(a-1)*(1-b));
376 Dp_loss = (f*(L/D) + n_bend90*0.3)*(rho*V_HTF^2/2);
377 end
378
379 function Warn=manageWarning(Warning)
380 % this function share the variable Warning among other funtions
381 persistent W
382 if isempty(W)
383     [W.PrCorr,W.WindCorr,W.TurbCorr,W.OilTemp,W.Iter] = deal (0);
384 end
385 W.PrCorr = Warning.PrCorr + W.PrCorr;
386 W.WindCorr = Warning.WindCorr + W.WindCorr;
387 W.TurbCorr = Warning.TurbCorr + W.TurbCorr;
388 W.OilTemp = Warning.OilTemp + W.OilTemp;
389 W.Iter = Warning.Iter + W.Iter;
390 % W = Warning;
391 Warn = W;
392 end
393
394 function out = inzialization()
395 %inzialization of fluid properties structure
396 out = struct(...

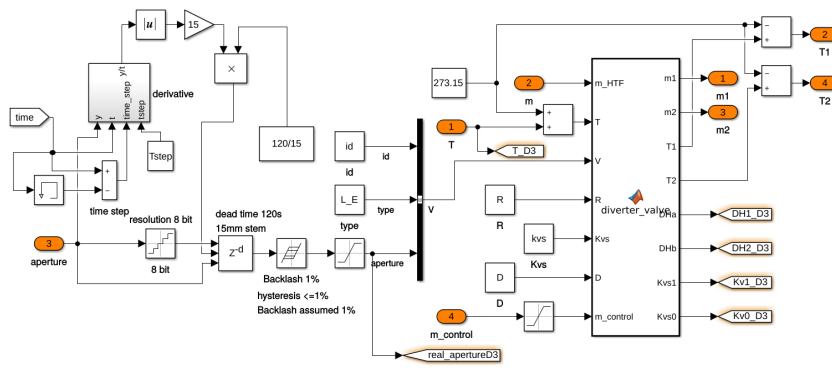
```

```

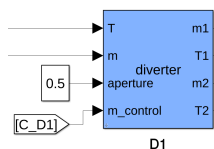
397 'oil',struct(...
398 'T',zeros(38,1),...
399 'rho',zeros(38,1),...
400 'cp',zeros(38,1),...
401 'r',zeros(38,1),...
402 'h',zeros(38,1),...
403 'lambda',zeros(38,1),...
404 'ni',zeros(38,1),...
405 'vap_press',zeros(38,1),...
406 'u',zeros(38,1),...
407 );
408 end
    
```

## A.6 Tee and diverters

The most significant contribution regarding the pressure losses are derived from the diverters and only a small portion from the tees. To reproduce the dynamic behavior of the electrical actuator, some additional blocks have been added to the aperture signal.



(a)



(b)

Figure A.14. The diverter block

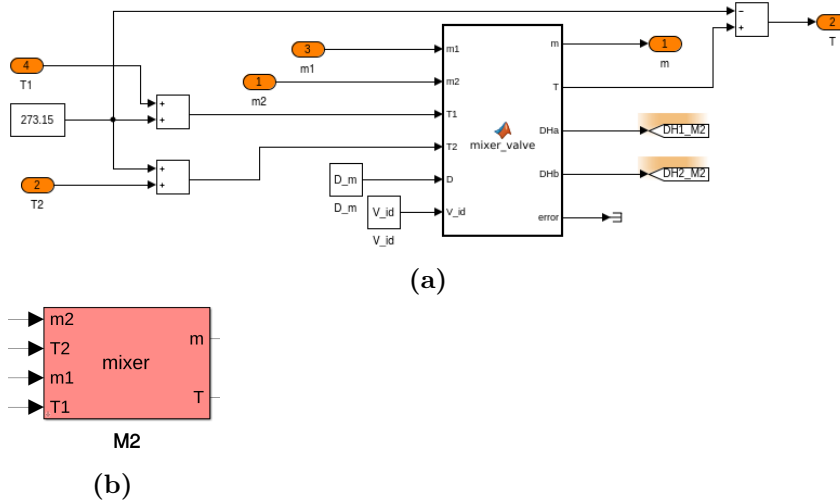


Figure A.15. The tee block

## diverter MATLAB code

```

1 function [m1,m2,T1,T2,DHa,DHb,Kvs1,Kvs0] = diverter_valve(m_HTF,T,V,R,Kvs,D,m_control)
2 coder.extrinsic('pwd','fullfile');
3 persistent tab
4 %loading of oil properties
5 if isempty(tab)
6     tab = initialization(); %creating the fields before to fill them
7     tab = load((fullfile(pwd,'data'),'oil_Table2.mat'));
8 end
9
10 %% valve pressure drops
11 % %% input
12 % V.id = 1; % type of 3 way valve
13 % V.type = 0; % 1 = lienar; 0 = equal percentage
14 % V.aperture = 0.5; % 0 < aperture < 1
15 % R = 50; % rangeability ( 20-50 )
16 % m_HTF = 3; % kg/s
17 % Kvs = 32;
18 % T = 400; %(K) inlet fluid temperature
19 % D = 0.05; % (m) valve nominal diameter
20 % load('oil_Table2.mat');
21 % inzialization
22 assert(m_HTF>=0,'flow rate D1 is negative');
23 [Kv1,Kv0,k,ka,kb] = deal(0);
24
25 %this block simulates the diverter valve
26 % through the control signal you can adjust the flow rate between the two
27 % outputs
28 % control --->  0 <= control <= 1
29
30 m1 = m_control*m_HTF;
31 m2 = m_HTF - m1;
32 T1 = T;
33 T2 = T;
34
35 if V.type == 1 % 1 = lienar
36     Kv1 = Kvs*(1/R + (1 - 1/R)*V.aperture);
37     Kv0 = Kvs*(1/R + (1 - 1/R)*(1 - V.aperture));
38 elseif V.type == 0 % 0 = equal percentage
39     Kv1 = Kvs*R*(V.aperture - 1);
40     Kv0 = Kvs*R*((1 - V.aperture) - 1);
41 end
42 if m_HTF == 0
43     [DHa,DHb] = deal(0);
44     [Kvs1,Kvs0] = deal(16);
45 else
46     rho = interp1(tab.oil.T,tab.oil.rho,T); % kg/m3
47     ni = interp1(tab.oil.T,tab.oil.ni,T)*10^-6; % m2/s
48     V_HTF = m_HTF/rho/(pi*D^2/4); % (m/s) fluid velocity
49     [Kvs1,Dp1] = KvDp(m1,rho,ni,D,Kv1);
50     [Kvs0,Dp0] = KvDp(m2,rho,ni,D,Kv0);
51
52     switch V.id
53         % --->|--> a
54         % |b
55         case 1 % diverter with controlled aperture

```

```

56         ka = 0.5; kb = 1.5; % diramazione: a dritta, b squadra
57     case 2 % aperture not controlled
58         ka = 0.5; kb = 1; % diramazione: a dritta, b squadra,
59     case 3 % aperture not controlled
60         k = 3; % diramazione doppia con T a squadra (confluenza non contemplata)
61     end
62
63     if V_id == 3 % splitter both side in bend direction
64         DHa = k*V_HTF^2*rho/(2*9.81); % (Pa) pressure drop
65         DHb = DHa; % same pressure drops
66     elseif V.aperture == 0 % controlled diverter
67         DHa = -1; % negative pressure drop = infinitive (closed)
68         DHb = kb*V_HTF^2*rho/(2*9.81) + Dp0; % (Pa) pressure drop bend
69     elseif V.aperture == 1 % controlled diverter
70         DHa = ka*V_HTF^2*rho/(2*9.81) + Dp1; % (Pa) pressure drop straight
71         DHb = -1; % negative pressure drop = infinitive (closed)
72     else % controlled diverter
73         DHa = ka*V_HTF^2*rho/2 + Dp1; % (Pa) pressure drop straight
74         DHb = kb*V_HTF^2*rho/2 + Dp0; % (Pa) pressure drop bend
75     end
76 end
77 end
78
79 function [Kvs,Dp] = KvDp(m_HTF,rho,ni,D,Kv)
80 Q = m_HTF/rho*3600; % (m3/h) fluid flow rate
81 Re = 4*Q/(pi*D*ni*3600); % D = diameter of the internal nozzle
82 C_factor = 1/(0.9935 + 2.878/Re^0.5 + 342.75/Re^1.5);
83 if C_factor <= 0.3
84     C_factor = 0.3; % Re mimum = 32.6
85 elseif C_factor >= 1
86     C_factor = 1;
87 end
88 Kvs = Kv*C_factor;
89 Dp = 10^5*(Q^2/Kvs^2); % (Pa) pressure drop
90 end
91
92 function out = inizialization()
93 %inizialization of fluid properties structure
94 out = struct(...
95     'oil',struct(...
96     'T',zeros(38,1),...
97     'rho',zeros(38,1),...
98     'cp',zeros(38,1),...
99     'r',zeros(38,1),...
100    'h',zeros(38,1),...
101    'lambda',zeros(38,1),...
102    'ni',zeros(38,1),...
103    'vap_press',zeros(38,1),...
104    'u',zeros(38,1))...
105    );
106 end

```

## Tee MATLAB code

```

1 function [m,T,DHa,DHb,error] = mixer_valve(m1,m2,T1,T2,D,V_id)
2 %this block simulates the mixing valve
3 % if one of the respective data in input are missing, for example is
4 % provided m1 and T2 only, error will be = 1
5 coder.extrinsic('pwd','fullfile');
6 persistent tab cp_old T_old
7 %loading of oil properties
8 if isempty(tab)
9     tab = inizialization(); %creating the fields before to fill them
10    tab = load((fullfile(pwd,'data','oil_Table2.mat')));
11 end
12 rho1 = interp1(tab.oil.T,tab.oil.rho,T1); cp1 = interp1(tab.oil.T,tab.oil.cp,T1);
13 rho2 = interp1(tab.oil.T,tab.oil.rho,T2); cp2 = interp1(tab.oil.T,tab.oil.cp,T2);
14 ka = 0; kb = 0;
15 switch V_id
16     % -->|<-- -->|<--
17     % | |
18     case 1 % asymmetric mixer
19         ka = 0.5; kb = 1; % confluenza: a dritta, b squadra
20     case 2 % symmetric mix
21         ka = 2; kb = 2; % confluenza: T a squadra,
22     end
23 V_HTF1 = m1/rho1/(pi*D^2/4); % (m/s) fluid velocity
24 V_HTF2 = m1/rho2/(pi*D^2/4); % (m/s) fluid velocity
25
26 DHa = ka*V_HTF1^2*rho1/2; % (Pa) pressure drop straight
27 DHb = kb*V_HTF2^2*rho2/2; % (Pa) pressure drop bend
28
29 if isempty(cp_old)
30     cp_old = 2;
31     T_old = 25 + 273.15;
32 end
33 m = m1 + m2;
34 if m == 0
35     cp = cp_old;

```

```

36     T = T_old;
37 else
38     cp = (cp1*m1 + cp2*m2)/m;
39     T = (m1*cp1*T1 + m2*cp2*T2)/(m1*cp1 + m2*cp2);
40     cp_old = cp;
41     T_old = T;
42 end
43 error = 0;
44 if (T==0) && (T1==0 && m1==0) || (T2==0 && m2 == 0) || cp<=0
45     error = 1;
46 end
47 end
48
49 function out = inzialization()
50 %inizialization of fluid properties structure
51 out = struct(...
52     'oil',struct(...
53     'T',zeros(38,1),...
54     'rho',zeros(38,1),...
55     'cp',zeros(38,1),...
56     'r',zeros(38,1),...
57     'h',zeros(38,1),...
58     'lambda',zeros(38,1),...
59     'ni',zeros(38,1),...
60     'vap_press',zeros(38,1),...
61     'u',zeros(38,1)...
62 );
63 end

```

## A.7 controller

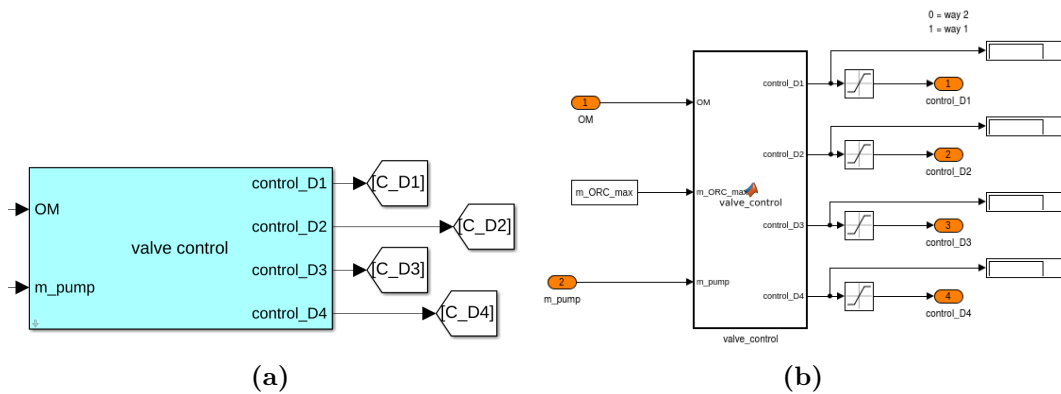


Figure A.16. The tee block

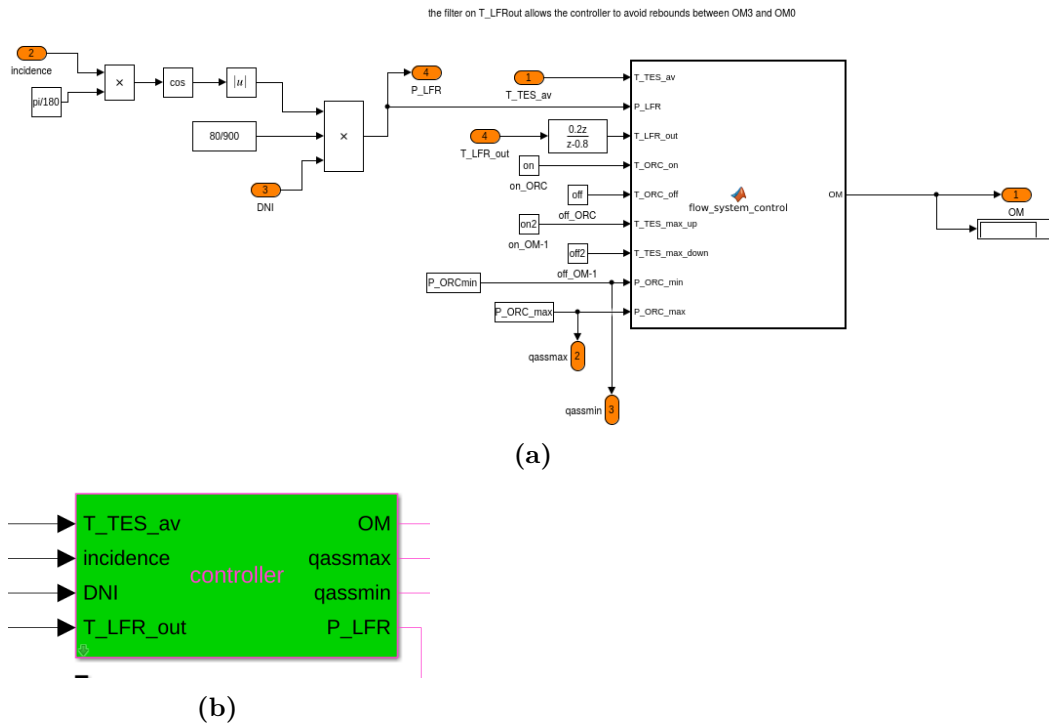


Figure A.17. The tee block

## Valve control MATLAB code

```

1 function [control_D1,control_D2,control_D3,control_D4] = valve_control(OM,m_ORC_max,m_pump)
2 % initialization
3 [control_D1,control_D2,control_D3,control_D4] = deal(-1);
4
5 switch OM
6     case {-1,1} % defocusing
7         control_D1 = 0;
8         control_D2 = 0; % not used
9         control_D3 = 1;
10        control_D4 = 0;
11
12    case 0
13        control_D1 = 0;
14        control_D2 = 0; % not used
15        control_D3 = 0;
16        control_D4 = 0;
17
18    case 2 % off
19        control_D1 = 0;
20        control_D2 = 0;
21        control_D3 = 1;
22        control_D4 = 0;
23
24    case 3 % LFR ----> TES
25        control_D1 = 1;
26        control_D2 = 0;
27        control_D3 = 0; % not used
28        control_D4 = 0;
29
30    case 4 % LFR ----> TES + ORC
31        if m_pump > m_ORC_max % OM4
32            control_D1 = 1 - m_ORC_max/m_pump;
33            control_D2 = 0;
34            control_D3 = 1;
35            control_D4 = 0;
36        else % shift to OM1
37            control_D1 = 0;
38            control_D2 = 0;
39            control_D3 = 1;
40            control_D4 = 0;
41        end
42
43    case 5 % TES ----> ORC
44        control_D1 = 1; % not used
45        control_D2 = 1; % m pump fixed at max
46        control_D3 = m_ORC_max/m_pump;
47        control_D4 = 1;
48
49    case 6 % LFR + TES ----> ORC

```

```

44     if m_pump > m_ORC_max % OM4
45         control_D1 = 1- m_ORC_max/m_pump;
46         control_D2 = 0;
47         control_D3 = 1;
48         control_D4 = 0;
49     else % OM6
50         control_D1 = 0;
51         control_D2 = 1;
52         control_D3 = m_ORC_max/m_pump; % m pump fixed at max
53         control_D4 = 1 - 1/m_pump; % 1 kg/s in LFR
54     end
55 end
56 end

```

## Main controller MATLAB code

```

1 function OM = flow_system_control(T_TES_av,P_LFR,T_LFR_out,T_ORC_on,T_ORC_off,...
2     T_TES_max_up,T_TES_max_down,P_ORC_min,P_ORC_max)
3 stat1 = ORC_power(P_LFR,P_ORC_min,P_ORC_max);
4 stat2 = on_off_ORC(T_TES_av,T_ORC_on,T_ORC_off); % hysteresis ORC on/off
5 stat3 = on_off_ORC(T_TES_av,T_TES_max_up,T_TES_max_down); % hysteresis ORC on/off OM4/OM-1
6 OM = 0;
7 switch stat1
8     case 0
9         switch stat2
10            case 0
11                OM = 2;
12            case 1
13                OM = 5;
14            end
15        case 1
16            switch stat2
17                case 0
18                    OM = 3;
19                case 1
20                    OM = 6;
21            end
22        case 2
23            OM = 1;
24        case 3
25            OM = 4;
26    end
27 if stat3
28     OM = -1; % defocusing
29 elseif OM ==3 && T_LFR_out < (T_TES_av + 10) % 10 degrees more to heat up the tubes
30     OM = 0;
31 end
32
33 end
34
35 function out1 = ORC_power(P_LFR,P_ORC_min,P_ORC_max)
36 if P_LFR == 0
37     out1 = 0; % ORC off
38 elseif P_LFR < P_ORC_min
39     out1 = 1; % power not sufficient to run the ORC
40 elseif (P_LFR >= P_ORC_min) && (P_LFR <= P_ORC_max)
41     out1 = 2; % ORC part load and nominal one
42 else
43     out1 = 3; % the extra power goes inside the TES
44 end
45 end
46
47 function out2 = on_off_ORC(T_TES_av,T_ORC_on,T_ORC_off)
48 % switch with hysteresis
49 % the switch has a variable setpoint based on the actual state
50 persistent Tset
51 if isempty(Tset)
52     Tset = T_ORC_on;
53 end
54 % hysteresis fo the tank
55 if T_TES_av >= T_ORC_on
56     Tset = T_ORC_off;
57 elseif T_TES_av <= T_ORC_off
58     Tset = T_ORC_on;
59 end
60
61 if T_TES_av >= Tset
62     out2 = 1;
63 else
64     out2 = 0;
65 end
66
67 end

```

## Appendix B

# Empirical correlations for the LFR wall heat transfer coefficient

Table B.1. Nusselt number for **mixed convection** for cylindrical horizontal tube pt1.

Author name	correlation	B.C.	Validity interval
Ghajar and Tam	$\bar{N}u_l = 1.24 \left[ \left( \frac{RePrD}{L} \right) + \dots \right. \\ \left. 0.025(GrPr)^{0.75} \right]^{1/3} \left( \frac{u_b}{u_w} \right)^{0.14}$	UHF laminar	$3 \leq x/d \leq 192$ $280 \leq Re \leq 3800$ $40 \leq Pr \leq 160$ $1 \cdot 10^3 \leq Gr \leq 2.8 \times 10^4$ $1.2 \leq \mu_b/\mu_w \leq 3.8$
Ghajar and Tam	$\bar{N}u_{tr} = Nu_l + \left\{ e^{\frac{a-Re}{b}} + Nu_t^c \right\}^c$	UHF transitional	$5 \leq Pr \leq 55$ $4 \cdot 10^3 \leq Gr \leq 2.5 \times 10^5$ $1.2 \leq \mu_b/\mu_w \leq 2.6$
Ghajar and Tam	$\bar{N}u_t = 0.023Re^{0.8}Pr^{0.385} \dots \\ (L/D)^{-0.0054} \left( \frac{\mu_b}{\mu_w} \right)^{0.14}$	UHF turbulent	$7 \cdot 10^3 \leq Re \leq 49 \cdot 10^3$ $4 \leq Pr \leq 34$ $1.1 \leq \mu_b/\mu_w \leq 1.7$
Strickland	$\bar{N}u_t = 6.3 + \left[ \frac{0.079f^{0.5}RePr}{(1 + Pr^{0.8})^{5/6}} \right] \\ f^{0.5} = \left[ \frac{1}{2.21 \ln \frac{Re}{7}} \right]$	UHF transitional and turbulent	$3 < Pr < 157.8$ $281 < Re < 5 \cdot 10^4$
Hwang	$\bar{N}u_l = 0.626Ra^{0.269}$	UWT laminar	$10^3 < Ra < 5 \cdot 10^8$
Oliver	$\bar{N}u_l = 1.75 \left( \frac{\mu_b}{\mu_w} \right)^{0.14} [Gz + \dots \\ 0.083(GrPr)^{0.75}]^{1/3}$	UWT laminar	-

**Table B.2.** Nusselt number for **mixed convection** for cylindrical horizontal tube pt2

Author name	correlation	B.C.	Validity interval
Metais	$\bar{Nu}_t = 0.469Re^{0.27}Pr^{0.21} \dots$ $Gr^{0.14}(D/L)^{0.36}$	UWT turbulent	-
Mon et. al. (1966)	$\bar{Nu} = 0.6(GrPrRe)^{0.2} \dots$ $G\left(1 + \frac{1.8}{(GrPrRe)^{0.2}}\right)$	UHF	$100 < Re < 13,000$
	(a) $Nu = [4.364 + 0.00106Re^{0.81} \cdot \dots$ $Pr^{0.45}(1 + 1.14e^{-0.063\frac{x}{D}}) + \dots$ $0.268(GrPr)^{0.25} \cdot \dots$ $(1 - e^{-\frac{0.042x}{D}})] \left(\frac{\mu_b}{\mu_w}\right)^{0.14}$	-	$121 < Re < 2,100$ $3.5 < Pr < 282.4$ $930 < Gr < 67.3 \cdot 10^3$
	(b) $Nu = 0.00392RePr^{\frac{1}{3}} \cdot \dots$	-	$4,600 < Re < 7,000$ $3.5 < Pr < 7.4$
Chen (1988)	$(1 + 1.19e^{-0.308\frac{x}{D}}) \left(\frac{\mu_b}{\mu_w}\right)^{0.14}$	-	$45,570 < Gr < 1.04 \cdot 10^6$ $7,000 < Re < 12.4 \cdot 10^3$
	(c) $Nu = 0.0142Re^{0.86}Pr^{\frac{1}{3}} \cdot \dots$ $(1 + 1.15e^{-\frac{x}{3D}}) \left(\frac{\mu_b}{\mu_w}\right)^{0.14}$	-	$3.5 < Pr < 7.4$ $45,570 < Gr < 1.04 \cdot 10^6$
	(d) $Nu = (1 - y)Nu_{(a)} + yNu_{(b)}$ $y = \left(\frac{Re - 2100}{4600 - 2100}\right)^{0.045}$	-	$2,100 < Re < 4,600$
Petukhov and Polyakov	$\bar{Nu} = 4.36 \left[1 + \frac{Ra}{1.8 \cdot 10^4}\right]^{0.045}$	UHF laminar	-

Table B.3. Nusselt number for forced convection for cylindrical horizontal tube pt1

Laminar regime			
Author name	correlation	B.C.	Validity interval
Meyer	$\bar{N}u = 4.36 + \bar{N}u_1 + \bar{N}u_2$ $\bar{N}u_1 = 1/L(-0.084Pr^{-0.2}L_{tMCD} + \dots$ $0.72Re^{0.54}Pr^{0.34}L_{tMCD}^{0.46})$ $\bar{N}u_2 = 1/L(0.207Gr^{0.305} - \dots$ $1.19Pr^{0.42})(ReD)^{-0.08} \cdot \dots$ $(L - L_{tMCD})$ $L_{tMCD} = \frac{2.4RePr^{0.6}D}{Gr^{0.57}}$	UHF	$3 < Pr_b < 7.4$ $541 < Gr < 4.01 \cdot 10^6$ $467 < Re < 3217$ $2.6 < Gz < 5589$
Engineering Sciences Data Unit (ESDU 2001)	$Nu = [3.66^3 + 0.7^3 + \dots$ $(1.77Gz^{1/3} - 0.7)^3]^{1/3}$		UWT thermal developing
ESDU (2001)	$Nu = [4.364^3 + 1 + \dots$ $(2.117Gz^{1/3} - 0.6)^3]^{1/3}$		UHF thermal developing
ESDU (2001)	$Nu = \left\{ 3.66^3 + 0.7^3 + \dots$ $(1.75Gz^{1/3} - 0.7)^3 + \dots$ $\left[ \frac{4}{\pi} \left( \frac{2}{1 + 22Pr} \right)^{1/6} Gz^{1/2} \right] \right\}^{1/3}$		UWT thermal and velocity developing
ESDU (2001)	$Nu = 0.924Pr^{1/3} \left( \frac{ReD}{x} \right)^{1/2}$		UHF thermal and velocity developing
Churchill (1977)	$\bar{N}u = \begin{cases} 4.364 \\ 3.657 \end{cases}$	UHF UWT	-

**Table B.4.** Nusselt number for **forced convection** for cylindrical horizontal tube pt2

Laminar regime			
Author name	correlation	B.C.	Validity interval
			$0.48 < Pr < 16700$
Sieder Tate	$\bar{N}u = 1.86Gz^{1/3} \left( \frac{\mu_b}{\mu_w} \right)^{0.14}$	UWT thermal and velocity developing	$0.0044 < \frac{\mu_b}{\mu_w} < 9.75$ $Gz^{1/3} < 2$
Hausen	$\bar{N}u = 3.66 + \frac{0.023Gz}{1 + 0.04Gz^{2/3}} \left( \frac{\mu_b}{\mu_w} \right)^{0.14}$	UWT developed velocity	$Pr > 0.7$
Hausen	$\bar{N}u = 4.36 + \frac{0.036Gz}{1 + 0.0011Gz} \left( \frac{\mu_b}{\mu_w} \right)^{0.14}$	UHF developing velocity	$Pr = 0.7$
Hausen	$\bar{N}u = 1.3 \left( \frac{RePr}{L/D} \right)^{0.33}$	UHF	$\frac{L/D}{RePr} < 0.01$

Table B.5. Nusselt number for forced convection for cylindrical horizontal tube pt3

turbulent regime			
Author name	correlation	B.C.	Validity interval
Meyer	$\bar{N}u = (0.417(Re - 1000)^{0.499} - \dots 8.2)Pr^{0.42}$	UHF	$2804 > Re > 9787$ $5.5 < Pr < 6.9$ $8.9 \cdot 10^2 < Gr < 1.4 \cdot 10^4$
Colburn and du Pont de (1933)	$\bar{N}u = 0.125RePr^{1/3}$	-	$Re > 10^5$ $0.7 < Pr < 160$
Dittus and Boelter (1930)	$\bar{N}u = 0.023Re^{4/5}Pr^n$ $n = 0.4$ for the fluid being heated; $n = 0.3$ for the fluid being cooled	UHF	$2500 < Re < 1.24 \cdot 10^5$ $0.7 < Pr < 120$
Sieder Tate (1936)	$\bar{N}u = 0.027Re^{4/5}Pr^{1/3} \left(\frac{\mu_b}{\mu_w}\right)^{0.14}$	UWT	$Re > 10^5$ $0.7 < Pr < 17600$
Hausen (1959)	$Nu = 0.037(Re^{0.75} - 180)Pr^{0.42} \cdot \dots \left[1 + \left(\frac{x}{D}\right)^{2/3}\right]$	-	-
First Petukhov (1970)	$\bar{N}u = \frac{f/8RePr}{1.07 + 12.7(f/8)^{1/2}(Pr^{2/3} - 1)} \cdot \dots \left(\frac{\mu_b}{\mu_w}\right)^n$ $n = 0.11$ for heating $n = 0.25$ for cooling	-	$10^4 < Re < 5 \cdot 10^6$ $0.7 < Pr < 16700$
Gnielinski (1976)	$\bar{N}u = \frac{\frac{f}{8}(Re - 1000)Pr_b(1 + (\frac{D}{L})^{2/3})}{1 + 12.7(\frac{f}{8})^{1/2}(Pr_b^{2/3} - 1)} \cdot \dots \left(\frac{Pr_b}{Pr_w}\right)^{0.11}$ $f = (1.82\log(Re) - 1.64)^{-2}$	UHF developing velocity	$3 \cdot 10^3 < Re < 5 \cdot 10^6$ $0.5 < Pr < 2000$
Gnielinski (1976)	$\bar{N}u = \frac{\frac{f}{2}(Re - 1000)Pr_b}{1 + 12.7(\frac{f}{2})^{1/2}(Pr_b^{2/3} - 1)} \cdot \dots \left(\frac{Pr_b}{Pr_w}\right)^{0.11}$ $f = (1.58\log(Re) - 3.28)^{-2}$	UHF developed velocity	$3 \cdot 10^3 < Re < 5 \cdot 10^6$ $0.5 < Pr < 2000$
churchill (1977)	$\bar{N}u = Nu_0 \frac{0.079(\frac{f}{8})^{1/2}RePr}{(1 + Pr^{4/5})^{5/6}}$	-	-
Ghajar and Tam (1994)	$\bar{N}u = 0.023Re^{4/5}Pr^{0.385} \cdot \dots \frac{x}{D}^{-0.0054} \left(\frac{\mu_b}{\mu_w}\right)^{0.14}$	UHF	$1.1 < \frac{\mu_b}{\mu_w} < 1.7$ $3 < x/D < 192$ $7 \cdot 10^3 < Re < 49 \cdot 10^3$ $4 < Pr < 34$

**Table B.6.** Nusselt number for **forced convection** for cylindrical horizontal tube pt3

<b>transitional regime</b>			
<b>Author name</b>	<b>correlation</b>	<b>B.C.</b>	<b>Validity interval</b>
Meyer	$\bar{N}u_{tr} = (0.00108Re - 2.49) \cdot \dots$ $Gr^{-0.04} Pr^2$	UWT transitional	$5.4 < Pr_b < 6.8$ $2.8 \cdot 10^4 < Gr < 3.2 \cdot 10^4$ $2520 < Re < 3361$
Ghajar and Tam	$\bar{N}u_{tr} = Nu_l + \left\{ e^{\frac{a-Re}{b}} + Nu_t^c \right\}^c$	UHF transitional	$1.6 \cdot 10^3 \leq Re \leq 10.7 \cdot 10^3$ $5 \leq Pr \leq 55$ $4 \cdot 10^3 \leq Gr \leq 2.5 \times 10^5$ $1.2 \leq \mu_b/\mu_w \leq 2.6$
Churchill (1977)	$\bar{N}u_{tr} = \left\{ \bar{N}u_l^{10} + \left[ \frac{e^{\frac{2200-R}{365}}}{\bar{N}u_l^2} + \frac{1}{\bar{N}u_t^2} \right]^{-5} \right\}^{-1/10}$ <i>where</i> : $\bar{N}u_l = 4.364$ $\bar{N}u_t = 6.3 + \frac{0.079f^{0.5} Re Pr}{(1 + Pr^{0.8})^{5/6}}$ $f^{0.5} = \frac{1}{2.21 \ln(Re/7)}$	UHF	<i>all Pr</i> $2,100 \leq Re \leq 10^6$ <i>transition flow regime</i>

**Table B.7.** Nusselt number for **natural convection** for cylindrical horizontal tube

<b>Author name</b>	<b>correlation</b>	<b>B.C.</b>	<b>Validity interval</b>
Ludovisi 2013	$\bar{N}u = 1.15 Ra^{0.22}$	UWT	$3 \cdot 10^4 \leq Ra \leq 10^{11}$ $1 \leq Pr \leq 20$



## Appendix C

# LFR wall temperature and Re number matrix

Here as follow are listed all the tables obtained by the run of the simulations aimed at assessing the wall temperature of the LFR using the Forristall model and the improved version of it. Moreover the respective Reynolds number is shown to assess which run is in laminar or turbulent regime. For sake of clarity, in the first column is reported only the DNI and not the "load coefficient" which is more understandable as order of magnitude. In these table 20 thermal nodes have been used.

DNI (W/m <sup>2</sup> )	inlet temperature (°C)										
	0	30	60	90	120	150	180	210	240	270	300
200	51.4	77.0	104.1	137.2	163.7	194.6	221.2	246.1	273.5	300.8	328.0
300	71.9	97.1	142.0	158.5	184.1	215.0	236.7	263.7	290.6	317.5	344.4
400	91.5	116.3	154.3	178.7	209.3	234.4	254.8	280.9	307.3	333.7	356.1
500	110.3	150.7	174.0	197.9	228.3	247.1	272.4	298.0	323.6	350.3	360.6
600	147.8	170.1	192.9	222.6	246.6	264.7	289.6	314.6	339.8	365.2	365.2
700	166.7	188.7	211.2	240.6	257.9	281.9	306.3	330.9	356.5	369.7	369.7
800	184.9	206.7	231.9	258.1	275.0	298.7	322.6	346.8	373.6	374.3	374.3
900	202.8	224.2	249.2	269.9	291.7	315.0	338.7	363.2	378.8	378.8	378.8
1000	220.1	241.4	267.6	285.5	308.1	331.1	354.4	380.7	383.3	383.3	383.3

**Table C.1.** LFR wall temperature with inlet HTF velocity of 0.125 (m/s) improved model

DNI (W/m <sup>2</sup> )	inlet temperature (°C)										
	0	30	60	90	120	150	180	210	240	270	300
200	37.5	62.2	88.8	116.2	147.2	173.9	201.7	229.9	258.2	286.6	315.1
300	51.2	75.2	101.3	128.5	159.9	185.2	212.3	240.0	267.8	295.9	324.0
400	63.7	87.4	113.5	140.7	172.1	196.1	222.7	249.8	277.3	305.0	332.8
500	75.5	103.2	125.8	159.6	181.3	206.6	232.8	259.5	286.6	313.9	341.5
600	86.8	116.2	138.1	171.5	191.9	216.8	242.6	268.9	295.7	322.8	350.1
700	97.8	129.7	150.5	183.1	202.2	226.7	252.2	278.2	304.7	331.5	356.9
800	130.0	143.9	162.8	194.2	212.3	236.5	261.6	287.4	313.5	340.1	359.5
900	141.3	156.9	174.8	199.2	222.1	246.0	270.8	296.3	322.3	348.8	362.1
1000	152.1	167.7	186.3	209.0	231.7	255.4	279.9	305.2	330.9	357.4	364.7

**Table C.2.** LFR wall temperature with inlet HTF velocity of 0.25 (m/s) improved model

DNI (W/m <sup>2</sup> )	inlet temperature (°C)										
	0	30	60	90	120	150	180	210	240	270	300
200	31.4	54.8	78.7	106.7	135.0	162.8	191.5	220.5	249.6	278.8	308.0
300	42.4	64.4	86.7	114.9	142.3	170.3	197.4	226.0	254.8	283.8	312.8
400	52.3	72.1	94.6	122.5	149.4	176.8	204.8	231.4	260.0	288.7	317.5
500	61.1	79.1	102.2	129.7	156.4	183.3	210.8	238.0	265.1	293.6	322.2
600	69.7	86.4	109.8	136.7	163.1	189.6	216.8	242.1	270.1	298.4	326.8
700	77.3	93.2	117.4	143.4	168.7	195.8	222.7	247.3	275.1	303.2	331.5
800	85.2	100.1	125.1	149.9	173.4	201.9	228.5	252.4	280.0	307.9	336.1
900	92.5	107.0	133.0	156.2	179.4	206.5	234.2	257.5	284.9	312.7	340.7
1000	100.9	113.8	141.1	162.3	185.2	211.6	239.9	262.6	289.8	317.4	345.2

**Table C.3.** LFR wall temperature with inlet HTF velocity of 0.5 (m/s) improved model

DNI (W/m <sup>2</sup> )	inlet temperature (°C)										
	0	30	60	90	120	150	180	210	240	270	300
200	28.8	47.2	71.4	99.1	127.7	156.8	186.1	215.6	245.1	274.7	304.2
300	39.0	53.6	76.8	103.5	132.4	160.2	189.3	218.5	247.9	277.3	306.8
400	47.8	59.3	82.0	107.8	136.5	163.6	192.4	221.5	250.7	280.0	309.3
500	55.7	64.5	87.0	111.9	140.5	168.6	195.5	224.4	253.4	282.6	311.8
600	63.7	69.8	91.7	116.0	144.4	172.2	198.6	227.3	256.1	285.2	314.4
700	71.1	74.8	96.4	120.0	148.3	175.7	201.6	230.1	258.8	287.8	316.9
800	77.8	79.6	100.8	123.9	152.1	178.6	204.6	233.0	261.6	290.4	319.4
900	85.0	84.1	105.1	127.7	155.9	179.9	207.6	235.8	264.2	293.0	321.8
1000	92.4	88.6	109.2	131.5	159.6	183.1	210.6	238.6	266.9	295.5	324.3

**Table C.4.** LFR wall temperature with inlet HTF velocity of 1 (m/s) improved model

DNI (W/m <sup>2</sup> )	inlet temperature (°C)										
	0	30	60	90	120	150	180	210	240	270	300
200	27.8	42.5	68.0	96.3	125.4	154.7	184.3	213.9	243.5	273.2	302.9
300	38.0	47.7	71.8	99.4	128.0	157.1	186.5	215.9	245.5	275.1	304.7
400	47.1	52.4	75.5	102.4	130.7	159.5	188.6	218.0	247.4	276.9	306.5
500	55.3	56.9	79.1	105.4	134.6	161.8	190.8	220.0	249.3	278.8	308.2
600	62.7	61.0	82.6	108.4	137.5	164.2	193.0	222.0	251.2	280.6	310.0
700	70.1	65.0	86.0	111.3	140.3	166.5	195.1	224.0	253.1	282.4	311.7
800	77.5	69.0	89.3	114.1	143.1	168.8	197.2	226.1	255.0	284.2	313.5
900	85.0	72.9	92.6	116.9	145.8	171.1	199.3	228.0	256.9	286.0	315.2
1000	92.4	76.7	95.8	119.7	148.5	173.3	201.5	230.0	258.8	287.8	317.0

**Table C.5.** LFR wall temperature with inlet HTF velocity of 1.5 (m/s) improved model

DNI (W/m <sup>2</sup> )	inlet temperature (°C)										
	0	30	60	90	120	150	180	210	240	270	300
200	2.03e+02	6.88e+02	1.50e+03	2.65e+03	4.19e+03	6.17e+03	8.63e+03	1.17e+04	1.53e+04	1.97e+04	2.47e+04
300	3.34e+02	9.02e+02	1.79e+03	3.03e+03	4.67e+03	6.74e+03	9.32e+03	1.25e+04	1.63e+04	2.07e+04	2.59e+04
400	4.98e+02	1.15e+03	2.12e+03	3.45e+03	5.17e+03	7.35e+03	1.01e+04	1.33e+04	1.73e+04	2.19e+04	2.71e+04
500	6.93e+02	1.42e+03	2.47e+03	3.89e+03	5.72e+03	8.00e+03	1.08e+04	1.42e+04	1.83e+04	2.30e+04	2.78e+04
600	9.19e+02	1.72e+03	2.86e+03	4.37e+03	6.29e+03	8.69e+03	1.16e+04	1.52e+04	1.93e+04	2.42e+04	2.83e+04
700	1.17e+03	2.06e+03	3.28e+03	4.88e+03	6.91e+03	9.42e+03	1.25e+04	1.61e+04	2.04e+04	2.51e+04	2.86e+04
800	1.46e+03	2.43e+03	3.74e+03	5.43e+03	7.56e+03	1.02e+04	1.34e+04	1.72e+04	2.16e+04	2.58e+04	2.88e+04
900	1.78e+03	2.83e+03	4.22e+03	6.01e+03	8.25e+03	1.10e+04	1.43e+04	1.82e+04	2.26e+04	2.63e+04	2.90e+04
1000	2.13e+03	3.26e+03	4.74e+03	6.63e+03	8.98e+03	1.18e+04	1.53e+04	1.93e+04	2.34e+04	2.67e+04	2.92e+04

Table C.6. LFR Re number with inlet HTF velocity of 0.125 (m/s) improved model

DNI (W/m <sup>2</sup> )	inlet temperature (°C)										
	0	30	60	90	120	150	180	210	240	270	300
200	2.15e+02	1.01e+03	2.47e+03	4.61e+03	7.51e+03	1.13e+04	1.60e+04	2.19e+04	2.91e+04	3.75e+04	4.76e+04
300	3.02e+02	1.18e+03	2.73e+03	4.95e+03	7.96e+03	1.18e+04	1.67e+04	2.27e+04	3.00e+04	3.86e+04	4.87e+04
400	4.06e+02	1.38e+03	3.00e+03	5.31e+03	8.41e+03	1.24e+04	1.73e+04	2.35e+04	3.09e+04	3.96e+04	5.00e+04
500	5.29e+02	1.58e+03	3.29e+03	5.68e+03	8.88e+03	1.29e+04	1.80e+04	2.43e+04	3.18e+04	4.07e+04	5.12e+04
600	6.68e+02	1.81e+03	3.59e+03	6.07e+03	9.36e+03	1.35e+04	1.87e+04	2.51e+04	3.28e+04	4.18e+04	5.24e+04
700	8.23e+02	2.04e+03	3.91e+03	6.49e+03	9.86e+03	1.41e+04	1.95e+04	2.60e+04	3.38e+04	4.30e+04	5.36e+04
800	9.95e+02	2.29e+03	4.24e+03	6.91e+03	1.04e+04	1.48e+04	2.02e+04	2.69e+04	3.48e+04	4.41e+04	5.46e+04
900	1.18e+03	2.56e+03	4.59e+03	7.35e+03	1.09e+04	1.54e+04	2.10e+04	2.78e+04	3.58e+04	4.53e+04	5.53e+04
1000	1.39e+03	2.84e+03	4.95e+03	7.80e+03	1.15e+04	1.61e+04	2.18e+04	2.87e+04	3.69e+04	4.65e+04	5.59e+04

Table C.7. LFR Re number with inlet HTF velocity of 0.25 (m/s) improved model

DNI (W/m <sup>2</sup> )	inlet temperature (°C)										
	0	30	60	90	120	150	180	210	240	270	300
200	2.95e+02	1.70e+03	4.46e+03	8.57e+03	1.42e+04	2.16e+04	3.09e+04	4.24e+04	5.65e+04	7.33e+04	9.32e+04
300	3.62e+02	1.86e+03	4.71e+03	8.90e+03	1.46e+04	2.21e+04	3.15e+04	4.32e+04	5.74e+04	7.43e+04	9.44e+04
400	4.31e+02	2.02e+03	4.95e+03	9.23e+03	1.50e+04	2.26e+04	3.21e+04	4.40e+04	5.83e+04	7.53e+04	9.56e+04
500	5.14e+02	2.19e+03	5.20e+03	9.57e+03	1.55e+04	2.31e+04	3.28e+04	4.47e+04	5.92e+04	7.64e+04	9.68e+04
600	6.03e+02	2.37e+03	5.46e+03	9.91e+03	1.59e+04	2.37e+04	3.34e+04	4.55e+04	6.01e+04	7.74e+04	9.80e+04
700	7.04e+02	2.56e+03	5.73e+03	1.03e+04	1.64e+04	2.42e+04	3.41e+04	4.63e+04	6.10e+04	7.85e+04	9.92e+04
800	8.13e+02	2.75e+03	6.01e+03	1.06e+04	1.68e+04	2.48e+04	3.48e+04	4.71e+04	6.20e+04	7.96e+04	1.00e+05
900	9.29e+02	2.96e+03	6.29e+03	1.10e+04	1.73e+04	2.54e+04	3.55e+04	4.79e+04	6.29e+04	8.07e+04	1.02e+05
1000	1.06e+03	3.17e+03	6.59e+03	1.14e+04	1.78e+04	2.59e+04	3.62e+04	4.88e+04	6.39e+04	8.18e+04	1.03e+05

Table C.8. LFR Re number with inlet HTF velocity of 0.5 (m/s) improved model

DNI (W/m <sup>2</sup> )	inlet temperature (°C)										
	0	30	60	90	120	150	180	210	240	270	300
200	4.95e+02	3.12e+03	8.47e+03	1.65e+04	2.76e+04	4.21e+04	6.05e+04	8.35e+04	1.12e+05	1.45e+05	1.84e+05
300	5.37e+02	3.25e+03	8.69e+03	1.68e+04	2.80e+04	4.26e+04	6.11e+04	8.42e+04	1.12e+05	1.46e+05	1.86e+05
400	5.90e+02	3.39e+03	8.92e+03	1.72e+04	2.84e+04	4.31e+04	6.18e+04	8.50e+04	1.13e+05	1.47e+05	1.87e+05
500	6.58e+02	3.55e+03	9.17e+03	1.75e+04	2.88e+04	4.37e+04	6.24e+04	8.57e+04	1.14e+05	1.48e+05	1.88e+05
600	7.24e+02	3.71e+03	9.41e+03	1.78e+04	2.92e+04	4.42e+04	6.30e+04	8.65e+04	1.15e+05	1.49e+05	1.89e+05
700	7.90e+02	3.87e+03	9.66e+03	1.81e+04	2.97e+04	4.47e+04	6.37e+04	8.73e+04	1.16e+05	1.50e+05	1.90e+05
800	8.61e+02	4.03e+03	9.90e+03	1.85e+04	3.01e+04	4.53e+04	6.43e+04	8.81e+04	1.17e+05	1.51e+05	1.92e+05
900	9.41e+02	4.20e+03	1.02e+04	1.88e+04	3.05e+04	4.58e+04	6.50e+04	8.88e+04	1.18e+05	1.52e+05	1.93e+05
1000	1.03e+03	4.38e+03	1.04e+04	1.91e+04	3.10e+04	4.63e+04	6.56e+04	8.96e+04	1.19e+05	1.53e+05	1.94e+05

Table C.9. LFR Re number with inlet HTF velocity of 1 (m/s) improved model

DNI (W/m <sup>2</sup> )	inlet temperature (°C)										
	0	30	60	90	120	150	180	210	240	270	300
200	7.08e+02	4.56e+03	1.25e+04	2.45e+04	4.10e+04	6.28e+04	9.02e+04	1.25e+05	1.67e+05	2.16e+05	2.76e+05
300	7.43e+02	4.68e+03	1.27e+04	2.48e+04	4.14e+04	6.32e+04	9.08e+04	1.25e+05	1.67e+05	2.17e+05	2.77e+05
400	7.83e+02	4.81e+03	1.29e+04	2.51e+04	4.18e+04	6.37e+04	9.14e+04	1.26e+05	1.68e+05	2.18e+05	2.78e+05
500	8.30e+02	4.94e+03	1.31e+04	2.54e+04	4.22e+04	6.42e+04	9.21e+04	1.27e+05	1.69e+05	2.19e+05	2.79e+05
600	8.85e+02	5.09e+03	1.34e+04	2.57e+04	4.26e+04	6.47e+04	9.27e+04	1.28e+05	1.70e+05	2.20e+05	2.80e+05
700	9.52e+02	5.25e+03	1.36e+04	2.61e+04	4.30e+04	6.53e+04	9.33e+04	1.28e+05	1.71e+05	2.21e+05	2.82e+05
800	1.02e+03	5.41e+03	1.39e+04	2.64e+04	4.34e+04	6.58e+04	9.39e+04	1.29e+05	1.72e+05	2.22e+05	2.83e+05
900	1.09e+03	5.57e+03	1.41e+04	2.67e+04	4.39e+04	6.63e+04	9.46e+04	1.30e+05	1.73e+05	2.23e+05	2.84e+05
1000	1.15e+03	5.73e+03	1.44e+04	2.70e+04	4.43e+04	6.69e+04	9.52e+04	1.31e+05	1.73e+05	2.24e+05	2.85e+05

Table C.10. LFR Re number with inlet HTF velocity of 1.5 (m/s) improved model

DNI (W/m <sup>2</sup> )	inlet temperature (°C)										
	0	30	60	90	120	150	180	210	240	270	300
200	278.8	301.0	322.0	330.4	215.4	232.6	253.6	276.5	300.4	324.7	349.3
300	375.7	392.8	409.2	410.6	251.7	267.2	286.7	307.9	330.5	353.9	377.5
400	449.6	463.2	473.5	474.0	284.2	298.9	317.2	337.6	359.5	382.1	403.4
500	508.1	519.4	525.8	525.6	316.3	328.5	346.2	366.5	387.6	409.2	421.0
600	556.4	566.1	570.3	569.9	349.9	357.1	374.9	394.2	414.6	435.2	438.3
700	597.5	605.9	607.5	608.1	384.0	384.8	402.2	420.8	440.4	455.4	455.4
800	633.3	640.8	641.0	641.0	416.6	411.4	428.3	446.6	465.3	472.1	472.1
900	665.1	671.9	671.6	671.2	447.6	437.1	453.3	471.1	488.6	488.6	488.6
1000	693.7	699.1	698.5	698.6	477.2	461.5	477.8	494.7	504.9	504.9	504.9

**Table C.11.** LFR wall temperature with inlet HTF velocity of 0.125 (m/s) Forristall model

DNI (W/m <sup>2</sup> )	inlet temperature (°C)										
	0	30	60	90	120	150	180	210	240	270	300
200	266.4	290.3	306.2	155.1	173.5	196.4	221.4	247.6	274.2	301.1	328.2
300	362.3	381.4	391.0	180.7	196.8	217.7	241.3	266.3	292.1	318.2	344.7
400	436.6	452.0	457.9	203.7	218.2	237.9	260.4	284.4	309.4	334.9	361.0
500	495.9	508.8	512.1	226.0	238.3	257.0	278.7	301.9	326.2	351.4	377.1
600	544.9	556.0	558.1	249.6	257.4	275.3	296.3	318.8	342.7	367.8	392.9
700	586.7	596.4	597.1	272.4	275.5	292.9	313.3	335.5	359.2	383.9	408.6
800	623.1	631.7	631.8	294.7	293.0	310.0	329.9	352.1	375.5	399.7	419.0
900	655.4	662.7	662.9	316.3	309.8	326.7	346.3	368.5	391.6	415.2	429.3
1000	684.4	690.6	690.9	337.6	326.0	342.9	362.9	384.7	407.4	430.6	439.5

**Table C.12.** LFR wall temperature with inlet HTF velocity of 0.25 (m/s) Forristall model

DNI (W/m <sup>2</sup> )	inlet temperature (°C)										
	0	30	60	90	120	150	180	210	240	270	300
200	259.9	284.6	107.4	125.4	149.4	175.5	202.8	230.7	258.9	287.3	315.7
300	355.0	375.1	126.2	141.1	163.1	187.9	214.2	241.4	269.0	296.9	325.0
400	429.4	445.9	144.6	155.9	176.2	199.8	225.3	251.9	279.0	306.5	334.2
500	489.1	502.0	163.3	169.6	188.7	211.4	236.1	262.1	288.8	315.9	343.3
600	538.5	549.0	181.4	182.8	200.8	222.6	246.7	272.2	298.4	325.1	352.5
700	580.7	589.4	198.9	195.3	212.4	233.5	257.1	282.1	307.9	334.3	361.5
800	617.4	624.8	216.0	207.2	223.6	244.2	267.2	291.8	317.3	343.5	370.6
900	649.9	656.3	232.7	218.9	234.5	254.6	277.2	301.3	326.6	352.7	379.5
1000	679.2	684.7	249.1	230.0	245.2	264.7	287.0	310.7	335.7	361.9	388.5

**Table C.13.** LFR wall temperature with inlet HTF velocity of 0.5 (m/s) Forristall model

DNI (W/m <sup>2</sup> )	inlet temperature (°C)										
	0	30	60	90	120	150	180	210	240	270	300
200	256.5	74.8	85.3	109.3	136.0	164.0	192.5	221.4	250.4	279.5	308.6
300	351.3	94.4	96.6	118.3	143.8	170.9	198.9	227.3	256.0	284.9	313.8
400	425.7	113.2	107.1	127.0	151.4	177.7	205.1	233.2	261.5	290.2	318.9
500	485.5	131.1	117.0	135.4	158.7	184.4	211.3	239.0	267.0	295.4	324.0
600	535.1	148.5	126.5	143.5	166.0	190.9	217.4	244.7	272.5	300.7	329.1
700	577.4	165.4	135.6	151.4	173.0	197.4	223.4	250.4	277.9	305.9	334.1
800	614.2	181.8	144.3	159.0	179.9	203.7	229.3	256.0	283.3	311.1	339.2
900	646.9	197.9	152.5	166.4	186.7	209.9	235.2	261.6	288.6	316.2	344.2
1000	676.3	213.5	160.4	173.6	193.3	216.1	240.9	267.1	293.9	321.3	349.2

**Table C.14.** LFR wall temperature with inlet HTF velocity of 1 (m/s) Forristall model

DNI (W/m <sup>2</sup> )	inlet temperature (°C)										
	0	30	60	90	120	150	180	210	240	270	300
200	255.4	59.1	77.6	103.5	131.2	159.8	188.8	218.0	247.3	276.7	306.1
300	350.0	71.2	85.8	110.0	136.8	164.7	193.3	222.2	251.3	280.5	309.7
400	424.4	83.2	93.6	116.3	142.2	169.6	197.7	226.3	255.2	284.2	313.4
500	484.3	94.9	101.0	122.4	147.5	174.3	202.1	230.5	259.1	288.0	317.0
600	533.9	106.4	108.1	128.4	152.8	179.1	206.5	234.6	263.0	291.7	320.6
700	576.3	117.5	114.9	134.2	157.9	183.7	210.8	238.6	266.8	295.4	324.2
800	613.2	128.4	121.6	139.8	162.9	188.3	215.1	242.7	270.7	299.1	327.7
900	645.9	139.0	128.1	145.5	167.9	192.9	219.3	246.7	274.5	302.8	331.3
1000	675.4	149.5	134.4	150.9	172.9	197.4	223.5	250.7	278.3	306.4	334.8

**Table C.15.** LFR wall temperature with inlet HTF velocity of 1.5 (m/s) Forristall model

DNI (W/m <sup>2</sup> )	inlet temperature (°C)										
	0	30	60	90	120	150	180	210	240	270	300
200	4.13e+03	5.77e+03	7.72e+03	6.79e+03	6.56e+03	8.42e+03	1.09e+04	1.40e+04	1.77e+04	2.20e+04	2.70e+04
300	7.33e+03	9.36e+03	1.17e+04	8.59e+03	8.25e+03	1.02e+04	1.28e+04	1.60e+04	1.99e+04	2.44e+04	2.89e+04
400	1.05e+04	1.28e+04	1.41e+04	1.03e+04	9.99e+03	1.20e+04	1.48e+04	1.82e+04	2.22e+04	2.67e+04	2.97e+04
500	1.35e+04	1.59e+04	1.62e+04	1.19e+04	1.18e+04	1.39e+04	1.68e+04	2.04e+04	2.45e+04	2.80e+04	2.99e+04
600	1.63e+04	1.88e+04	1.83e+04	1.38e+04	1.36e+04	1.59e+04	1.89e+04	2.26e+04	2.62e+04	2.88e+04	3.00e+04
700	1.88e+04	2.12e+04	1.93e+04	1.56e+04	1.56e+04	1.80e+04	2.11e+04	2.45e+04	2.73e+04	2.92e+04	3.01e+04
800	2.08e+04	2.25e+04	1.99e+04	1.70e+04	1.76e+04	2.01e+04	2.31e+04	2.59e+04	2.81e+04	2.94e+04	3.02e+04
900	2.19e+04	2.28e+04	2.06e+04	1.87e+04	1.97e+04	2.21e+04	2.46e+04	2.68e+04	2.85e+04	2.95e+04	3.02e+04
1000	2.23e+04	2.27e+04	2.11e+04	2.05e+04	2.17e+04	2.37e+04	2.57e+04	2.75e+04	2.88e+04	2.96e+04	3.02e+04

**Table C.16.** LFR Re number with inlet HTF velocity of 0.125 (m/s) Forristall model

DNI (W/m <sup>2</sup> )	inlet temperature (°C)										
	0	30	60	90	120	150	180	210	240	270	300
200	7.48e+03	1.07e+04	8.80e+03	7.05e+03	9.83e+03	1.36e+04	1.85e+04	2.45e+04	3.17e+04	4.02e+04	5.03e+04
300	1.33e+04	1.73e+04	1.12e+04	8.67e+03	1.15e+04	1.54e+04	2.04e+04	2.66e+04	3.41e+04	4.28e+04	5.31e+04
400	1.92e+04	2.37e+04	1.34e+04	1.03e+04	1.32e+04	1.72e+04	2.24e+04	2.88e+04	3.65e+04	4.55e+04	5.58e+04
500	2.47e+04	2.96e+04	1.51e+04	1.20e+04	1.49e+04	1.91e+04	2.45e+04	3.11e+04	3.90e+04	4.82e+04	5.77e+04
600	2.99e+04	3.50e+04	1.75e+04	1.37e+04	1.67e+04	2.11e+04	2.66e+04	3.34e+04	4.15e+04	5.09e+04	5.87e+04
700	3.46e+04	3.99e+04	1.86e+04	1.55e+04	1.86e+04	2.30e+04	2.88e+04	3.57e+04	4.40e+04	5.33e+04	5.93e+04
800	3.89e+04	4.39e+04	2.05e+04	1.73e+04	2.04e+04	2.51e+04	3.10e+04	3.81e+04	4.66e+04	5.50e+04	5.96e+04
900	4.26e+04	4.39e+04	2.21e+04	1.91e+04	2.24e+04	2.71e+04	3.32e+04	4.06e+04	4.92e+04	5.63e+04	5.98e+04
1000	4.40e+04	4.30e+04	2.38e+04	2.10e+04	2.43e+04	2.92e+04	3.55e+04	4.31e+04	5.13e+04	5.71e+04	5.99e+04

**Table C.17.** LFR Re number with inlet HTF velocity of 0.25 (m/s) Forristall model

DNI (W/m <sup>2</sup> )	inlet temperature (°C)										
	0	30	60	90	120	150	180	210	240	270	300
200	1.42e+04	2.05e+04	7.08e+03	1.09e+04	1.66e+04	2.41e+04	3.35e+04	4.53e+04	5.95e+04	7.63e+04	9.63e+04
300	2.53e+04	3.32e+04	8.65e+03	1.25e+04	1.83e+04	2.59e+04	3.55e+04	4.75e+04	6.20e+04	7.91e+04	9.94e+04
400	3.65e+04	4.55e+04	1.03e+04	1.41e+04	2.00e+04	2.77e+04	3.76e+04	4.98e+04	6.45e+04	8.20e+04	1.02e+05
500	4.72e+04	5.03e+04	1.19e+04	1.57e+04	2.17e+04	2.96e+04	3.97e+04	5.22e+04	6.71e+04	8.48e+04	1.05e+05
600	5.70e+04	5.43e+04	1.36e+04	1.74e+04	2.35e+04	3.15e+04	4.19e+04	5.46e+04	6.97e+04	8.77e+04	1.09e+05
700	6.62e+04	5.91e+04	1.53e+04	1.91e+04	2.52e+04	3.35e+04	4.40e+04	5.69e+04	7.24e+04	9.06e+04	1.12e+05
800	7.45e+04	6.25e+04	1.71e+04	2.08e+04	2.70e+04	3.55e+04	4.62e+04	5.94e+04	7.51e+04	9.35e+04	1.14e+05
900	8.22e+04	6.33e+04	1.88e+04	2.25e+04	2.89e+04	3.75e+04	4.85e+04	6.18e+04	7.77e+04	9.65e+04	1.16e+05
1000	8.73e+04	6.09e+04	2.06e+04	2.43e+04	3.08e+04	3.96e+04	5.07e+04	6.43e+04	8.05e+04	9.94e+04	1.17e+05

**Table C.18.** LFR Re number with inlet HTF velocity of 0.5 (m/s) Forristall model

DNI (W/m <sup>2</sup> )	inlet temperature (°C)										
	0	30	60	90	120	150	180	210	240	270	300
200	2.76e+04	6.46e+03	1.10e+04	1.90e+04	3.02e+04	4.49e+04	6.34e+04	8.66e+04	1.15e+05	1.48e+05	1.88e+05
300	4.92e+04	8.38e+03	1.25e+04	2.05e+04	3.20e+04	4.69e+04	6.57e+04	8.91e+04	1.17e+05	1.51e+05	1.91e+05
400	7.12e+04	1.04e+04	1.40e+04	2.22e+04	3.37e+04	4.87e+04	6.78e+04	9.15e+04	1.20e+05	1.54e+05	1.95e+05
500	9.21e+04	1.23e+04	1.56e+04	2.37e+04	3.55e+04	5.07e+04	7.00e+04	9.39e+04	1.23e+05	1.57e+05	1.98e+05
600	1.11e+05	1.42e+04	1.72e+04	2.54e+04	3.72e+04	5.26e+04	7.22e+04	9.64e+04	1.26e+05	1.60e+05	2.01e+05
700	1.29e+05	1.62e+04	1.88e+04	2.70e+04	3.90e+04	5.46e+04	7.44e+04	9.89e+04	1.28e+05	1.63e+05	2.05e+05
800	1.46e+05	1.82e+04	2.04e+04	2.88e+04	4.08e+04	5.66e+04	7.67e+04	1.01e+05	1.31e+05	1.67e+05	2.08e+05
900	1.61e+05	2.03e+04	2.21e+04	3.05e+04	4.27e+04	5.86e+04	7.90e+04	1.04e+05	1.34e+05	1.70e+05	2.11e+05
1000	1.74e+05	2.23e+04	2.38e+04	3.23e+04	4.46e+04	6.07e+04	8.13e+04	1.07e+05	1.37e+05	1.73e+05	2.15e+05

**Table C.19.** LFR Re number with inlet HTF velocity of 1 (m/s) Forristall model

DNI (W/m <sup>2</sup> )	inlet temperature (°C)										
	0	30	60	90	120	150	180	210	240	270	300
200	4.10e+04	7.49e+03	1.51e+04	2.70e+04	4.36e+04	6.56e+04	9.33e+04	1.28e+05	1.70e+05	2.20e+05	2.79e+05
300	7.31e+04	9.32e+03	1.66e+04	2.87e+04	4.55e+04	6.76e+04	9.55e+04	1.30e+05	1.73e+05	2.23e+05	2.83e+05
400	1.06e+05	1.10e+04	1.81e+04	3.03e+04	4.74e+04	6.97e+04	9.79e+04	1.33e+05	1.76e+05	2.26e+05	2.86e+05
500	1.37e+05	1.29e+04	1.97e+04	3.19e+04	4.92e+04	7.17e+04	1.00e+05	1.36e+05	1.78e+05	2.29e+05	2.90e+05
600	1.66e+05	1.48e+04	2.12e+04	3.36e+04	5.10e+04	7.37e+04	1.02e+05	1.38e+05	1.81e+05	2.33e+05	2.93e+05
700	1.92e+05	1.65e+04	2.29e+04	3.52e+04	5.29e+04	7.57e+04	1.05e+05	1.41e+05	1.84e+05	2.36e+05	2.97e+05
800	2.17e+05	1.85e+04	2.45e+04	3.69e+04	5.47e+04	7.77e+04	1.07e+05	1.43e+05	1.87e+05	2.39e+05	3.00e+05
900	2.40e+05	2.03e+04	2.61e+04	3.86e+04	5.66e+04	7.98e+04	1.09e+05	1.46e+05	1.90e+05	2.42e+05	3.04e+05
1000	2.60e+05	2.23e+04	2.78e+04	4.04e+04	5.84e+04	8.19e+04	1.12e+05	1.48e+05	1.93e+05	2.45e+05	3.07e+05

**Table C.20.** LFR Re number with inlet HTF velocity of 1.5 (m/s) Forristall model

# Bibliography

- [1] Aavid Thermacore | Boyd Corporation. Available from: <https://www.boydcorp.com/thermacore.html>.
- [2] API Standard 520 Sizing, Selection, and Installation of Pressure-relieving Devices, Part II-Installation. Tech. rep. Available from: [www.api.org](http://www.api.org).
- [3] Archimede Solar Energy. Available from: [http://www.archimedesolarenergy.it/it/\\_prodotti.htm](http://www.archimedesolarenergy.it/it/_prodotti.htm).
- [4] ARPA-E | FOCUS. Available from: <https://arpa-e.energy.gov/?q=arpa-e-programs/focus>.
- [5] Capstone Turbine Corporation (CPST). Available from: <https://www.capstoneturbine.com/>.
- [6] Data - Eurostat. Available from: <https://ec.europa.eu/eurostat/web/energy/data>.
- [7] Data & Statistics - IEA. Available from: [https://www.iea.org/data-and-statistics?country=WORLD{&}fuel=Energysupply{&}indicator=Totalprimaryenergysupply\(TPES\)bysource](https://www.iea.org/data-and-statistics?country=WORLD{&}fuel=Energysupply{&}indicator=Totalprimaryenergysupply(TPES)bysource).
- [8] Department of Energy. Available from: <https://www.energy.gov/>.
- [9] Design and simulation of a prototype of a small-scale solar CHP system based on evacuated flat-plate solar collectors and Organic Rankine Cycle | Request PDF. Available from: <https://www.researchgate.net/publication/311450974{&}Design{&}and{&}simulation{&}of{&}a{&}prototype{&}of{&}a{&}small-scale{&}>
- [10] EES: Engineering Equation Solver | F-Chart Software : Engineering Software. Available from: <http://www.fchart.com/ees/>.
- [11] Electricity price statistics - Statistics Explained. Available from: <https://ec.europa.eu/eurostat/statistics-explained/index.php/Electricity{&}price{&}statistics>.
- [12] Electricity use per household | Electricity Consumption Efficiency| WEC. Available from: <https://www.enerdata.net/consulting/energy-efficiency-evaluation.html>.
- [13] Elianto S.R.L - Home. Available from: <http://www.eliantocsp.it/index.php/it/>.

- [14] ENEA Agenzia nazionale per le nuove tecnologie, l'energia e lo sviluppo economico sostenibile. Available from: <https://www.enea.it/it>.
- [15] Energy efficient buildings | Energy. Available from: <https://ec.europa.eu/energy/topics/energy-efficiency/energy-efficient-buildings{ }en?redir=1>.
- [16] EnergyPlus | EnergyPlus. Available from: <https://energyplus.net/>.
- [17] ENOGIA | The small turbine ORC company. Available from: <http://enogia.com/wp/7-2-5/>.
- [18] EU Buildings Database | Energy. Available from: <https://ec.europa.eu/energy/eu-buildings-database{ }en?redir=1>.
- [19] Final energy consumption by sector and fuel in Europe — European Environment Agency. Available from: <https://www.eea.europa.eu/data-and-maps/indicators/final-energy-consumption-by-sector-10/assessment>.
- [20] Immersion Cooling - 3M Novec | 3M United Kingdom. Available from: <https://www.3m.co.uk/3M/en{ }GB/novec-uk/applications/immersion-cooling/>.
- [21] Innova-Microsolar. Available from: <http://innova-microsolar.eu/>.
- [22] Kyoto Protocol - Targets for the first commitment period | UNFCCC. Available from: <https://unfccc.int/process-and-meetings/the-kyoto-protocol/what-is-the-kyoto-protocol/kyoto-protocol-targets-for-the-first-commitment-period>.
- [23] MathWorks - Creatori di MATLAB e Simulink - MATLAB e Simulink - MATLAB & Simulink. Available from: <https://it.mathworks.com/>.
- [24] Natural gas price statistics - Statistics Explained. Available from: <https://ec.europa.eu/eurostat/statistics-explained/index.php/Natural{ }gas{ }price{ }statistics>.
- [25] NIST & The Smart Grid | NIST. Available from: <https://www.nist.gov/el/smart-grid/about-smart-grid/nist-and-smart-grid>.
- [26] Northumbria University. Available from: <https://www.northumbria.ac.uk/>.
- [27] Paris Agreement | Climate Action. Available from: <https://ec.europa.eu/clima/policies/international/negotiations/paris{ }en>.
- [28] Rigid conduit for fluid flow in thermal liquid systems - MATLAB - MathWorks Italia. Available from: <https://it.mathworks.com/help/physmod/simscape/ref/pipet1.html>.
- [29] SolTrace | Concentrating Solar Power | NREL. Available from: <https://www.nrel.gov/csp/soltrace.html>.

- [30] S.TRA.TE.G.I.E. srl. Available from: <http://www.strategiesrl.com/eng/Default.aspx>.
- [31] SWEP brazed plate heat exchangers - SWEP. Available from: <https://www.swep.net/>.
- [32] Thermac, Air handling. Available from: <http://www.thermac.it/>.
- [33] Therminol 62 | High-Performance Heat Transfer Fluids. Available from: <https://www.therminol.com/products/Therminol-62>.
- [34] Therminol® VP1 Heat Transfer Fluid | TDS | Eastman Chemical Company. Available from: [https://productcatalog.eastman.com/tds/ProdDatasheet.aspx?product=71093459#{#}\\_{\\_}ga=2.109130758.269779649.1594215338-434036767.1594215338](https://productcatalog.eastman.com/tds/ProdDatasheet.aspx?product=71093459#{#}_{_}ga=2.109130758.269779649.1594215338-434036767.1594215338).
- [35] TRNSYS : Transient System Simulation Tool. Available from: <http://www.trnsys.com/>.
- [36] Universitat de Lleida. Available from: <http://www.udl.cat/ca/>.
- [37] Welcome to CoolProp — CoolProp 6.4.0 documentation. Available from: <http://www.coolprop.org/>.
- [38] Yazaki Energy Systems, Inc. Available from: <http://www.yazakienergy.com/>.
- [39] DIRECTIVE 2004/8/EC OF THE EUROPEAN PARLIAMENT AND OF THE COUNCIL of 11 February 2004 on the promotion of cogeneration based on a useful heat demand in the internal energy market and amending Directive 92/42/EEC. Tech. rep. (2004).
- [40] Doc. CEN/TC 228 N556 CEN/TC 228 CEN/TC 228 WI 032 Heating systems in buildings-Method for calculation of system energy requirements and system efficiencies-Part 3-1 Domestic hot water systems, characterisation of needs (tapping requirements) Einführendes. Tech. rep. (2006).
- [41] DIRECTIVE 2009/28/EC OF THE EUROPEAN PARLIAMENT AND OF THE COUNCIL of 23 April 2009 on the promotion of the use of energy from renewable sources and amending and subsequently repealing Directives 2001/77/EC and 2003/30/EC (2009). Available from: <https://eur-lex.europa.eu/legal-content/EN/TXT/HTML/?uri=CELEX:32009L0028{&}from=ES>.
- [42] Renewables 2019 Global Status Report. Tech. Rep. JuNE, REN21 (2019).
- [43] Special features Type 3374 Electric Actuator. Tech. rep. (2019). Available from: [www.samsongroup.com](http://www.samsongroup.com).
- [44] ABBAS, R., MUÑOZ, J., AND MARTÍNEZ-VAL, J. Steady-state thermal analysis of an innovative receiver for linear Fresnel reflectors. *Applied Energy*, **92** (2012), 503. Available from: <https://linkinghub.elsevier.com/retrieve/pii/S0306261911007768>, doi:10.1016/j.apenergy.2011.11.070.

- [45] ABOELWAFI, O., FATEEN, S. E. K., SOLIMAN, A., AND ISMAIL, I. M. A review on solar Rankine cycles: Working fluids, applications, and cycle modifications. *Renewable and Sustainable Energy Reviews*, **82** (2018), 868. doi:10.1016/j.rser.2017.09.097.
- [46] AICHMAYER, L., SPELLING, J., AND LAUMERT, B. Preliminary design and analysis of a novel solar receiver for a micro gas-turbine based solar dish system. *Solar Energy*, **114** (2015), 378. doi:10.1016/j.solener.2015.01.013.
- [47] AL JUBORI, A., DAABO, A., AL-DADAH, R. K., MAHMOUD, S., AND ENNIL, A. B. Development of micro-scale axial and radial turbines for low-temperature heat source driven organic Rankine cycle. *Energy Conversion and Management*, **130** (2016), 141. doi:10.1016/j.enconman.2016.10.043.
- [48] ANDERSON, B. Brayton-cycle baseload power tower CSP system project report. Tech. Rep. December (2013). Available from: <http://www.osti.gov/scitech/biblio/1166984>, doi:10.2172/1166984.
- [49] ANGRISANI, G., ROSELLI, C., SASSO, M., AND TARIELLO, F. Dynamic performance assessment of a micro-trigeneration system with a desiccant-based air handling unit in Southern Italy climatic conditions. *Energy Conversion and Management*, **80** (2014), 188. doi:10.1016/j.enconman.2014.01.028.
- [50] ANTONELLI, M., BACCIOLI, A., FRANCESCONI, M., AND DESIDERI, U. Dynamic modelling of a low-concentration solar power plant: A control strategy to improve flexibility. *Renewable Energy*, **95** (2016), 574. doi:10.1016/j.renene.2016.04.053.
- [51] ARTECONI, A., ET AL. Multi-Country Analysis on Energy Savings in Buildings by Means of a Micro-Solar Organic Rankine Cycle System: A Simulation Study. *Environments*, **5** (2018), 119. Available from: <http://www.mdpi.com/2076-3298/5/11/119>, doi:10.3390/environments5110119.
- [52] ARTECONI, A., ET AL. Multi-Country Analysis on Energy Savings in Buildings by Means of a Micro-Solar Organic Rankine Cycle System: A Simulation Study. *Environments*, (2018). doi:10.3390/environments5110119.
- [53] ARTECONI, A., ET AL. Simulation analysis of an innovative micro-solar 2kWe Organic Rankine Cycle plant coupled with a multi-apartments building for domestic hot water supply. In *Energy Procedia*, vol. 158, pp. 2225–2230. Elsevier Ltd (2019). doi:10.1016/j.egypro.2019.01.168.
- [54] ASHRAE. Methods of Testing to Determine the Thermal Performance of Solar Collectors (ANSI Approved). Tech. rep., ashrae2003 (2003).
- [55] ATANASIU, B., MAIO, J., AND STANIASZEK, D. Overview of the EU-27 building policies and programmes-WP5 ENTRANZE. Tech. rep. Available from: <http://www.entranze.eu>.
- [56] BACCIOLI, A. AND ANTONELLI, M. Control variables and strategies for the optimization of a WHR ORC system. In *Energy Procedia*, vol. 129, pp. 583–590. Elsevier Ltd (2017). doi:10.1016/j.egypro.2017.09.212.

- [57] BAO, J. AND ZHAO, L. A review of working fluid and expander selections for organic Rankine cycle. *Renewable and Sustainable Energy Reviews*, **24** (2013), 325. Available from: <http://dx.doi.org/10.1016/j.rser.2013.03.040>, doi:10.1016/j.rser.2013.03.040.
- [58] BARBIERI, E. S., SPINA, P. R., AND VENTURINI, M. Analysis of innovative micro-CHP systems to meet household energy demands. *Applied Energy*, **97** (2012), 723. doi:10.1016/j.apenergy.2011.11.081.
- [59] BARBÓN, A., BARBÓN, N., BAYÓN, L., AND SÁNCHEZ-RODRÍGUEZ, J. A. Optimization of the distribution of small scale linear Fresnel reflectors on roofs of urban buildings. *Applied Mathematical Modelling*, **59** (2018), 233. doi:10.1016/j.apm.2018.01.040.
- [60] BELL, I. H., QUOILIN, S., GEORGES, E., BRAUN, J. E., GROLL, E. A., HORTON, W. T., AND LEMORT, V. A generalized moving-boundary algorithm to predict the heat transfer rate of counterflow heat exchangers for any phase configuration. *Applied Thermal Engineering*, **79** (2015), 192. doi:10.1016/j.applthermaleng.2014.12.028.
- [61] BELLOS, E. Progress in the design and the applications of linear Fresnel reflectors – A critical review. *Thermal Science and Engineering Progress*, **10** (2019), 112. doi:10.1016/j.tsep.2019.01.014.
- [62] BELLOS, E., SKALTSAS, I., PLIAKOS, O., AND TZIVANIDIS, C. Energy and financial investigation of a cogeneration system based on linear Fresnel reflectors. *Energy Conversion and Management*, **198** (2019), 111821. doi:10.1016/j.enconman.2019.111821.
- [63] BELLOS, V., NALBANTIS, I., AND TSAKIRIS, G. Friction Modeling of Flood Flow Simulations. *Journal of Hydraulic Engineering*, **144** (2018), 04018073. Available from: [http://ascelibrary.org/doi/10.1061/\(ASCE\)HY.1943-7900.0001540](http://ascelibrary.org/doi/10.1061/(ASCE)HY.1943-7900.0001540), doi:10.1061/(ASCE)HY.1943-7900.0001540.
- [64] BERNSTEIN, L., ET AL. Climate Change 2007 Synthesis Report. Tech. rep., IPCC (2007).
- [65] BIANCHI, M., BRANCHINI, L., DE PASCALE, A., ORLANDINI, V., OTTAVIANO, S., PINELLI, M., SPINA, P. R., AND SUMAN, A. Experimental Performance of a Micro-ORC Energy System for Low Grade Heat Recovery. In *Energy Procedia*, vol. 129, pp. 899–906. Elsevier Ltd (2017). doi:10.1016/j.egypro.2017.09.096.
- [66] BIANCHI, M., DE PASCALE, A., AND MELINO, F. Performance analysis of an integrated CHP system with thermal and Electric Energy Storage for residential application. *Applied Energy*, **112** (2013), 928. doi:10.1016/j.apenergy.2013.01.088.

- [67] BIANCHI, M., DE PASCALE, A., AND SPINA, P. R. Guidelines for residential micro-CHP systems design. *Applied Energy*, **97** (2012), 673. doi:10.1016/j.apenergy.2011.11.023.
- [68] BIANCHI, M., ET AL. Experimental Investigation with Steady-State Detection in a Micro-ORC Test Bench. In *Energy Procedia*, vol. 126, pp. 469–476. Elsevier Ltd (2017). doi:10.1016/j.egypro.2017.08.222.
- [69] BOUVIER, J. L., MICHAUX, G., SALAGNAC, P., KIENTZ, T., AND ROCHIER, D. Experimental study of a micro combined heat and power system with a solar parabolic trough collector coupled to a steam Rankine cycle expander. *Solar Energy*, **134** (2016), 180. doi:10.1016/j.solener.2016.04.028.
- [70] BOYAGHCHI, F. A. AND HEIDARNEJAD, P. Thermo-economic assessment and multi objective optimization of a solar micro CCHP based on Organic Rankine Cycle for domestic application. *Energy Conversion and Management*, **97** (2015), 224. doi:10.1016/j.enconman.2015.03.036.
- [71] BUKER, M. S. AND RIFFAT, S. B. Building integrated solar thermal collectors - A review (2015). doi:10.1016/j.rser.2015.06.009.
- [72] CALIANO, M., BIANCO, N., GRADITI, G., AND MONGIBELLO, L. Economic optimization of a residential micro-CHP system considering different operation strategies. *Applied Thermal Engineering*, **101** (2016), 592. doi:10.1016/j.applthermaleng.2015.11.024.
- [73] CHAITANYA PRASAD, G. S., REDDY, K. S., AND SUNDARARAJAN, T. Optimization of solar linear Fresnel reflector system with secondary concentrator for uniform flux distribution over absorber tube. *Solar Energy*, **150** (2017), 1. doi:10.1016/j.solener.2017.04.026.
- [74] CHANG, H., WAN, Z., ZHENG, Y., CHEN, X., SHU, S., TU, Z., AND CHAN, S. H. Energy analysis of a hybrid PEMFC–solar energy residential micro-CCHP system combined with an organic Rankine cycle and vapor compression cycle. *Energy Conversion and Management*, **142** (2017), 374. doi:10.1016/j.enconman.2017.03.057.
- [75] CHEMISANA, D., ROSELL, J. I., RIVEROLA, A., AND LAMNATOU, C. Experimental performance of a Fresnel-transmission PVT concentrator for building-façade integration. *Renewable Energy*, **85** (2016), 564. doi:10.1016/j.renene.2015.07.009.
- [76] CHENG, Z.-D., HE, Y.-L., AND QIU, Y. A detailed nonuniform thermal model of a parabolic trough solar receiver with two halves and two inactive ends. *Renewable Energy*, **74** (2015), 139. doi:10.1016/J.RENENE.2014.07.060.
- [77] CHERTKOV, M. AND NOVITSKY, N. N. Thermal Transients in District Heating Systems. *Energy*, (2018). doi:10.1016/j.energy.2018.01.049.

- [78] CIMINI, G., CORRADINI, M. L., IPPOLITI, G., ORLANDO, G., AND PIRRO, M. A rapid prototyping scenario for power factor control in permanent magnet synchronous motor drives: Control solutions for interleaved boost converters. *Electric Power Components and Systems*, **42** (2014), 639. Available from: <https://www.tandfonline.com/doi/abs/10.1080/15325008.2014.880969>, doi:10.1080/15325008.2014.880969.
- [79] CIOCCOLANTI, L., TASCIONI, R., AND ARTECONI, A. Mathematical modelling of operation modes and performance evaluation of an innovative small-scale concentrated solar organic Rankine cycle plant. *Applied Energy*, (2018). doi:10.1016/j.apenergy.2018.03.189.
- [80] CIOCCOLANTI, L., TASCIONI, R., AND ARTECONI, A. Mathematical modelling of operation modes and performance evaluation of an innovative small-scale concentrated solar organic Rankine cycle plant. *Applied Energy*, **221** (2018), 464. doi:10.1016/j.apenergy.2018.03.189.
- [81] CIOCCOLANTI, L., TASCIONI, R., BOCCI, E., AND VILLARINI, M. Parametric analysis of a solar Organic Rankine Cycle trigeneration system for residential applications. *Energy Conversion and Management*, **163** (2018), 407. doi:10.1016/j.enconman.2018.02.043.
- [82] COMMISSION ON ENVIRONMENT, W. Report of the World Commission on Environment and Development: Our Common Future Towards Sustainable Development 2. Part II. Common Challenges Population and Human Resources 4. Tech. rep.
- [83] COMODI, G., CIOCCOLANTI, L., AND RENZI, M. Modelling the Italian household sector at the municipal scale: Micro-CHP, renewables and energy efficiency. *Energy*, **68** (2014), 92. doi:10.1016/j.energy.2014.02.055.
- [84] DEL HOYO ARCE, I., HERRERO LÓPEZ, S., LÓPEZ PEREZ, S., RĂMĂ, M., KLOBUT, K., AND FEBRES, J. A. Models for fast modelling of district heating and cooling networks. *Renewable and Sustainable Energy Reviews*, (2018). doi:10.1016/j.rser.2017.06.109.
- [85] DEMIRKAYA, G., PADILLA, R., FONTALVO, A., LAKE, M., AND LIM, Y. Thermal and Exergetic Analysis of the Goswami Cycle Integrated with Mid-Grade Heat Sources. *Entropy*, **19** (2017), 416. Available from: <http://www.mdpi.com/1099-4300/19/8/416>, doi:10.3390/e19080416.
- [86] DÉNARIÉ, A., APRILE, M., AND MOTTA, M. Heat transmission over long pipes: New model for fast and accurate district heating simulations. *Energy*, (2019). doi:10.1016/j.energy.2018.09.186.
- [87] EVERTS, M. AND MEYER, J. P. Flow regime maps for smooth horizontal tubes at a constant heat flux. *International Journal of Heat and Mass Transfer*, **117** (2018), 1274. doi:10.1016/j.ijheatmasstransfer.2017.10.073.

- [88] FENG, Z., BABU, S., BLENCOE, J. G., ANOVITZ, L. M., SANTELLA, M. L., DAVID, S. A., KORINKO, P. S., RIDGE, O., AND RIVER, S. Hydrogen Permeability and Integrity of Hydrogen Delivery Pipelines. Tech. rep., U.S. Department of Energy (2005).
- [89] FERREIRA, A. C., SILVA, J., TEIXEIRA, S., TEIXEIRA, J. C., AND NEBRA, S. A. Assessment of the Stirling engine performance comparing two renewable energy sources: Solar energy and biomass. *Renewable Energy*, **154** (2020), 581. doi:10.1016/j.renene.2020.03.020.
- [90] FONG, K. F. AND LEE, C. K. Investigation of climatic effect on energy performance of trigeneration in building application. (2017). Available from: <http://dx.doi.org/10.1016/j.applthermaleng.2017.08.049>, doi:10.1016/j.applthermaleng.2017.08.049.
- [91] FORRISTALL, R. Heat Transfer Analysis and Modeling of a Parabolic Trough Solar Receiver Implemented in Engineering Equation Solver. Tech. rep. (2003).
- [92] FOSSATI, J. P., GALARZA, A., MARTÍN-VILLATE, A., ECHEVERRÍA, J. M., AND FONTÁN, L. Optimal scheduling of a microgrid with a fuzzy logic controlled storage system. *International Journal of Electrical Power & Energy Systems*, **68** (2015), 61. doi:10.1016/j.ijepes.2014.12.032.
- [93] FREEMAN, J., GUARRACINO, I., KALOGIROU, S. A., AND MARKIDES, C. N. A small-scale solar organic Rankine cycle combined heat and power system with integrated thermal energy storage. *Applied Thermal Engineering*, **127** (2017), 1543. doi:10.1016/j.applthermaleng.2017.07.163.
- [94] FREEMAN, J., HELLGARDT, K., AND MARKIDES, C. N. Working fluid selection and electrical performance optimisation of a domestic solar-ORC combined heat and power system for year-round operation in the UK. *Applied Energy*, **186** (2017), 291. doi:10.1016/j.apenergy.2016.04.041.
- [95] FUBARA, T. C., CECELJA, F., AND YANG, A. Modelling and selection of micro-CHP systems for domestic energy supply: The dimension of network-wide primary energy consumption. *Applied Energy*, **114** (2014), 327. doi:10.1016/j.apenergy.2013.09.069.
- [96] GARCIA-SAEZ, I., MÉNDEZ, J., ORTIZ, C., LONCAR, D., BECERRA, J. A., AND CHACARTEGUI, R. Energy and economic assessment of solar Organic Rankine Cycle for combined heat and power generation in residential applications. *Renewable Energy*, **140** (2019), 461. doi:10.1016/j.renene.2019.03.033.
- [97] GAVAGNIN, G., RECH, S., SÁNCHEZ, D., AND LAZZARETTO, A. Optimum design and performance of a solar dish microturbine using tailored component characteristics. *Applied Energy*, **231** (2018), 660. Available from: <https://doi.org/10.1016/j.apenergy.2018.09.140>, doi:10.1016/j.apenergy.2018.09.140.

- [98] GRIESE, M., HOFFARTH, M. P., SCHNEIDER, J., AND SCHULTE, T. Hardware-in-the-Loop simulation of an optimized energy management incorporating an experimental biocatalytic methanation reactor. *Energy*, **181** (2019), 77. doi:10.1016/j.energy.2019.05.092.
- [99] GUERCIO, A. AND BINI, R. Biomass-fired Organic Rankine Cycle combined heat and power systems. In *Organic Rankine Cycle (ORC) Power Systems: Technologies and Applications*, pp. 527–567. Elsevier Inc. (2017). ISBN 9780081005118. doi:10.1016/B978-0-08-100510-1.00015-6.
- [100] HADORN, J. C. Advanced Storage Concepts for Active Solar Energy. In *EUROSUN 2008; 1st international congress on heating, cooling, and buildings*, pp. 2085–2092 (2008). Available from: <http://www.iea-shc.org/>, doi:978-1-61782-228-5.
- [101] HE, Y. L., XIAO, J., CHENG, Z. D., AND TAO, Y. B. A MCRT and FVM coupled simulation method for energy conversion process in parabolic trough solar collector. *Renewable Energy*, **36** (2011), 976. doi:10.1016/j.renene.2010.07.017.
- [102] HEPNER, H. *Master Thesis Transient Measurement Method for the Determination of Parabolic Trough Receiver Heat Losses under Field Conditions - Testing and Optimization*. master thesis, RWTH AACHEN UNIVERSITY (2014).
- [103] HERNANDEZ, A., DESIDERI, A., GUSEV, S., IONESCU, C. M., DEN BROEK, M. V., QUOILIN, S., LEMORT, V., AND DE KEYSER, R. Design and experimental validation of an adaptive control law to maximize the power generation of a small-scale waste heat recovery system. *Applied Energy*, **203** (2017), 549. doi:10.1016/j.apenergy.2017.06.069.
- [104] HO, T., MAO, S. S., AND GREIF, R. Comparison of the Organic Flash Cycle (OFC) to other advanced vapor cycles for intermediate and high temperature waste heat reclamation and solar thermal energy. *Energy*, **42** (2012), 213. Available from: <http://dx.doi.org/10.1016/j.energy.2012.03.067>, doi:10.1016/j.energy.2012.03.067.
- [105] HUANG, S., WANG, W., BRAMBLEY, M. R., GOYAL, S., AND ZUO, W. An agent-based hardware-in-the-loop simulation framework for building controls. *Energy and Buildings*, **181** (2018), 26. doi:10.1016/j.enbuild.2018.09.038.
- [106] HUANG, Z., LI, Z. Y., AND TAO, W. Q. Numerical study on combined natural and forced convection in the fully-developed turbulent region for a horizontal circular tube heated by non-uniform heat flux. *Applied Energy*, **185** (2017), 2194. doi:10.1016/j.apenergy.2015.11.066.
- [107] HUBER, D. AND WALTER, H. Forced convection heat transfer in the transition region between laminar and turbulent flow for a vertical circular tube. *International Conference on Theoretical and Applied Mechanics, International*

- Conference on Fluid Mechanics and Heat and Mass Transfer - Proceedings*, (2010), 132.
- [108] HUDSON, J. *Numerical Techniques for Conservation Laws with Source Terms*. Ph.D. thesis, University of Reading. Available from: <https://www.reading.ac.uk/web/files/math/J{ }Hudson.pdf>.
- [109] HUNG, T. C., SHAI, T. Y., AND WANG, S. K. A review of organic rankine cycles (ORCs) for the recovery of low-grade waste heat. *Energy*, **22** (1997), 661. doi:10.1016/S0360-5442(96)00165-X.
- [110] HWANG, G. J. AND LAI, H. C. Laminar convective heat transfer in a horizontal isothermal tube for high Rayleigh numbers. *International Journal of Heat and Mass Transfer*, **37** (1994), 1631. doi:10.1016/0017-9310(94)90178-3.
- [111] INCROPERA, F.; DEWITT, D. . *Fundamentals of Heat and Mass Transfer*. sith editi edn. (2006). ISBN \*978-0-471-45728-2. doi:10.1017/CB09781107415324.004.
- [112] INTERNATIONAL, A. *Alloy Digest Sourcebook: Stainless Steels* (2000). ISBN 978-0-87170-649-2. Available from: <https://www.asminternational.org/materialsreference/-/journal{ }content/56/10192/06940G/PUBLICATION>.
- [113] ISLAM, M. T., HUDA, N., ABDULLAH, A. B., AND SAIDUR, R. A comprehensive review of state-of-the-art concentrating solar power (CSP) technologies: Current status and research trends. *Renewable and Sustainable Energy Reviews*, **91** (2018), 987. doi:10.1016/j.rser.2018.04.097.
- [114] JÄGER-WALDAU, A. PV Status Report 2019, JRC science for policy report. Tech. rep., Joint Research Center (2019). Available from: <https://ec.europa.eu/jrc{ }0Ahttps://ec.europa.eu/jrc/sites/jrcsh/files/kjna29938enn{ }1.pdf>, doi:10.2760/326629.
- [115] KACZMARCZYK, T. Z., ŻYWICA, G., AND IHNATOWICZ, E. Experimental study of a low-temperature micro-scale organic Rankine cycle system with the multi-stage radial-flow turbine for domestic applications. *Energy Conversion and Management*, **199** (2019), 111941. doi:10.1016/j.enconman.2019.111941.
- [116] KUMAR, V., SHRIVASTAVA, R. L., AND UNTAWALE, S. P. Fresnel lens: A promising alternative of reflectors in concentrated solar power. *Renewable and Sustainable Energy Reviews*, **44** (2015), 376. doi:10.1016/j.rser.2014.12.006.
- [117] LEBREUX, M., LACROIX, M., AND LACHIVER, G. Fuzzy and feedforward control of an hybrid thermal energy storage system. *Energy and Buildings*, **38** (2006), 1149. doi:10.1016/j.enbuild.2006.02.005.
- [118] LI, J., PEI, G., LI, Y., WANG, D., AND JI, J. Energetic and exergetic investigation of an organic Rankine cycle at different heat source temperatures. *Energy*, **38** (2012), 85. doi:10.1016/j.energy.2011.12.032.

- [119] LI, L., GE, Y. T., LUO, X., AND TASSOU, S. A. Experimental investigations into power generation with low grade waste heat and R245fa Organic Rankine Cycles (ORCs). *Applied Thermal Engineering*, **115** (2017), 815. doi:10.1016/j.applthermaleng.2017.01.024.
- [120] LI, S., MA, H., AND LI, W. Dynamic performance analysis of solar organic Rankine cycle with thermal energy storage. *Applied Thermal Engineering*, **129** (2018), 155. doi:10.1016/j.applthermaleng.2017.10.021.
- [121] LIU, L., ZHU, T., GAO, N., AND GAN, Z. A Review of Modeling Approaches and Tools for the Off-design Simulation of Organic Rankine Cycle. *Journal of Thermal Science*, **27** (2018), 305. doi:10.1007/s11630-018-1023-2.
- [122] LU, S. AND GOSWAMI, D. Y. Theoretical analysis of ammonia-based combined power/refrigeration cycle at low refrigeration temperatures. *International Solar Energy Conference*, (2002), 117. doi:10.1115/SED2002-1042.
- [123] LUDOVISI, D. AND GARZA, I. A. Natural convection heat transfer in horizontal cylindrical cavities: A computational fluid dynamics (CFD) investigation. In *American Society of Mechanical Engineers, Power Division (Publication) POWER*, vol. 2. American Society of Mechanical Engineers (2013). ISBN 9780791856062. doi:10.1115/POWER2013-98014.
- [124] LUND, H., ET AL. The status of 4th generation district heating: Research and results. *Energy*, **164** (2018), 147. Available from: <https://linkinghub.elsevier.com/retrieve/pii/S0360544218317420>, doi:10.1016/j.energy.2018.08.206.
- [125] MAHKAMOV, K., ET AL. Development of a small solar thermal power plant for heat and power supply to domestic and small business buildings. In *American Society of Mechanical Engineers, Power Division (Publication) POWER*, vol. 1. American Society of Mechanical Engineers (ASME) (2018). ISBN 9780791851395. doi:10.1115/POWER2018-7336.
- [126] MAJDI, L., GHAFFARI, A., AND FATEHI, N. Control strategy in hybrid electric vehicle using fuzzy logic controller. In *2009 IEEE International Conference on Robotics and Biomimetics, ROBIO 2009*, pp. 842–847 (2009). ISBN 9781424447756. doi:10.1109/ROBIO.2009.5420563.
- [127] MALDONADO, J., FULLANA-PUIG, M., MARTÍN, M., SOLÉ, A., FERNÁNDEZ, Á., DE GRACIA, A., AND CABEZA, L. Phase Change Material Selection for Thermal Energy Storage at High Temperature Range between 210 °C and 270 °C. *Energies*, **11** (2018), 861. Available from: <http://www.mdpi.com/1996-1073/11/4/861>, doi:10.3390/en11040861.
- [128] MANFRIDA, G., SECCHI, R., AND STAŃCZYK, K. Modelling and simulation of phase change material latent heat storages applied to a solar-powered Organic Rankine Cycle. *Applied Energy*, **179** (2016), 378. doi:10.1016/j.apenergy.2016.06.135.

- [129] MARTINEZ, S., MICHAUX, G., SALAGNAC, P., AND BOUVIER, J. L. Micro-combined heat and power systems (micro-CHP) based on renewable energy sources (2017). doi:10.1016/j.enconman.2017.10.035.
- [130] MARTINEZ, S., MICHAUX, G., SALAGNAC, P., AND FAURE, J.-L. Numerical Investigation of Energy Potential and Performance of a Residential Building-Integrated Solar - Chp System. (2018), 1.
- [131] MEHRFELD, P., ET AL. Dynamic evaluations of heat pump and micro combined heat and power systems using the hardware-in-the-loop approach. *Journal of Building Engineering*, **28** (2020), 101032. doi:10.1016/j.jobe.2019.101032.
- [132] MENG, F., WANG, E., ZHANG, F., AND ZHAO, C. PERFORMANCE COMPARISON OF TRANSCRITICAL CO<sub>2</sub> POWER CYCLE, ORGANIC RANKINE CYCLE AND KALINA CYCLE FOR LOW TEMPERATURE GEOTHERMAL SOURCE. In *5 th International Seminar on ORC Power Systems orc2019* (2019).
- [133] MICHELS, H. AND PITZ-PAAL, R. Cascaded latent heat storage for parabolic trough solar power plants. *Solar Energy*, **81** (2007), 829. doi:10.1016/j.solener.2006.09.008.
- [134] MODI, A., KÆRN, M. R., ANDREASEN, J. G., AND HAGLIND, F. Thermo-economic optimization of a Kalina cycle for a central receiver concentrating solar power plant. *Energy Conversion and Management*, **115** (2016), 276. Available from: <http://dx.doi.org/10.1016/j.enconman.2016.02.063>, doi: 10.1016/j.enconman.2016.02.063.
- [135] MOHAMMADI, E., FADAEINEDJAD, R., AND MOSCHOPOULOS, G. An electromechanical emulation-based study on the behaviour of wind energy conversion systems during short circuit faults. *Energy Conversion and Management*, **205** (2020), 112401. doi:10.1016/j.enconman.2019.112401.
- [136] MURUGAN, S. AND HORÁK, B. A review of micro combined heat and power systems for residential applications (2016). doi:10.1016/j.rser.2016.04.064.
- [137] NI, J., ZHAO, L., ZHANG, Z., ZHANG, Y., ZHANG, J., DENG, S., AND MA, M. Dynamic performance investigation of organic Rankine cycle driven by solar energy under cloudy condition. *Energy*, **147** (2018), 122. doi: 10.1016/j.energy.2018.01.032.
- [138] OKAFOR, I. F., DIRKER, J., AND MEYER, J. P. Influence of circumferential solar heat flux distribution on the heat transfer coefficients of linear Fresnel collector absorber tubes. *Solar Energy*, **107** (2014), 381. doi:10.1016/j.solener.2014.05.011.
- [139] OKAFOR, I. F., DIRKER, J., AND MEYER, J. P. Influence of non-uniform heat flux distributions on the secondary flow, convective heat transfer and friction factors for a parabolic trough solar collector type absorber tube. *Renewable Energy*, **108** (2017), 287. doi:10.1016/j.renene.2017.02.053.

- [140] OMA, J.; MALDONADO, J.M.; DE GRACIA, A.; GIMBERNAT, T.; BOTARGUES, T. C. L. Benchmarking of Energy Storage, Demand of Residential Buildings. In *Proc. 14th Int. Conf. Energy (Enerstock 2018)*. Adana, Turkey (2018).
- [141] OUF MAYYAS, A. R., KUMAR, S., PISU, P., RIOS, J., AND JETHANI, P. Model-based design validation for advanced energy management strategies for electrified hybrid power trains using innovative vehicle hardware in the loop (VHIL) approach. *Applied Energy*, **204** (2017), 287. doi:10.1016/j.apenergy.2017.07.028.
- [142] PADILLA, R. V., DEMIRKAYA, G., GOSWAMI, D. Y., STEFANAKOS, E., AND RAHMAN, M. M. Heat transfer analysis of parabolic trough solar receiver. *Applied Energy*, **88** (2011), 5097. doi:10.1016/j.apenergy.2011.07.012.
- [143] PANGBORN, H., ALLEYNE, A. G., AND WU, N. A comparison between finite volume and switched moving boundary approaches for dynamic vapor compression system modeling. *International Journal of Refrigeration*, **53** (2015), 101. doi:10.1016/j.ijrefrig.2015.01.009.
- [144] PATIL, V. R., BIRADAR, V. I., SHREYAS, R., GARG, P., OROSZ, M. S., AND THIRUMALAI, N. C. Techno-economic comparison of solar organic Rankine cycle (ORC) and photovoltaic (PV) systems with energy storage. *Renewable Energy*, **113** (2017), 1250. doi:10.1016/j.renene.2017.06.107.
- [145] PEI, G., LI, J., LI, Y., WANG, D., AND JI, J. Construction and dynamic test of a small-scale organic rankine cycle. *Energy*, **36** (2011), 3215. doi:10.1016/j.energy.2011.03.010.
- [146] PEREIRA, J. S., RIBEIRO, J. B., MENDES, R., VAZ, G. C., AND ANDRÉ, J. C. ORC based micro-cogeneration systems for residential application - A state of the art review and current challenges (2018). doi:10.1016/j.rser.2018.04.039.
- [147] PETROLLESE, M. AND COCCO, D. Optimal design of a hybrid CSP-PV plant for achieving the full dispatchability of solar energy power plants. *Solar Energy*, **137** (2016), 477. doi:10.1016/j.solener.2016.08.027.
- [148] PRICE, H., LÜPFERT, E., KEARNEY, D., ZARZA, E., COHEN, G., GEE, R., AND MAHONEY, R. Advances in parabolic trough solar power technology. *Journal of Solar Energy Engineering, Transactions of the ASME*, **124** (2002), 109. doi:10.1115/1.1467922.
- [149] PUGI, L., GALARDI, E., CARCASI, C., RINDI, A., AND LUCCHESI, N. Preliminary design and validation of a Real Time model for hardware in the loop testing of bypass valve actuation system. *Energy Conversion and Management*, **92** (2015), 366. doi:10.1016/j.enconman.2014.12.061.
- [150] QIAO, H., AUTE, V., AND RADERMACHER, R. An Improved Moving Boundary Heat Exchanger Model with Pressure Drop. *International Refrigeration and Air Conditioning Conference*, (2014), 1.

- [151] QIAO, H., LAUGHMAN, C. R., AUTE, V., AND RADERMACHER, R. An advanced switching moving boundary heat exchanger model with pressure drop. *International Journal of Refrigeration*, **65** (2016), 154. Available from: <http://dx.doi.org/10.1016/j.ijrefrig.2016.01.026>, doi:10.1016/j.ijrefrig.2016.01.026.
- [152] QUOILIN, S., AUMANN, R., GRILL, A., SCHUSTER, A., LEMORT, V., AND SPLIETHOFF, H. Dynamic modeling and optimal control strategy of waste heat recovery Organic Rankine Cycles. *Applied Energy*, **88** (2011), 2183. doi:10.1016/j.apenergy.2011.01.015.
- [153] QUOILIN, S., BROEK, M. V. D., DECLAYE, S., DEWALLEF, P., AND LEMORT, V. Techno-economic survey of organic rankine cycle (ORC) systems. *Renewable and Sustainable Energy Reviews*, **22** (2013), 168. doi:10.1016/j.rser.2013.01.028.
- [154] QUOILIN, S., OROSZ, M., HEMOND, H., AND LEMORT, V. Performance and design optimization of a low-cost solar organic Rankine cycle for remote power generation. *Solar Energy*, **85** (2011), 955. doi:10.1016/j.solener.2011.02.010.
- [155] RAMOS, A., CHATZOPOULOU, M. A., FREEMAN, J., AND MARKIDES, C. N. Optimisation of a high-efficiency solar-driven organic Rankine cycle for applications in the built environment. (2018). Available from: <http://creativecommons.org/licenses/by/4.0/>, doi:10.1016/j.apenergy.2018.06.059.
- [156] RANIERI, S., PRADO, G. A., AND MACDONALD, B. D. Efficiency reduction in stirling engines resulting from sinusoidal motion. *Energies*, **11** (2018), 1. doi:10.3390/en11112887.
- [157] RATZEL, A. C., HICKOX, C. E., AND GARTLING, D. K. TECHNIQUES FOR REDUCING THERMAL CONDUCTION AND NATURAL CONVECTION HEAT LOSSES IN ANNULAR RECEIVER GEOMETRIES. *J Heat Transfer Trans ASME*, **101** (1979), 108. doi:10.1115/1.3450899.
- [158] REN, J. Sustainability prioritization of energy storage technologies for promoting the development of renewable energy: A novel intuitionistic fuzzy combinative distance-based assessment approach. *Renewable Energy*, **121** (2018), 666. doi:10.1016/j.renene.2018.01.087.
- [159] ROMERO RODRÍGUEZ, L., SALMERÓN LISSÉN, J. M., SÁNCHEZ RAMOS, J., RODRÍGUEZ JARA, E. Á., AND ÁLVAREZ DOMÍNGUEZ, S. Analysis of the economic feasibility and reduction of a building's energy consumption and emissions when integrating hybrid solar thermal/PV/micro-CHP systems. *Applied Energy*, **165** (2016), 828. doi:10.1016/j.apenergy.2015.12.080.
- [160] ROSATO, A., SIBILIO, S., AND CIAMPI, G. Dynamic performance assessment of a building-integrated cogeneration system for an Italian residential application. *Energy and Buildings*, **64** (2013), 343. doi:10.1016/j.enbuild.2013.05.035.

- [161] ROSATO, A., SIBILIO, S., AND SCORPIO, M. Dynamic performance assessment of a residential building-integrated cogeneration system under different boundary conditions. Part I: Energy analysis. *Energy Conversion and Management*, **79** (2014), 731. doi:10.1016/j.enconman.2013.10.001.
- [162] SAMSON AG. T 8136. Tech. rep. (2001). Available from: [www.samson.de](http://www.samson.de).
- [163] SANTOS, J. J., PALACIO, J. C., REYES, A. M., CARVALHO, M., FREIRE, A. J., AND BARONE, M. A. Concentrating Solar Power. Tech. Rep. 2/5, International Renewable Energy Agency (2012). doi:10.1016/B978-0-12-812959-3.00012-5.
- [164] SARBU, I. AND SEBARCHIEVICI, C. A comprehensive review of thermal energy storage. *Sustainability (Switzerland)*, **10** (2018). doi:10.3390/su10010191.
- [165] SEBASTIÁN, A., ABBAS, R., VALDÉS, M., AND CASANOVA, J. Innovative thermal storage strategies for Fresnel-based concentrating solar plants with East-West orientation. *Applied Energy*, **230** (2018), 983. doi:10.1016/j.apenergy.2018.09.034.
- [166] SERRANO-LÓPEZ, R., FRADERA, J., AND CUESTA-LÓPEZ, S. Molten salts database for energy applications. (2013). Available from: <http://arxiv.org/abs/1307.7343><http://dx.doi.org/10.1016/j.cep.2013.07.008>, arXiv:1307.7343, doi:10.1016/j.cep.2013.07.008.
- [167] STATMEYER, J. E. AND CROSS, H. ANALYSIS OF FLOW IN NETWORKS OF CONDUITS OR CONDUCTORS Puca: Tranr-rnu Corra (1936).
- [168] STREICHER, W., BONY, J., CITHERLET, S., HEINZ, A., PUSCHNIG, P., SCHRANZHOFER, H., AND SCHULTZ, J. M. Simulation Models of PCM Storage Units A Report of IEA Solar Heating and Cooling programme-Task 32 "Advanced storage concepts for solar and low energy buildings" Report C5 of Subtask C Contributions from. Tech. rep. (2008). Available from: [www.iwt.tugraz.at](http://www.iwt.tugraz.at).
- [169] STRICKLAND, D. T. *HEAT TRANSFER MEASUREMENTS IN THE TRANSITION REGION FOR A HORIZONTAL CIRCULAR TUBE WITH A SQUARE-EDGED ENTRANCE*. Ph.D. thesis, Oklahoma State University (1990).
- [170] SUGANTHI, L., INIYAN, S., AND SAMUEL, A. A. Applications of fuzzy logic in renewable energy systems – A review. *Renewable and Sustainable Energy Reviews*, **48** (2015), 585. doi:10.1016/j.rser.2015.04.037.
- [171] TACCANI, R., OBI, J. B., DE LUCIA, M., MICHELI, D., AND TONIATO, G. Development and Experimental Characterization of a Small Scale Solar Powered Organic Rankine Cycle (ORC). In *Energy Procedia*, vol. 101, pp. 504–511. Elsevier Ltd (2016). doi:10.1016/j.egypro.2016.11.064.
- [172] TAM, L. M. Transitional heat transfer in plain horizontal tubes. *Heat Transfer Engineering*, **27** (2006), 23. doi:10.1080/01457630600559538.

- [173] TASCIONI, R., CIOCCOLANTI, L., DEL ZOTTO, L., AND HABIB, E. NUMERICAL INVESTIGATION OF PIPELINES MODELING IN SMALL-SCALE CONCENTRATED SOLAR COMBINED HEAT AND POWER PLANTS. *Energies*, (2019).
- [174] TCHANCHE, B. F., LAMBRINOS, G., FRANGOUDAKIS, A., AND PAPADAKIS, G. Low-grade heat conversion into power using organic Rankine cycles - A review of various applications. *Renewable and Sustainable Energy Reviews*, **15** (2011), 3963. doi:10.1016/j.rser.2011.07.024.
- [175] TIAN, Z., PERERS, B., FURBO, S., AND FAN, J. Annual measured and simulated thermal performance analysis of a hybrid solar district heating plant with flat plate collectors and parabolic trough collectors in series. *Applied Energy*, **205** (2017), 417. Available from: <https://doi.org/10.1016/j.apenergy.2017.07.139>, doi:10.1016/j.apenergy.2017.07.139.
- [176] VAN DER HEIJDE, B., ET AL. Dynamic equation-based thermo-hydraulic pipe model for district heating and cooling systems. *Energy Conversion and Management*, (2017). doi:10.1016/j.enconman.2017.08.072.
- [177] VAN ZALK, J. AND BEHRENS, P. The spatial extent of renewable and non-renewable power generation: A review and meta-analysis of power densities and their application in the U.S. *Energy Policy*, **123** (2018), 83. doi:10.1016/j.enpol.2018.08.023.
- [178] VARGAS, J. V. AND BEJAN, A. Thermodynamic optimization of the match between two streams with phase change. *Energy*, **25** (2000), 15. doi:10.1016/S0360-5442(99)00052-3.
- [179] VIJAYARAGHAVAN, S. AND GOSWAMI, D. Y. On evaluating efficiency of a combined power and cooling cycle. *Journal of Energy Resources Technology, Transactions of the ASME*, **125** (2003), 221. doi:10.1115/1.1595110.
- [180] VILLARINI, M., TASCIONI, R., ARTECONI, A., AND CIOCCOLANTI, L. Influence of the incident radiation on the energy performance of two small-scale solar Organic Rankine Cycle trigenerative systems: A simulation analysis. *Applied Energy*, **242** (2019), 1176. doi:10.1016/j.apenergy.2019.03.066.
- [181] VIVIAN, J., DE URIBARRI, P. M. Á., EICKER, U., AND ZARRELLA, A. The effect of discretization on the accuracy of two district heating network models based on finite-difference methods. In *Energy Procedia*, vol. 149, pp. 625–634. Elsevier Ltd (2018). doi:10.1016/j.egypro.2018.08.227.
- [182] WANG, H. AND MENG, H. Improved thermal transient modeling with new 3-order numerical solution for a district heating network with consideration of the pipe wall's thermal inertia. *Energy*, (2018). doi:10.1016/j.energy.2018.06.214.
- [183] WANG, R., JIANG, L., MA, Z., GONZALEZ-DIAZ, A., WANG, Y., AND ROSKILLY, A. Comparative Analysis of Small-Scale Organic Rankine Cycle

- Systems for Solar Energy Utilisation. *Energies*, **12** (2019), 829. Available from: <https://www.mdpi.com/1996-1073/12/5/829>, doi:10.3390/en12050829.
- [184] WANG, Y., TANG, Q., WANG, M., AND FENG, X. Thermodynamic performance comparison between ORC and Kalina cycles for multi-stream waste heat recovery. *Energy Conversion and Management*, **143** (2017), 482. doi:10.1016/j.enconman.2017.04.026.
- [185] WANG, Y., YOU, S., ZHANG, H., ZHENG, X., ZHENG, W., MIAO, Q., AND LU, G. Thermal transient prediction of district heating pipeline: Optimal selection of the time and spatial steps for fast and accurate calculation. *Applied Energy*, (2017). doi:10.1016/j.apenergy.2017.08.061.
- [186] WANG, Z., SUN, S., LIN, X., LIU, C., TONG, N., SUI, Q., AND LI, Z. A remote integrated energy system based on cogeneration of a concentrating solar power plant and buildings with phase change materials. *Energy Conversion and Management*, **187** (2019), 472. doi:10.1016/j.enconman.2019.02.094.
- [187] WEI, L., LEI, Q., ZHAO, J., DONG, H., AND YANG, L. Numerical simulation for the heat transfer behavior of oil pipeline during the shutdown and restart process. *Case Studies in Thermal Engineering*, (2018). doi:10.1016/j.csite.2018.07.002.
- [188] WEI, L., LEI, Q., ZHAO, J., DONG, H., AND YANG, L. Numerical simulation for the heat transfer behavior of oil pipeline during the shutdown and restart process. *Case Studies in Thermal Engineering*, (2018). doi:10.1016/j.csite.2018.07.002.
- [189] WETTER, M. AND GOV, M. GenOpt manual. Tech. rep. (2016). Available from: <http://simulationresearch.lbl.gov>.
- [190] XU, G., SONG, G., ZHU, X., GAO, W., LI, H., AND QUAN, Y. Performance evaluation of a direct vapor generation supercritical ORC system driven by linear Fresnel reflector solar concentrator. *Applied Thermal Engineering*, **80** (2015), 196. doi:10.1016/j.applthermaleng.2014.12.071.
- [191] XU, G., YU, W., GRIFFITH, D., GOLMIE, N., AND MOULEMA, P. Toward Integrating Distributed Energy Resources and Storage Devices in Smart Grid. *IEEE Internet of Things Journal*, **4** (2017), 192. Available from: [/pmc/articles/PMC5774658/?report=abstracthttps://www.ncbi.nlm.nih.gov/pmc/articles/PMC5774658/](https://www.ncbi.nlm.nih.gov/pmc/articles/PMC5774658/), doi:10.1109/JIOT.2016.2640563.
- [192] XU, H., LI, Y., SUN, J., AND LI, L. Transient model and characteristics of parabolic-trough solar collectors: Molten salt vs. synthetic oil. *Solar Energy*, **182** (2019), 182. doi:10.1016/J.SOLENER.2019.02.047.
- [193] XU, L., STEIN, W., KIM, J.-S., TOO, Y. C. S., GUO, M., AND WANG, Z. Transient numerical model for the thermal performance of the solar receiver. *Applied Thermal Engineering*, **141** (2018), 1035. doi:10.1016/J.APPLTHERMALENG.2018.05.112.

- [194] YA., C. *Heat transfer and mass transfer: a practical approach*. McGraw Hill Book Company, 3rd edn. (2006). ISBN 978-0071257398.
- [195] YANG, G. AND ZHAI, X. Q. Optimal design and performance analysis of solar hybrid CCHP system considering influence of building type and climate condition. *Energy*, **174** (2019), 647. doi:10.1016/j.energy.2019.03.001.
- [196] YU, C., XU, J., AND SUN, Y. Transcritical pressure Organic Rankine Cycle (ORC) analysis based on the integrated-average temperature difference in evaporators. *Applied Thermal Engineering*, **88** (2015), 2. Available from: <https://linkinghub.elsevier.com/retrieve/pii/S1359431114010291>, doi:10.1016/j.applthermaleng.2014.11.031.
- [197] YILMAZ, İBRAHİM HALİL SOYLEMEZ, M. S. Thermo-mathematical modeling of parabolic trough collector. *Energy Conversion and Management*, **88** (2014), 768. doi:10.1016/j.enconman.2014.09.031.
- [198] ZEITOUN, O. Heat transfer for laminar flow in partially heated tubes. Tech. rep., King Saud University.
- [199] ZHANG, Y., DENG, S., ZHAO, L., LIN, S., NI, J., MA, M., AND XU, W. Optimization and multi-time scale modeling of pilot solar driven polygeneration system based on organic Rankine cycle. *Applied Energy*, **222** (2018), 396. doi:10.1016/j.apenergy.2018.03.118.
- [200] ZIVIANI, D., BEYENE, A., AND VENTURINI, M. Advances and challenges in ORC systems modeling for low grade thermal energy recovery. *Applied Energy*, **121** (2014), 79. doi:10.1016/j.apenergy.2014.01.074.